Interface Structure and Electronic Properties of $SrTiO_3$ and $YBa_2Cu_3O_{7-\delta}$ Crystals and Thin Films

Dissertation
zur Erlangung des Doktorgrades
des Fachbereichs Physik
der Universität Hamburg

vorgelegt von

Sebastian Thieß
aus Hamburg

Hamburg
2007

Gutachter der Dissertation:	Prof. Dr. R. L. Johnson
	Prof. Dr. K. Scharnberg
Gutachter der Disputation:	Prof. Dr. R. L. Johnson
	Dr. habil. J. Zegenhagen
Datum der Disputation:	31. August 2007
Vorsitzender des Prüfungsausschusses:	Dr. habil. H. D. Rüter
Vorsitzender des Promotionsausschusses:	Prof. Dr. G. Huber
Dekan des Fachbereichs Physik:	Prof. Dr. A. Frühwald

Abstract

Two new extensions of the X-ray standing wave (XSW) technique, made possible by the intense highly collimated X-ray beams from undulators at the ESRF, are described in this thesis. First, the XSW method was applied in a structural study to solve the nucleation mechanism of the high temperature superconductor $YBa_2Cu_3O_{7-\delta}$ on the (001) surface of $SrTiO_3$. Second, the valence electronic structures of $SrTiO_3$ and $YBa_2Cu_3O_{7-\delta}$ were investigated. Finally, recent developments in the field of photoelectron spectroscopy in the hard X-ray region are described.

The X-ray standing wave method is used in combination with fluorescence, Auger or photoelectron spectroscopy and lends very high spatial resolution power to these analytical techniques. Previously, the XSW method has been used for structure determination of surfaces and interfaces. The currently available X-ray intensities permit extensions to the XSW technique. Two recently established applications, described in this thesis, are XSW real space imaging and XSW valence electronic structure analysis.

XSW real space imaging was employed to analyse the atomic structure of 0.5 and 1.0 layers of $YBa_2Cu_3O_{7-\delta}$ deposited on $SrTiO_3$(001). Three-dimensional images of the atomic distributions were reconstructed for each of the elements from experimentally determined Fourier components of the atomic distribution functions. The images confirmed the formation of a perovskite precursor phase prior to the formation of the $YBa_2Cu_3O_{7-\delta}$ phase during the growth of the first monolayer of the film.

XSW valence electronic structure analysis applied to $SrTiO_3$ identified the valence band contributions arising from the strontium, titanium, and oxygen sites of the crystal lattice. Relations between the site-specific valence electronic structure and the lattice structure were established. The experimental results agree very well with predictions by state-of-the-art *ab initio* calculations. X-ray absorption cross sections for valence states of the solid were determined. Applied to $YBa_2Cu_3O_{7-\delta}$, the XSW valence electronic structure analysis revealed the local electronic structures at the two nonequivalent copper sites to be similar, in contrast to theoretical predictions.

Grenzflächenstruktur und elektronische Eigenschaften von $SrTiO_3$ und $YBa_2Cu_3O_{7-\delta}$ Kristallen und dünnen Schichten

Kurzfassung

In der vorliegende Arbeit werden zwei erweiterte Anwendungen der Methode der Stehenden Röntgenwellenfelder (XSW-Methode) vorgestellt, die durch die hohe Brillanz der Undulatorstrahlung am ESRF ermöglicht wurden. Zum einen wurde die XSW-Methode im Rahmen einer strukturellen Studie dazu verwandt, den Aufwachsmechanismus des Hochtemperatur-Supraleiters $YBa_2Cu_3O_{7-\delta}$ auf der (001)-Oberfläche von $SrTiO_3$ zu klären. Zum anderen wurden die valenzelektronischen Strukturen von $SrTiO_3$ und $YBa_2Cu_3O_{7-\delta}$ untersucht. Des weiteren beschäftigt sich diese Arbeit mit jüngsten Entwicklungen auf dem Gebiet der Photoelektronenspektroskopie im harten Röntgenbereich.

Die Methode der Stehenden Röntgenwellenfelder wird in Verbindung mit Fluoreszenz-, Auger- und Photoelektronenspektroskopie benutzt und verleiht diesen analytischen Methoden sehr hohes räumliches Auflösungsvermögen. Bisher wurde die XSW-Methode lediglich für strukturelle Untersuchungen von Oberflächen und Grenzflächen genutzt. Die mittlerweile zur Verfügung stehenden Röntgenlichtintensitäten haben aber eine Erweiterung dieser Technik ermöglicht. Zwei erst in letzter Zeit entwickelte Methoden, angewandt im Rahmen dieser Arbeit, sind die XSW-Bildgebungstechnik und die valenzelektronische Strukturanalyse.

Die XSW-Bildgebungstechnik wurde zur strukturellen Analyse einer 0.5 und einer 1.0 Lagen dicken $YBa_2Cu_3O_{7-\delta}$-Schicht auf $SrTiO_3(001)$ herangezogen. Dreidimensionale Abbildungen der atomaren Verteilungen wurden, basierend auf experimentell ermittelten Fourierkomponenten der atomaren Verteilungsfunktionen, für die einzelnen Elemente rekonstruiert. Die Bilder bestätigten, daß sich vor der Entstehung der endgültigen stabilen $YBa_2Cu_3O_{7-\delta}$-Phase eine Perovskitphase als Vorläufer bildet.

Durch die valenzelektronische Strukturanalyse wurden die Beiträge zum Valenzband von $SrTiO_3$ von den mit Strontium, Titan und Sauerstoff besetzten Gitterplätzen bestimmt. Beziehungen zwischen der lokalen elektronischen Struktur an den Gitterplätzen und der Struktur des Kristallgitters wurden hergestellt. Die experimentellen Ergebnisse stimmen sehr gut mit theoretischen Vorhersagen dem gegenwärtigen Entwicklungsstand entsprechender DFT-Rechnungen überein. Röntgenabsorptions-Wirkungsquerschnitte für Valenzzustände des Festkörpers wurden bestimmt. Im Falle des $YBa_2Cu_3O_{7-\delta}$ ergab die valenzelektronische Strukturanalyse keinerlei Unterschiede zwischen den lokalen valenzelektronischen Strukturen an den beiden nicht-äquivalenten Kupferplätzen. Dies steht im Gegensatz zu theoretischen Vorhersagen.

Contents

List of Figures

List of Tables

Chapter 1

Introduction

New experimental opportunities opened up for physicists in 1994 with the appearance of most brilliant synchrotron light at third generation storage rings. One of the powerful tools for surface science available at synchrotron light sources is the X-ray standing wave (XSW) method. Its strength consists in the very high spatial resolution of the order of 0.01 Å, which the technique lends to common spectroscopic methods, like fluorescence, Auger, or photoelectron spectroscopy. The XSW technique is applicable if the wavelength of the X-rays is of the order of unit cell dimensions, which corresponds to an X-ray photon energy of typically few keV.

The X-ray standing wave method utilizes the spatial intensity modulation of an X-ray interference field, which is typically generated by the coherent superposition of an incident and a Bragg-reflected X-ray beam. By scanning the photon energy or the angle of the incident beam through the range of Bragg reflection, the intensity maxima of the wavefield are moved by half the diffraction plane spacing over the distribution of atoms in the unit cell. The X-ray absorption profile for specific elements, indirectly detected from the fluorescence, Auger or photoelectron signal, exhibits a shape characteristic of the elemental distribution in the unit cell. Selecting the photon energy or the incident angle of the beam within the Bragg range allows positioning the wavefield to preferentially excite individual lattice sites.

Conventionally, the high spatial resolution has been exploited for structural studies only, like the investigation of adsorbed atoms and molecules on well-characterized single crystal surfaces. In order to fully exploit the nowadays available brilliant X-ray beams, the XSW method has been continuously developed and improved. As a consequence, new fields of application for the XSW technique have emerged: Besides extended structural studies, investigations of electronic properties of surfaces and interfaces as well as of bulk material have eventually become possible. This thesis will chiefly deal with two recently established applications of the XSW method: The first one is XSW real space imaging, which is an extension of the conventional XSW application for structure determination. XSW imaging was employed to solve the nucleation mechanism of the high temperature superconductor $YBa_2Cu_3O_{7-\delta}$ (transition temperature $\sim$90 K) on the (001) surface of $SrTiO_3$. The second one is XSW valence electronic structure analysis, which is a means to spatially decompose electronic band structures over the contributing lattice sites. This method was applied to identify the partial density of valence

states contributed by the individual lattice sites for the ternary oxide $SrTiO_3$ and for the more complex oxide $YBa_2Cu_3O_{7-\delta}$. This thesis deals further with the extension of X-ray photoelectron spectroscopy (XPS) into the hard X-ray range up to 13.5 keV. The particularly large bulk sensitivity of hard X-ray photoelectron spectroscopy (HAXPES) was exploited to chemically analyse the reactive $YBa_2Cu_3O_{7-\delta}(001)$ surface prepared under less stringent *ex situ* conditions.

The early stages of epitaxial growth processes, i.e., oriented crystalline growth on single crystal substrates, can comprise complicated nucleation mechanisms. This can in particular be the case for multi-elemental compounds with a complex unit cell, such as high-temperature superconductors. During the growth of the first monolayer of such materials, surface and interface free energies can force the creation of a precursor phase, which is composed of smaller subunit cells. As soon as a critical amount of material has deposited, a phase transition takes place and the complex unit cells form. A key role for the relationship between growth, texture and electronic properties of epitaxial layers plays the solid interface. Interfaces are formed by few atomic layers that connect two solids with commonly similar but not identical lattice structures. The elastic strain of the deposited film introduced by its forced perfect lattice match with the substrate crystal (pseudomorphism) and the surface structure of the substrate influence the growth mode and the properties of the film from the very beginning. For controlling the properties of high-temperature superconducting thin layers, exploiting the self-organisation during the nucleation and film growth by providing a suitable substrate surface has proved useful. Likewise the carrier doping, the transition temperature, the critical current density and the directionality of the current transport can be tailored by the strain and the texture of the thin film. The understanding of the relationship between interface formation and electronic properties of epitaxial systems is of fundamental interest but has also great importance for future applications.

In this thesis, XSW imaging was applied to study the atomic structure of 0.5 and 1.0 layers of $YBa_2Cu_3O_{7-\delta}$ deposited on the (001) surface of $SrTiO_3$ by pulsed laser deposition. XSW core level photoemission yield was recorded for a number of Bragg reflections for all elements present in film and substrate. The XSW yield profile across the Bragg range is characterised by two parameters, a phase and an amplitude. In the simplest case, the phase and the amplitude are the structural parameters P^H and F^H, but the phase and the amplitude can also be influenced by anisotropic angular effects in photoemission. The parameters P^H and F^H represent the phase and amplitude of the Fourier coefficients of atomic distribution functions. By Fourier inversion, three-dimensional real space images of the atomic distribution for each element were rendered. The images confirmed a model for the nucleation mechanism that was suggested by Haage *et al.* [1], who proposed, based on their STM and STS results, the formation of an $(Y/Ba)CuO_{3-\delta}$ mixed perovskite precursor phase. The starting sequence of the Y/Ba planes was determined, and a simple structural model for the first deposited $YBa_2Cu_3O_{7-\delta}$ layer was derived upon refinement. The study has contributed to the understanding of the nucleation of a heteroepitaxially grown complex material.

Structure and chemical composition define the properties of materials and, more specifically, the electronic properties and the band structure of solids. Density functional theory (DFT) has been very successful in describing electronic properties of a

large class of materials by predicting their density of states. However, an experimental technique to directly verify these predictions has been lacking for a long time. Recently, different author groups around J. Woicik [2–5] have extended the XSW technique for collecting electronic information. Woicik *et al.* [2] probed individual lattice sites in the unit cell of TiO_2 for their partial intensity contribution to the valence band XPS spectrum.

The studies carried out for this thesis are a continuation of Woicik's *et al.* work on two more complex materials, the ternary oxide $SrTiO_3$ and the high temperature superconductor $YBa_2Cu_3O_{7-\delta}$. The yield contributions to the $SrTiO_3$ valence band spectrum coming from the strontium, titanium and oxygen sites were identified. The site-specific valence electronic structure was related to the lattice structure within a σ and π bonding scheme of a molecular orbital model. Comparison with state-of-the-art *ab initio* calculations allowed further angular momentum resolved analysis of the electronic structure. The comparison of calculations and experimental data allowed determining X-ray absorption cross sections for valence states of the solid, which are *a priori* unknown. The experimental values were compared to tabulated values for the free atom; deviations were related to solid state effects.

The XSW study on the $YBa_2Cu_3O_{7-\delta}$ valence band revealed the in-plane copper site and the chain copper site, which are nonequivalent by symmetry, as the originating lattice sites of the principal valence yield contributions. The XSW experiments were carried out using both soft and hard X-rays for different Bragg reflections. As a striking result, the XSW analysis does not confirm the differences between the local electronic structures at the two copper sites, which are predicted by *ab initio* calculations.

Photoemission is a comparatively surface sensitive technique in the ultraviolet and even in the soft X-ray range, owing to the strong interaction of the emitted photoelectrons with matter. This surface sensitivity represents an inherent limitation of the technique for some types of study: The investigation of bulk properties may be hindered by a large signal contribution coming from surface states. Furthermore, the preparation of surfaces with well-defined properties, which are chemically highly reactive, often requires stringent preparation conditions, such as sample cleaving in UHV at liquid helium temperatures, in order to obtain a surface that is stable and clean for a sufficient period of time to carry out the experiment. One possibility to increase the bulk sensitivity of photoelectron spectroscopy and, thus, to reduce the influence of surface signals, is extending photoemission into the hard X-ray range, exploiting the increased attenuation length for photoelectrons with high kinetic energy. Hard X-ray photoelectron spectroscopy employing synchrotron radiation in the energy range up to 10–15 keV for the investigation of buried layers and valence states is a newly developing field at third generation X-ray sources. Growing interest and activity became recently apparent particularly in Japan.

An $YBa_2Cu_3O_{7-\delta}(001)$ surface prepared in ambient air was chemically analysed by photoemission in the hard X-ray range at photon energies between 5.1 and 13.5 keV. A hard X-ray photoelectron spectroscopy setup developed by our research group was used for the measurements. The enhanced bulk sensitivity resulted in signal contributions from surface states and contaminants being efficiently suppressed, though not entirely removed. A drawback, however, results from the strongly reduced photoionisation cross

sections at high photon energy. The XPS signal from light elements or from bulk states with higher angular momenta can suffer a significant loss in intensity. Photoionisation cross sections for a variety of electronic levels of gold are investigated as a function of excitation energy up to 14.5 keV in the appendix.

This thesis is structured as follows:

- Chapter 2 gives a brief overview of structural and electronic properties of $SrTiO_3$ and $YBa_2Cu_3O_{7-\delta}$.
- Chapter 3 describes the basics of X-ray photoelectron spectroscopy and the X-ray standing wave method, which was used in two different applications in this work: The principles of XSW imaging and XSW valence electronic analysis are explained in detail.
- Chapter 4 deals with experimental aspects. The tools and facilities used for sample preparation and the X-ray experiments are described.
- In chapters 5–8, the scientific results are presented. The XSW imaging study of the nucleation of $YBa_2Cu_3O_{7-\delta}$ on $SrTiO_3(001)$ is described in chapter 5, the hard X-ray photoemission study on $YBa_2Cu_3O_{7-\delta}(001)$ in chapter 6, and the XSW valence electronic analyses for $SrTiO_3$ and $YBa_2Cu_3O_{7-\delta}$ are described in chapters 7 and 8, respectively.
- Chapter 9 concludes the thesis with a summary of the results and an outlook.

The influence of angular anisotropy in XPS on the results is discussed in the appendix.

Chapter 2

Properties of $SrTiO_3$ and $YBa_2Cu_3O_{7-\delta}$

2.1 $SrTiO_3$

$SrTiO_3$ belongs to the material class of the perovskites, ternary oxides of a structure ABO_3, where A is mostly a group I–II element and B is mostly a transition metal. The occupation of the A and B sites is very variable; Goodenough [6] has reviewed more than 50 different perovskites. The (at room temperature) cubic unit cell of $SrTiO_3$ with a lattice constant of 3.905 Å is shown in Fig. 2.1(a). The octahedral corner-shared TiO_6 units form a tightly bonded network, which makes up the structural backbone of the lattice. The perfect crystal is an insulator, owing to the (formal) d^0 configuration of the titanium ion. Introduction of lattice defects, like oxygen vacancies by vacuum annealing, or substitution of titanium ions by dopants transforms the material into a wide gap semiconductor.

The chemical bonds in $SrTiO_3$ have a highly ionic character, but the covalent contribution to the titanium-oxygen bonds is not negligible. The perovskite structure is ideal for investigating the electronic structure of linear metal-oxygen-metal bonds of octahedrally coordinated metal ions. Direct metal-metal interactions are not possible due to an oxygen atom lying midway inbetween two titanium neighbours. Oxygen-oxygen interactions are comparatively weak, since they have to get over distances twice as large as the titanium-oxygen bond lengths. In tight-binding descriptions of the perovskite electronic structure, interactions between atoms of the same element have often been considered weak enough to be treated as perturbations. In $SrTiO_3$, the influence of the highly ionized and electronically rather passive strontium ion on the titanium-oxygen covalency is small. Strontium, with a very low electronegativity of 1.0, has transferred electrons to the TiO_3 array and does not strongly compete for electrons. The detailed investigation of the electronic structure of $SrTiO_3$ will be subject of chapter 7.

Relating the valence electronic structure to the atomic structure of a solid requires a physical description of the valence charge, which connects the atoms in the solid. The molecular orbital model (also named linear combination of atomic orbitals, LCAO model) is a description between, as far as the strength of the interatomic interaction is concerned, the ligand field model, which applies to strictly localized electrons of

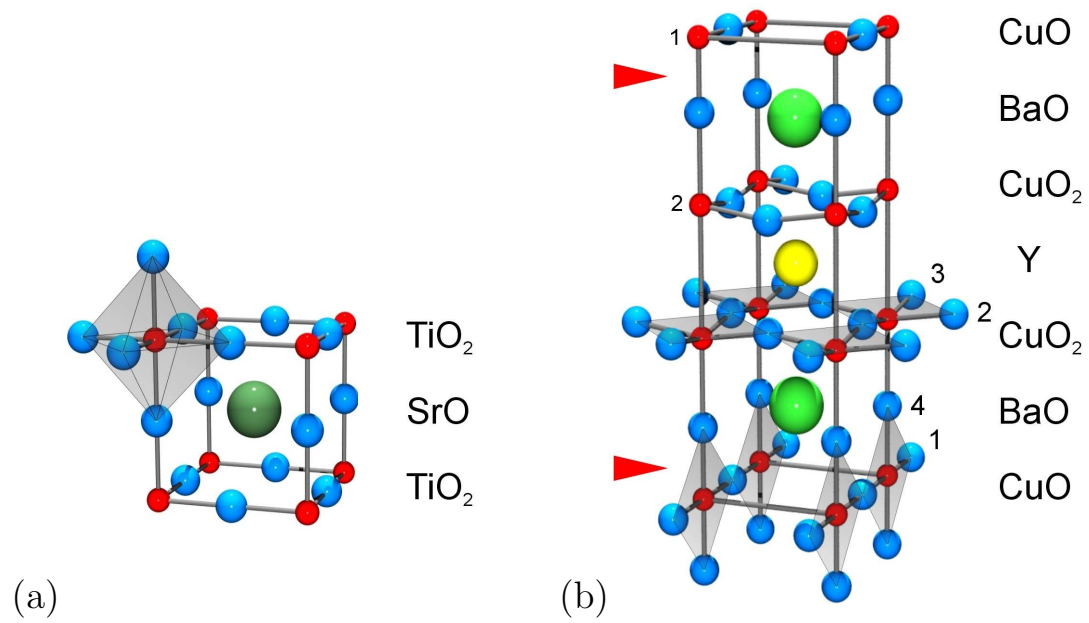

Figure 2.1: Crystal structures of $SrTiO_3$ and $YBa_2Cu_3O_7$. (a) The unit cell of $SrTiO_3$ is depicted with the titanium atoms at the corners. Alternatively, by shifting the origin by half a space diagonal, the strontium atoms will be found at the corners and the oxygen atoms face-centered. Each titanium atom is surrounded by an octahedron of oxygen atoms. (b) The symmetry-inequivalent copper and oxygen sites of the $YBa_2Cu_3O_7$ structure are labelled. Cleavage planes are marked by arrows. The four-fold copper coordination of the planar and the ribbon-like structures is shown shaded.

weakly interacting atoms, and the band model, which applies to valence wave functions extended over many atoms. Considering a basic molecular orbital model for an isolated octahedral TiO_6 structural unit is instructive for interpreting the valence electronic structure of $SrTiO_3$:

An energy level diagram for valence electrons of a $(TiO_6)^{8-}$ cluster (O_h point group) is shown in Fig. 2.2. Interaction of the atomic Ti $3d$, $4s$ and $4p$ orbitals with the atomic O $2s$ and $2p$ orbitals forms bonding, antibonding and nonbonding cluster molecular orbitals. The principle of bonding interaction within this scheme is the following: The atomic orbitals of the titanium centre ion and of the surrounding oxygen ligands are decomposed over symmetry into orbital components, which are labelled by the according Mulliken term symbols. Those components of the centre ion and of the ligands that agree in symmetry combine to form bonding or antibonding molecular orbitals. Those components without counterparts of the corresponding symmetry, such as two of the oxygen $2p$ components, form nonbonding molecular orbitals. A theoretical treatment of the bonding interaction is given in the book by Cotton [9]. The occupied molecular orbitals that are relevant for describing the $SrTiO_3$ valence band are emphasized by a shaded box in Fig. 2.2. The symmetry of the atomic orbitals, which combine to form these molecular orbitals, is depicted in the lower part of the figure. The molecular orbitals can be energetically split into four groupings, as cluster DV-Xα calculations [10]

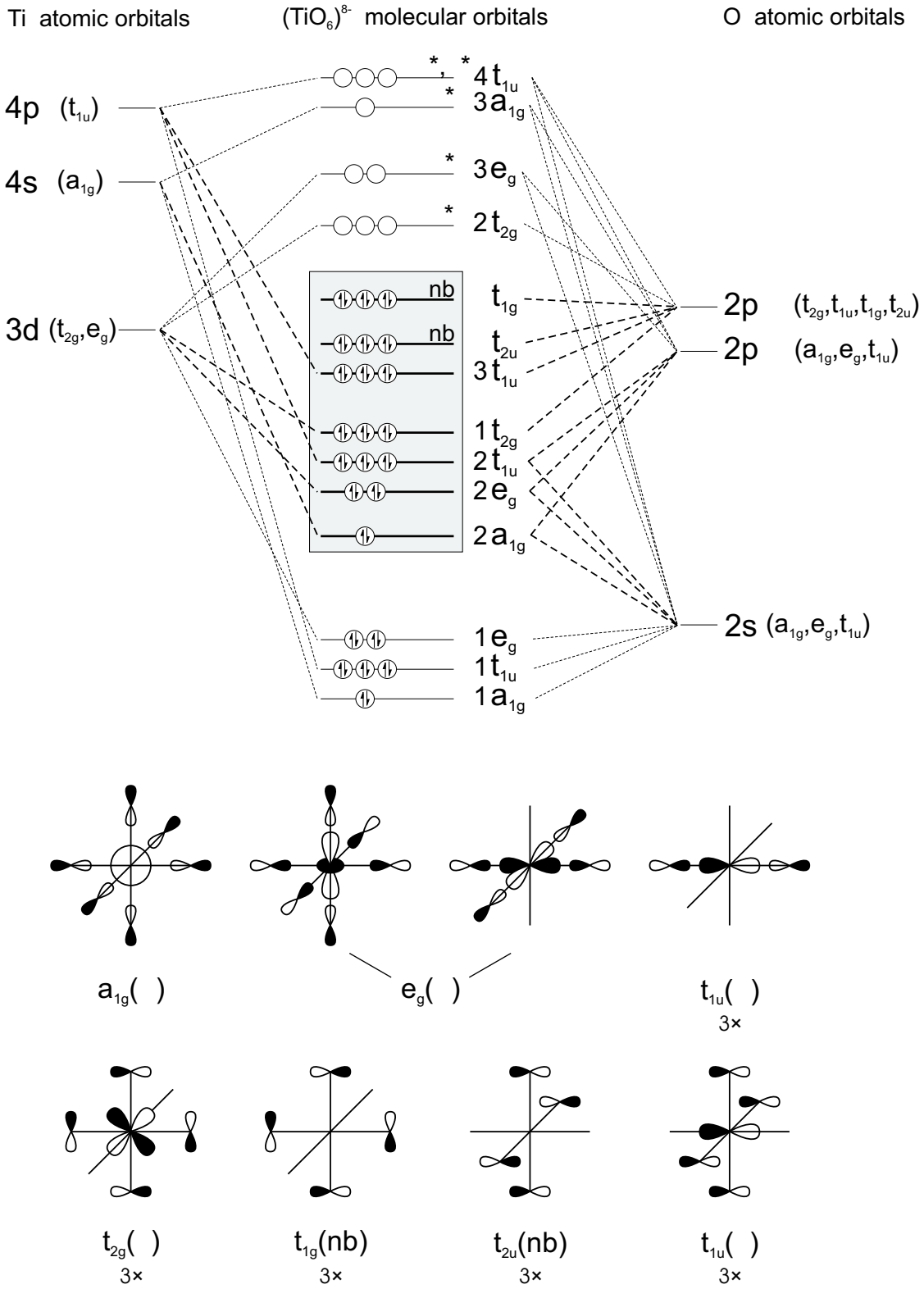

Figure 2.2: Molecular orbital scheme for an octahedral $(TiO_6)^{8-}$ cluster (not drawn to scale; nb = nonbonding) [7]. The lower part of the figure depicts the symmetry of the atomic orbitals [8], which form the molecular orbitals emphasized by the shaded box.

predict, and the energy spacing between these groupings is qualitatively represented in the figure. Since the strontium ion is not involved in the important bonding interactions in $SrTiO_3$, the molecular orbital scheme for a cluster of titanium octahedrally coordinated to oxygen can be applied to approximately describe the bonding interactions in $SrTiO_3$.

2.2 $YBa_2Cu_3O_{7-\delta}$

The lattice structure of the high-temperature superconducting oxide $YBa_2Cu_3O_{7-\delta}$ is shown in Fig. 2.1(b). The oxidized phase of the material has an orthorhombic centrosymmetric unit cell with lattice parameters $a = 3.82$ Å, $b = 3.89$ Å, and $c = 11.68$ Å. The unit cell can be viewed as an oxygen-deficient perovskite structure with a superlattice-like ordering of an yttrium and two symmetry-related barium atoms in c direction. Besides one yttrium and one barium site there are two copper and four oxygen sites, making eight symmetry-inequivalent lattice sites in total. The one-dimensional copper oxide chains, which are formed by the Cu(1) and O(1) atoms, together with the neighbouring apical O(4) atoms make up ribbon-like structures running in b direction. The Cu(2) atoms and its surrounding O(2) and O(3) atoms form the corrugated two-dimensional copper oxide a, b planes. First determinations of the atomic positions in the unit cell were carried out on single crystals by X-ray diffraction [11]; the results were refined later on by neutron diffraction [12]. The layered crystal structure is the cause for strongly anisotropic electronic properties, like the electrical transport.

The ribbon-like structures and the copper oxide planes form separate, only weakly coupled electronic units, as DOS calculations predict. Theoretical partial DOS for the eight lattice sites of $YBa_2Cu_3O_{7-\delta}$ are shown later in Fig. 8.1 in the introduction of chapter 8, which deals with a site-specific valence band study. The local electronic structures at the O(1) and O(4) sites in the ribbon-like feature resemble each other. This can be accounted for by the square four-fold coordination of these oxygen sites to the chain copper site. Owing to the weak coupling, a distinct local electronic structure occurs at the O(2) and O(3) sites in the planes, which are similarly four-fold coordinated to copper. The fact that the Cu(1) and Cu(2) atoms formally occur in different oxidation states (+III and +II, respectively) to neutralize the unit cell has little relevance. Experimentally, Cu^{II} is mainly found, but hardly any Cu^{III}.

Superconductivity (below temperatures of ∼90 K) takes place in the CuO_2 planes. A basic introduction into the field of high-temperature superconductivity is given by the book by Burns [13]. The BaO–CuO–BaO blocks act as charge reservoirs. Reducing $YBa_2Cu_3O_{7-\delta}$ removes the weakliest bonded oxygen atoms at the O(1) site and creates vacancies, which interrupt the chains and reduce the coordination of the Cu(1) atoms. This will vary the charge carrier concentration in the copper oxide planes [14], which is the most important parameter for controlling the superconducting transition temperature.

$YBa_2Cu_3O_{7-\delta}$ has a mixed ionic and metallic character. Beyond the metallic chains and planes, a very low charge density in the unit cell is found from valence charge density simulations [15]. The yttrium and barium ions are highly ionized, and the

yttrium site becomes magnetically isolated to a certain extent. For this reason, many rare earth elements can, despite their magnetic moments, be substituted onto the yttrium site without disturbing superconductivity by pair-breaking effects. The fact that ions of different sizes can be substituted can be exploited to vary the a and b lattice parameters in order to attain a better lattice matching between substrate crystals and grown superconducting thin films.

Cleavage of $YBa_2Cu_3O_{7-\delta}$ occurs normal to the c axis at the CuO–BaO interface, exposing two possible terminations as indicated in Fig. 2.1(b) by the arrows. Finding the cleavage interface at this position, as deduced from STM studies by Edwards, Markert and de Lozanne [16] and confirmed by STM studies of other groups [17], is somewhat surprising, given the considerably longer bonding distance from the O(4) site to the Cu(2) site than to the Cu(1) site and the corresponding reduction in bonding charge. Unlike for cuprates, like $Bi_2Sr_2CaCu_2O_8$, where cleavage naturally occurring between van-der-Waals-bonded layers yields relatively inert cleavage surfaces, cleavage of $YBa_2Cu_3O_{7-\delta}$ breaks chemical bonds and produces chemically very reactive surfaces.

Chapter 3

Introduction to X-ray Standing-Wave Techniques

This chapter describes the basics of the X-ray standing wave technique and its two recently developed applications: XSW real space imaging, a method for determining atomic distributions without *a priori* structural knowledge, is described in section 3.3 and XSW valence electronic structure analysis, which allows site-specifically decomposing valence photoemission spectra of solids and determining photoionisation cross sections of valence electrons, is explained in section 3.4.

3.1 Fluorescence, Auger and Photoelectron Spectroscopy

Fluorescence, Auger and photoelectron spectroscopy, which are described in detail in the literature [18–21], are briefly summarized in this section with regard to their application in combination with the XSW method. Fluorescence, Auger and photoelectron spectroscopy belong to the most important experimental techniques for chemically analysing smallest amounts of matter, such as sub-monolayer coverages of atoms in different chemical states on crystal surfaces. If combined with the XSW method, these techniques gain high spatial sensitivity, which is a powerful additional capability. The XSW method in turn, which employs the X-ray wavefield as a probe, can utilize these three techniques for indirectly monitoring the local photoabsorption at specific lattice sites. Some characteristic properties of these techniques when used for monitoring the X-ray absorption are described in the following.

In XSW experiments, the X-ray absorption by the material under study is detected in the vicinity of a Bragg reflection. Monitoring the X-ray absorption by a small amount of material deposited as a thin film on a bulk substrate cannot be easily achieved by an absorption-type experiment. The absorption of a photon is therefore indirectly detected by the photoelectron, which is emitted in the primary photoexcitation process, or by Auger electrons or fluorescence photons, which are both emitted during the subsequent decay of the generated core hole over the secondary emission channel (i.e., the emission is not a direct consequence of the initial photoabsorption). Fig. 3.1 shows the initial

stage of the decay cascade of the photoexcitation. The photoabsorbing element can be identified by the energy of the emitted electron or photon, which is determined by the energy level scheme characteristic for every element.

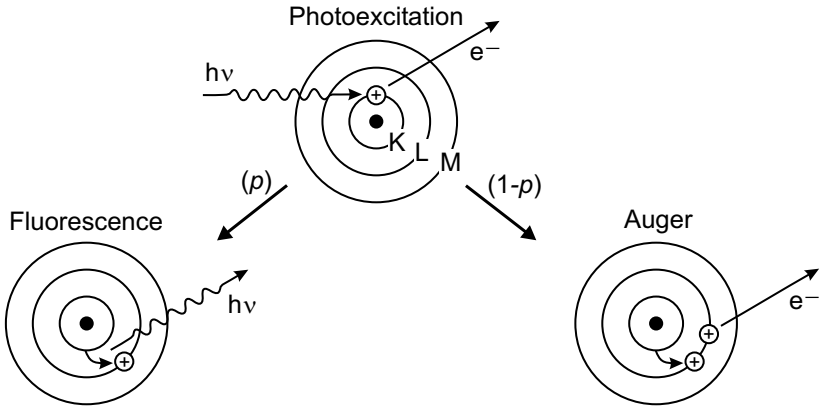

Figure 3.1: Photoexcitation of an atom and decay cascade (from Zegenhagen [22]). The fluorescence process occurs with probability p and competes with the Auger process for the first step of the decay cascade. In each decay step, a positively charged core hole generated either by the initial photoabsorption or a subsequent decay process moves to a higher shell.

All three spectroscopic techniques are element specific. This is in particular advantageous for structural XSW studies, like XSW direct imaging, because elements with similar atomic numbers can be easily discriminated. Combining XSW with XPS additionally allows accessing indirect information about the chemical environment of the emitting atom from chemical shifts in core level binding energy. The energy of Auger electrons and fluorescence light, in contrast, is mostly independent of chemical shifts, such that the specific emitting species can frequently not be indentified. XPS allows XSW studies of the electronic structure of a solid and can be employed to directly probe the valence band.

The polarisation of the incident X-ray photon influences the primary photoemission process, when the initial core hole is generated. As a consequence, the angular intensity distribution of the emitted photoelectrons is strongly anisotropic. As long as the dipole approximation can be applied, the differential photoemission intensity excited by an XSW field into a confined acceptance solid angle of an electron analyser is, at any detection angle, proportional to the total photoabsorption rate. However, if multipole effects become significant, the emission characteristics becomes dependent on photon energy within the range of Bragg reflection, owing to the presence of two waves with different propagation directions. The photoemission yield is no longer proportional to the X-ray absorption, a fact that can considerably complicate the XSW data analysis. Secondary emission processes remain unaffected by the X-ray polarisation, because during the relaxation process of the initial core hole the information about its creation is lost. The Auger and fluorescence processes exhibit therefore isotropic emission characteristics (provided that electron diffraction effects are negligible, which holds true for high kinetic electron energies).

Secondary emission processes are not exclusively initiated by those core holes that were generated by the applied X-ray beam. Emission of Auger electrons or fluorescence light can occur as a result of core holes created by processes, like impact ionization by other inelastically scattered Auger- and photoelectrons or fluorescence photoabsorption. This means that the decay cascade of a photoexcitation can initiate secondary emission events in atoms other than the one where the primary photoabsorption took place (and, hence, at other lattice sites). If the secondary emission rate from other atoms is no longer negligible compared to the rate from atoms where the primary core hole was created, the measured XSW Auger or fluorescence emission profile will no longer be congruent with the XSW absorption profile and will not be rigorously representative of the position of the photoabsorption site. In structural studies of adsorbates on crystal surfaces, the secondary emission profile measured for the adsorbate will typically contain a superimposed component of the emission profile for the substrate. Stanzel *et al.* [23] deposited layers of oxygen-containing organic NTCDA molecules on a silver substrate crystal. They estimated the additional fraction of O KLL Auger transitions (at 531 eV energy) induced by inelastic scattering of photons and electrons originating from the silver substrate at an incident photon energy of 2.625 keV to a value as high as 50%. Generally, above threshold, the probability for the creation of a core hole in a foreign atom in a secondary process increases with the energy difference between the exciting incident photon and the Auger absorption edge. Low energy Auger electrons as well as low energy fluorescence emission lines are therefore not suitable for monitoring the X-ray absorption rate in XSW measurements, when the energy of the X-ray beam is too high.

The signal-to-background ratio is one of the criteria to decide whether to prefer XPS or Auger signal detection. The ratio generally improves with rising kinetic energy of the emitted electrons. Low energy electron signals are accompanied by a high background of slow secondary and inelastically scattered electrons. This will be the case for photoelectrons excited from deep core levels with binding energies close to the incident photon energy. Here, a better signal-to-background ratio will occur for Auger electron emission, which results from decay of the deep primary core holes and displays high kinetic energy. For low binding energies the situation is reversed. Here, photoemission excited from shallow core levels is highly energetic, while Auger transitions between shallow electronic levels result in low electron kinetic energies.

X-ray fluorescence spectroscopy reaches a larger information depth[1] than electron spectroscopy. Since photons interact with matter much weakly than charged electrons, fluorescence is more sensitive to bulk material and can access information from a depth of the order of 1 μm below the surface. The sensitivity to surface states and to the cleanliness of the surface is by far less critical. On the other hand, if the thickness of the sample is comparable to the penetration depth of the X-ray field, extinction effects have to be taken into consideration: Dynamical theory of X-ray diffraction predicts a variation in penetration depth of the X-rays over the range of Bragg reflection. When investigating bulk material, like single crystal samples, extinction effects influence the shape of the XSW fluorescence yield profile. Recently, there have been attempts to

[1] A precise definition of terms relating to surface sensitivity is given by Powell *et al.* [24].

increase the bulk sensitivity of electron spectroscopy. By employing hard X-rays, the kinetic energy of the emitted Auger and photoelectrons is raised in order to exploit the increase in attenuation length in the probed material.

The employment of fluorescence spectroscopy is not restricted to (ultra)high vacuum environment, as the electron detection methods are, but is also possibe in ambient air. This has practical advantages for the experimental data acquisition. The sample can be mounted on a diffractometer, which allows quickly accessing many different Bragg reflections, as required for, e.g., XSW real space imaging. The detection of low energy fluorescence signals in particular from light elements, like oxygen, however, can be hampered by the high signal absorption in air. Fluorescence emission from light elements is additionally weakened by the strong preference to populate the competing Auger decay channel.

XPS was the most frequently used technique in combination with the XSW method for the present thesis work. The detailed description of the photoemission process and the conclusions drawn from the dipole approximation in the following provide a basis for interpreting XPS/XSW studies of valence electronic structures.

Photoelectron Spectroscopy

By the photoelectric effect, electrons are released from occupied electronic states and escape from the irradiated sample into the vacuum in all directions. In X-ray photoelectron spectroscopy, the emitted electrons are analysed with regard to their kinetic energy and, in the soft X-ray range, also to their emission direction [25]. From their kinetic energy, the binding energy of the photoelectrons prior to their excitation can be inferred, and element-specific chemical information for the sample material can be deduced. Describing the manybody process of photoemission in the simplified non-interacting particle picture, the binding energy E_B and the observable kinetic energy E_{kin} are related by conservation of energy

$$E_{kin} = h\nu - E_B - \Phi_A, \tag{3.1}$$

as Fig. 3.2 illustrates. The work function of the spectrometer Φ_A, a constant, has to be taken into consideration, while the work function of the sample Φ_S has no influence.

The Hamiltonian H of a single electron in an effective potential $V(\mathbf{r})$ of a crystal, to which an external electromagnetic field with vector potential $\mathbf{A}(\mathbf{r})$ is applied, can be separated into two parts: one part H^0 referring to the unperturbed crystal electron, and a first-order perturbation part H^1 describing the electron-photon interaction:[2]

$$\begin{aligned} H &= \frac{1}{2m}\left(\mathbf{p} - \frac{e}{c}\mathbf{A}(\mathbf{r})\right)^2 + V(\mathbf{r}) = H^0 + H^1 \qquad \text{where} \\ H^0 &= \frac{\mathbf{p}^2}{2m} + V(\mathbf{r}) \qquad \text{and} \\ H^1 &= \frac{-e}{2mc}(\mathbf{A}(\mathbf{r})\cdot\mathbf{p} + \mathbf{p}\cdot\mathbf{A}(\mathbf{r})) + \frac{e^2}{2mc^2}\mathbf{A}^2(\mathbf{r}) \end{aligned} \tag{3.2}$$

[2] charge sign convention: $e < 0$ so that the negative charge of the electron is e.

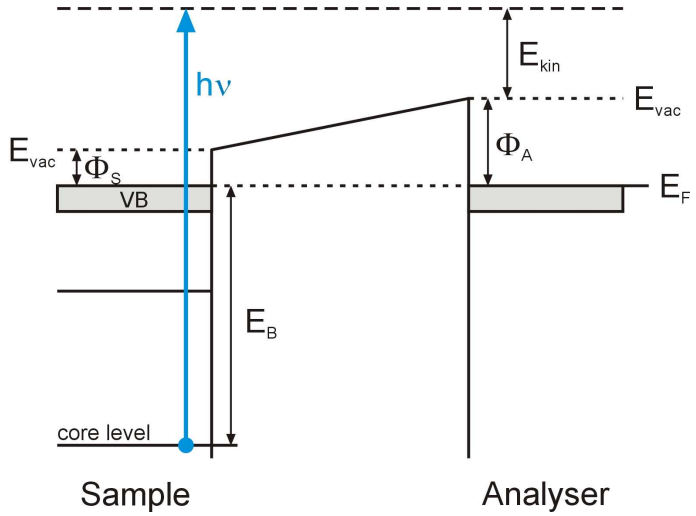

Figure 3.2: Schematic diagram of the energetics of the photoemission process in the non-interacting particle picture (from Ertl and Küppers [26]). Sample and analyser are electrically connected so that their Fermi energies E_F are at the same level. The binding energy E_B is usually referenced to the Fermi level of a metallic sample, which is marked by the highest kinetic energy of electrons in a spectrum and can experimentally be easily determined.

and where $\mathbf{r}$ is the position vector from a reference point. Relativistic contributions, like the spin interaction with the radiation magnetic field, are not taken into consideration. Terms linear in $\mathbf{A}(\mathbf{r})$ describe the photoabsorption, while the term quadratic in $\mathbf{A}(\mathbf{r})$ accounts for two-photon processes like elastic scattering, i.e., creation and annihilation of one photon at the same time, and can be omitted. Using the Coulomb gauge, the Hamiltonian that describes the interaction with the external field becomes

$$H^1 = \frac{-e}{mc}\mathbf{A}(\mathbf{r}) \cdot \mathbf{p}. \tag{3.3}$$

In a more formal description, the photoemission process is a coherent one-step process, which can be phenomenologically divided into three independent steps: the optical excitation, the travel of the photoelectron to the surface and the escape into the vacuum. The transition probability (given by the *Golden Rule*)

$$w_{fi} = \frac{2\pi}{\hbar}|\langle f^N|H^1|i^N\rangle|^2\delta(E_f^N - E_i^N - h\nu) \tag{3.4}$$

for the optical excitation from an N-electron initial eigenstate $|i^N\rangle$ into a possible final eigenstate $|f^N\rangle$ of the Hamiltonian H^1 is obtained as the linear response of the N-electron system from applying first-order perturbation theory (while the second order describes resonant scattering). $E_i^N = E_i^{N-1} - E_B^{\mathbf{k}}$ and $E_f^N = E_f^{N-1} + E_{kin}$ are the initial and final state energies, $E_B^{\mathbf{k}}$ is the binding energy of the photoelectron when it propagates inside the solid with momentum $\hbar\mathbf{k}$. Owing to a finite acceptance angle of the spectrometer, the $\mathbf{k}$-selection rule is relaxed at X-ray energies and electronic states are sampled over the entire Brillouin zone. The angle-integrated XPS intensity

$I(E_{kin})$ measured as a function of the kinetic energy is proportional to the transition probability between all possible initial and final states, i.e., $I(E_{kin}) \propto \sum_{\mathbf{k}} \sum_{i,f} w_{fi}$.

The evaluation of the bracket in Eq. 3.4, and therefore of the XPS intensity $I(E_{kin})$, is complicated by the interaction of the escaping photoelectron and the relaxation of the system of the (N-1) electrons left behind. The interaction is neglected within the so-called *sudden approximation* for the final state: The escape of the photoelectron is assumed to occur fast compared to the response of the remaining (N-1) electrons to the creation of the hole state. This can be an appropriate assumption for photoelectrons with high kinetic energies, as in XPS. The electronic transition of the one-electron state of the photoelectron and the response of the (N-1)-electron system can be treated as two independent processes, which are only linked by the law of energy conservation. The wave function of the photoelectron can be separated by factorizing the Slater determinants $|i^N\rangle = C|i, i^{N-1}\rangle$ and $|f^N\rangle = C|f, f^{N-1}\rangle$ with the operators C antisymmetrizing the N-electron wave functions to satisfy the Pauli principle. $|i^{N-1}\rangle$ is not an eigenstate and is better expressed in its second quantised form $|i^{N-1}\rangle = a_{\mathbf{k}}|i^N\rangle$ with the annihilation operator $a_{\mathbf{k}}$ as a remnant of the N-electron eigenstate, where one electron has been instantaneously removed. Subsequent to the optical excitation, $|i^{N-1}\rangle$ relaxes into one of the possible excited eigenstates $|f_s^{N-1}\rangle$ of the final state $|f^{N-1}\rangle = \sum_s c_s|f_s^{N-1}\rangle$. The excitations s, e.g., like phonons and plasmons, give rise to satellite peaks in addition to the spectral main line. The bracket in Eq. 3.4 can be written as a product

$$\langle f^N|H^1|i^N\rangle = \langle f|H^1|i\rangle \sum_s \langle f_s^{N-1}|a_{\mathbf{k}}|i^N\rangle \tag{3.5}$$

of the one-electron matrix element

$$\langle f|H^1|i\rangle = \frac{-e}{2mc}\langle f|\mathbf{A}(\mathbf{r})\cdot\mathbf{p}|i\rangle \tag{3.6}$$

and a sum of overlap integrals, each of which giving the probability that the remaining (N-1)-electron system is left is the corresponding excited state s. In XPS, the one-electron wavefunctions $|i\rangle$ and $|f\rangle$ are eigenstates of H^0 with energies $E_B^{\mathbf{k}}$ and E_{kin}, respectively. The initial state $|i\rangle$ can generally be a localized bound state, i.e., a core level state, or a delocalised Bloch state, i.e., a valence or conduction state. At high kinetic energies of a few hundred electron volt and beyond, when the crystal potential represents a small perturbation only, the final state $|f\rangle$ quickly approaches a plane wave. The transition matrix element

$$M_{fi} \equiv \langle f|\mathbf{A}(\mathbf{r})\cdot\mathbf{p}|i\rangle \tag{3.7}$$

in Eq. 3.6 can often be simplified by the dipole approximation, as will be explained further below.

The travel of the excited photoelectron to the sample surface is characterized by elastic and inelastic scattering events, which limit the information depth of photoelectron spectroscopy. After having travelled an average distance equal to the effective attenuation length λ, only a fraction (1/e) of the excited photoelectrons has not suffered inelastic scattering, where all carried information about the originating electronic

state is lost. The attenuation of the photoemission intensity I_0 from a depth t below the sample surface can be approximately described by the exponential law

$$I = I_0 \exp(-t/\lambda \sin \alpha), \tag{3.8}$$

where I is the measured intensity and α is the take-off angle of the electrons. The probability of an electron to be inelastically scattered is determined by the sample material and the kinetic energy of the electron. The effective attenuation length λ is shorter than the inelastic mean free path, which is the average distance that an electron with a given energy travels between successive inelastic collisions, because elastic electron scattering lengthens the electron trajectory in the material. The influence of the elastic scattering is often negligible for light elements. A more detailed discussion is given by Powell [24].

The energy resolution in X-ray photoelectron spectroscopy is intrinsically limited by life time broadening for the created hole state and probably by momentum conservation for photoelectron and excited atom at high electron energies [27]. The bandwidth of the X-ray beam and the energy resolution of the photoelectron analyser represent experimental limitations. For semiconductor samples, another limitation occurs from band bending effects (Fermi level pinning): Band bending results from the formation of a positive space charge within the probed depth λ of the semiconductor surface as shown in Fig. 3.3. The created charge density depends on the dynamic equilibrium between the photo current and the sample drain current and determines the variation of

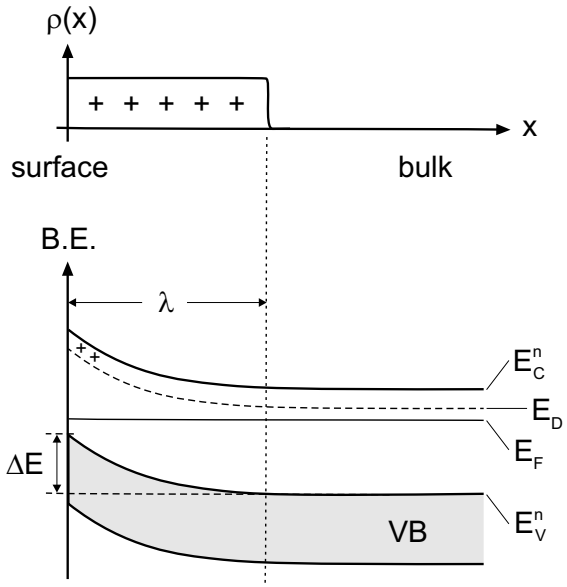

Figure 3.3: Schematic diagram of the band bending effect at a semiconductor surface. A surface layer of positive charge density $\rho(x)$ is created by the photocurrent (top). The x axis denotes the direction normal to the sample surface towards the bulk. The band scheme (bottom) illustrates the upward band bending by ΔE. The XPS probing depth is denoted λ. E_C^n and E_V^n are the positions of the conduction and valence band edges deep in the n-region. E_D denotes the ground state of the donors.

the sample potential across the probed depth. The broadening of spectroscopic features results from the continuous shift in binding energy of the probed states, as indicated in the figure, integrated over the probed depth. The broadening effect on photoemission spectra can be described by a convolution with a function of an approximately triangular shape. When photoemission is excited by synchrotron light, the band bending is expected to be larger than for laboratory source light and can, depending on the conductivity of the sample, be of the order of electron volt.

Angular Effects in Photoelectron Spectroscopy

The one-particle transition matrix element M_{fi} in Eq. 3.7, which describes the interaction between the electromagnetic wave and the photoelectron, can be simplified by applying the dipole approximation. For a photoexcitation by a single plane wave $\mathbf{A}(\mathbf{r}) = A_0 e^{i(\mathbf{k}\cdot\mathbf{r}-\omega t)}\mathbf{e}$, where $\mathbf{e}$ is the polarisation vector, the matrix element reads

$$M_{fi} \propto \langle f|e^{i\mathbf{k}\cdot\mathbf{r}}\mathbf{e}\cdot\mathbf{p}|i\rangle. \tag{3.9}$$

A sufficient but not necessary condition for the applicability of the dipole approximation is that the variation in the spatial part $e^{i\mathbf{k}\cdot\mathbf{r}}$ of the wave phase is small over the extent of the initial wavefunction. It is convenient to decompose the positon vector of the absorbing electron into a sum $\mathbf{r} = \mathbf{r}_{\text{core}} + \mathbf{r}_{\text{el}}$ of the position vectors of the closest atomic core $\mathbf{r}_{\text{core}}$ and the electron position $\mathbf{r}_{\text{el}}$ relative to that core. In a multipole expansion, the exponential phase factor is expanded into series at the position of the atomic core next to the absorbing electron:

$$e^{i\mathbf{k}\cdot(\mathbf{r}_{\text{core}}+\mathbf{r}_{\text{el}})} = e^{i\mathbf{k}\cdot\mathbf{r}_{\text{core}}}(1 + i\mathbf{k}\cdot\mathbf{r}_{\text{el}} - \ldots). \tag{3.10}$$

If $|\mathbf{k}\cdot\mathbf{r}_{\text{el}}| \ll 1$, omitting all terms except the zero-order dipole term yields the matrix element

$$M_{fi} \propto e^{i\mathbf{k}\cdot\mathbf{r}_{\text{core}}}\langle f|\mathbf{e}\cdot\mathbf{p}|i\rangle \qquad \text{(E1)} \tag{3.11}$$

for electric dipole transitions. Term (E1) is no longer a function of the electronic coordinates. The absorption process takes place virtually at the centre of the atom. If this approximation — the dipole approximation — cannot be applied, two first-order terms have to be included in the matrix element,

$$\begin{aligned} -(m\omega/2)\,\langle f|(\mathbf{k}\cdot\mathbf{r})(\mathbf{e}\cdot\mathbf{r})|i\rangle \qquad & \text{(E2)} \qquad \text{and} \\ (i/2)\,\langle f|(\mathbf{k}\times\mathbf{r})\cdot\mathbf{l}|i\rangle \qquad & \text{(M1)}, \end{aligned} \tag{3.12}$$

where term (E2) accounts for electric quadrupole transitions and term (M1) for magnetic dipole transitions [28].

The selection rules for dipole transitions require angular momentum transfer to the photoelectron of $\Delta l = \pm 1$, which can be accomplished by the transfer of the photon spin. Quadrupole transitions, which require an angular momentum transfer $\Delta l = 0, \pm 2$ to the photoelectron, necessitate angular momentum contributions from the electron itself. In a semiclassical depiction, electron angular momentum cannot be transferred at the core position. Quadrupole transitions are therefore likely to occur mainly outside the core region, while dipole transitions can occur virtually at the atomic core [29].

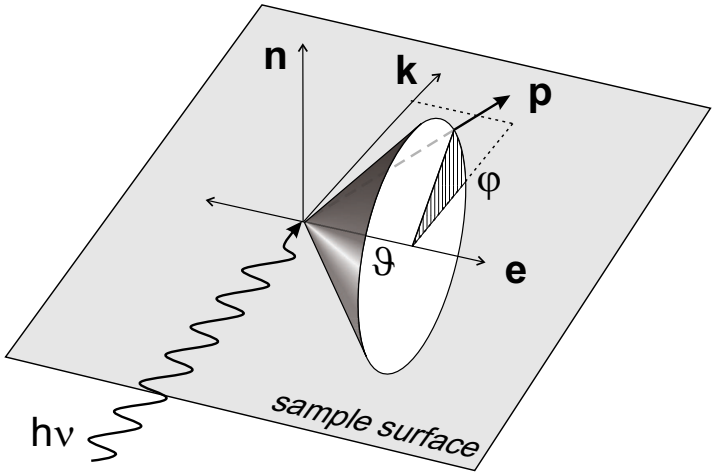

Figure 3.4: Angular geometry for XPS. The X-ray beam with momentum $\hbar\mathbf{k}$ and polarization vector $\mathbf{e}$ is incident on a sample surface. The vectors $\mathbf{e}$, $\mathbf{k}$, and $\mathbf{n} \equiv \mathbf{e} \times \mathbf{k}$ form a trihedron. Photoelectrons with momentum $\mathbf{p}$ are emitted at angles $\vartheta \equiv \angle(\mathbf{e}, \mathbf{p})$ and φ, which is the angle between $\mathbf{k}$ and the projection of $\mathbf{p}$ onto the $\mathbf{k}$-$\mathbf{n}$ plane.

The angular distribution of the photoemission intensity, which in dipole approximation is proportional to the modulus squared of the matrix element M_{fi} given by Eq. 3.11, is not isotropic. The photoelectron differential cross section for linearly polarized light was shown by Cooper and Zare [30] to have the general form

$$\frac{d\sigma(\vartheta,\varphi)}{d\Omega} = \frac{\sigma_{tot}}{4\pi}[1 + \beta P_2(\cos\vartheta)], \tag{3.13}$$

where σ_{tot} represents the angle-integrated photoionisation cross section. $P_2(\cos\vartheta) = (3\cos^2\vartheta - 1)/2$ is the second order Legendre polynomial. ϑ and φ define the angle between the directions of the ejected electron and the polarization of the incident X-ray light, as specified in Fig. 3.4. The angular anisotropy of the emitted intensity distribution is described by the asymmetry parameter β, which is strongly dependent on angular momentum. When the quadrupole terms (E2) and (M1) given by Eq. 3.12 are included in the matrix element, higher order terms of the expansion of the cross section over Legendre polynomials have to be included to describe the angular distribution: From the expansion of $|M_{fi}|^2 \propto |\mathrm{E1}+\mathrm{E2}+\mathrm{M1}|^2$, Cooper [31,32] included the dominant interference terms $\mathrm{E1}\cdot\mathrm{E2}$ and $\mathrm{E1}\cdot\mathrm{M1}$. For this quadrupole approximation, he derived the expression

$$\frac{d\sigma(\vartheta,\varphi)}{d\Omega} = \frac{\sigma_{tot}}{4\pi}[1 + \beta P_2(\cos\vartheta) + (\gamma\cos^2\vartheta + \delta)\sin\vartheta\cos\varphi] \tag{3.14}$$

for linearly polarized light parametrized in terms of an electric quadrupole parameter γ and a magnetic dipole parameter δ. Theoretical values for these parameters are tabulated in the literature. Eqs. 3.13 and 3.14 both are valid for the X-ray field of a single incident beam (i.e., they do not describe the angular distribution of photoelectrons excited under a Bragg condition by an X-ray interference field). In the newly explored

hard X-ray range for photoemission, even higher order multipole terms of the matrix element can become important. Derevianko *et al.* [33,34] extended Eq. 3.14 further by including second-order terms and three additional octupole parameters.

The matrix element for electric dipole transitions (E1) can be transformed into two equivalent forms, a length form and an acceleration form. The length form illustrates the dipole emission characteristics. Substituting the momentum operator $\mathbf{p} = (-im/\hbar)[\mathbf{r}, H^0]$ into Eq. 3.11 yields

$$\begin{aligned} \langle f|\mathbf{e}\cdot\mathbf{p}|i\rangle &= \frac{-im}{\hbar}\langle f|\mathbf{e}\cdot[\mathbf{r},H^0]\ |i\rangle &= \frac{-im}{\hbar}\langle f|\mathbf{e}\cdot\mathbf{r}H^0 - H^0\mathbf{e}\cdot\mathbf{r}|i\rangle \\ &= \frac{im}{\hbar}(E_{kin}-E_B^{\mathbf{k}})\langle f|\mathbf{e}\cdot\mathbf{r}|i\rangle &= im\omega\langle f|\mathbf{e}\cdot\mathbf{r}|i\rangle \end{aligned} \tag{3.15}$$

with the dipole operator $\mathbf{e}\cdot\mathbf{r}$. The emitting atom is coupled to the electric dipole moment of a locally constant electromagnetic field. This leads to a dipole-like angular distribution pattern for the emitted photoelectrons.

The photoemission process has to fulfill the laws of energy and momentum conservation. The acceleration form of Eq. 3.11 demonstrates that these conditions are fulfilled only in a confined spatial region:

$$\begin{aligned} \langle f|\mathbf{e}\cdot\mathbf{p}|i\rangle &= \frac{1}{E_{kin}-E_B^{\mathbf{k}}}\langle f|[H^0,\mathbf{e}\cdot\mathbf{p}]|i\rangle &= \frac{1}{E_{kin}-E_B^{\mathbf{k}}}\langle f|[V(\mathbf{r}),\mathbf{e}\cdot\mathbf{p}]|i\rangle \\ &= \frac{1}{E_{kin}-E_B^{\mathbf{k}}}\langle f|i\hbar\mathbf{e}\cdot(\nabla V(\mathbf{r}))|i\rangle &= \frac{i}{\omega}\langle f|\mathbf{e}\cdot(\nabla V(\mathbf{r}))|i\rangle, \end{aligned} \tag{3.16}$$

where the gradient of the crystal potential $\nabla V(\mathbf{r})$ has the form of a classical force: It is the atom embedded in the crystal lattice, which absorbs the recoil of the excited photoelectron, such that the total momentum is conserved. The incident photon provides the energy to release the electron from the atom, while the momentum contributed by the photon is negligible in this process. The absorption of the recoil happens preferentially in a confined spatial region in the vicinity of the atomic core, which will be called the *emission volume* in the following.

The electron emission volume is confined to a region in the unit cell, where the overlap integral of the three spatially dependent functions $|i\rangle$, $|f\rangle$ and $\nabla V(\mathbf{r})$ in Eq. 3.16 do not vanish. The spatial dependences of these three functions are schematically shown in Fig. 3.5, where $|i\rangle$ represents a valence state. The one-electron wavefunction of the valence initial state $|i\rangle$ varies rapidly and overlaps sizeably with the also rapidly oscillating wave function $|f\rangle$ of the emitted photoelectron exclusively in the vicinity of atomic cores. Inbetween the cores the wave function overlap integrates out to zero; the quasi-free valence electrons in the solid do not experience any photoexcitation here. The crystal potential, the third function in the bracket, exhibits large gradients only in the vicinity of the atomic cores. The atom bound in the solid can absorb the momentum transferred from the photoelectron exclusively if the excitation takes place in this region close to the core. The emission volumes for all photoelectrons that cause comparable momentum transfer to the lattice should therefore be similar. This means that electrons originating from the valence band and from shallow core levels can be expected to be emitted from about the same spatial region.

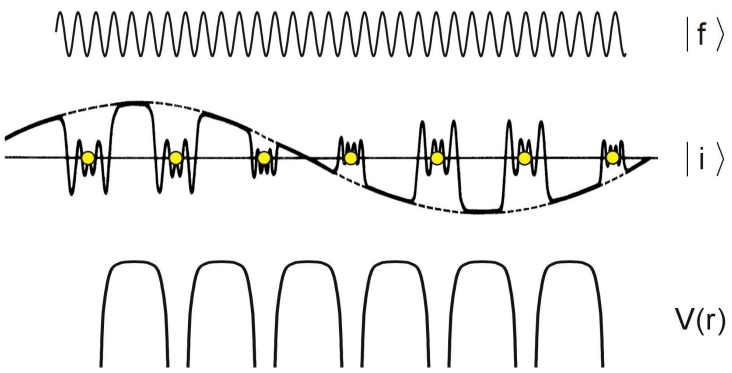

Figure 3.5: Characteristic spatial dependences of quantities in the transition matrix element. Shown are the spatial variations of the real (or imaginary) parts of a plane wave $|f\rangle$, which describes the free photoelectron, and of a Bloch wave $|i\rangle$ along a line of ions in a crystal, which represents a valence one-electron initial state. The Bloch wave function shows atomic oscillations in the vicinity of the cores and slowly-varying plane-wave-like behaviour inbetween the cores. $V(\mathbf{r})$ is the crystal potential.

The dipole approximation may sometimes be applied even in the X-ray regime. The physical reason is that the region of intersection of the emission volume and the initial state wave function is so small that the variation of the spatial part $e^{i\mathbf{k}\cdot\mathbf{r}}$ of the phase of the applied electromagnetic field is negligible there. The variation may not necessarily be negligible over the spatial extent of the initial state wavefunction, as demanded by the conventionally used criterion $|\mathbf{k}\cdot\mathbf{r}_{\mathrm{el}}| \ll 1$ for the applicability of the dipole approximation. The negligible phase variation of the external field over the emission volume is the physical criterion for the applicability of the dipole approximation.

The above consideration can have a large impact on photoionisation cross sections for shallow electronic states. The cross section for a very weakly bound state depends strongly on whether the corresponding atom is a free atom or an atom embedded in a solid. The cross section will depend on the degree of charge delocalisation, i.e., on the spatial dependence of the initial state wave function, but also on spatial differences between a central potential and the potential landscape present in a solid. The photoionisation cross section of a specific electronic level of an atom will vary from material to material, depending on the specific chemical environment of the emitting atom in the hosting compound.

3.2 Basic Theory of X-ray Standing Waves

The X-ray standing wave technique was reported as a tool for structure determination with chemical selectivity and high spatial resolution by Batterman [35, 36] already at the end of the 1960s, i.e., before the development of surface X-ray diffraction or scanning tunneling microscopy. With the availability of synchrotron radiation, the XSW method started to enjoy increasing popularity from the beginning of the 1980s

and has meanwhile become a standard experimental technique. The presentation of the general principles of the XSW method in this section partially follows the descriptions given by Woodruff [18,37] and Nelson *et al.* [38].

An X-ray standing wave interference field with a sinusoidal spatial modulation of the electric-field intensity can be generated by the coherent superposition of an incident and typically a Bragg-reflected monochromatic X-ray beam. The total electric field resulting from the superposition of the incident wave $\mathbf{E}_0$ and the reflected wave $\mathbf{E}_H$ is given by

$$\mathbf{E}(\mathbf{r},t) = (E_0 e^{i\mathbf{k}_0\cdot\mathbf{r}}\mathbf{e}_0 + E_H e^{i\mathbf{k}_H\cdot\mathbf{r}}\mathbf{e}_H)e^{-i\omega t}, \tag{3.17}$$

where $\mathbf{e}_0$ and $\mathbf{e}_H$ are the polarization vectors. The wave vectors are connected via the reciprocal lattice vector $\mathbf{H}$ by the Bragg condition $\mathbf{H} = \mathbf{k}_H - \mathbf{k}_0$. For σ polarization and a symmetrical Bragg reflection, squaring the field amplitude results in the standing wavefield intensity

$$\mathbf{I}(\mathbf{r},E) = |\mathbf{E}(\mathbf{r},t)|^2 = |E_0|^2\left[1 + R(E) + 2\sqrt{R(E)}\cos\left(\nu(E) - \mathbf{H}\cdot\mathbf{r}\right)\right] \tag{3.18}$$

at an arbitrary point $\mathbf{r}$ (extinction effects are left out of consideration). The last term represents the interference term. The relation between the complex field amplitudes $E_H/E_0 = \sqrt{R}e^{i\nu}$ is determined by the energy dependent reflectivity $R(E)$ of the crystal and the energy dependent phase $\nu(E)$ of the reflected wave with respect to the incident wave. The periodicity of the standing wavefield is given by the diffraction plane spacing $d_H = 2\pi/|\mathbf{H}|$ and is independent of photon energy E within the range of the Bragg reflection.

The reflectivity curve as well as the phase relation between the incident and reflected waves under a Bragg condition can be very accurately described by the dynamical theory of X-ray diffraction [39,40] based on atomic scattering factors and crystal structure factors. Dynamical theory is a classical theory, which in contrast to the kinematical theory takes multiple scattering into account. The attenuation of the X-rays by each atomic layer of the crystal leads to a finite penetration depth of the beam (extinction). The small phase shift for forward scattered fractions of the beam causes the Bragg reflection to extend over a finite energy or angular range (Darwin width). The properties of the standing wavefield are fully determined by the reflectivity curve, which in turn results from the structure of the crystal.

The XSW method exploits the phase shift, which occurs between the incident and the reflected beam, when a Bragg reflection is traversed. The Bragg reflection can be sweeped through by either varying, at synchrotron light sources, the photon energy or, when using laboratory X-ray sources with fixed beam energy, the incident angle. The phase shift from π to 0 causes the XSW field to shift towards the crystal bulk by $d_H/2$, thereby moving over the distribution of atoms in the unit cell. As the reflection is sweeped through, the intensity maxima of the XSW field arrive on the diffraction planes, which are those planes normal to $\mathbf{H}$ that represent the centre of mass of the electronic distribution in $\mathbf{H}$ direction. Under most experimental conditions, the X-ray absorption by an atom is proportional to the field intensity it experiences. The lineshape of the atomic XSW absorption profile, i.e., the absorption as a function of photon energy or incident angle, is characteristic of the position of the absorbing atom relative to the diffraction planes. This is the basis of the XSW method.

If photoabsorption is indirectly measured by detecting the photoelectron yield, the angular dependence of the photoemitted intensity has to be taken into account. Generally, "differential" photoelectron yields $dY/d\Omega$ corresponding to differential cross sections $d\sigma/d\Omega$ are measured, because electron spectrometers have a limited acceptance solid angle. If the dipole approximation can be applied, the probability for the photoexcitation of one atom by a standing wavefield is calculated from a sum of the dipole matrix elements $\mathrm{E1}_0$ for the incident beam $\mathbf{k}_0$ and $\mathrm{E1}_H$ for the reflected beam $\mathbf{k}_H$ given by Eq. 3.11. The XSW yield profile

$$\begin{aligned}\left(\frac{dY(E)}{d\Omega}\right)_{\text{dipole}} &\propto |M_{fi}|^2 \propto |\mathrm{E1}_0 + \mathrm{E1}_H|^2 \\ &\propto 1 + R(E) + 2\sqrt{R(E)}\cos\left(\nu(E) - \mathbf{H}\cdot\mathbf{r}_{\text{core}}\right) \end{aligned} \tag{3.19}$$

is independent of the photon wave vector. The advantage if the dipole approximation can be applied is that the photoelectron yield measured under XSW conditions is truly proportional to the X-ray absorption cross section.

This situation changes if non-dipolar terms in the transition matrix element become significant and the dipole approximation can no longer be applied. The interference between the dipole contributions and the $\mathbf{k}$ dependent quadrupole contributions results in a pronounced movement of the photoelectron emission cone, when the Bragg energy range is traversed. Vartanyants and Zegenhagen [28, 41] took the interference between electric dipole (E1) and electric quadrupole (E2) transitions into account and neglected the weaker magnetic transitions, when they derived an analytic expression for the XSW yield profile for backreflection geometry: The excited photoelectron yield

$$\left(\frac{dY(E)}{d\Omega}\right)_{\text{quadrupole}} \propto 1 + S_R R(E) + 2\sqrt{R(E)}|S_I|\cos\left(\nu(E) - \mathbf{H}\cdot\mathbf{r}_{\text{core}} + \psi\right) \tag{3.20}$$

is no longer proportional to the X-ray absorption. The angular-momentum dependent quadrupole parameters S_R and $S_I = |S_I|e^{i\psi}$ need to be known in order to relate the absorption and emission rates. Vartanyants and Zegenhagen [28, 41, 42] derived theoretical expressions for these parameters for initial states with angular momentum $l = 0$, while expressions for p and d initial states have apparently not yet been determined.

The XSW photoelectron yield $Y(E)$ excited from a distribution of N atoms of one element or chemical species at positions $\mathbf{r}_j$ in a crystal is the sum of the yield contributions from each individual atom. In dipole approximation, the yield profile is obtained from a summation over N profiles described by Eq. 3.19 and results in

$$\begin{aligned} Y_d(E) &\propto 1 + R(E) + 2\sqrt{R(E)}\,\frac{1}{N}\sum_{j=1}^{N}\cos\left(\nu(E) - \mathbf{H}\cdot\mathbf{r}_j\right) \\ &= 1 + R(E) + 2\sqrt{R(E)}\,F^H\cos\left(\nu(E) - 2\pi P^H\right), \end{aligned} \tag{3.21}$$

where the coherent position P^H is the mean phase of the N atoms in the XSW field and the coherent fraction F^H is a measure for the spread of the atomic distribution along $\mathbf{H}$ direction. For a perfectly ordered distribution of atoms and a Debye-Waller

factor approximated by unity, F^H and P^H represent the amplitude and the phase of the geometrical structure factor for the atoms in the unit cell.

The line shape of the XSW absorption profile for an ensemble of atoms is strongly dependent on the coherent position P^H, i.e., of the mean position of the atoms with respect to the origin chosen for the geometrical structure factor. Fig. 3.6 illustrates the large variation in profile modulation, which provides the XSW method with a high spatial resolution.

If quadrupole contributions to the XPS yield cannot be neglected, the XSW yield profile from a distribution of N atoms analogously results from a summation over N profiles given by Eq. 3.20 to

$$Y_q(E) \propto 1 + S_R R(E) + 2\sqrt{R(E)}|S_I|F^H \cos\big(\nu(E) - 2\pi P^H + \psi\big). \tag{3.22}$$

The acceleration form of the transition matrix element, which was derived in the previous section and which is given by Eq. 3.16, showed that photoexcitation preferentially occurs in the vicinity of atomic cores. A direct experimental proof that photoemission takes place in a confined spatial region was given by Woicik *et al.* [3], who carried out XSW measurements on a core level and the valence level of metallic copper. The recorded XSW yield profiles for the Cu 3p shell (77 eV binding energy) and the valence level shown in Fig. 3.7(a) revealed almost identical modulation amplitudes and, hence, coherent fractions. This phenomenon was already previously observed for the 3d level and the valence level of germanium [2]. Fig. 3.7(b) shows high-resolution spectra for the Cu 3d valence level and the rather free-electron-like Cu 4s conduction level. The spectra were recorded for selected photon energies within the Bragg range, i.e., for different XSW positions, but they exhibit the same XSW modulations. Since basically identical coherent fractions were obtained for core, valence and conduction electrons, the authors concluded that nearly all ($> 95\%$) of the valence and conduction band emission arises from the same localized emission volume, as for the Cu 3p core emission [43]. Valence emission from inbetween the atomic cores would have significantly reduced the coherent fraction for the valence signal. The region between the atomic cores was concluded to be basically transparent for X-rays. The valence states occur in the X-ray photoemission spectra of the valence band with different weight.

The small spatial extension of the emission volume can allow applying the dipole approximation for valence emission, even if the less stringent conventional condition $|\mathbf{k} \cdot \mathbf{r}_{\mathrm{el}}| \ll 1$ is not satisfied for valence states. It shall be noted, however, that the small size of the emission volume does not guarantee the applicability of the dipole approximation, since even for core level states, influences of quadrupole effects can be observed in XPS.

3.3 XSW Real Space Imaging

A new image rendering application of the XSW technique results from the opportunity at third generation synchrotrons to take large XSW data sets comprising many Bragg reflections within a reasonable period of time. The possibility of focussing the X-ray beam guarantees high XPS intensities even for higher reflection orders. XSW real

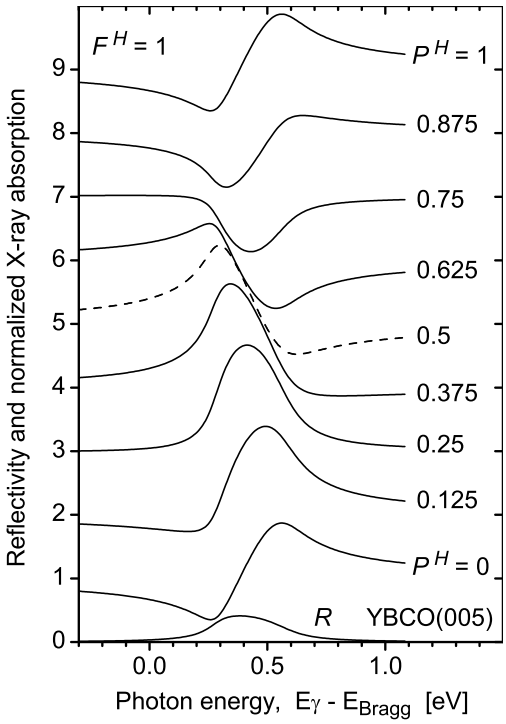

Figure 3.6: Line shape variation of an XSW absorption profile as a function of coherent position. The absorption profiles were simulated for the $YBa_2Cu_3O_{7-\delta}(005)$ reflection at $E_{\mathrm{Bragg}} = 2.661$ keV for a variety of coherent positions P^H and a fixed coherent fraction $F^H = 1$ based on dynamical theory of X-ray diffraction. The curves are normalized to the absorption off of the Bragg condition and are offset for clarity.

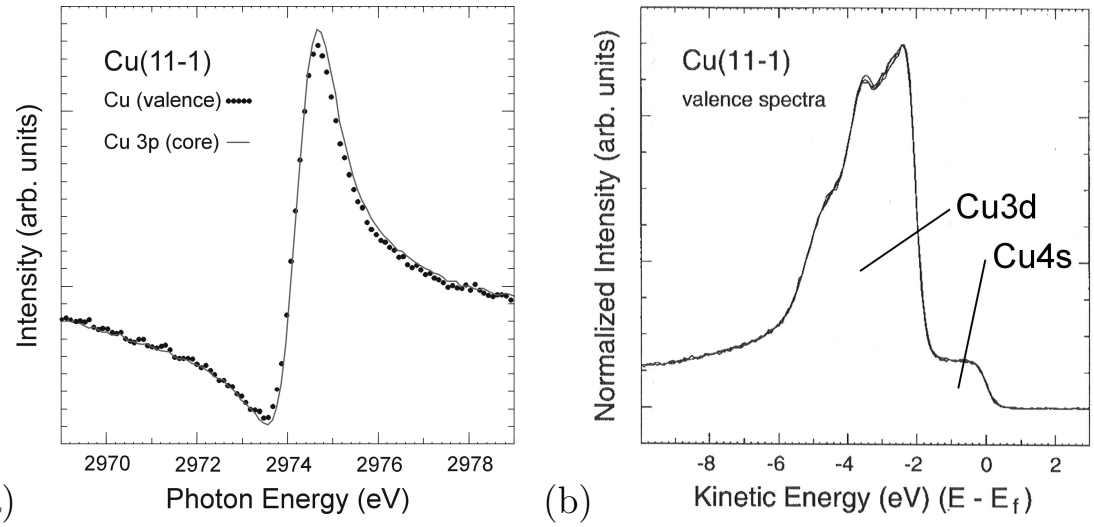

Figure 3.7: XSW data from Woicik *et al.* for valence and core states in metallic copper. (a) XSW yield profiles recorded for the Cu 3*p* and the valence signal. (b) Comparison of copper valence band spectra (normalized to peak height and aligned in binding energy) measured at distinct photon energies within the range of the $(11\overline{1})$ Bragg reflection. Figures taken from Woicik *et al.* [3].

space imaging represents a new and very direct way to three-dimensionally depict the atomic structure of crystal bulk material or a surface adsorbate with very high spatial resolution. Since XSW is usually combined with spectroscopic methods that are chemically selective, like XPS or fluorescence, the atomic distributions can be identified specifically for each element or even for individual chemical species. XSW imaging is capable of sensing even dilute concentrations of light elements and does not require long range order for the investigated structure. The method therefore efficiently complements conventional analytical tools for structure analysis, like SXRD, but is limited by its requirement for samples of high crystalline quality.

Diffraction techniques, like SXRD, suffer from one serious disadvantage — the phase problem: The measured quantity is the intensity of the diffracted beam, which is proportional to the square of the complex scattering amplitude. The phase of the scattering amplitude, however, which contains basically information about the phase relation of all the individual scattered rays and therefore information about distances between the scattering centres, is not experimentally accessible. As a consequence, diffraction data recorded in reciprocal space cannot be directly Fourier inverted to deliver the atomic structure in real space. Rather, the data analysis requires recovery of the phase information from a generally highly redundant set of diffracted intensity data, which is not a trivial iterative procedure. A good guess of the expected atomic structure usually constitutes the starting point for elaborating a structural model that is consistent with the data.

The key strength of XSW real space imaging as an interference technique is its phase sensitivity on the atomic scale. This property lends the method its capability to produce images of atomic distributions by direct Fourier inversion without the requirement of any guesswork on structural models. The coherent fraction F^H and position P^H obtained from an XSW yield profile measured for a reflection $\mathbf{H}$ represent the amplitude and the phase of the $\mathbf{H}$th Fourier component

$$G^H_{\text{exp}} = \int_{\text{unit cell}} d\mathbf{r}\, \rho(\mathbf{r})\, e^{i2\pi\mathbf{H}\cdot\mathbf{r}} = F^H e^{i2\pi P^H} \tag{3.23}$$

of the atomic distribution function $\rho(\mathbf{r})$ for the probed element. Each reflection can thus provide one (complex) geometrical structure factor G^H for each elemental sublattice. Measuring a sufficient number of different geometrical structure factors and directly back transforming them into real space yields the normalised atomic density

$$\rho(\mathbf{r}) = \sum_H G^H_{\text{exp}} e^{-i2\pi\mathbf{H}\cdot\mathbf{r}} \tag{3.24}$$

for each element. Exploiting the symmetry relation $P^{\bar{H}} = -P^H$ for a centrosymmetric crystal, this equation reads

$$\rho(\mathbf{r}) = 1 + 2\sum_H F^H \cos 2\pi(P^H - \mathbf{H}\cdot\mathbf{r}). \tag{3.25}$$

The more Fourier components are included in the image reconstruction, the more clearly the spatial distribution of atoms can be resolved and the more the oscillating background that results from the finiteness of the Fourier expansion is reduced.

The reconstructed images represent the probed structures projected into the unit cell of the XSW generating lattice, owing to the limitation to (hkl) Fourier components obtained from substrate (hkl) reflections. In other words, a depiction of the sampled structure "modulo" the lattice of the substrate crystal is obtained. The information on a length scale beyond the dimensions of the substrate unit cell is missing in order to reconstruct a true unfolded image. Unfolding structures of dimensions beyond the substrate unit cell, like supercell structures, will require additional information about their geometry.

XSW real space imaging is also applicable in cases where the unknown structure under study itself generates the standing wavefield, which is used as a probe. An XSW study requires some minimum information about the structure in advance in order to find the Bragg reflections. But it is possible to solve the structure without any further *a priori* knowledge, i.e., without knowledge of the bulk structure factors, which are required for the XSW analysis. This is possible by an iterative procedure described by Cheng *et al.* [44]. The procedure is entirely model-independent.

Structural Refinement

The real space images, which are obtained by the XSW imaging method as described above, will allow generating one unique structural model. This requires that the images were created from sufficiently large XSW data sets such that the atomic positions are well resolved and the crystal symmetry can be identified. Fitting the model to the data allows a structural refinement, which yields the precise coordinates of the individual atoms. Selected model parameters that are of interest can be determined, e.g. strain or lattice site occupacies. For this purpose, geometrical structure factors G^H_{model} are calculated for the structural model for all elements and all reflections H used in the XSW experiment. The refinement is carried out directly in reciprocal space by varying the free model parameters such that the squared deviation of the structure factors is minimised:

$$\sum_{\text{all elements}} \sum_{H} |G^H_{\mathrm{model}} - G^H_{\mathrm{exp}}|^2 \stackrel{!}{=} \min. \tag{3.26}$$

It has to be taken into consideration at this stage that the structural information contained in the experimentally determined values G^H_{exp} is disguised in particular by two physical effects. The influences of the thermal lattice dynamics and the attenuation of the emitted photosignal cannot be removed from the experimental data. When fitting a structural model to the data according to Eq. 3.26, these effects need to be included in the calculation of the values G^H_{model}. These values can generally be well described by the expression

$$G^H_{\mathrm{model}} = F^H e^{i2\pi P^H} = \frac{\sum_s e^{-z_s/(\lambda \sin\alpha)}\, o_s\, (1 - f^H)\, e^{-M_s}\, e^{i2\pi \mathbf{H}\cdot\mathbf{r}_s}}{\sum_s e^{-z_s/(\lambda \sin\alpha)}\, o_s}, \tag{3.27}$$

where the sum extends over all lattice sites s in the unit cell of the probed structure that are at least partially occupied by the corresponding element. In the presence of a superstructure, which can be induced by a surface reconstruction, the summation has to be carried out over all sites within the supercell. Likewise, for epitaxially grown

submonolayer coverages or coverages that are terminated by incomplete unit cells, the summation has to be carried out over a suitable characteristic volume element of the film that is larger than the unit cell.

The attenuation of the photosignal coming from a depth z below the sample surface is taken into account by an exponential weighting factor. The attenuation length for the photoelectrons is denoted λ, and α is the electron take-off angle with respect to the sample surface. The attenuation length is strongly dependent on the density of the sample material and on the kinetic energy of the photoelectrons. The occupancy o_s of site s is a value ranging from 0 to 1 and allows reducing the weight of signals originating from superstructure sites. The incoherent fraction f^H takes the signal contribution from the disordered fraction of an elemental distribution into account [45]. The measured XSW signal represents a time average over the thermal oscillations of the atoms in the lattice. While the phase P^H of the measured geometrical structure factor is determined by the mean atomic positions, the amplitude F^H is reduced by the influence of thermal vibration. This reduction is taken into consideration by including an exponential factor with the (dynamical) Debye-Waller factor M_s for each lattice site s. The Debye-Waller factor is related to the atomic mean square displacement $\langle u^2 \rangle$, which for simplicity can be assumed to be isotropic, via the temperature B factors [46], resulting in the relation $M = 8\pi^2 \langle u^2 \rangle \sin^2 \theta / \lambda^2$.

3.4 XSW Valence Electronic Structure Analysis

The investigation of the electronic structure of solids employing the XSW method is another comparatively new field of increasing interest in the XSW community besides XSW real space imaging, which is described in the previous chapter. Conventionally, the XSW technique has been used for structural studies; adsorbate structures on single crystal surfaces have been determined with atomic resolution. For this purpose, photoemission needs to be measured only from core levels in order to indirectly determine the photoabsorption. XSW yield profiles are recorded and the coherent positions and fractions extracted for a number of suitable Bragg reflections, and the absolute positions of adsorbate atoms are determined by triangulation. Besides, core level XPS data also allowed quantitative chemical composition analysis (ESCA). But the full analytical capability of photoelectron spectroscopy – which intrinsically constitutes one of the most direct methods of studying the electronic structure of solids – was yet not made use of.

Indirect information on the electronic structure can be deduced from measuring photoemission from chemically shifted components of core levels under XSW conditions. Chemical shifts in core level binding energies result from changes in the valence electronic structure of atoms caused by the chemical environment. Chemical shifts can be observed when atoms of the same element populate nonequivalent lattice sites [47, 48]. So far, the XSW method has been applied to chemically shifted components of core level signals for structural studies only. Different sites occupied by the same element could be discriminated [49–52]. When monitoring core level photoemission signals, the chemical selectivity of the analytical tool XPS and the spatial resolution power of the

XSW method can be advantageously combined. Core level XPS signals from different elements are mostly well separated in binding energy and can be well discriminated. Chemically shifted components of core level XPS signals can also be separated in many cases, while more effort during the data analysis may need to be spent on separating signals that overlap in binding energy.

Direct information on the electronic structure can be gained from immediately probing valence states by photoemission. The valuable information of the photoelectron momentum, pertaining to electronic dispersion relations $E(\mathbf{k})$ for the electrons propagating inside the solid and the unique possibility of band structure mapping, is still difficult to access at X-ray photon energies with the experimental tools available nowadays. On the other hand, additional high spatial resolution can be attained by recording photoemission under standing wave conditions. This is only possible in the X-ray regime with radiation wavelengths of the order of unit cell dimensions. Hardly any other experimental technique other than XPS in combination with the XSW method, hence X-ray photoemission in a spatially resolved way, allows determining site-specific electronic structures. In addition, with the help of DOS calculations, photoionisation cross sections for valence electrons delocalised in the solid can be experimentally determined. In contrast to core level XPS, where XPS signals from individual elements are well separated in binding energy or where chemically shifted components partially overlap, the valence band spectrum is a superposition of fully overlapping signals from different lattice sites. A direct elemental assignment of the spectral features is not possible. However, by employing site-specific photoemission and performing a quantitative XSW analysis, the individual valence signal contributions can be discriminated.

In the following, the principle of an XSW electronic structure analysis using XPS will be outlined in order to enable an understanding how lattice site-specific valence electronic information can be obtained experimentally. The strongly bound electronic core states of the free atom are little affected when the solid state is formed; chemical shifts in binding energy occur. The weakly bound states in contrast, which rearrange to form the valence and conduction bands and which are involved in the chemical bondings, are responsible for most of the physical properties of the solid state. We aim at decomposing the valence spectrum $Y(E_B)$ into a direct sum

$$Y(E_B) = \sum_{\text{nonequivalent lattice sites } s}^{m} Y_s(E_B) \tag{3.28}$$

of lattice site-specific valence contributions $Y_s(E_B)$. These partial spectra may either originate from single lattice sites, or they may come from groups of equivalent lattice sites in the unit cell that are occupied by the same elemental species. Sites, which are equivalent by symmetry and which are populated by only one element, can be considered as the same. Their XPS spectra and, hence, their individual valence yield contributions are identical and can be combined in one yield component $Y_s(E_B)$. Single sites and groups of equivalent sites represent the smallest atomic units, the valence contributions of which can be resolved, and are denoted by the variable s. The number of nonequivalent sites s in the unit cell shall be denoted m. As an example, we distinguish between $m = 3$ nonequivalent lattice sites s in the bulk perovskite unit cell, one

site s for each element, where the three equivalent oxygen sites have been identified. In context with the electronic structure analysis for perovskites, the terms "site-specific" and "element-specific" become synonymous.

Each valence contribution $Y_s(E_B)$ from site s in Eq. 3.28 can be associated with a characteristic XSW absorption profile, which depends on the chosen reflection. When sweeping the photon energy through the range of a Bragg reflection, the maxima of the standing wavefield traverse half the diffraction plane spacing and move over the distribution of lattice sites. The partial contribution $Y_s(E_B)$ to the valence yield excited from site s undergoes a modulation of the form

$$\begin{aligned} Y_s(E_B, E_\gamma) &= Y_s(E_B)[1 + R(E_\gamma) + 2\sqrt{R(E_\gamma)}F_s^H \cos\left(\nu(E_\gamma) - 2\pi P_s^H\right)] \\ &\equiv Y_s(E_B) I_s(E_\gamma), \end{aligned} \tag{3.29}$$

where the intensity modulation term in square brackets for a quadrupole-insensitive experimental setup was introduced in section 3.2. $Y_s(E_B)$ is the reference spectrum of the photoemission yield excited from site s due to the incident beam alone, i.e., the yield excited off of the Bragg condition. The modulation term depends on the reflection, which has to be carefully chosen as described below, and is characterised by the structural parameters, the coherent position P_s^H and coherent fraction F_s^H of the sub-lattice formed by the site s. For contributions coming from single lattice sites, simply $F_s^H = 1$ and $P_s^H = \mathbf{H}\cdot\mathbf{r}_s$, where $\mathbf{r}_s$ is the position vector of the lattice site. As we work in the linear regime, the modulation term is a separate photon energy dependent factor, which can be summarised in the variable $I_s(E_\gamma)$. In dipole approximation $I_s(E_\gamma)$ also describes the modulation of all the core level signals coming from site s, which is identical to the modulation of $Y_s(E_B, E_\gamma)$.

In order to experimentally gain the XSW modulation information for the individual valence contributions $Y_s(E_B)$, we exploit the fact that the dipole approximation can be applied to the valence photoexcitation with little residual error (see the discussion for Cu valence electrons in context with Fig. 3.7 on page 25). The valence signal modulation $I_s(E_\gamma)$, which is not directly accessible by experiment, can be derived from one of the core level signals from site s. This is usually possible as long as an XPS geometry insensitive to the quadrupole effect is chosen, which is a geometry with the electron detector mounted along the polarisation direction of the beam. In all other arrangements, $I_s(E_\gamma)$ cannot be directly inferred from core level XSW profiles due to the influence of multipole effects: While for core level states, the quadrupole parameters γ and δ have been calculated so that their influence on the XSW profiles could be taken into consideration, these parameters are not known for delocalised valence states. Quadrupole parameters for strongly delocalised and hybridised states depend on the particular electronic distribution in the solid. Choosing a quadrupole-insensitive XPS geometry will therefore avoid influence of such additional unknown parameters that would introduce additional systematic errors in the XSW analysis of the electronic structure. An experimental investigation of the influence of multipole effects on core level XSW profiles can be found in appendix B.2.

A prerequisite for the complete valence band decomposition into m components according to Eq. 3.28 is that core level XPS signals from all m nonequivalent sites s

can be clearly identified in order to monitor the modulation $I_s(E_\gamma)$ of each component $Y_s(E_B)$. Overlap of core level signals from different elements or small chemical shifts, insufficient to allow signal separation from different species of one element, may not allow resolving the valence band contributions from the corresponding individual sites. In this case, the valence band contribution from a combination of sites s can be identified. Alternatively, if a complete decomposition into m components is desired, the set of experimentally obtained modulation profiles can be completed by theoretically calculated modulation profiles.

The experimental data required for an electronic structure analysis consist of core level and valence band XSW data sets collected for properly chosen Bragg reflections. Relative core level intensities (with respect to the off-Bragg intensity) from each site s and high resolution VB spectra are recorded for $n \geq m$ different photon energies $E_\gamma = E_{\gamma\ 1}, \ldots, E_{\gamma\ n}$ within the energy range of each reflection. The number of standing wave positions n must be chosen at least equal to the number m of sites s but may also be larger for experimental reasons. The information gained from an XSW measurement at a single reflection H in principle allows separating all contributions $Y_s(E_B)$ whose modulations $I_s(E_\gamma)$ are linearly independent and show contrast in line shape. In practice, sufficient contrast is usually obtained only between XSW modulations that are characterised by different coherent positions P_s^H. Information gained from different suitable reflections may need to be combined in order to identify all of the m components $Y_s(E_B)$.

The site-specific valence contributions are obtained from decomposing the VB spectra recorded at different standing wave positions with respect to the lattice. Preferential excitation of specific lattice sites at certain XSW positions enhances the valence band spectral features characteristic of the increased yield contribution. The VB spectra $Y(E_B, E_\gamma)$ differ in line shape and represent differently weighted linear combinations of site-specific yield contributions $Y_s(E_B)$. The weighting factor of each individual contribution varies according to its characteristic XSW modulation $I_s(E_\gamma)$. The system of linear equations

$$Y(E_B, E_{\gamma\ i}) = \sum_{s=1}^{m} I_s(E_{\gamma\ i}) Y_s(E_B) \qquad i = 1, \ldots, n \tag{3.30}$$

obtained by inserting Eq. 3.29 into Eq. 3.28 is overdetermined if the number of XSW positions n exceeds the number m of nonequivalent sites s. The m functions $Y_s(E_B)$ that come closest to solving the system of equations can be obtained by least squares fitting and constitute the result of the XSW electronic structure analysis. The sum $\sum_s Y_s(E_B)$ represents the valence band $Y(E_B)$ for unity X-ray intensity at the Bragg photon energy, which is identical in line shape to the spectrum obtained several electron volt off of the Bragg condition.

An alternative conventional technique that can provide specific spatial information about the electronic structure is resonant photoelectron spectroscopy. Resonant photoemission uses the fact that certain spectral features increase in intensity when the photon energy is scanned through the absorption edge of one of the constituent elements in the sample. The origin of the enhancement is the coherent superposition of

the direct transition to the final state and an indirect transition, which is caused by the Auger process of an excited core electron. The presence of a resonance in certain ranges of the valence band allows identifying the elemental origin of spectral features and gives a clue about the character of the associated bonds. To give an example, Higuchi *et al.* provided information about the influence of Nb [53] and La [54] doping on the degree of hybridisation between Ti $3d$- and O $2p$-derived states in $SrTiO_3$. The authors measured photoemission from the $SrTiO_3$ valence band at the Ti $3p \rightarrow 3d$ optical absorption edge. Resonant features of the VB, which is mainly derived from O $2p$ states that are not expected to resonate at those photon energies, were attributed to strong Ti-O hybridization. The authors observed an increase of the Ti $3d$ contribution to the valence band upon Nb doping and a decrease upon La doping and concluded that degree of hybridization had changed corresponding to the ion charge.

Compared to the XSW method, resonant photoelectron spectroscopy is an experimentally "less direct" method for deducing site-specific valence electronic information. Resonant photoemission is a comparably more complex physical process, and in addition a quantitative analysis is more difficult to carry out. Owing to the selection rule for dipole transitions $\Delta l = \pm 1$, the applicability of resonant photoemission is less universal and is restricted by the limited number of possible decay channels for a given system. Distinguishing signals of the same element populating two nonequivalent lattice sites is possible with the XSW method but cannot be achieved by means of resonant photoelectron spectroscopy.

Chapter 4

Experimental Details

While the principles of XSW real space imaging and XSW electronic structure analysis are explained in the previous chapter, the experimental facilities used for performing experiments with these techniques and the laboratory for the sample preparation are described in the following sections. New developments, such as a UHV cleaving device for small crystals and a setup for photoemission in the hard X-ray regime are presented. The methods employed for the sample preparation and characterization at the initial stage of an experiment are described. A general overview of the XSW data acquisition procedure and the data analysis is given.

4.1 Beamline ID32 and Experimental Stations

The beamline ID32 is one out of three insertion device beamlines at the ESRF dedicated to surface physics. A diffractometer, which is suitable for surface X-ray diffraction experiments, and a UHV chamber for X-ray photoemission and fluorescence spectroscopy are installed. For radiation protection, the two experimental stations are housed by lead-shielded hutches. The experiments are carried out under camera surveillance by computer remote control.

The experimental stations are located at the end of the beamline, the setup of which for spectroscopy is sketched in Fig. 4.1. The horizontally polarised X-ray beam is generated by the relativistic electrons, which circulate in the ESRF storage ring with a kinetic energy of 6 GeV, passing periodic arrangements of magnets called undulators. Three undulators of 1.6 m length each are installed at ID32. A photon energy between 2.3 and 30 keV can be selected by adjusting the undulator gap and tuning a liquid nitrogen cooled primary Si(111) double crystal monochromator with a relative energy resolution of $\Delta E/E = 1.3\times10^{-4}$, where the heat load on the first silicon crystal is limited by white beam slits. The bandwidth of the X-ray beam can be reduced further by a secondary monochromator; a variety of different Si reflections with different band pass are available. The unfocussed monochromatic beam is typically 0.8(v)×1.2(h) mm in size.

For the beamline setup for the use of the diffractometer, a mirror with SiO_2, Cr and Pt coatings is available for vertical focussing and harmonics rejection. An automatic filter system for the incident beam is installed to prevent the szintillator detector from

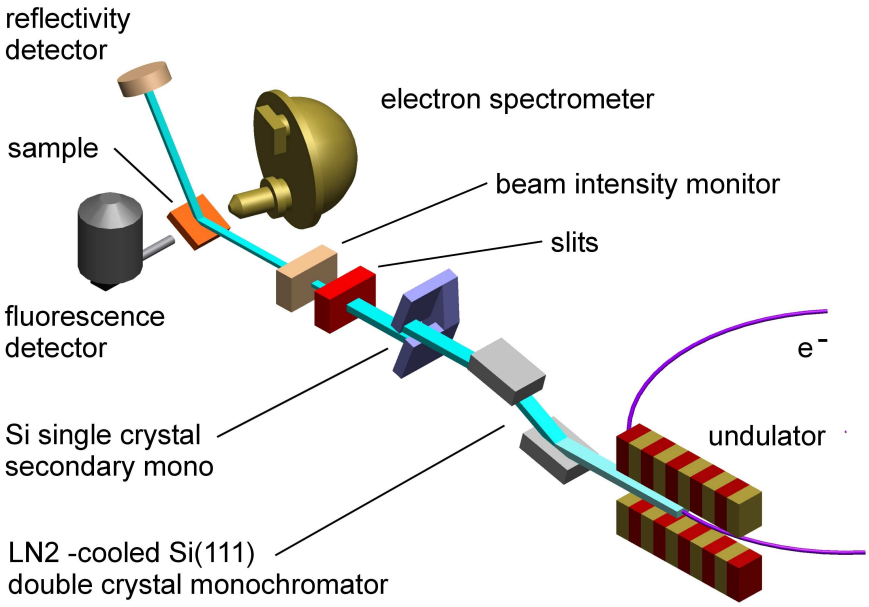

Figure 4.1: Schematic of the essential X-ray optical devices of the ID32 beamline set up for XPS and XSW.

saturation. The six-circle kappa diffractometer in the upstream experimental hutch, which is shown in Fig. 4.2(a), can be used for SXRD measurements as well as for XSW experiments with fluorescence detection. In combination with a small UHV "baby" chamber with a Be dome, samples can be investigated in UHV environment. The baby chamber can be mounted on the topmost circle of the sample arm, the φ circle, or alternatively on an additional high-load tower, which can be mounted on the lowest circle of the sample arm, the ω' circle. The arrangement of the circles is described by Thorkildsen [55]. Having six circles allows measurements with the sample surface aligned once in the vertical for SXRD experiments in pure σ polarization, where the diffractometer can be used as a Eulerian (2×2)-circle goniometer, and once in the horizontal for SXRD and XSW experiments, where the strongly vertically collimated beam is exploited best. For these purposes, the kappa geometry is much more practical than alternative arrangements of the six circles, because the space in front of the diffractometer is left unobstructed for the fluorescence detector mounting.

When the beamline is set up for using the UHV chamber, the cross section of the beam is defined by two orthogonal pairs of slits. The relative incident intensity ("monitor") is measured from the drain current of a thin metal foil passed by the X-rays. The beam hits the sample in UHV environment, where photoemission and fluorescence can be measured. The reflected beam is detected by an insulated metal plate, and the sample reflectivity is obtained on a relative scale from the photo current of the plate. The UHV chamber in the downstream experimental hutch shown in Fig. 4.2(b) with a base pressure of 2×10^{-10} mbar is equipped with a Perkin-Elmer PHI model 10-360 hemispherical electron energy analyser with a 16-channel detection

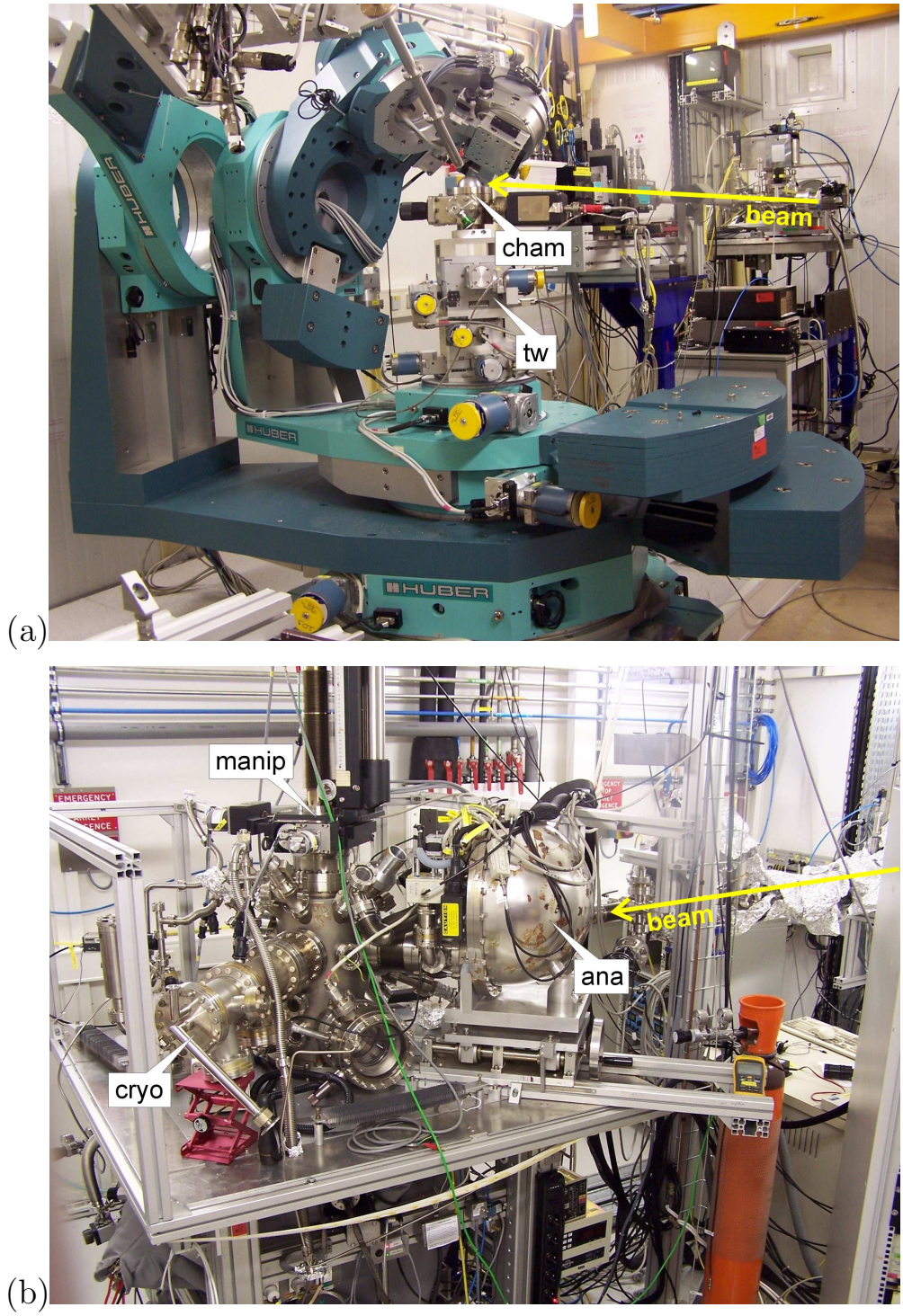

Figure 4.2: Photographs of (a) the six-circle kappa diffractometer and (b) the UHV chamber at beamline ID32. The direction of the incident beam is marked by an arrow. The transfer "baby" chamber ("cham"), which is shown in more detail in Fig. 4.7, can also be mounted on an additional tower ("tw"). The UHV chamber with the hemispherical electron energy analyser ("ana") is shown with the vertical manipulator ("manip") and the cryostat ("cryo") mounted. The fluorescence detector is not shown.

system. The operational range of electron energies is up to 4.8 keV. A Gresham Sirius liquid nitrogen cooled solid state detector with ∼130 eV energy resolution can be used, which is separated from the UHV by a 0.3 μm mylar window such that fluorescence can be detected also from light elements, like oxygen. Also available are LEED and surface preparation tools, such as Knudsen evaporation cells, a quartz balance, and a sputter ion gun. The three linear and two rotational degrees of freedom of the vertical manipulator allow sample positioning and angular alignment. The manipulator head is connected to a liquid helium continuous flow cryostat by a copper braid for cooling. The sample temperature is monitored by a Schottky diode and a thermocouple attached to the sample head and reaches 35–40 K within 45–60 min starting from room temperature. The indirect sample heating reaches up to 600 °C.

For the hard X-ray photoelectron spectroscopy described in chapter 6 and in appendix F, the energy range of the PHI electron analyser was extended from 4.8 to 14.8 keV by adding a specially designed supplementary retarding lens. The lens was designed by C. Kunz and M. Renier [56]. An insulated manipulator head, which matches the geometry of the lens and which allows for high-voltage sample biasing, was constructed and mounted on a horizontal manipulator.

The supplementary retarding lens images photoelectrons from a sample onto the focal point of the PHI hemispherical analyser as shown in Fig. 4.3(a). The electrons emerging from the sample biased up to +10 kV relative to earth traverse an electric retarding field and are handed over to the PHI Omega type lens at earth potential. The supplementary retarding lens is mounted in a μ-metal shielding cylinder, which was attached to the PHI Omega lens as shown in Fig. 4.3(b). The sample is located inside the well screened entrance of the lens. The X-ray beam enters through a conical aperture in the lens and shield. The aperture with a half angle of ±5° allows for the reflected beam to leave in XSW experiments close to back reflection geometry. The manipulator head shown in Fig. 4.3(c) accommodates 10×10 mm sample plates and the crystal cleaving devices shown in Fig. 4.10(c). The head is electrically insulated by a sapphire rod and thermally decoupled from the manipulator and can be cooled down to ∼35 K within typically 45 min. The PHI analyser together with the supplementary retarding lens can be retracted to give access to the sample for transfer and cleaving.

A simple concept with only one focussing electrode was chosen for the supplementary retarding lens, which consists of three lens elements as sketched in Fig. 4.3(d). The lens design aimed at collecting photoelectrons from the sample over a solid angle as large as possible, and focussing these electrons by matching the acceptance specifications of the PHI electron analyser, such as acceptance solid angle and focal spot size (∼100 μm). As the SIMION [57] simulation of the photoelectron trajectories in Fig. 4.4(a) shows, good imaging properties were achieved for photoelectrons emitted from the sample into a cone with a half angle of ±6°. The focal spot size of the supplementary lens at the position of the sample, which was experimentally measured to be ∼200 μm, makes reasonable use of the incident beam size. The potential landscape depicted in Fig. 4.4(b) illustrates the principle of functioning of the lens. Electrons entering the interior of the lens are strongly decelerated and then focussed by the central cylindrical electrode. In order to enable focussing, the required minimum time of flight inside the static focussing electrode is attained by slowing down the electrons to

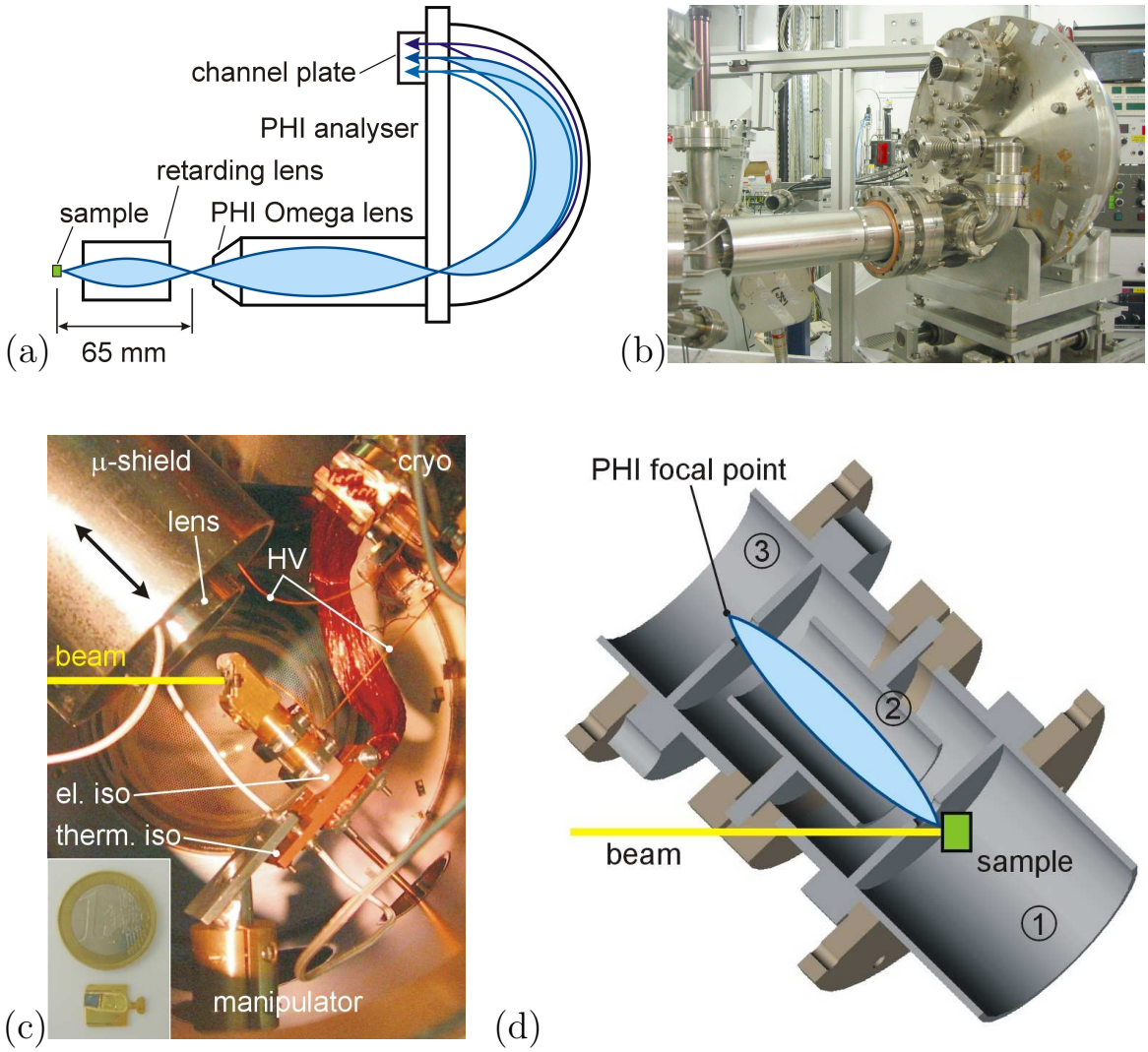

Figure 4.3: Hard X-ray photoemission apparatus at beamline ID32. (a) Schematic of the photoelectron enveloppe inside the arrangement of supplementary retarding lens and PHI hemispherical analyser. (b) Photograph of the retarding lens in a μ-metal tube attached to the PHI electron analyser. (c) Photograph of the setup inside the UHV chamber (top view). The μ-metal tube with the retarding lens is retracted. Samples mounted on plates of the type shown in the inset can be biased at high voltage. The manipulator head is electrically insulated by a sapphire rod. The head is thermally isolated from the manipulator rod and can be cooled via a copper braid by a liquid helium cryostat. The rotary manipulator is mounted on an xyz stage. (d) Schematic cross section of the retarding lens. The three lens elements (numbered), which are biased at different potentials, are insulated from each other by polyester rings. The sample is located in the large field-free volume of lens element 1. Lens element 2 acts as the focussing electrode.

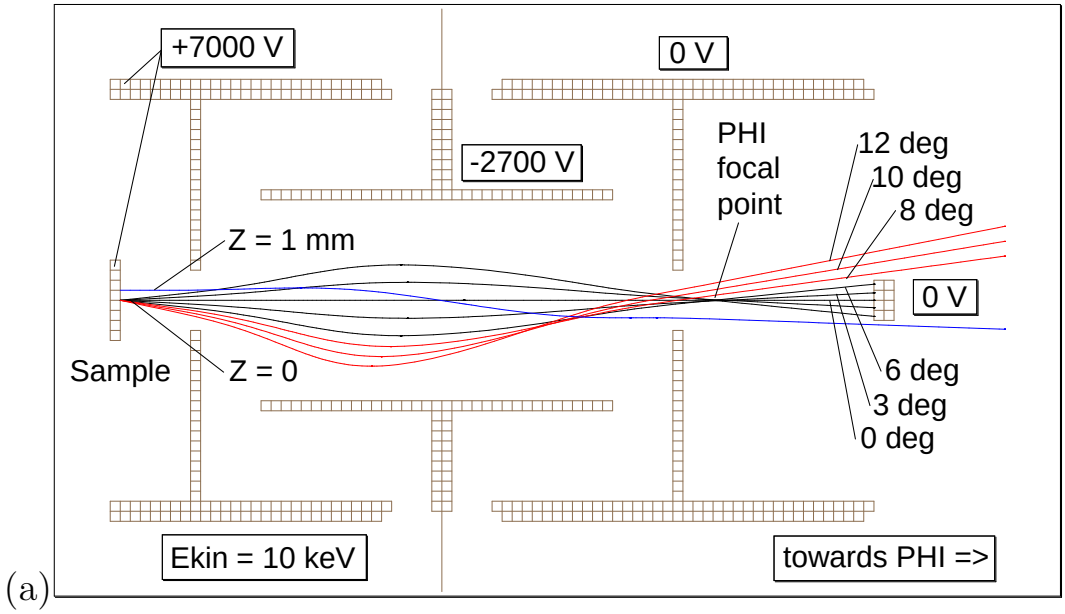

(a)

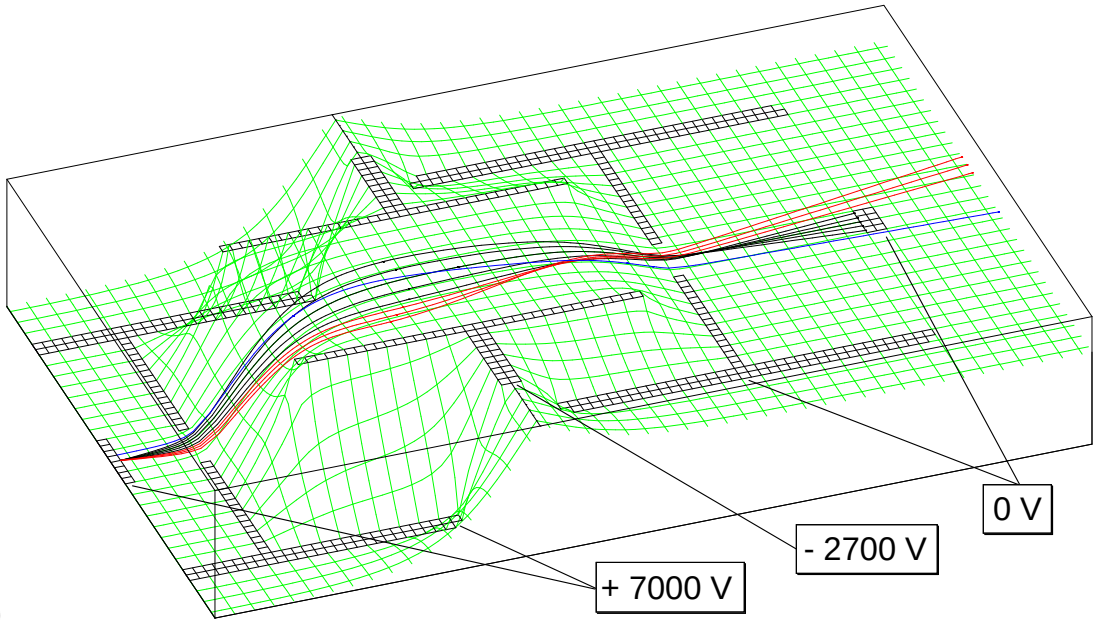

(b)

Figure 4.4: Simulation of electron trajectories inside the supplementary retarding lens (longitudinal section). (a) Trajectories for different electron take-off angles (marked) from the sample and radial positions z under typical operating conditions. (b) Potential landscape inside the electrostatic retarding lens. For the shown example, electrons with an initial kinetic energy of 10 keV are retarded by 7 keV and are handed over to the PHI electron analyser with a residual kinetic energy of 3 keV.

a kinetic energy of a few hundred electron volt.

With the supplementary retarding lens in operation, spectra of a limited energy range were recorded by scanning in parallel the retarding voltage of the PHI Omega lens and the focussing voltage of the retarding lens, while the sample potential was kept constant. Constant transmission over a reasonable energy range is achieved, but defocussing and loss in intensity are unavoidable for wider scan ranges. A total instrumental energy resolution of 220 meV was determined from measuring the width of the Fermi edge of gold as shown in Fig. 4.5.

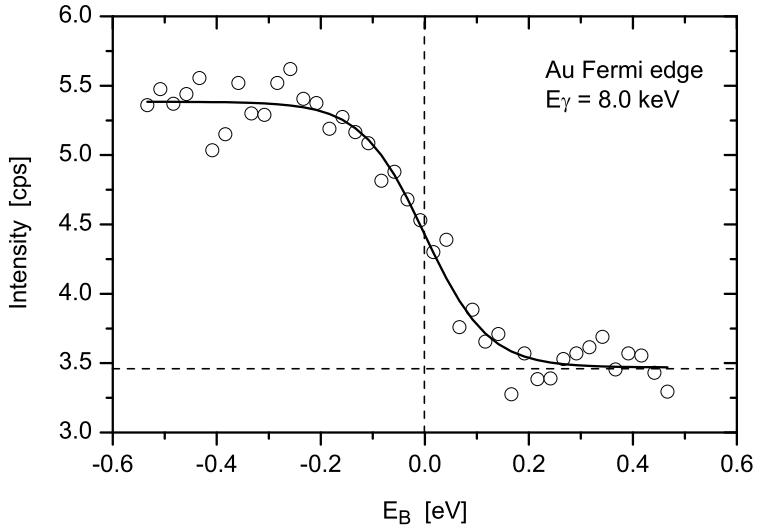

Figure 4.5: XPS spectrum of the Fermi edge of gold. The data (room temperature, Si(444) secondary monochromator, 5.95 eV pass energy for the PHI analyser) were fitted by a Fermi function convolved by a Gaussian function of 220 meV FWHM width, which represents the instrumental resolution. Sampling time: 200 s/data point. (The high dark-count rate results from faulty PHI electron analyser electronics.)

First attempts to increase the photoelectron yield at high photon energies by matching the X-ray beam spot and the analyser focal spot sizes employed beryllium compound refractive lenses to focus the X-ray beam. At a photon energy of 8.7 keV, the incident beam from two undulators of 800×800 μm defined by the white beam slits was focussed down to a size of 45×480 μm at the sample position, yielding a photoelectron gain of a factor 4–5. However, the use of the available compound refractive lenses imposes strong constraints as far as the choice of the photon energy is concerned. For XSW experiments it is basically impossible to select a photon energy such that the following three conditions are fulfilled at the same time:

- At a fixed focal length determined by the beamline setup, an integer number of lenses can be used. Around 8 keV, this restricts the possible photon energies available for experiment into narrow ranges of 50–100 eV separated by steps of 1.2 keV.
- XSW experiments may require back reflection geometry for the sample, where the Bragg angle is close to 90°.

- Using the Si(444) or Si(555) reflections for the secondary monochromator requires back reflection geometry in order to accept the full beam divergence of 10–20 μrad.

A focussing system based on silicon Fresnel zone plate lenses has been tested and will be installed in front of the UHV chamber, allowing horizontal and vertical focussing down to a 1×10 μm spot size.

4.2 Surface Characterization Laboratory

The laboratory associated with the ID32 beamline provides a working environment, which is independent of the beamline operation. A variety of surface preparation and characterization tools are available for making samples during or before upcoming beamtimes. Samples with freshly prepared surfaces can be carried to the experimental stations at beamline ID32 for X-ray experiments in one of the three transfer "baby" chambers without breaking the UHV. For sample transfer under less critical conditions in high vacuum, a transfer chamber consisting of an ion pump and a transfer rod attached to a UHV cross was used. The sample transfer allows combining reciprocal space and real space measurement techniques to obtain complementary information on the same sample. SXRD and the XSW methods presented in the previous chapters 3.3 and 3.4 yield rather integral information about a surface, while STM and STS provide a very localised picture of structural and electronic properties.

The smaller one of the two UHV systems in the laboratory houses an Omicron STM with a tripod scanner. A small preparation chamber contains LEED and surface preparation tools.

The large UHV system with a base pressure of less than 1×10^{-10} mbar consists of an arrangement of several vacuum chambers, which contain different tools as sketched in Fig. 4.6. The chambers are connected by an R2P2 transfer system; the pivoted linear drive allows passing around the ID32 standard sample plates, which are compatible with the baby chambers and the UHV system at the beamline. A standard Omicron STM with a single-tube scanner, a combined setup for LEED and Auger spectroscopy and Knudsen-type effusion cells for MBE are available. For STM operation the UHV system can be lifted to float on pressurized air dampers. In the annealing chamber surfaces can be prepared by argon ion sputtering and annealing by either direct ohmic heating or by indirect heating up to temperatures of 930 °C. The sample temperature is monitored by a pyrometer. A home-built low temperature STM had not been implemented into the system by the time the experimental work was finished. For the pulsed laser deposition, which is described in section 4.3, pulsed UV light ($\lambda = 248$ nm) of a KrF Excimer laser (Lambda Physik model Compex 205) is coupled through a quartz window into the PLD chamber, which is under high vacuum, and is then focussed on a target of the source material for the deposition. Since precise temperature control is an important issue for the reproducibility of growth conditions, a mirror image arrangement of the thermocouple and the sample substrate with respect to the platinum filament was chosen for the PLD substrate heater.

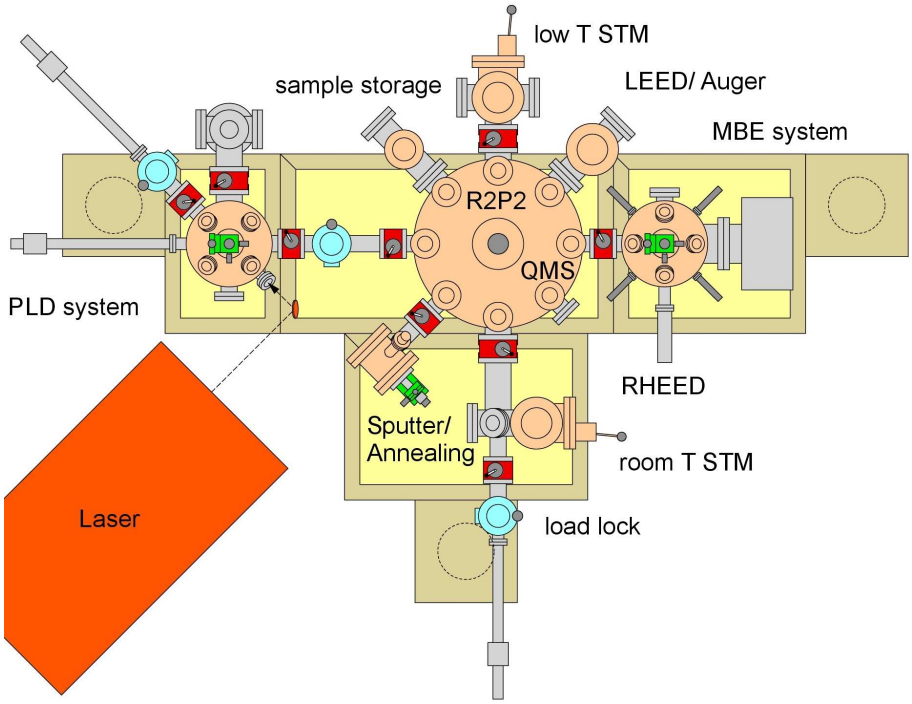

Figure 4.6: Schematic of the large UHV system in the Surface Characterization Laboratory.

The three identical ID32 baby chambers (weight ∼10 kg) as shown in Fig. 4.7 can be used for sample transfer in UHV between Surface Characterization Laboratory and beamline, where the chambers can be mounted on the diffractometer. The hemispherical beryllium dome, which has an inner radius of 31.5 mm and a thickness of 0.4 mm, is transparent to X-rays and contains the sample. A 20 litre ion pump powered by battery is connected to the transfer chamber opposite the sample introduction port. The cold cathode gauge has a large operational range down to 1×10^{-10} mbar. Additional sample cooling and heating are currently being incorporated.

4.3 Sample Preparation Techniques

Thin films and submonolayer coverages of $YBa_2Cu_3O_{7-\delta}$, which were characterized within the scope of this thesis work, were prepared by hetero- and homoepitaxial growth employing pulsed laser deposition. The preparation of clean $SrTiO_3(001)$ and $YBa_2Cu_3O_{7-\delta}(001)$ single crystal surfaces required different methods, namely vacuum annealing and low temperature cleaving, respectively.

Pulsed Laser Deposition

For preparing high-temperature superconducting thin films pulsed laser deposition has been employed, which besides chemical vapour deposition and off-axis magnetron sputtering is the most commonly used technique. PLD is a simple-to-use, comparably clean

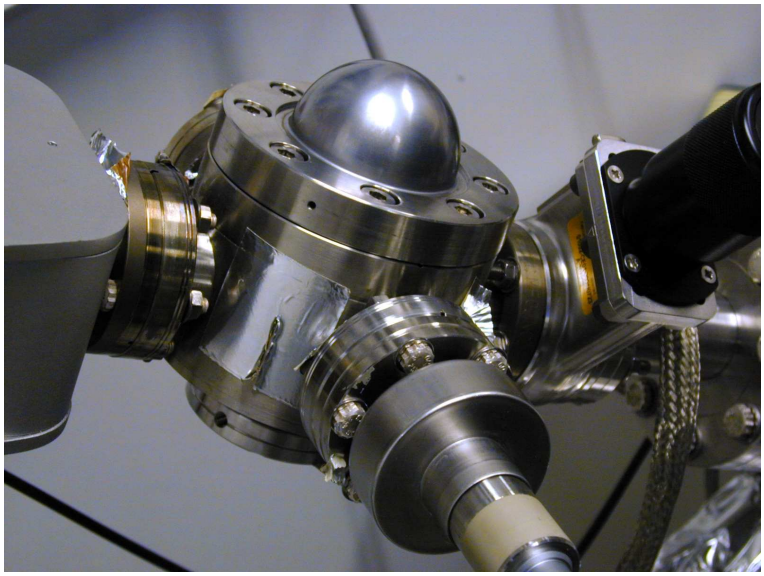

Figure 4.7: Photograph of an ID32 transfer "baby" chamber. The baby chambers allow UHV transfer of samples with freshly prepared surfaces from the Surface Characterization Laboratory to the beamline and subsequent measurements on the diffractometer.

deposition method with the source material evaporated by UV-light from outside the UHV system. The main advantage of PLD is the stoichiometric transfer of the source material to the substrate; the composition of the source material is retained in the deposited film [58]. For this reason PLD is particularly suitable for depositing complex oxide materials containing many elements. The principle of the material transfer from target to substrate is simple: Source material is ablated by the absorption of pulsed laser light of high energy density and is deposited on a substrate. The deposition process is described in more detail in the following.

The interaction of the incident light pulse with the polycrystalline $YBa_2Cu_3O_{7-\delta}$ target material (Superconductive Components, Inc., USA) comprises thermal and electronic excitation and thermionic emission at the beginning of the laser pulse, followed by absorption processes by the as-created dense plasma of evaporated material as described by Bhattacharya *et al.* [59]. The source material is ablated as a whole despite of the different vapour pressures of the constituent elements. Phenomenologically, the absorption of UV radiation with an energy density[1] of $\sim$2 J/cm^2 within 25 ns laser pulse length leads to a local explosion-like ablation of the target material, which is basically heated instantaneously far above the evaporation temperature of $YBa_2Cu_3O_{7-\delta}$ of about 1900 °C. Emission of macroscopic particles of molten material up to a few micrometre in size, which are detrimental to the properties of the film, may occur due to subsurface superheating [60, 61], which can be a drawback of PLD. The Excimer laser was operated at 1 Hz, and in order to distribute the deposited heat load and avoid

[1]The laser light with an energy of 240 mJ per pulse was focussed to an area of about 6×2 mm on the target surface. Under these conditions, the power density of the radiation amounts to 80 MW/cm^2.

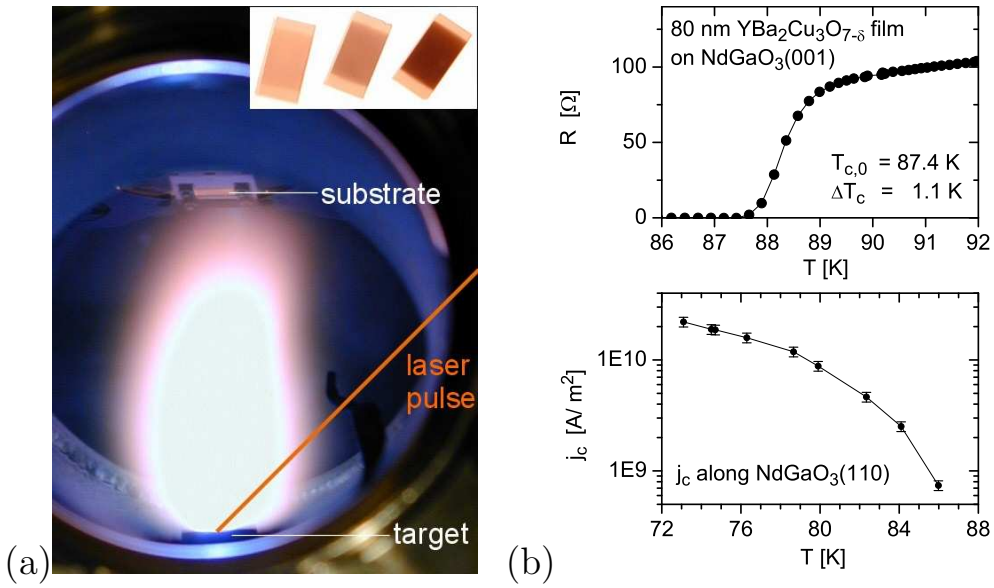

Figure 4.8: $YBa_2Cu_3O_{7-\delta}$ thin film preparation by pulsed laser deposition. (a) Photograph of the ∼7 cm heigh plasma plume taken through a viewport of the PLD chamber. The UV laser pulse, which is incident on the polycrystalline $YBa_2Cu_3O_{7-\delta}$ target, is schematically indicated by a line. The substrate would be positioned in the outer region of the redish zone of the plume. The inset shows $YBa_2Cu_3O_{7-\delta}$ films of different thicknesses deposited on $SrTiO_3$ substrates 10×5 mm in size. (b) Film characterization: Temperature dependences of the resistance R and the critical current density j_c for an $YBa_2Cu_3O_{7-\delta}$ film grown on $NdGaO_3$.

crater formation, the target was rotated at a frequency of about 1/7 Hz. Homogeneous ablation of the target improves the homogeneity in composition and thickness of the film.

Highly excited atoms, ions, electrons and small molecules are ejected from the target surface, forming an adiabatically expanding, highly luminous plasma plume directed normal to the surface as shown in Fig. 4.8(a). The plume has the same stoichiometric composition as the source material. The particles in the plume with kinetic energies of the order 10–100 eV [62] are decelerated by atomic collisions with the surrounding oxygen atmosphere ($p \approx 0.5$ mbar) such that resputtering of already deposited material has negligible influence on the film growth, as has been experimentally confirmed for the case of $Bi_2Sr_2CaCu_2O_8$ [63]. The atmosphere provides oxygen for the $YBa_2Cu_3O_x$ phase formation; the red-brownish colour at the edge of the plume is indicative of molecular oxide formation. We have observed that this tinge of the plasma plume fringe is absent when depositing in argon atmosphere; the plume remains entirely bluish. An interesting survey over the dynamics and the chemical processes inside the plasma is given by Singh and Kumar [64].

The condensation of particles takes place far from thermodynamic equilibrium; the partial pressures for the individual species in the plasma exceed their equilibrium vapour pressures significantly. The film nucleation process is largely determined by

the interfacial energies and the diffusion kinetics at the surface as summarised by Haage [65]. The surface energy situation requires the formation of a critical nucleus size before the condensed phase can transform into the $YBa_2Cu_3O_6$ phase, which is the thermodynamically stable phase for the film at the growth temperature, and the Stranski-Krastanov growth mechanism sets in. The pseudomorphic growth, i.e., the growth mode where the lattice structure of the monocrystalline substrate is matched by the growing layer, is limited to a critical thickness of about 13 nm on $SrTiO_3(001)$ [66] and less than 12 nm on $NdGaO_3(001)$ [67]. The substrate temperature of 760 °C facilitates a high surface mobility of the condensing particles (a surface diffusion length of $\geq$20 nm has been estimated [68]), which leads to good film epitaxy. The growth rate of the *c*-axis oriented tetragonal $YBa_2Cu_3O_6$ film is typically 0.7 Å per laser pulse under the chosen conditions.

The deposited film is oxygenated by subsequent annealing at an oxygen pressure of 800 mbar at 450 °C for 30 min. A phase transition from the semiconducting tetragonal to the metallic orthorhombic $YBa_2Cu_3O_{7-\delta}$ phase with $\delta < 0.1$ takes place according to the phase diagram [69–71]. The formation at this stage of either a single domain or twin domains for internal strain compensation depends on the symmetry of the surface unit cell of the substrate. The sample is let cool down to room temperature in the oxygen in order to prevent losses of the volatile oxygen.

The experimental deposition parameters, such as the substrate temperature, the gas pressure, the position of the substrate with respect to the plume and the energy density of the light pulses were empirically optimized with regard to the superconducting transition temperature. The film quality was monitored by recording resistance curves $R(T)$ as shown in Fig. 4.8(b) by four-probe measurements, which yielded transition temperatures[2] $T_{c,0}$ of typically 90 K with transition widths ΔT_c (90%–10%) of typically 1–2 K. For selected samples, the temperature dependence of the critical current density j_c was measured, which gives an idea about the nature of weak links and antiphase boundaries present in the film. For these measurements, two four-probe sample rods with integrated PID temperature control for the use inside a liquid helium dewar were designed and built and existing control software was extended.

Vacuum Annealing

A suitable procedure for preparing clean well-ordered perovskite surfaces for XSW-experiments is vacuum annealing. Etching and argon ion sputtering have the disadvantage of creating defects and modifying the surface stoichiometry [72, 73], which can lead to pronounced segregation of one of the constituent elements. While fracturing yields clean bulk-terminated surfaces, it cannot be excluded that application of the necessary high forces generates dislocations and deteriorates the crystallinity of the crystal bulk, compromising XSW experiments.

[2]The transition temperature obtained from transport measurements is determined by the current percolation, where already one established current path causes zero resistivity. $T_{c,0}$ is here defined as the temperature, where the resistivity drops below the detection limit of 10^{-8} Ωcm, and agrees well with the temperature of the magnetic transition due to the Meissner effect, which is integrated over the entire sample volume.

At annealing temperatures beyond 900 °C the surface contamination has well desorbed and the $SrTiO_3$ surface mobility is sufficiently high to allow for surface ordering and the formation of large terraces [74, 75]. In UHV a homogeneous TiO_2 termination forms by fractional SrO sublimation. But neither the particular surface termination, whether this would be a TiO_2 or a SrO surface layer, nor the particular surface structure of the sample — at least 8 different $SrTiO_3$ surface reconstructions are known [76] — are of major importance for the XPS-measurements as long as alteration of the surface stoichiometry is confined to a depth small compared to the electron escape depth. As-grown insulating $SrTiO_3$ is reduced by annealing at temperatures of 900 °C and above in UHV for several hours and becomes n-type conductive with a maximum carrier concentration of 10^{18}–10^{19} electrons/cm^3 [77–79]. The obtained conductance has the advantage to prevent the sample from charging when applying electron spectroscopic methods like XPS, LEED and AES, and XPS peak positions in XSW experiments will not shift. The density of extrinsic states generated in the 3.2 eV wide band gap, which indicates the creation of bulk oxygen vacancies [80], is most likely too low to be detected by XPS.

Crystal Growth and Cleaving

The twinned $YBa_2Cu_3O_{7-\delta}$ single crystals used in this work were grown by C. T. Lin [81] from a highly concentrated melt in excess of $Ba_3Cu_7O_{10}$ in a zirconia crucible by the temperature oscillation method between 960 and 970 °C [82, 83]. The crystals are rectangular in shape. The edges are parallel to the a and b axes and are typically few millimetres long. The thickness in c direction amounts to a fraction of a millimetre. While thin crystals most often displayed two sides that were shiny and smooth by eyesight, the thicker crystals often revealed one rougher side.

The (001) surfaces of an $YBa_2Cu_3O_{7-\delta}$ crystal grown by the temperature oscillation method are not equivalent. Their different morphologies result from the growth mechanism, which unlike epitaxial growth by PLD takes place close to thermodynamic equilibrium. The crystal growth starts by seed-free nucleation in a locally undercooled zone in the melt. Spiral growth sets in and continues only on the (001) crystal surface that shows spiral hillocks. On the other surface the growth is forced to stop once the spiral pits are filled and a flat surface has formed. The morphology of a single spiral hillock is determined by its growth anisotropy and the kink density at its step edges, which are strong functions of the growth temperature. As the spiral hillocks grow, their bases spread outward and coalesce, forming new continuous layers of the crystal but also individual mosaic domains. The SEM and AFM investigations by Lin [84, 85] on surface defects, revealed by chemical etching, supported this picture of growth: While the growth side of the crystals showed hillocks and screw dislocations, the botton side of the same crystal specimen showed flattened hillocks only. The density of spiral hillocks on the (001) surface was estimated to be 10^3/mm^2 (as in 1994). Spiral hillocks form around dislocation lines caused by impurities, which are additionally introduced into the melt by the reactive hot copper oxides corroding the crucible material. Erb *et al.* [86] report the purity obtained for $YBa_2Cu_3O_{7-\delta}$ crystals depending on the crucible material, which is 99.5–99.9 at.% when using zirconia crucibles. The

crystal growth process stops when the valleys inbetween the hillocks are filled up and a plane surface has formed. Unfinished growth leaves the crystal surface rough.

The oxygen content of the as-grown crystals with a tetragonal structure was adjusted to $\delta \approx 0.05$ by annealing in flowing pure oxygen at a pressure of 1 bar at temperatures between 530 °C at the beginning and 435 °C towards the end of a period of 7 days. The slowest process is the thermal cracking of the oxygen molecules into reactive radicals (and for this reason ozone annealing works quicker); the speed of reaction is determined by the annealing temperature. The oxygen diffusion in $YBa_2Cu_3O_{7-\delta}$ with a speed of the order of a few μm/h is a comparably fast process. Superconducting transition temperatures of typically 90–92 K were obtained from magnetization curves $M(T)$ as shown in Fig. 4.9. The transition width[3] largely depends on the completeness of the oxygen diffusion process and is determined by the length of the annealing. A homogeneous oxygen distribution is of importance also for spatial regularity of the lattice parameters.

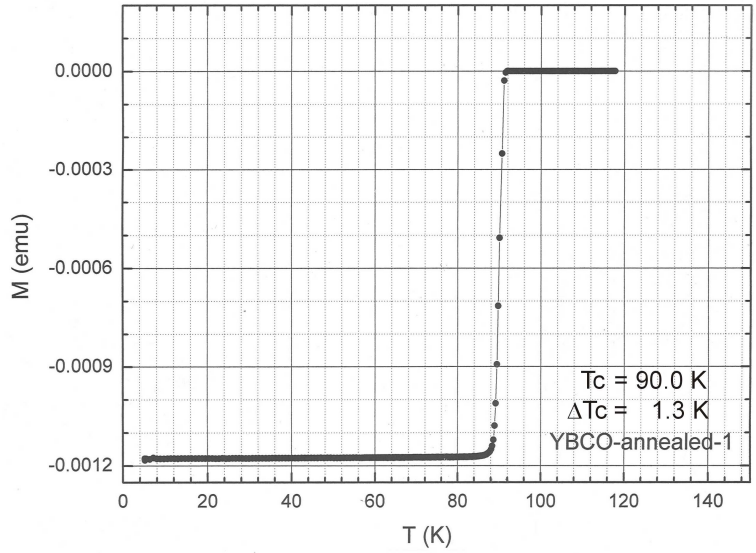

Figure 4.9: Magnetization curve for a typical oxygen-annealed $YBa_2Cu_3O_{7-\delta}$ single crystal sample, yielding the superconducting transition temperature T_c and the transition width ΔT_c. The measurements were performed with a SQUID magnetometer by E. Brücher [87].

Low-temperature crystal cleaving in UHV represents the only method for preparing chemically clean $YBa_2Cu_3O_{7-\delta}(001)$ surfaces without contaminant phases. The highly reactive surfaces are stable only at temperatures below 40 K [88,89]. However, cleaving does not guarantee a clean, undamaged surface: Crystals, in particular those thicker than a few 10 μm, often grow with inclusions of impurity phases and preferentially cleave where these phases appear in extended layers. A chemical analysis by ESCA of the surfaces prepared by cleaving is therefore generally advisable. The XPS spectrum

[3] ΔT_c is defined as the temperature difference between the onset of the Meissner effect and 50% sample magnetization, at which stage the dc-resistivity has already dropped to zero.

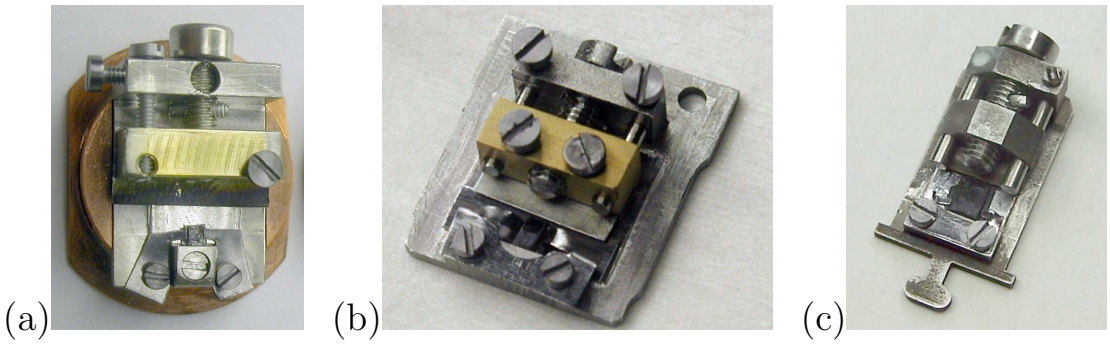

Figure 4.10: Photographs of crystal cleaving devices. Each device is shown with an $YBa_2Cu_3O_{7-\delta}$ crystal mounted. (a) The 1st generation devices made out of steel were mounted on ESRF beamline ID08 standard copper sample plates. (b) The 2nd generation molybdenum devices are shaped like ID32 standard sample plates (width 18 mm). (c) The 3rd generation molybdenum devices are 10 mm wide and were designed for the hard X-ray photoemission setup shown in Fig. 4.3.

for the barium d levels are particularly sensitive to the chemical state of the surface. Criteria to assess the quality of the surfaces from photoemission spectra were given by Vasquez [89]. XPS spectra of clean surfaces were presented by Brundle and Fowler [90] and can be used as a reference.

Two different surface terminations schematically indicated in Fig. 2.1(b) on page 6 are possible for cleaved pure $YBa_2Cu_3O_{7-\delta}$ crystalline material. The existence of a mixed CuO_3/BaO surface termination has to be taken into consideration when applying surface sensitive spectroscopic techniques with sampling depths comparable to the relatively large c lattice constant [91].

If and how much damage is caused to the sample by cleaving is experimentally difficult to determine. Comparing reflectivity curves, which were recorded from the pristine and the cleaved crystal surfaces, we observed a broadening after most cleaves. The width and the line shape of the reflectivity curve varied strongly over the cleaved surface. The broadening can be indicative of sample regions exposed that are enriched with impurity phases; these regions will exhibit lower crystalline quality than the intrinsic bulk material. Additional lattice defects, like dislocations, or possibly even macroscopic crystal damage, like microcracks, may be expected to result from the forces applied, which are capable of breaking chemical bonds.

X-ray standing wave investigations require strain-free crystal sample mounting. Strain build-up during curing and sample cooling rules out the use of epoxy glue for this purpose. The commonly employed method of breaking the crystal glued to a sample plate by applying a force via a post glued to its top surface can therefore not be employed. While the back reflection geometry is generally chosen to minimise the broadening influence of sample mosaicity on the reflectivity curve, this geometry is the most sensitive one to strain. Broadening effects due to strain can be comparable or even larger than those due to mosaic spread: By applying Bragg's law in its differential form, a distribution in lattice constant as small as $\Delta d/d = 10^{-4}$ corresponds to an angular width of $\Delta\theta = 0.1^\circ$ in the X-ray regime, which is comparable to the

mosaicity of a typical sample specimen. In order to accomplish a surface preparation by cleaving in UHV and, at the same time, strain-free crystal mounting allowing XSW measurements, crystal cleaving devices were developed. The cleaving devices shown in Fig. 4.10 were built for different experimental stations at ESRF beamlines. The principle of functioning is that a hard molybdenum blade carried by a guided block is pushed against the crystal by turning a screw. A UHV screwdriver is mounted on a rotary feedthrough on a linear drive. The crystal, which is filed into hat-shape, is gently held in position by tantalum foil without exertion of force. Slices of 200 μm thickness have been successfully cleaved off $YBa_2Cu_3O_{7-\delta}$ crystals. The devices are suitable for cleaving crystals up to 3–4 mm in size.

4.4 XSW Data Acquisition and Data Reduction

The samples investigated within the framework of the thesis were prepared in the Surface Characterization Laboratory, where also first examinations were carried out. A prepared sample is transferred in a transportable vacuum chamber in high vacuum or UHV from the laboratory to the UHV chamber at the undulator beamline ID32 at the ESRF and is mounted on the manipulator head inside the chamber. Surfaces of high-temperature superconductor crystals are prepared in the chamber by cooling and subsequent cleaving, using the cleaving devices developed for this purpose. The sample surface is aligned in the point of intersection of the X-ray beam and the axis of the photoelectron or fluorescence analyser by optimizing the detected signal. The chemical state and the mosaicity of the prepared surface are analysed.

An XSW measurement was carried out by establishing a Bragg condition in σ polarization geometry with an incident angle of the beam of typically 86–87°. The broadening influence of sample mosaicity on the reflectivity curve, which reduces the intensity modulation of the X-ray wavefield, is minimised in back reflection geometry. In an XSW scan, the primary monochromator is scanned stepwise through the energy range of the Bragg reflection of the sample, and the generated X-ray standing wavefield is moved throught the unit cell of the crystal. At each of the typically 41 energy steps, i.e., XSW positions, the incident and reflected beam intensities and one or more photoelectron spectra in previously defined binding energy ranges are recorded. XSW measurements are usually carried out for a number of suitable Bragg reflections. The chemical state of the studied surface is monitored in regular intervals.

Certain types of XSW measurements require customized data acquisition algorithms. Valence band investigations using XPS, such as XSW valence electronic structure analysis, require relatively long acquisition times to gain spectra of good statistics. The stability of the beamline ID32, in particular long-term photon energy drifts, limit the time to perform an accurate XSW scan to about 15 min. Data of sufficient accuracy are gained by recording a sequence of identical fast XSW scans, such as exemplarily shown in the schematic in Fig. 7.4 on page 91. The spectra taken in the individual scans are aligned and added together.

The recorded data are immediately analysed after the first scans of the experiment in order to verify faultless data acquisition and, if need be, to correct experimental

mistakes. XSW yield profiles are determined from the integrated intensities of the XPS or fluorescence spectra after background subtraction. The recorded electron yields are normalized to the yield measured off of the Bragg condition. The rocking curve of the sample is obtained on an arbitrary reflectivity scale.

Fitting theoretical expressions given by Eqs. 3.21 and 3.22 to an XSW yield profile yields the coherent position and fraction of an element for a specific reflection. The programme *DARE* by J. Zegenhagen [29] can be used for this purpose. Either the dipole approximation can be applied, or the influence of quadrupole effects can be included, based on experimentally determined quadrupole parameters S_R and $S_I = |S_I|e^{i\psi}$.

The fitting requires knowledge of the absolute reflectivity $R(E)$ of the sample and the phase relation $\nu(E)$ between the two interfering X-ray waves across the Bragg range. Both quantities are not obtained experimentally. The programme *DARE* calculates the reflectivity (Darwin) curve and the phase relation for a perfect crystal sample from atomic scattering factors and geometrical structure factors based on dynamical theory of X-ray diffraction. The reflectivity and phase curves are then convolved by the calculated reflectivity curve for the monochromator in order to take the broadening by the finite bandwidth of the X-ray beam into consideration. Dispersion does not need to be taken into consideration here, owing to the small beam divergence. Additional broadening of the sample rocking curve is often caused by mosaic spread of the sample, and in back reflection potentially also by strain. These two influences can be approximated by artificially broadening the reflectivity curve of the monochromator: By simulating a crystal miscut (where the diffraction planes are not parallel to the optical crystal surface) described by the asymmetry parameter b [92], the beam divergence can be artificially increased. Adjusting the parameter b for the monochromator crystal varies the ratio of beam width and beam divergence, the product of which is constant by Liouville's theorem. The b factor is chosen such that the energy range of the convolved sample Darwin curve matches the experimental XSW scan range. A concomitant effect of introducing a b factor is an additional energy offset of the reflectivity curve with respect to the kinematical Bragg energy. The measured reflectivity curve is then scaled to the calculated curve by adjusting two parameters, the absolute reflectivity and the curve position with respect to the Bragg energy.

The statistical error of the coherent positions, which are obtained by the data fitting, amount to typically $\pm 1\%$ of the diffraction plane spacing d_H. The error in coherent fraction is about $\pm 1.5\%$. Systematic errors, which can result from errors in the absolute reflectivity or the used quadrupole parameters, affect the the coherent fraction much stronger than the coherent position. Since the coherent position represents the more important quantity for many experiments, like XSW real space imaging, the XSW method enjoys a relatively large robustness and constitutes a reliable technique in surface science.

Chapter 5

Nucleation of $YBa_2Cu_3O_{7-\delta}$ on $SrTiO_3(001)$

X-ray standing wave imaging, a recently established application of the XSW method, was used for a structural study. A motivation for investigating the growth of the first monolayer of the high-temperature superconductor $YBa_2Cu_3O_{7-\delta}$ on the (001) surface of $SrTiO_3$ and a brief summary of the known facts will introduce the reader to the subject. After describing the preparation of submonolayer $YBa_2Cu_3O_{7-\delta}$ coverages and the experimental data acquisition, Fourier-expansion solutions of the atomic distributions yielded by the imaging technique will be presented. A structural model for a submonolayer coverage will be proposed with the help of supplementary SXRD investigations. The nucleation mechanism will be discussed.

5.1 Introduction

Thin films are grown by means of experimental techniques that are distinct from those used for the preparation of bulk material, like crystals. Correspondingly, thin film growth takes place under different thermodynamical conditions, and the present surface and interface energies lead to an entirely different nucleation mechanism: While the growth of crystals can start by a spontaneous nucleation in an undercooled zone of a melt and a material-specific mechanism immediately sets in to continue the stoichiometric growth under conditions close to thermodynamic equilibrium, complicated processes can occur during the nucleation of thin films, i.e., during the growth of the initial monolayer. This is particularly the case for heteroepitaxial growth of multielement compounds with a complex unit cell, like high-temperature superconductors. Once a critical nucleus size is exceeded, the influence of the interface energy diminishes and a characteristic film growth mode takes over. Since the first unit cell layer acts as a nucleus for the growth of the subsequent layers and can thereby influence the properties of the entire deposited film [93, 94], investigating the nucleation can shed some light on the relationship between the growth mode and the structure of such epitaxial systems.

Based on their scanning tunneling microscopy (STM) and spectroscopy (STS) inves-

tigations on submonolayer coverages of $YBa_2Cu_3O_{7-\delta}$ on $SrTiO_3$(001), Haage *et al.* [1] have proposed a subunit cell nucleation mechanism for this material system. The authors deduced their nucleation model indirectly from morphological and directly from electronic information provided by these real space techniques, while they could not directly probe the lattice and interfacial structures of the film. In the present study, a complementary reciprocal space X-ray method is applied to investigate the atomic structures directly. The recently developed real space imaging application of the XSW technique is chemically selective and represents an ideal tool to obtain direct images of the atomic distributions for each element. Cheng *et al.* [44] demonstrated the application of the XSW method as an element specific Fourier technique in one dimension. We have employed this technique to reconstruct three-dimensional real space images of the atomic structure of $YBa_2Cu_3O_{7-\delta}$ submonolayer deposits in order to unravel the nucleation mechanism further.

The X-ray standing wave technique was already applied for structural investigations on thin layers of the $ReBa_2Cu_3O_{7-\delta}$ superconductor family, Re = rare earth, on $SrTiO_3$ surfaces. Author groups around Kazimirov studied the location of the rare earth atoms in thin films [95, 96]. The structure of interfaces has been of particular interest: While CuO and CuO_2 layers of $ReBa_2Cu_3O_{7-\delta}$ were excluded as the starting layers for the growth on $SrTiO_3$(001) by Nakanishi *et al.* [97], the CuO layer was found to be the starting layer for the growth on $NdGaO_3$(001) by Lee *et al.* [98].

The STM and STS studies by Haage *et al.* [1] suggested that $YBa_2Cu_3O_{7-\delta}$ films deposited on $SrTiO_3$(001) nucleate as a cubic, semiconducting phase of an (Y/Ba)$CuO_{3-\delta}$ mixed perovskite composition as schematically shown in case (A) of Fig. 5.1: The STM measurements on a 0.5 ML coverage revealed terrace steps shown in Fig. 5.2(a) with heights of 0.4 and 0.8 nm, which is equal to the height of one or two perovskite units. These step heights indicated submonolayer islands in the film. (The thickness of 0.5 ML may have been quoted too large by the authors. Given a covered surface area of about 50%, a more realistic value may be 0.25 ML.) The same observation had already been made earlier for a 1 ML coverage by Jiang and Zegenhagen [74]. The STS measurements in Fig. 5.2(b) showed that the band gap at the Fermi surface closes upon completing a stack of three perovskite-like subunit cells, which indicated a transition from a semiconducting to a metallic phase. The transformation was interpreted as the formation of the $YBa_2Cu_3O_{7-\delta}$ phase. A mechanism for the smooth overgrowth of single substrate steps without anti-phase boundaries was suggested by a variation of the initial stacking sequence, as indicated by cases (B) and (D) in Fig. 5.1. Cases (B) and (D) were suggested to be the only possible stacking sequences [99].

5.2 Sample Preparation

$SrTiO_3$ single crystal substrates (supplier Crystal, Berlin) of high crystalline quality were selected for the XPS/XSW investigations of $YBa_2Cu_3O_{7-\delta}$ coverages. The narrow mosaic distribution of the crystals shown in Fig. 5.3 did not broaden the reflectivity curves for the used Bragg reflections in back scattering geometry. The 0.02 wt.% Nb doping (relative to the amount of titanium) of the $SrTiO_3$ resulted in n-type conduc-

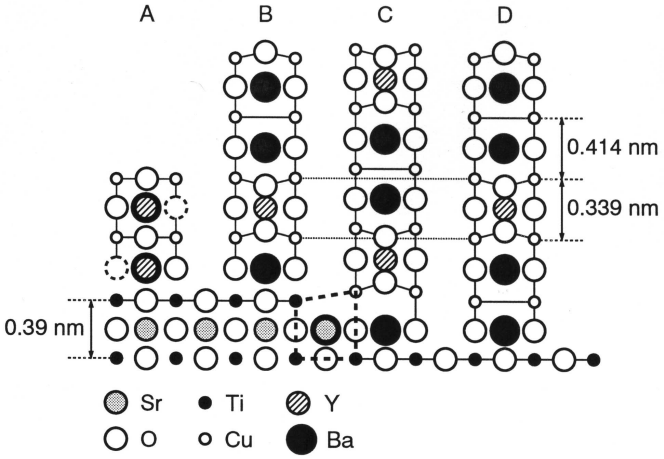

Figure 5.1: Schematic model for the nucleation of $YBa_2Cu_3O_{7-\delta}$ on $SrTiO_3(001)$ proposed by Haage *et al.*. The deposited material nucleates as (A) an (Y/Ba)$CuO_{3-\delta}$ mixed perovskite and transforms upon exceeding a critical amount into the $YBa_2Cu_3O_{7-\delta}$ phase, which is shown (B) on an upper step edge and (C) on a substrate terrace. The alternative stacking sequence (D) on the terrace achieves matching with sequence (B) across the terrace step. Figure taken from Haage *et al.* [1]. (Oxygen atoms in the yttrium planes in cases (B)–(D) drawn by mistake and not intended by the authors.)

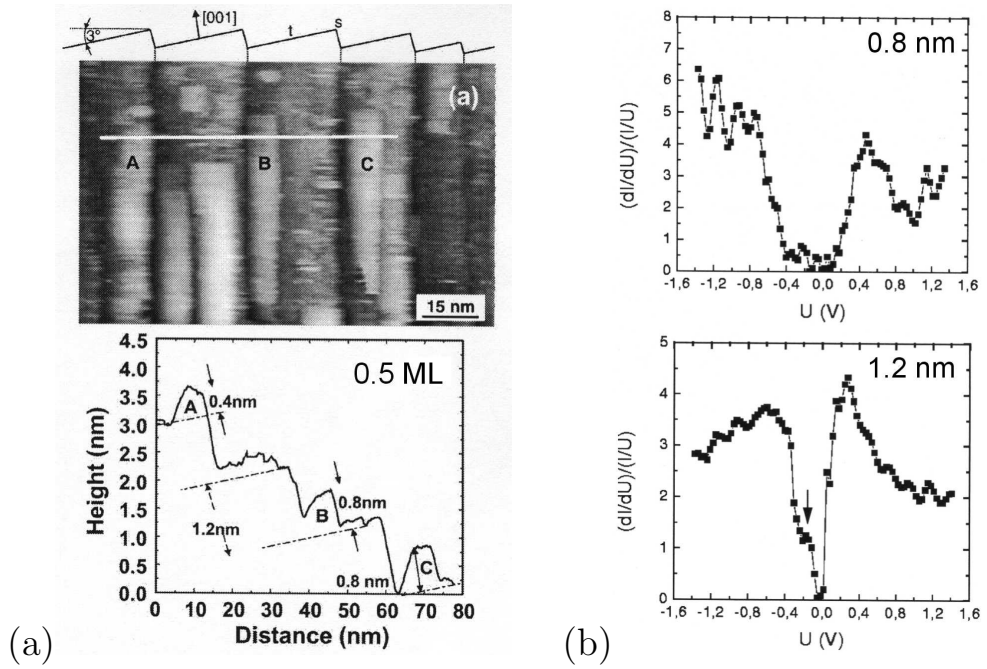

Figure 5.2: Results of STM and STS investigations by Haage *et al.* [1] on $YBa_2Cu_3O_{7-\delta}$ submonolayer coverages deposited on $SrTiO_3(001)$. (a) STM image of the surface morphology of a 0.5 ML coverage and cross section along the indicated line. Three building blocks of the film are denoted A, B and C. (b) Normalized tunneling conductance as a function of the applied bias voltage taken on the surface of 0.8 and 1.2 nm high islands (appearing in 0.5 and 0.8 ML coverages, respectively).

tivity and enabled electron diffraction and photoemission experiments. The additional conductivity gained by the reduction during UHV annealing was not retained, since the oxygen loss was reversed during the film growth by PLD in oxygen atmosphere. The crystals were 10×5×1 mm in size. The misorientation of the surface normal was measured to be ∼0.3° towards the [100] direction.

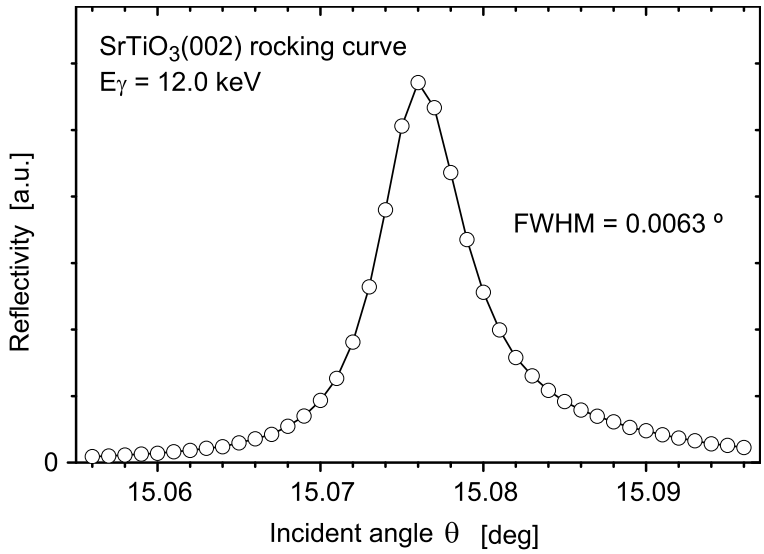

Figure 5.3: Reflectivity curve representing the mosaic spread of the $SrTiO_3$ substrate crystals that were used for the XSW experiments. The data were recorded without **q** resolution. The size of the incident beam was 0.4 × 0.4 mm.

$YBa_2Cu_3O_{7-\delta}$ coverages of 0.5 and 1.0 monolayers[1] thickness, corresponding to 8 and 17 laser pulses in accordance with the PLD calibration described below, were prepared immediately before the X-ray measurements according to the following standard procedure:

(i) Preparation of a well-ordered TiO_2-terminated $SrTiO_3(001)$ surface by annealing at a temperature of ∼930 °C and pressures $<1\times10^{-8}$ mbar for 3 hours.

(ii) Characterization of the surface at room temperature by LEED.

(iii) Heating of the $SrTiO_3(001)$ substrate to 760 °C in pure oxygen at a partial pressure of 0.5 mbar. Deposition of the $YBa_2Cu_3O_{7-\delta}$ coverage by PLD at 240 mJ pulse energy and a repetition rate of 1 Hz.

(iv) Oxygen treatment at 450 °C in 0.8 bar pure oxygen atmosphere for 20 min, followed by cooling to room temperature in the oxygen.

(v) Characterization of the coverage by LEED and (at the beamline) chemical analysis by XPS.

[1]One monolayer of $YBa_2Cu_3O_{7-\delta}$ is defined here as the amount of material contained in a homogeneous layer with a thickness of the unit-cell height of 1.17 nm.

The annealed $SrTiO_3(001)$ substrates had clean surfaces, which mainly exhibited a weak double domain c(4×2) reconstruction. Fig. 5.4 shows that the LEED pattern indicative of a c(2×2) reconstruction observed for the deposited coverages remained stable for several days until completion of the XSW study. Since the deposited coverages are only few atomic layers thick, a reconstruction could potentially have some limited influence on the coherent positions of certain elements. SRXD measurements confirmed, however, no reconstruction to be present on a length scale larger than the short coherence length of LEED.

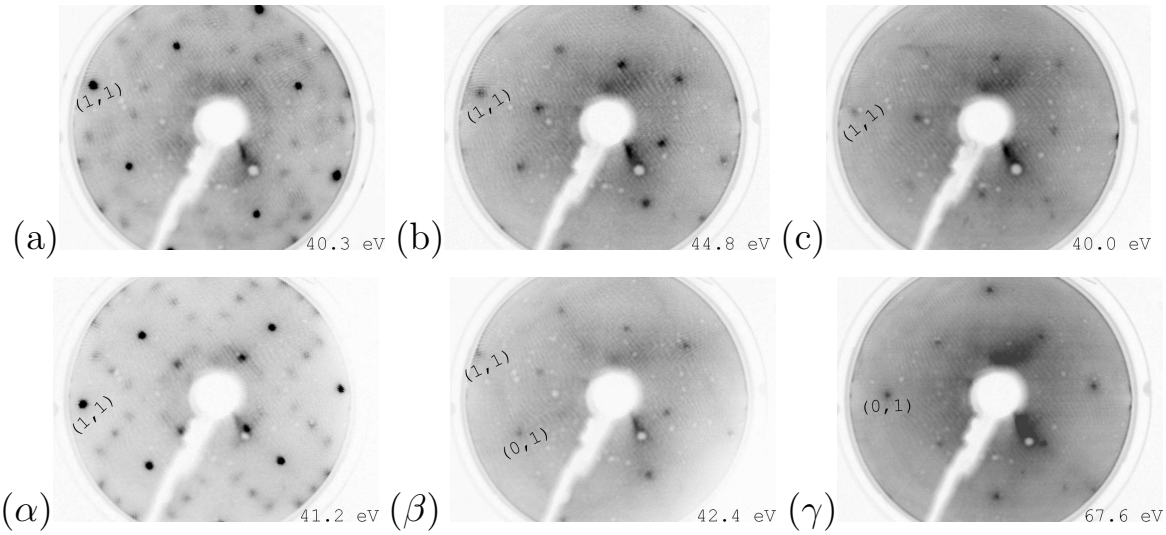

Figure 5.4: LEED patterns for $SrTiO_3(001)$ surfaces without and with $YBa_2Cu_3O_{7-\delta}$ coverages. The sequence for the 0.5 ML coverage is labelled in latin, for the 1.0 ML in greek letters. (a/α) Mainly c(4×2) reconstruction of the UHV-annealed $SrTiO_3(001)$ surfaces. (b/β) Pattern of a c(2×2) reconstruction for the $YBa_2Cu_3O_{7-\delta}$ coverages immediately after deposition and (c/γ) after completion of the XSW study.

The chemical analysis based on core level XPS revealed noticable changes upon increasing the coverage from 0.5 to 1 ML. A larger areal fraction of the 0.5 ML coverage seems to be BaO terminated. This is evidenced in Fig. 5.5 by a Ba $3d_{5/2}$ component that is chemically shifted by 1 eV towards higher binding energies, owing to the modified coordination of barium atoms at the surface, whereas at the same time the O 1s spectrum remains identical to that for $SrTiO_3$. Any other barium oxide phase would have identified itself by a chemically shifted oxygen component [90]. Upon further deposition, completing the first monolayer, the surface termination changes: The shifted barium component vanishes, leaving a single-featured signal coming from barium entirely in bulk environment. The shape of the O 1s signal transforms — and here the fractional oxygen XPS signal coming from the single monolayer coverage becomes clearly discernible from the substrate signal —, towards the characteristic shape for oxygen in the $YBa_2Cu_3O_{7-\delta}$ phase.

An attempt to investigate the morphology of the deposited $YBa_2Cu_3O_{7-\delta}$ coverages by STM was not successful. The conductivity of the samples or the contact to the

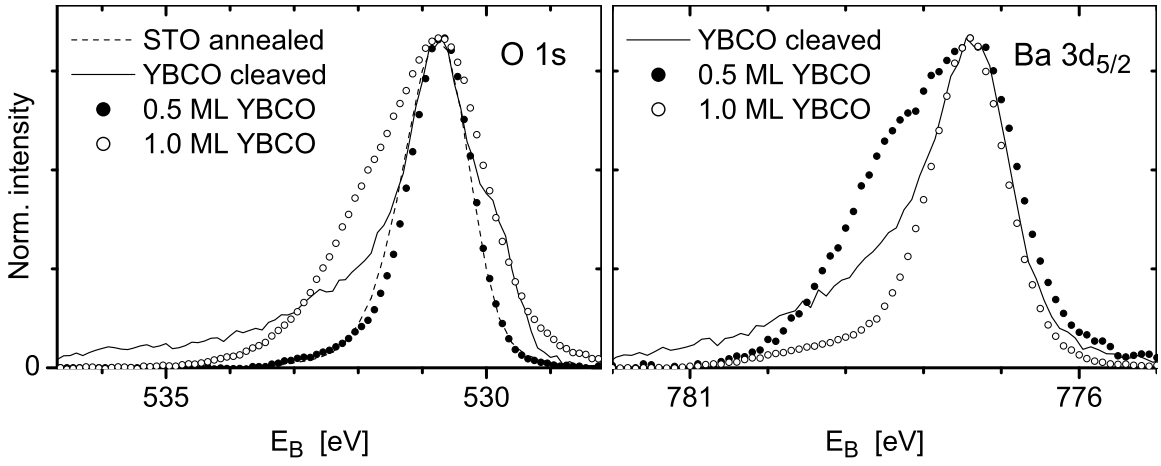

Figure 5.5: Core level XPS spectra for 0.5 and 1.0 ML coverages of $YBa_2Cu_3O_{7-\delta}$ on $SrTiO_3$(001). The O 1s and Ba 3$d_{5/2}$ spectra recorded at $E_\gamma = 3.18$ keV are compared to clean spectra taken from Figs. 7.7 and 8.2. The signal peaks from the two materials are aligned in energy.

metallic sample holders turned out to be insufficient. The samples were observed to charge by 50–80 V during the electron diffraction and photoemission measurements depending on the drain current. Complementary real space information about the surface termination, the height of step edges and possible island growth would have been of great help for the structure determination.

Calibration of the PLD Deposition Rate

The deposition rate attained with PLD settings optimized for $YBa_2Cu_3O_{7-\delta}$ film growth was calibrated by quantitative fluorescence measurements. The thicknesses of four test $YBa_2Cu_3O_{7-\delta}$ films were determined, which were deposited onto $SrTiO_3$(001) by 140, 70, 34 and 17 laser pulses. The results were compared to the qualitatively different information from the periodicity of Laue oscillations in reflectivity measurements.

The Cu $K\alpha$ fluorescence yield I_{Cu} measured from the copper contained in the deposited film is related to the atomic density per unit area ρ_{Cu} by the proportionality $I_{\mathrm{Cu}} \propto \rho_{\mathrm{Cu}}\, N_{\mathrm{Cu}}\, \sigma_{\mathrm{Cu}\,1s}\, p_{\mathrm{Cu}}\, t_{\mathrm{Cu}}$. N_{Cu} denotes the photon flux incident on the sample. With the probability given by the photoabsorption cross section $\sigma_{\mathrm{Cu}\,1s}$ a Cu 1s core hole is created, which then decays via the fluorescence channel as indicated in Fig. 3.1 on page 12 with the probability p_{Cu} calculated by Krause [100]. Secondary excitation cannot take place with the used photon energy of 15 keV. On its way to the detector, the emitted Cu $K\alpha$ fluorescence light passes the air gap and a 50 μm thick aluminum foil, which was used as a z–1 filter to absorb the partially superimposed Ti $K\alpha$ signal that saturated the detector. The transmission t_{Cu} is a product of an experimentally determined value for the foil and a calculated value [101] for the air gap.

The thickness of the $YBa_2Cu_3O_{7-\delta}$ films was inferred from the copper density per unit area based on the assumption of a stoichiometric film with 3 copper atoms per

unit cell. The copper density was determined from the $K\alpha$ intensity ratio $I_{\mathrm{Cu}}/I_{\mathrm{As}}$ from Cu (8.0 keV) and As (10.5 keV), using a silicon reference sample with an implantation dose of arsenic $\rho_{\mathrm{As}} = 1.04{\times}10^{15}$ atoms/cm^2 concentrated entirely within the extinction depth of the X-rays:

$$\rho_{\mathrm{Cu}} = \frac{I_{\mathrm{Cu}}}{I_{\mathrm{As}}} \frac{\sigma_{\mathrm{As}\,1s}}{\sigma_{\mathrm{Cu}\,1s}} \frac{p_{\mathrm{As}}}{p_{\mathrm{Cu}}} \frac{t_{\mathrm{As}}}{t_{\mathrm{Cu}}} \frac{N_{\mathrm{As}}}{N_{\mathrm{Cu}}} \rho_{\mathrm{As}}. \tag{5.1}$$

The fluorescence measurements were carried out on the diffractometer at beamline ID32 at ambient atmosphere using a Si(Li) solid state detector. The incident beam was 0.4 × 0.4 mm in size. The thicknesses t_{film} of the four films are listed in Tab. 5.1. Based on the calibration by X-ray fluorescence, the deposition rate amounts to ∼17 laser pulses per monolayer $YBa_2Cu_3O_{7-\delta}$ (leaving the film grown by 140 laser pulses out of consideration).

Laser pulses	Fluorescence			Reflectivity
	t_{film} [ML]	t_{film} [nm]	Rate [pulses/ML]	t_{film} [nm]
140	5.96	6.96	23.5	9.85
70	3.77	4.41	18.5	6.58
34	1.97	2.30	17.3	3.5
17	1.00	1.17	17.0	

Table 5.1: PLD deposition rates for $YBa_2Cu_3O_{7-\delta}$ films. The film thicknesses t_{film} of four films ablated on $SrTiO_3$(001) were determined by quantitative fluorescence measurements as well as by reflectivity measurements.

The specular[2] reflectivity of the $SrTiO_3$ crystals covered by the deposited films exhibits Laue oscillations, which are generated by interference of the beams reflected from the film-surface and film-substrate interfaces. Fig. 5.6 shows these oscillations, which are also known as Kiessig fringes [102], for three of the samples. The well-developed oscillations even for large momentum transfer, i.e., for the measured l-values up to 12 and beyond (not shown), are indicative of coverages with sharp interfaces on a micrometre length scale (corresponding to the coherence length of the beam). By Bragg's equation, the film thickness t_{film} and the characteristic oscillation period ΔL are related via $(t_{\mathrm{film}}/c) = (1/\Delta L)$, where we assume the $YBa_2Cu_3O_{7-\delta}$ lattice parameter along the surface normal to be the bulk value of $c = 11.68$ Å. Counting up a few oscillations or determining the FWHM of the Bragg peaks, which equals ΔL, results in the thicknesses listed in Tab. 5.1, which exceed those values determined by the fluorescence calibration. This deviation, which is believed to be beyond the experimental error for the fluorescence measurements (while there are hardly any sources of error for the reflectivity scans), can be accounted for by island growth. The arrangement of the deposited material in islands instead of completed layers makes the coverages appear thicker in reflectivity measurements. The formed islands are of quite uniform height, because the oscillation pattern would be washed out otherwise. The calibration of the PLD deposition rate by fluorescence is in agreement with the amount of deposited material found by SXRD for a 0.5 ML sample.

[2] *specular* — The momentum transfer $\mathbf{q}$ is parallel to the interface normal.

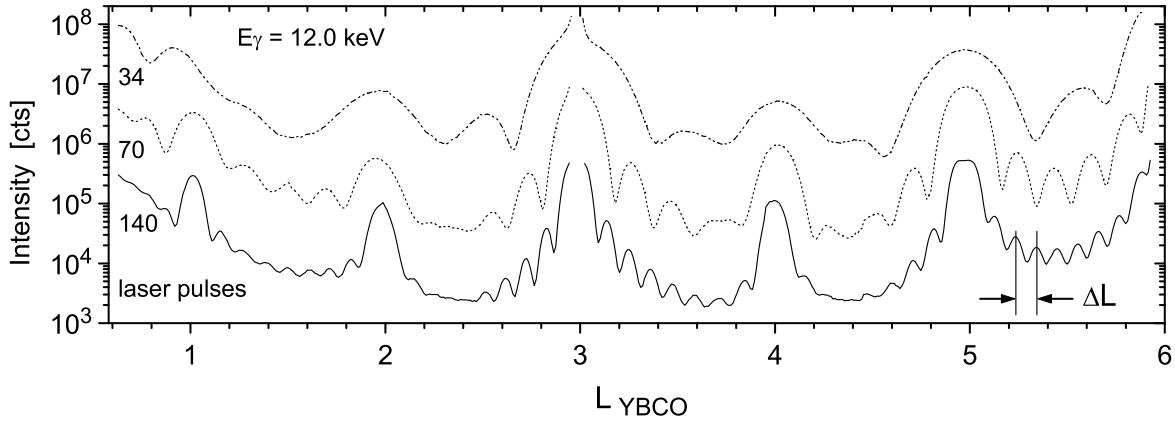

Figure 5.6: Specular reflectivity for thin $YBa_2Cu_3O_{7-\delta}$ coverages on $SrTiO_3(001)$. The curves for the coverages prepared by 70 and 34 laser pulses are offset by factors 20 and 400. The Laue oscillations are separated by ΔL.

5.3 XPS/XSW Measurements

For the XPS/XSW measurements and the chemical characterization by XPS, which was described in the previous section, the $YBa_2Cu_3O_{7-\delta}$ samples prepared in the Surface Characterization Laboratory were transferred under high vacuum to the UHV chamber at beamline ID32. The beamline was set up with the photoelectron analyser mounted at $\vartheta = 45°$ within the polarization plane, which is a geometry sensitive to quadrupole contributions. XPS/XSW data sets were recorded in back scattering geometry for core level signals from all six elements contained in the samples. For comparability reasons, the same electronic levels were probed for the two samples, since the choice of the electronic level has influence on the XSW modulation amplitude (see appendix B). The strongest Bragg reflections with the excited photoemission within the energy range accessible by the photoelectron analyser were selected for the experiment. The seven independent reflections are schematically depicted in Fig. 5.7. For the sample with the 1 ML coverage, additional XSW data were taken for the $SrTiO_3(022)$ reflection. Most of the recorded supplementary fluorescence and Auger data were strongly affected by secondary excitation from the substrate, as the XSW analysis revealed, and were therefore not taken into consideration in the analysis.

5.4 Analysis: 3D Image Rendering

An overview of the fitted reflectivity curves and XSW yield profiles for the individual electronic levels is given for each of the $SrTiO_3(hkl)$ reflections in Figs. 5.8 and 5.9 for the 0.5 and 1 ML samples. The coherent positions and fractions listed in Tab. 5.2 resulted from fitting the expression for the photoelectron yield including quadrupole effects given by Eq. 3.20 to the data. The coherent positions are given with respect to an origin chosen at the titanium site.

The dipole approximation, which has been widely accepted to be adequate for

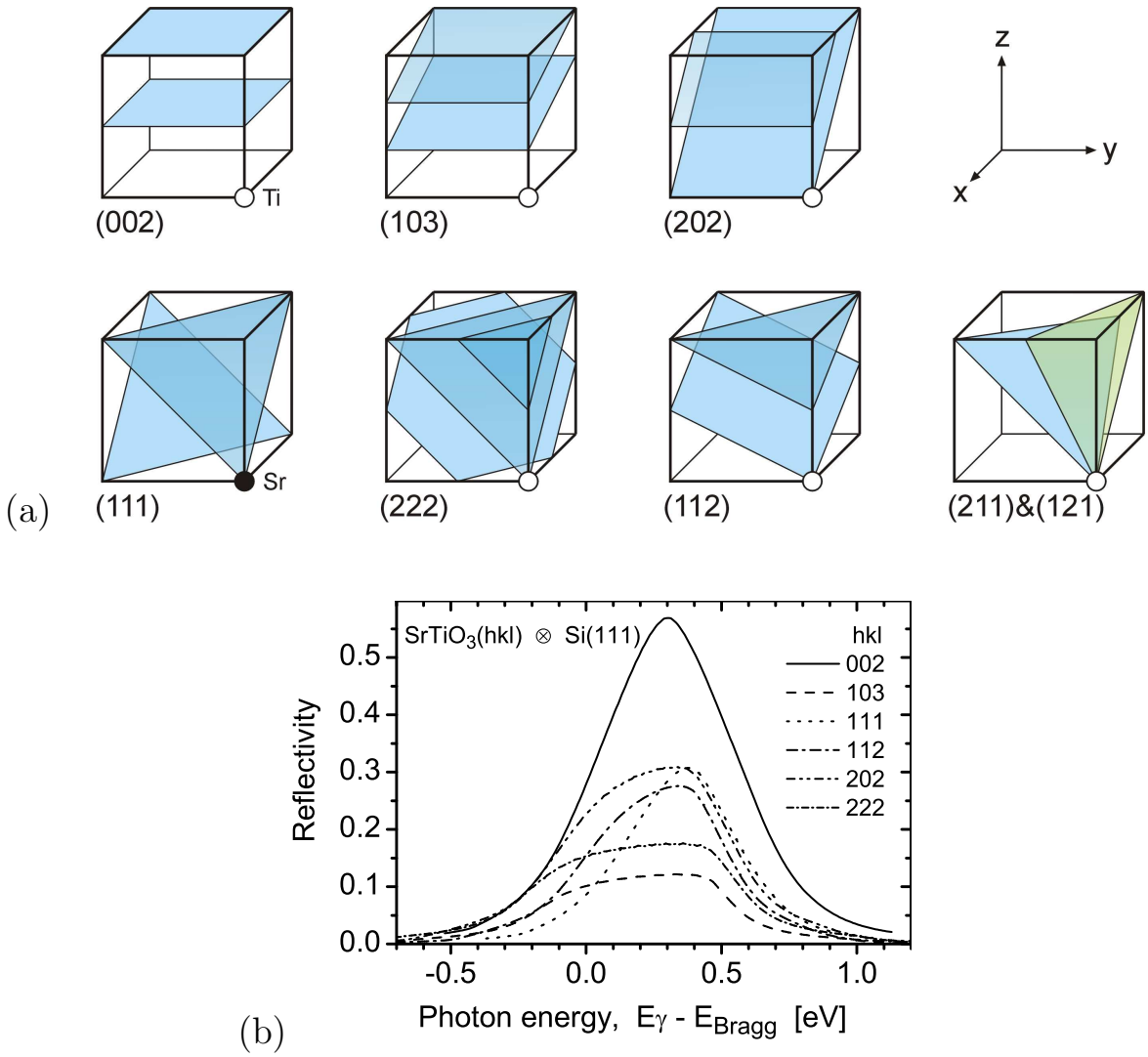

Figure 5.7: Schematic overview of $SrTiO_3(hkl)$ reflections. (a) Position of the diffraction planes, which is defined as the centre of mass of the electron density distribution projected on the scattering vector **H**, in the unit cell. (b) Reflectivity curves for an ideal crystal lattice in back reflection, simulated on the basis of dynamical theory of X-ray diffraction. The curves are convolved by a Si(111) reflectivity curve in order to include the broadening by the monochromator.

describing photoemission at photon energies in the lower keV range for a long time, was not applicable in the present study. Quadrupole effects, which alter the XSW yield profiles, were found to be significant. In a separate, systematic investigation reported in appendix B, approximate quadrupole parameters for a number of electronic shells were determined, using the sample with the 1 ML coverage. The empirical parameters listed in Tab. B.1 were used to account for the quadrupole effects in the data, except for the copper data, where no values were available. The resulting systematic error for the coherent position of copper is estimated to be not more than 0.03, since angular effects would rather affect the modulation amplitude (and hence the apparent coherent

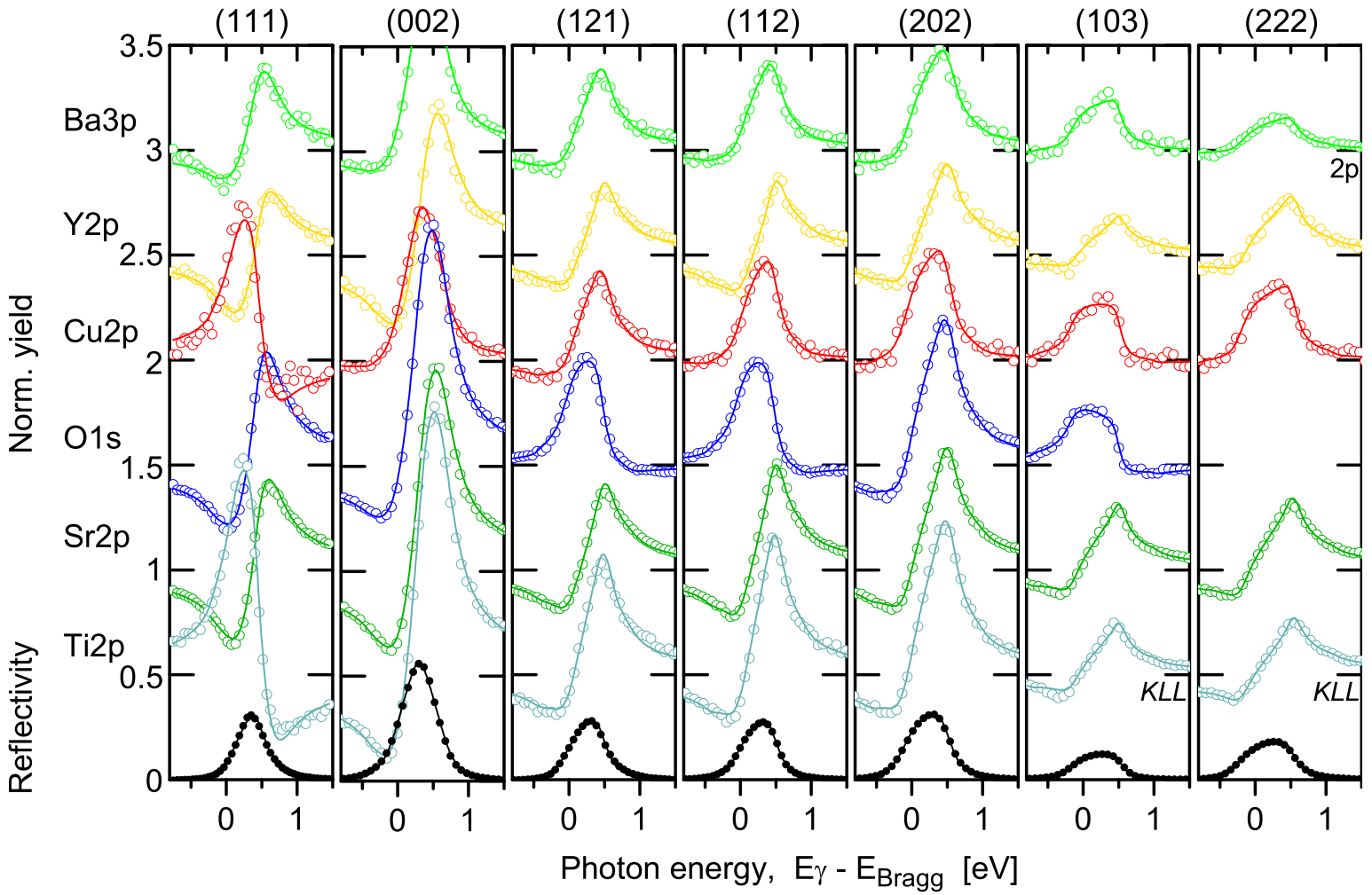

Figure 5.8: XSW data for a $YBa_2Cu_3O_{7-\delta}$ coverage of 0.5 ML on the $SrTiO_3(001)$ surface. The reflectivity and the normalised XSW yield profiles recorded for different $SrTiO_3(hkl)$ reflections were fitted by taking quadrupole contributions into consideration.

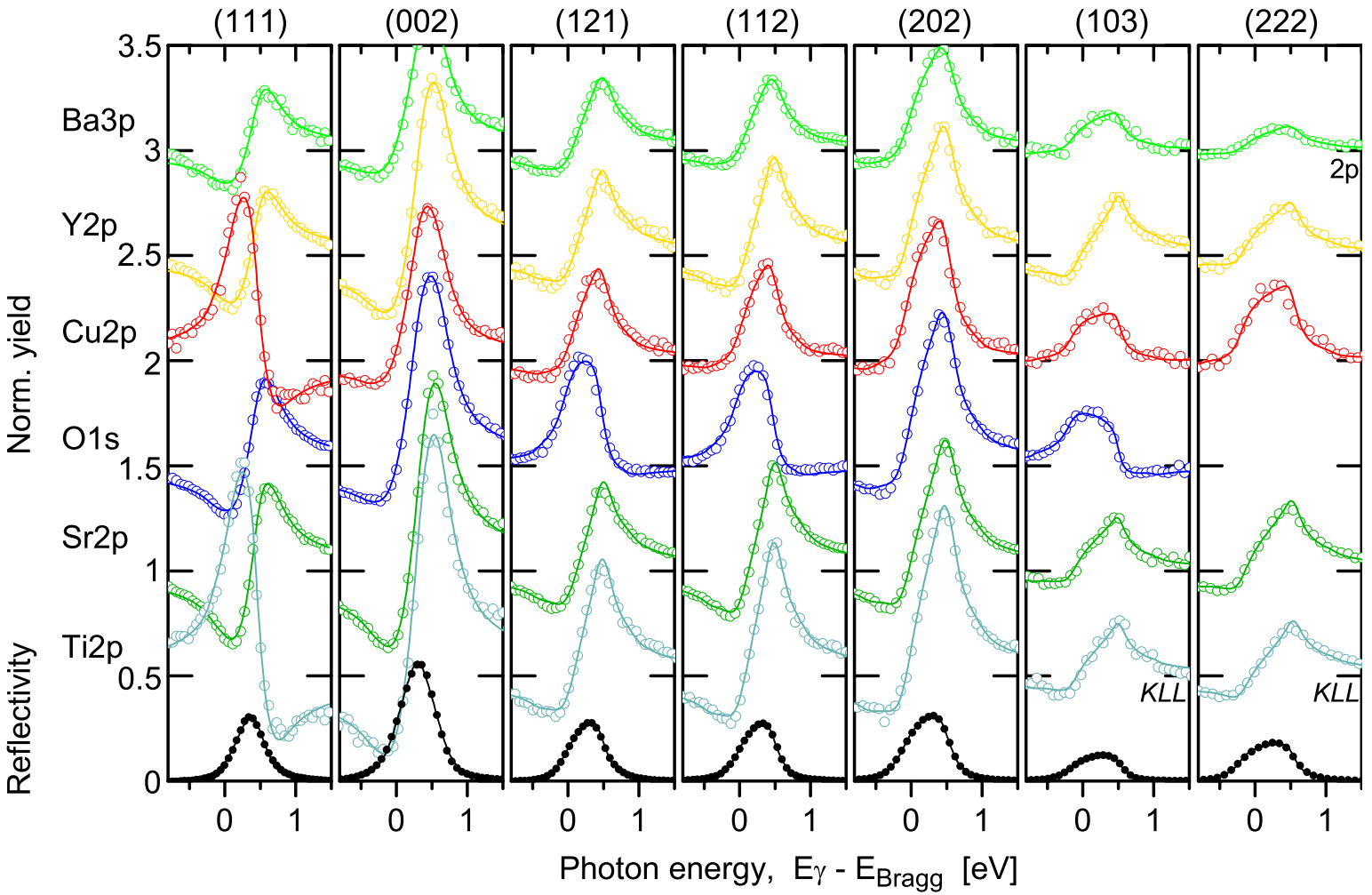

Figure 5.9: XSW data for a $YBa_2Cu_3O_{7-\delta}$ coverage of 1.0 ML on the $SrTiO_3(001)$ surface. For the (103) and (222) reflections the Ba $2p$ level and the Ti KLL Auger transition were probed. The curves are vertically offset by multiples of 0.5 for clarity.

fraction) than the line shape (and hence the coherent position) of the XSW yield curves. The statistical uncertainties for the values tabulated in Tab. 5.2 typically amount to ± 0.015 for the coherent positions and ± 0.02 for the coherent fractions.

ML	El. level	P^H / F^H						
		$SrTiO_3(hkl)$						
		(111)	(002)	(121)	(112)	(202)	(103)	(222)
0.5	Ba 3*p*	0.530	0.065	0.024	0.053	0.047	0.267	0.931
		0.503	0.349	0.447	0.319	0.383	0.228	0.221
	Y 2*p*	0.466	0.983	0.984	0.978	0.004	0.037	0.040
		0.847	0.853	0.752	0.842	0.742	0.579	0.644
	Cu 2*p*	0.995	0.126	0.074	0.216	0.201	0.368	0.222
		0.829	0.221	0.522	0.389	0.426	0.674	0.570
	O 1*s*	0.525	0.050	0.561	0.573	0.045	0.545	/
		0.755	0.622	0.191	0.219	0.645	0.389	
	Sr 2*p*	0.507	0.036	0.001	0.022	0.036	0.089	0.033
		0.957	0.947	0.863	0.998	0.923	0.954	0.901
	Ti 2*p*	0.032	0.039	0.018	0.038	0.037	0.065	0.991
		0.921	0.866	0.752	0.842	0.790	0.777	0.870
1	Ba 3*p*	0.492	0.004	0.997	0.998	0.054	0.061	0.880
		0.564	0.404	0.530	0.425	0.388	0.178	0.349
	Y 2*p*	0.475	0.027	0.020	0.033	0.087	0.063	0.043
		0.752	0.816	0.726	0.849	0.851	1.000	0.506
	Cu 2*p*	0.983	0.066	0.092	0.161	0.192	0.286	0.214
		0.987	0.451	0.494	0.398	0.709	0.426	0.586
	O 1*s*	0.498	0.014	0.565	0.611	0.074	0.565	/
		0.646	0.506	0.242	0.250	0.569	0.386	
	Sr 2*p*	0.502	0.024	0.013	0.032	0.057	0.099	0.053
		0.945	0.924	0.806	0.962	0.917	0.646	0.751
	Ti 2*p*	0.031	0.022	0.012	0.028	0.055	0.074	0.997
		0.910	0.845	0.743	0.839	0.846	0.766	0.780

Table 5.2: Coherent positions P^H and fractions F^H for elements in 0.5 and 1.0 ML coverages of $YBa_2Cu_3O_{7-\delta}$ on the $SrTiO_3(001)$ surface. The coherent positions are given with respect to an origin attached to the titanium site. The values were obtained by fitting the data shown in Figs. 5.8 and 5.9.

The data recorded for the $SrTiO_3(022)$ and (202) reflections for the 1 ML sample are identical within the experimental error. This agrees with the picture of pseudomorphic nucleation of the deposited coverages, maintaining the 4-fold symmetry of the $SrTiO_3$ surface unit cell. Lateral surface relaxation of the substrate in the vicinity of step edges, leading to rectangular distortions of the surface unit cell [94], seems to be restricted to a small fraction of the surface area, because the surface miscut of the substrate crystals was small.

By direct Fourier inversion of the XSW data, three-dimensional images of the atomic density distribution for all elements contained in the substrate and in the deposited coverages were generated. The structure determination of the coverages was in this way completely independent of any model. The reason is that all properties of the used probe, the standing wavefield, required to be known can be derived exclusively from the known structure of the XSW-generating substrate material. To render the atomic distributions, the four-fold crystal symmetry around the surface normal was exploited. 29 (for oxygen 25) Fourier components for symmetry-equivalent reflections were included in the Fourier inversion according to Eq. 3.25. By taking this symmetry

into consideration, the statistical weight of the experimentally measured Fourier coefficients for the (121) and (002) reflections is altered in the 3D images by factors 2 and 0.25, respectively. The obtained images display the unit cell of the coverage modulo the XSW-generating crystal lattice, i.e., the reconstructed images represent the atomic positions of the coverages projected into the $SrTiO_3$ unit cell. Since the growth is pseudomorphic, only the component of the atomic distribution along the surface normal (which is along the vertical in the figures) is projected, while the in-plane components directly reproduce the true atomic coordinates.

The reconstructed atomic densities for the six elements shown in Figs. 5.10 and 5.11 for the 0.5 and 1.0 ML samples represent the projections into the $SrTiO_3$ unit cell with the titanium atoms at the corners. Periodic artificial background resulting from the finiteness of the Fourier series has been removed to a large extent using a filter function but is still visible in the the cube corners for yttrium, barium, and strontium. The extent of the atoms in Figs. 5.10 and 5.11 is not representative of the atomic size nor the uncertainty in the atomic position (which is estimated to be of the order of 1% of the lattice parameter) but results from the finite number of Fourier components. The 3D images are distorted by two effects, which are still included in the data: The finite inelastic mean free path of the photoelectrons results in the surface-near atomic layers of the probed material being overrepresented, i.e., the rendered images contain the surface sensitivity of photoemission. The second effect is due to the increase in the dynamical Debye-Waller factor for higher order reflections. Since the coherent fractions included the effect of thermal vibrations, the Fourier components recorded at high photon energies are underweighted by up to 20%.

The precise atomic positions obtained for the submonolayer coverage and for the completed first monolayer allow deducing the nucleation mechanism of $YBa_2Cu_3O_{7-\delta}$ on $SrTiO_3(001)$. Important information can already be obtained without refinement from regarding the direct images: It becomes immediately apparent that the structures of the 0.5 and 1.0 ML coverages are very similar and both consist of perovskite or perovskite-like units. These face-sharing $BaCuO_{3-x}$ (BCO) or $YCuO_{3-x}$ (YCO) units have their corners occupied by copper, whereas the barium or yttrium resides at the centre site. The images cannot prove that $YBa_2Cu_3O_{7-\delta}$ does not nucleate as a complete unit cell from the very beginning of the growth; this issue has been solved by previous STM investigations by Haage *et al.* as shown in Fig. 5.2. Rather, since the deposited coverage of 0.5 ML consists of only few atomic layers — and the number of layers is known from the calibration and from supplementary SXRD measurements presented further below —, the particular stacking sequence of the first pseudo-perovskite blocks of the growing film can be inferred from the projected atomic positions. This issue has not been entirely solved by previous studies, and the models suggested in Fig. 5.1 for the structure of the initial $YBa_2Cu_3O_{7-\delta}$ layer on the substrate can be tested.

The atomic positions found for strontium and titanium in the substrate are, as expected, the bulk positions. At the interface between the substrate and the submonolayer $YBa_2Cu_3O_{7-\delta}$ phase, the copper replaces the titanium and extends the titanium sublattice into the epitaxial coverage. Remarkably, the projected position of the copper atoms in the 0.5 ML sample is raised by more than 10% of the $SrTiO_3$ lattice

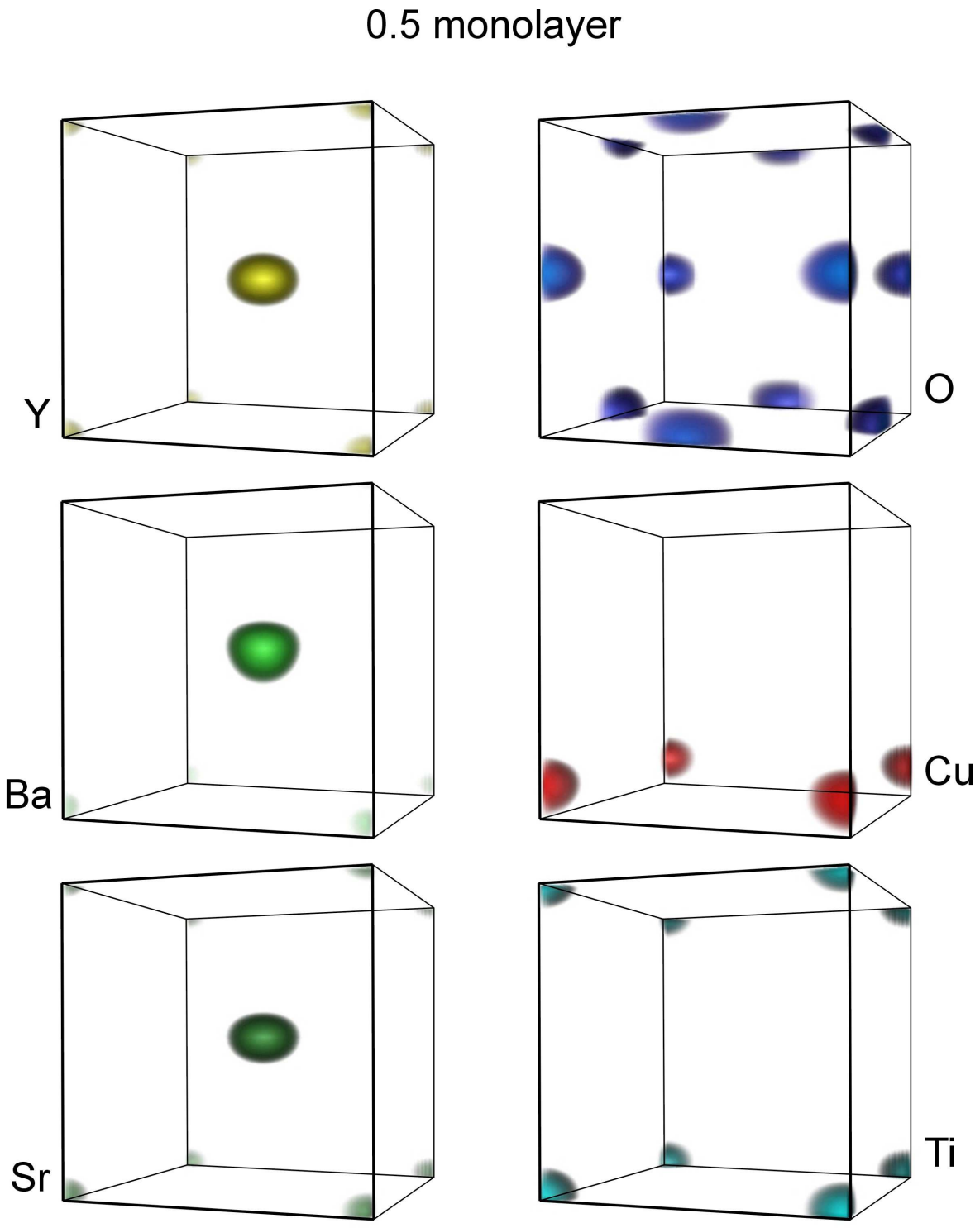

Figure 5.10: Reconstructed images of elemental atomic distributions projected into the $SrTiO_3$ unit cell for a 0.5 ML coverage of $YBa_2Cu_3O_{7-\delta}$ on the $SrTiO_3(001)$ surface. For each element the colour scale is normalised to the maximum atomic density.

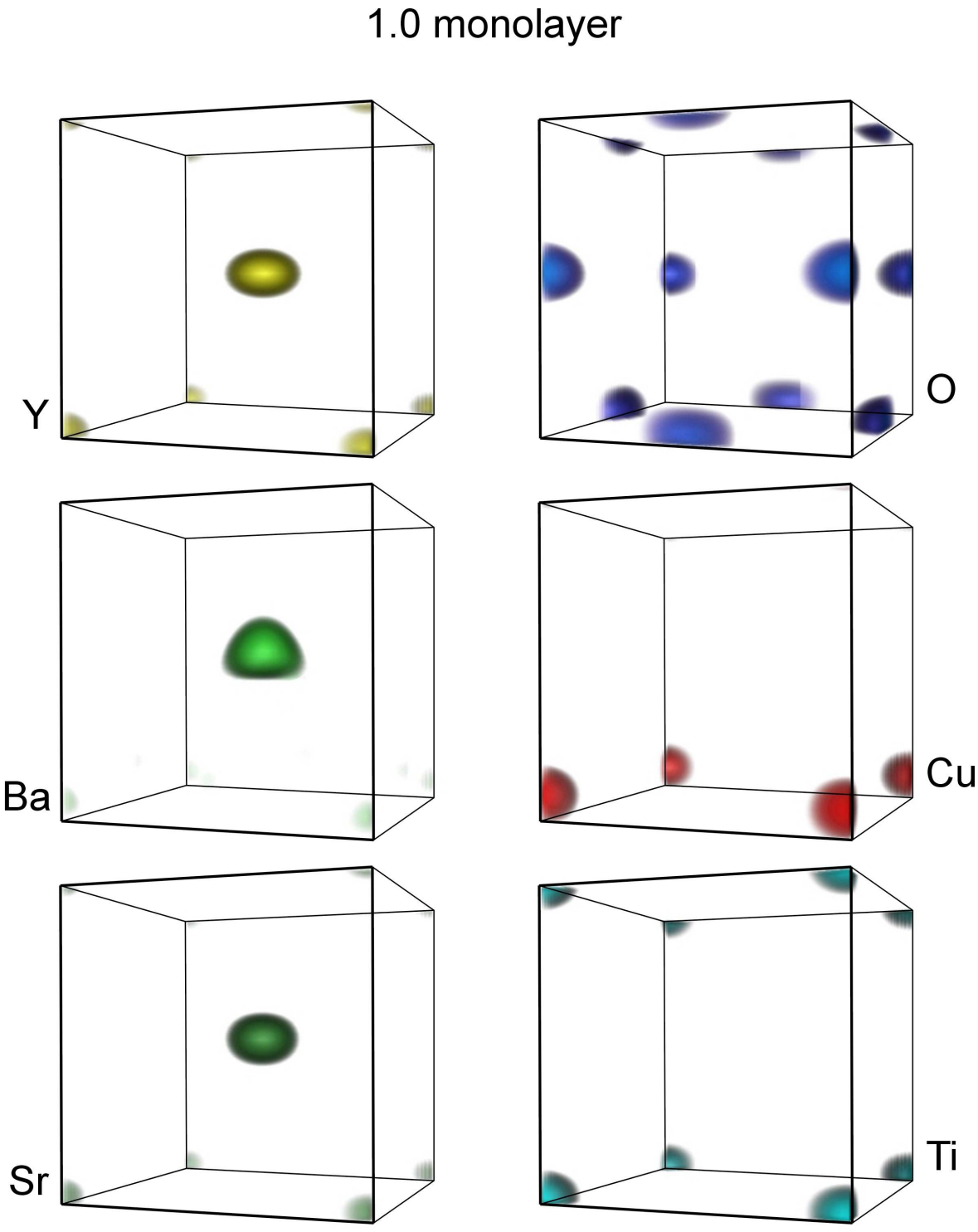

Figure 5.11: Reconstructed images for a 1.0 ML coverage of $YBa_2Cu_3O_{7-\delta}$ on the $SrTiO_3(001)$ surface. An affine linear intensity scale was chosen in order to suppress artificial background, which results from the finiteness of the Fourier expansion.

constant with respect to the titanium position. At the same time, the yttrium position is projected exactly into the centre of the $SrTiO_3$ unit cell within the experimental uncertainty. The distribution of barium atoms does not share the centre position with the yttrium; the barium is elevated with respect to the yttrium by ∼5% of the $SrTiO_3$ lattice constant. The position of the oxygen contained in the coverage is raised with respect to the bulk positions in the substrate, leading to the increased average position observed for the total oxygen. The offset observed depends also on the intensity ratio between the XPS signals coming from substrate and coverage.

The obtained atomic positions indicate that two distinct layer spacings occur in the submonolayer $YBa_2Cu_3O_{7-\delta}$ phase: The raised copper position can be accounted for by an initial layer of orthorhombic perovskite-like subunit cells, which exhibit a c lattice constant larger than the one of $SrTiO_3$. If such subunit cells occur stacked, the shift of the copper with respect to the titanium accumulates and can easily reach the observed offset larger than 10% of the lattice constant. The elevated copper position does not result from an enlarged interfacial distance between the substrate and the first atomic layer of the coverage. This case is ruled out by the well-centered position of the yttrium, provided that the yttrium cations do not rest largely off of the centre of the perovskite-like cells. It has to be concluded that the building blocks consist of two kinds of perovskite-like subunit cells with different heights.

$YBa_2Cu_3O_{7-\delta}$ does not seem to nucleate as a random perovskite, i.e., as a perovskite with the central site randomly occupied by either an yttrium or a barium cation. This interpretation is suggested by the significantly different projected positions obtained for the yttrium and the barium, which are separated by 5% of the $SrTiO_3$ lattice constant. A random distribution would lead to identical positions for the two elements. Certain layers of perovskite-like subunit cells therefore seem to be enriched in barium, other layers in yttrium.

A plausible picture for the structure of the nucleating material is that BCO and YCO units of different height and arranged in distinct layers already exist before completion of the first monolayer $YBa_2Cu_3O_{7-\delta}$. The YCO subunit cell with a lattice constant $c = 0.339$ nm (in bulk material) is 13% smaller than the $SrTiO_3$ cell, owing to the probable absence of oxygen in the yttrium planes for chemical reasons. The unstrained BCO subunit cell with a lattice constant $c = 0.414$ nm is larger than the $SrTiO_3$ cell by about 6%, which equals about half the copper displacement. The large displacement of the copper therefore suggests that the $YBa_2Cu_3O_{7-\delta}$ nucleation starts with a double layer of BCO subunit cells, while YCO as a first layer can be ruled out. Since the position of the yttrium becomes difficult to explain without including a third perovskite-like layer, a structural model with an initial stacking sequence (BCO)–(BCO)–(YCO), starting from the substrate interface, is suggested. Additional experimental justification for including a third layer into a model for a coverage of nominally 1.5 perovskite layers thickness would be desirable and is given in the following section. Before verifying the agreement of this model and the data by a refinement, the projected elemental positions for the 1.0 ML sample will be discussed:

Upon increasing the coverage from 0.5 to 1.0 ML only little change in the projected atomic positions was observed. In order to emphasize this change, Fig. 5.12 shows the difference between the atomic density distributions projected onto the $SrTiO_3(001)$

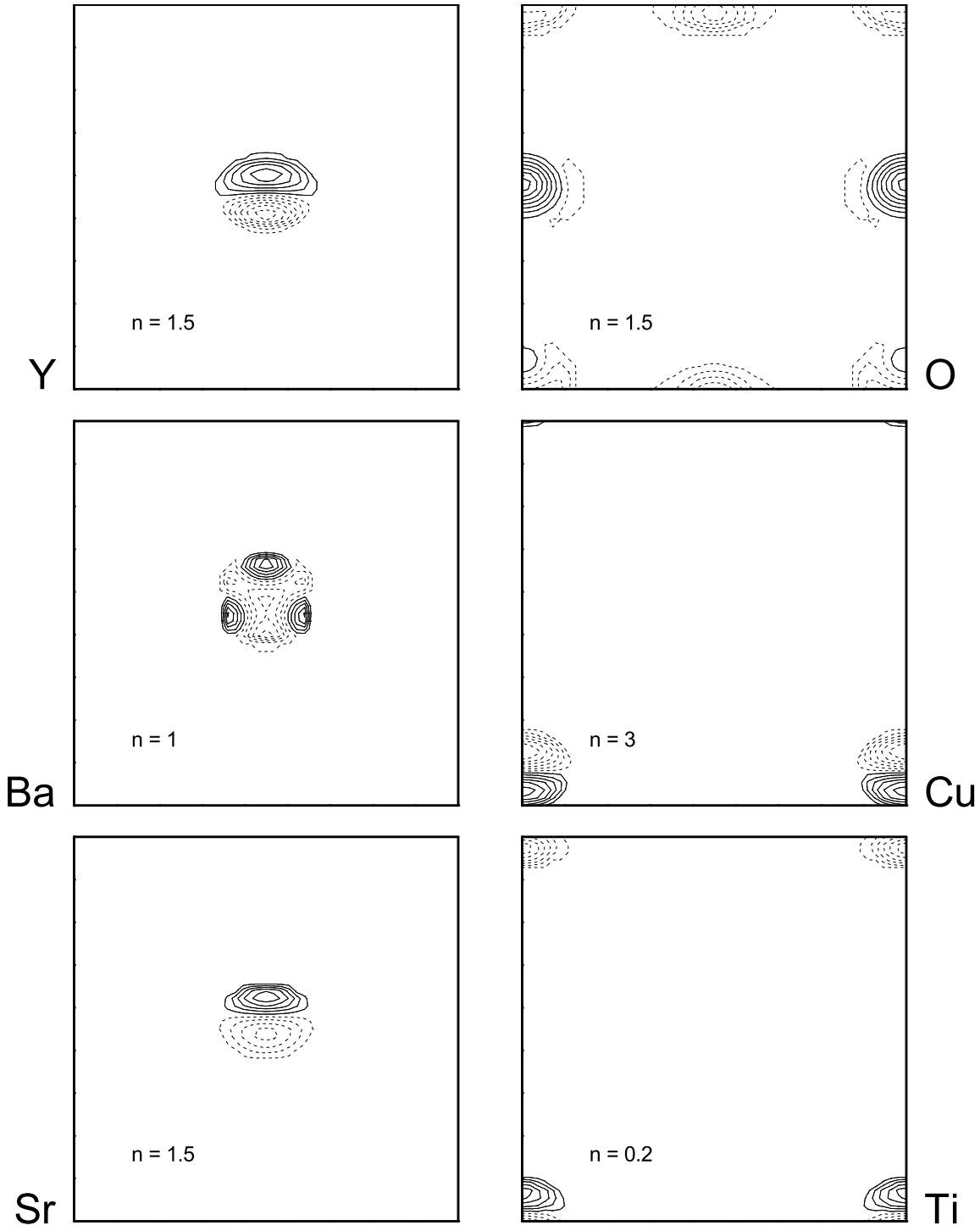

Figure 5.12: Atomic density difference maps for 0.5 and 1.0 ML coverages of $YBa_2Cu_3O_{7-\delta}$ on $SrTiO_3(001)$. The differences in elemental atomic density are projected into the $SrTiO_3$ unit cell and are further projected onto the (100) plane. Positive density changes when increasing the $YBa_2Cu_3O_{7-\delta}$ coverage from 0.5 ML to 1.0 ML are indicated by solid lines, negative changes are represented by dotted lines. Contours of constant atomic density are separated by n atoms per $SrTiO_3$ unit cell.

plane for each element. The artificial background has been removed to the greatest possible extent. Possible remaining influences of multipole effects contained in the data (in particular for copper) will widely cancel in the difference maps by the subtraction of the data sets. The positions of titanium and strontium have basically remained unchanged; the small differences seen in the maps can be explained by variations in local substrate quality. The projected position of the yttrium is increased slightly, while the barium is shifted into the opposite direction towards the substrate. While remaining still clearly elevated, the copper draws noticeably nearer to the titanium position, which would be in agreement with BCO forming the fourth subunit cell layer as the film grows. In contrast to the yttrium planes, the barium planes contain oxygen. The increasing occupancy of the projected (0, 0, c/2) oxygen site can be interpreted as the corresponding further increase in the BCO vs. YCO ratio in the coverage.

5.5 Analysis: Refinement

A structural model for submonolayer coverages of $YBa_2Cu_3O_{7-\delta}$ on the (001) surface of $SrTiO_3$ can be achieved by deconvoluting the direct images presented in the previous section. The images cannot be deconvolved unambiguously without supplementary information on a length scale beyond the dimension of the $SrTiO_3$ unit cell that is not accessible to XSW, like the number of deposited perovskite-like layers and the supercell ordering of the central site cations barium and yttrium. The good quality of the reflectivity data taken on test films (Fig. 5.6) suggested measuring such information by SXRD. A refinement yields the precise atomic positions for the deposited subunits.

Surface Diffraction: 0.5 ML $YBa_2Cu_3O_{7-\delta}$ on $SrTiO_3(001)$

For the 0.5 ML coverage a small SXRD data set comprising 6 crystal truncation rods, which are shown in Fig. 5.13(a), was recorded and analysed by T.-L. Lee [103]. The data were taken at $E_\gamma = 15.0$ keV photon energy from the sample in a baby chamber under high vacuum, which had been transferred and mounted on the diffractometer at beamline ID32. For technical reasons diffraction data could not be taken for the 1 ML sample.

The data analysis yielded the electron densities for the uppermost atomic layers of the sample. The electron densities are modulated along the z direction (normal to the sample surface) as shown in Fig. 5.13(b) and have an uncertainty of estimated 20%. The number of electrons at each cation site is determined by two factors, the number of electrons owned by the cation and the occupancy of the site. Since SXRD is not chemically selective to determine the cation and cannot discriminate between these two factors, a stoichiometric random perovskite model with an alternating Cu and mixed $Y_{1/3}Ba_{2/3}$ layer sequence and the corresponding layer occupancy shown in Fig. 5.13(c) represents one of the possible interpretations of the data. The oxygen has not been included in the model, since the weakly scattering oxygen hardly contributes to the diffracted intensity. The structure of the model can be interpreted as 3 layers of stoichiometric perovskite-like subunit cells of about 70, 50 and 30% occupancy judged by the values for copper, as the dotted line in Fig. 5.13(c) indicates. A further layer of

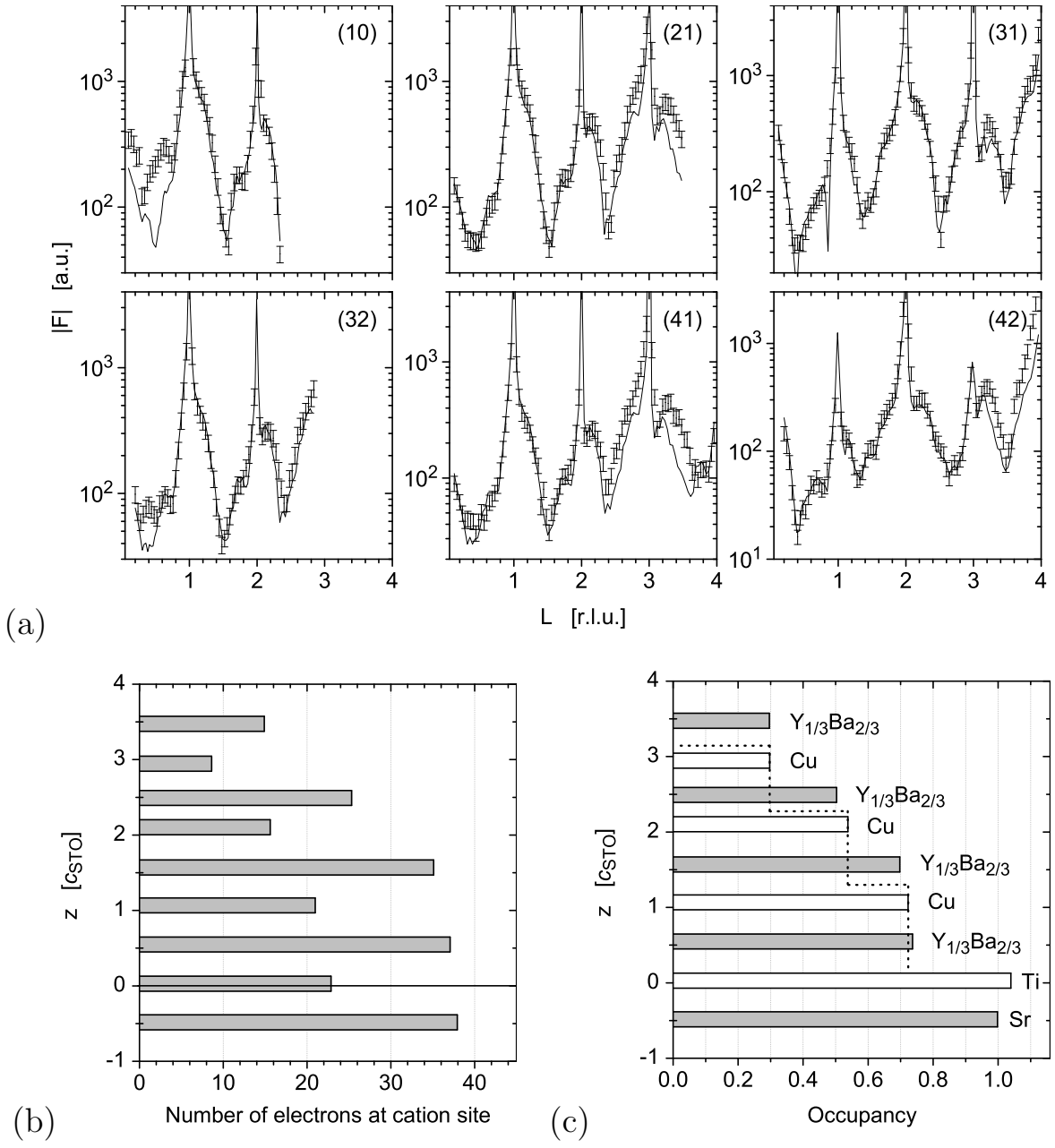

Figure 5.13: SXRD data and analysis for 0.5 ML $YBa_2Cu_3O_{7-\delta}$ on $SrTiO_3(001)$. (a) Crystal truncation rods with the calculated intensity given by the solid lines. The position (hk) in reciprocal space is given for each rod. The l values are given in reciprocal lattice units (r.l.u.). (b) Electron densities for the topmost atomic layers of the sample resulting from the data fit. The layer positions are given in units of $c_{SrTiO_3} = 3.905$ Å with respect to the surface of the ideal substrate crystal at $z = 0$. (c) Atomic occupancy for a stoichiometric random perovskite model with an alternating Cu and $Y_{1/3}Ba_{2/3}$ layer sequence. The dotted line marks 3 perovskite-like layers covered by an additional $Y_{1/3}Ba_{2/3}$ layer. Figures (a) and (b) adapted from Lee [103].

yttrium or barium, as suggested by the XPS chemical analysis of the surface, generates a stable Y/BaO termination. Possible interdiffusion at the substrate interface has not been taken into consideration in this model.

The diffraction results prove that the $SrTiO_3(001)$ surface is not fully wetted during the $YBa_2Cu_3O_{7-\delta}$ nucleation process; this gives rise for the deposited material to partially populate a third perovskite-like layer. About 30% of the substrate area remains bare, while another 30% is already covered by a full monolayer $YBa_2Cu_3O_{7-\delta}$. Island growth, which has already been suggested by a comparison of reflectivity and fluorescence measurements on test samples of few monolayers thickness, is confirmed for a coverage, which contains 1.55 layers of copper (according to the used model) and therefore has an average thickness of 0.5 ML $YBa_2Cu_3O_{7-\delta}$.

Indirect information about the ordering of the barium and yttrium cations is provided by the lattice spacings, while the two elements cannot be chemically discriminated by SXRD directly. The measured layer spacings are in very good agreement with the stacking sequence (BCO)–(BCO)–(YCO) that was postulated on the basis of the XSW results. The bottom two atomic double layers of the deposit each exceed, characteristic of BCO, the $SrTiO_3$ cell in height and are topped by a third rather narrow atomic double layer of a height equal to that of a YCO unit. Possible relaxation of the uppermost atomic layer of each terrace does not appear to account for the variation in layer spacing. In total, the height of the three double layers equals the height of three $SrTiO_3$ cells.

The occupancy profile in Fig. 5.13(c) contradicts, however, a possible (BCO)–(BCO)–(YCO) sequence and agrees with the random perovskite model. The reason is that a model that contains a pure YCO layer cannot be constructed: It is not possible to enrich any of the $Y_{1/3}Ba_{2/3}$ mixed layers in the model in Fig. 5.13(c) with the lighter element yttrium, thereby increasing the occupancy of the corresponding layer to maintain the same electron density, without producing an unphysical occupational overhang over the copper layer directly underneath.

Concluding, there is apparently no simple and unique perovskite-based structural model that could explain both the measured electron density profile for the film and the measured layer distances at the same time. Since the size of the SXRD data set is insufficient for a detailed independent structural analysis, it needs to be verified whether the data allow other possible solutions with a comparable quality of the fit. The SXRD analysis could therefore not provide a unique solution for the Y/Ba ordering. The only information we shall draw from SXRD is the confirmation that the investigated 0.5 ML $YBa_2Cu_3O_{7-\delta}$ coverage is composed of 3 perovskite-like layers with a gradually decreasing occupancy (which we assume to be 70, 50 and 30%). This information could not be gained by XSW.

Modelling: 0.5 ML $YBa_2Cu_3O_{7-\delta}$ on $SrTiO_3(001)$

The XSW and SXRD data have suggested a structural model for a 0.5 ML coverage of $YBa_2Cu_3O_{7-\delta}$ on $SrTiO_3(001)$. The model is based on 3 incomplete layers of perovskite-like but orthorhombic BCO and YCO units, which are of different height and represent the main structural elements of the coverage. The stacking sequence

of the BCO and YCO units is not fully unambiguous. Cases (B) and (D) in Fig. 5.1 on page 53 are confirmed as the two possible scenarios: The experimental results support an initial stacking sequence (BCO)–(BCO)–(YCO), while the alternative sequence (BCO)–(YCO)–(BCO) should not be entirely discarded. All sequences starting with an YCO layer can be ruled out, however. Also stacking of mixed perovskite units that have cubic symmetry, as shown in the case (A), can be ruled out.

Within the framework of this chapter we shall confine ourselves to verifying to what extent the given simple models (B) and (D) or a combination of both, i.e., taking islands with distinct stacking sequences into consideration, can account for the data. The main difference between these models consists in the Y/Ba supercell ordering, which could not be unravelled by SXRD. Despite the fact that this information is on a length scale not accessible by XSW, the XSW data still provide indications on the cation ordering, owing to the fact that the studied coverage is an ultra-thin film: Since the coverage comprises only few atomic layers, the stacking sequence of the perovkite-like building blocks is strongly correlated with the geometrical structure factors for the elements and for this reason can be identified from the measured coherent positions and fractions. It is not expected that the suggested simple models fit perfectly and can explain all the experimental data.

Developing a structural model for the refinement requires some considerations about the model details, and suitable fitting parameters have to be selected. The model assumes fixed occupancies of 70, 50 and 30% for the first, second and third pseudo-perovskite layer. The relative atomic positions for the YCO and BCO units are supposed identical to those in bulk $YBa_2Cu_3O_{7-\delta}$. This means that the orthorhombic BCO units are not centrosymmetric; the barium position is slightly off of the centre, and the O(4) site is not edge-centered but is shifted towards the Cu(1) site. The superconducting planes are corrugated. Perfect atomic order is assumed and no incoherent fractions are introduced. Possible interdiffusion at the substrate interface or surface relaxation are not taken into consideration. The most influential physical effects, like the elastic strain, the photoelectron mean free path, and the thermal lattice dynamics, were included in the model:

Pseudomorphic growth causes distortion of the nucleating BCO and YCO units along the interface normal. The distortion arises from the tensile strain parallel to the interface by the tendency of the subunits to match the larger substrate lattice. The strain component ϵ_3 normal to the interface is related to the components ϵ_1 and ϵ_2 in the interfacial plane via the elastic constants c_{ij} by $\epsilon_3 = -(c_{13}\epsilon_1 + c_{23}\epsilon_2)/c_{33}$, where index i denotes the direction of the strain and index j the corresponding surface. It is assumed that the BCO and YCO units have identical elastic constants that are equal to those of $YBa_2Cu_3O_{7-\delta}$ with $c_{13} = 71$, $c_{23} = 95$ and $c_{33} = 186$ GPa at room temperature, as determined by Lei *et al.* [104] using resonant ultrasound spectroscopy. The unit cell of $YBa_2Cu_3O_{7-\delta}$ is predicted to contract by 1.1% along the surface normal owing to the strain, yielding a lattice parameter of $c = 11.56$ Å. Hence, strain normal to the interface needs to be taken into consideration in the structural model.

The strong attenuation of the photoemission signal within few atomic layers affects the measured geometrical structure factors. This attenuation needs to be included in the structure factor calculations for the structural model. The yield contributions from

the individual sites are exponentially weighted, as described by Eq. 3.27, dependent on the ratio of the attenuation length and the path length of the photoelectron in the sample. The energy dependence of the attenuation length has been taken on from the universal curve given by Seah and Dench [105].

For higher order reflections the thermal movement of the atoms has a stronger influence on the experimentally measured coherent fractions. The Debye-Waller factors included in the model were determined for all lattice sites from (isotropic) mean-square atomic vibrational amplitudes, which were measured by Abramov *et al.* [106] for $SrTiO_3$ by X-ray diffraction. The values for $YBa_2Cu_3O_{7-\delta}$ are given by Chaplot [107] in terms of temperature B factors from X-ray and neutron diffraction measurements and calculations. (It should not be attempted to derive Debye-Waller factors from the Debye temperature for non-simple-cubic structures with more than one element. Imprecise results would be obtained, because the atomic masses and the atomic oscillation amplitudes are not identical for the symmetry-inequivalent sites.)

The fitting of the structural model to the data was carried out in reciprocal space by minimizing the squared deviations of the geometrical structure factors for the elemental sublattices and all seven measured reflections. Two fitting parameters were used: the interfacial distance between substrate and film, and the strain parallel to the interface normal.

The model with the (BCO)–(BCO)–(YCO) stacking sequence, case (D) in Fig. 5.1, agrees very well with the data for a 0.5 ML coverage of $YBa_2Cu_3O_{7-\delta}$ on $SrTiO_3(001)$. Fig. 5.14 depicts the refinement of the structure and shows the fitting of the geometrical structure factors. The fit determined the distance between the uppermost TiO_2 layer of the substrate and the first layer of barium atoms to be 2.07 Å. This means an almost perfect continuation of the $SrTiO_3$ lattice by the $YBa_2Cu_3O_{7-\delta}$ lattice with an additional small vertical spacing of $\sim$2% of the $SrTiO_3$ lattice parameter at the interface. The fit yields a contraction of the BCO and YCO units along the interface normal of 3.6% owing to strain, corresponding to a c lattice parameter for $YBa_2Cu_3O_{7-\delta}$ of 11.26 Å. Despite the significant deviation from the predicted amount of strain of 1.1%, the positions of the cation planes, and in particular the cation layer spacings, agree very well with those determined by SXRD as indicated in Fig. 5.14(a).

The good agreement of the experimental and calculated geometrical structure factors in Fig. 5.14(b) suggests that the model correctly describes the structure of the majority of the $YBa_2Cu_3O_{7-\delta}$ units. This conclusion can be drawn from the very good fit of the coherent positions, which were determined experimentally with high accuracy. The deviations in coherent fraction for barium and copper require further explanation. The coherent fractions for barium show similar trends but differ apparently by a constant factor. This may be related to increased atomic disorder for this element (an incoherent fraction was not included in the fitting) or to including quadrupole parameters that were experimentally overestimated, as confirmed by Fig. B.2. In contrast to this rather general deviation, a remarkable difference for one single parameter most likely indicates some inadequacy of the structural model. This is the case for the copper coherent fraction in the (002) reflection. The value $F_{\mathrm{Cu}}^{002} = 0.23$ shows that the modulation of the measured copper signal is almost cancelled. There are some good reasons to assume increased atomic disorder in submonolayer films, which the model

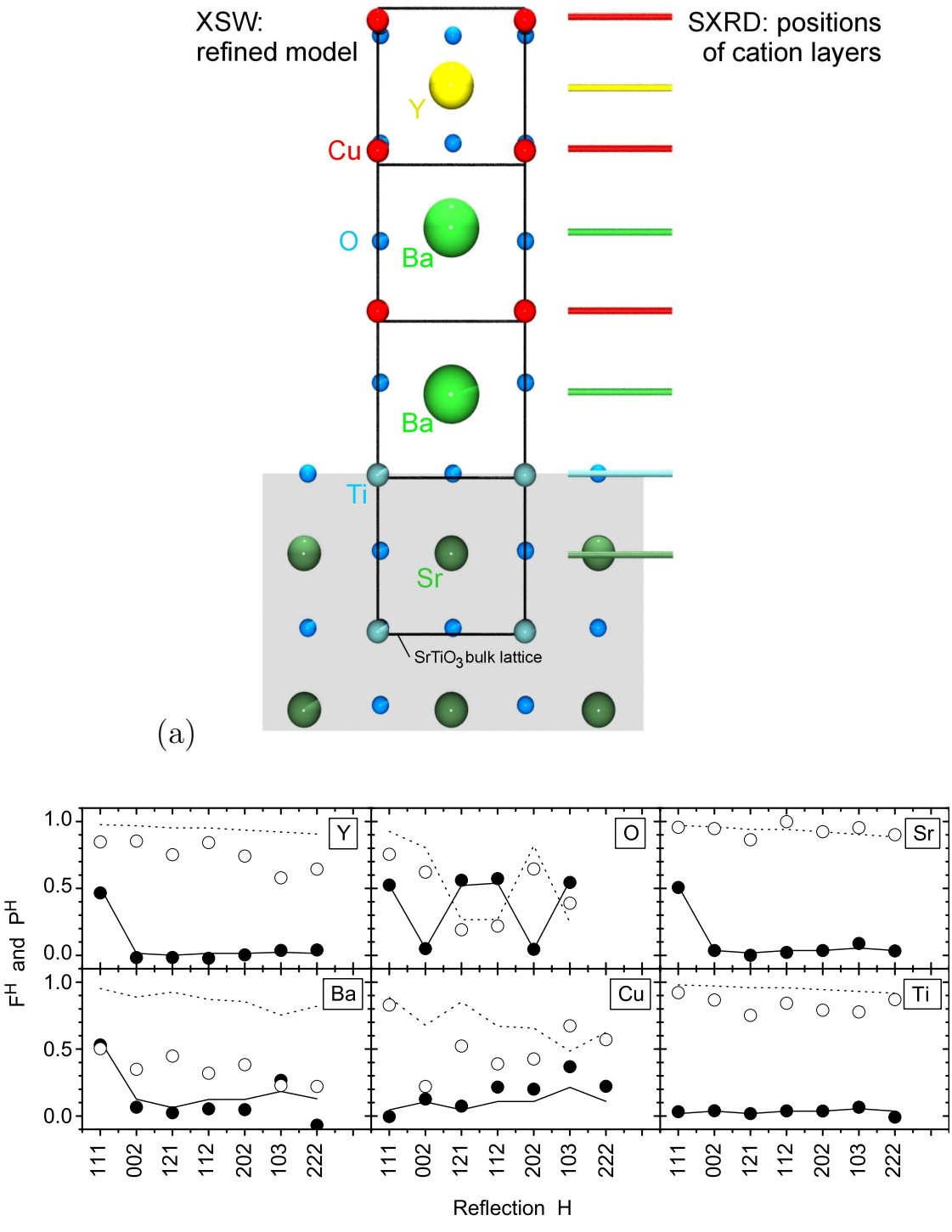

Figure 5.14: Refined model for 0.5 ML $YBa_2Cu_3O_{7-\delta}$ on $SrTiO_3(001)$. (a) Structure with a (BCO)–(BCO)–(YCO) stacking sequence. The cubic $SrTiO_3$ bulk lattice is drawn superimposed for comparison. The positions of the cation layers gained by SXRD are indicated by lines on the right side. (b) Experimentally determined phases P^H (full symbols) and amplitudes F^H (open symbols) of the element-specific geometrical structure factors. The fit result is indicated by the lines (solid line: P^H, dotted line: F^H).

(that assumes an ideal lattice) cannot account for:

Stoichiometric considerations give the following picture of the nucleation mechanism: The suggested model for the 0.5 ML coverage of $YBa_2Cu_3O_{7-\delta}$ does not contain sufficient yttrium to be stoichiometric due to the fact that the three perovskite layers are not fully occupied. If a nonstoichiometric deposition during PLD can be excluded for chemical reasons, i.e., if the plasma plume is stoichiometric and the sticking coefficients for yttrium and barium are comparable, then the building blocks of such complex compounds have to be stoichiometric at all stages of the growth of the first monolayer. This picture has to be brought into line with the experimental observations from the XSW imaging. The consequence of submonolayer coverages having bulk stoichiometry is that a certain degree of atomic disorder must necessarily exist: The nucleation process starts with subunits of a perovskite cell thickness and inevitably a stoichiometric Y/Ba composition. Upon further precipitation of material an energetically driven Y/Ba cation reordering vertically across the layers has to take place in order to enrich the base perovskite layer with barium, as indirectly concluded from the raised copper position in the 3D direct images. This diffusion process appears plausible even for already buried cations, given the large atomic mobility at the high growth temperature. The yttrium will then, according to the model, accumulate in the third perovskite layer once its formation has started, and a phase transition will take place at this stage of the growth, as the first monolayer $YBa_2Cu_3O_{7-\delta}$ has now been completed. Hence, the forced $YBa_2Cu_3O_{7-\delta}$ stoichiometry for subunits of one or two perovskite units height causes atomic disorder and has to be additionally taken into consideration in more rigorous structural models. As a consequence of disorder the elemental coherent fractions are reduced.

A structural (and electronic) phase transition takes place once a stack of three perovskite layers is completed, since the amount of material is sufficient to now form complete unit cells of the stable $YBa_2Cu_3O_{7-\delta}$ phase. The phase transition is "continuous", since the transition is basically facilitated by the Y/Ba cation diffusion and reordering, accompanied by the corresponding oxygen diffusion such that no oxygen is present in the yttrium planes. Relatively little structural change was therefore found by the comparison of the structures of the 0.5 and 1.0 ML coverages in Fig. 5.12. The electronic phase transition results from the band structure of the newly formed phase and comprises the formation of electrical conductivity in the copper chains and planes, as observed by Haage *et al.* by STS in Fig. 5.2(b).

A further aspect in the discussion of the Y/Ba cation ordering is the overgrowth of substrate steps. Antiphase boundaries, which exhibit YCO and BCO units adjacent to each other (under the development of strain), will form when subunits grown on different substrate terraces coalesce. The suppression mechanism for the energetically unfavourable antiphase boundary formation suggested by Haage *et al.*, which is given by the overgrowth structure between (B) and (D) in Fig. 5.1, is confined to one single terrace step, since the height compensation by a BCO layer cannot accumulate; stacks of three and more BCO units are likely to become chemically instable since $BaCuO_3$ does not exist. Hence, an XSW measurement samples an area that extends over many terraces and therefore over domains separated by antiphase boundaries. A model with a single perovskite stacking sequence is therefore unlikely to account for the measured

structure.

The presence of antiphase boundaries and the existence of atomic disorder in subunits of one or two perovskite cells height are good reasons to extend the discussed structural model (D) by including a distinct, second possible stacking sequence. Attempting a structural refinement based solely on model (B) in Fig. 5.1 with a stacking sequence (BCO)–(YCO)–(BCO) yielded unphysical results for the strain and the interfacial spacing. However, a combination of the stacking sequences (B) and (D) for noncoalesced subunits appeared plausible: The copper planes that terminate the structural units (BCO)–(BCO) and (BCO)–(YCO) reveal a height difference of $\sim c_{SrTiO_3}/4$, which causes the coherent fraction F_{Cu}^{002} to decrease. Using the fit results for the strain and interfacial distance obtained for model (D) as fixed parameters and using the occupancies of the perovkite layers as fitting parameters resulted in a very good fit of the copper coherent positions. Fractions F_{Cu}^{002} below 0.6 could not be achieved with this model. This suggests that the structure of the film is of higher complexity, either due to disorder or additional structural elements, like single atomic layers of the surplus material.

5.6 Conclusion and Outlook

XSW real space imaging was applied to investigate the atomic structure of 0.5 and 1.0 ML coverages of $YBa_2Cu_3O_{7-\delta}$ deposited onto the (001) surface of a $SrTiO_3$ single crystal. SXRD provided supplementary information. The investigation has contributed to understanding the nucleation mechanism of a heteroepitaxially grown complex material:

Three-dimensional real space images of the elemental atomic distributions confirm directly that the structure of submonolayer $YBa_2Cu_3O_{7-\delta}$ coverages is based on perovskite-like subunit cells. The building blocks are therefore formed by double atomic layers. Stacking order to a large degree for the yttrium and barium cations indicates that the material attempts to arrange in the $YBa_2Cu_3O_{7-\delta}$ sequence from the very beginning of the growth. Barium seems to accumulate in the initial two subunit-cell layers, while yttrium is rather found from the third layer on. This was indirectly deduced from atomic layer distances. The starting sequence of the growth, which was not exactly known before this study, seems therefore to be (BCO)–(BCO)–(YCO) in accordance with model (D) in Fig. 5.1 for most of the film. During the nucleation, the substrate surface is not entirely wetted. The deposited material nucleates in islands, and the stacking of perovskite-like units occurs to be energetically at least as favourable as the wetting of the remaining bare substrate surface area.

Provided $YBa_2Cu_3O_{7-\delta}$ stoichiometry of the material at all stages of the growth, the following description of the nucleation is obtained: The bulk structure of the film is complex and can therefore not be formed immediately; a sufficient amount of material has to be deposited. For this reason, a structure based on perovskite subunit cells is formed during the initial stage of the growth. The formation of the bulk structure requires atomic reordering: Most importantly, this concerns diffusion processes for the Y/Ba cations towards the supercell ordering in the $YBa_2Cu_3O_{7-\delta}$ bulk and the corre-

sponding diffusion of oxygen to occupy barium layers but not yttrium layers. These diffusion processes give rise to a phase transition that is continuous; the formation of the complex $YBa_2Cu_3O_{7-\delta}$ phase is a matter of sufficient deposited material.

The findings are in agreement with the interpretation by Haage *et al.* of their STM/STS results that a perovskite precursor phase is formed during the nucleation stage, while the perovskite-like building blocks are not cubic as proposed by the authors. Their picture of a perovkite phase with a randomly occupied rare earth site, as depicted in model (A) in Fig. 5.1, is likely to be correct for the structure of thin coverages of no more than ∼0.25 ML, where stacking of the building blocks has not largely set in. The authors' picture deduced from enthalpy considerations that a phase transition occurs upon exceeding a critical nucleus size may need some correction; owing to permanent diffusion processes normal to the surface, the $YBa_2Cu_3O_{7-\delta}$ stacking sequence tends to form immediately, even before completion of the first bulk unit cell.

For future studies, the results have suggested an XSW imaging experiment on a coverage even thinner than 0.5 ML without any completed unit cells to investigate the Y/Ba cation ordering. It can be verified whether the proposed double-layer based growth, which may give indications on the slowest kinetic step during the film growth, still holds true. Experimentally, higher reflection orders could be accessed to obtain even more detailed direct images by using the HAXPES setup.

Chapter 6

Hard X-Ray Photoelectron Spectroscopy

Photoelectron spectroscopy at high photon energies can be employed to probe bulk electronic states. By the development of a supplementary high-voltage retarding lens, the operational range of electron energies of a commercial hemispherical photoelectron analyser installed at beamline ID32 at the ESRF has been extended. The feasibility of bulk sensitive valence band spectroscopy at high brilliance third generation X-ray sources is demonstrated.

6.1 Introduction

Photoelectron spectroscopy is a surface sensitive technique due to the strong interaction of electrons with matter. The travel of a photoelectron from the photoexcited atom through the bulk material towards the sample surface is characterised by the inelastic mean free path (neglecting here the influence of elastic scattering, which becomes relevant mainly for materials that contain heavy elements), after which the photoelectron suffers an energy loss owing to an inelastic scattering event. The photoelectron will then no longer carry the desired information about the electronic state it was excited from in terms of its former binding energy. The inelastic mean free path is relatively short and varies only slowly with electron kinetic energy, as the empirically determined universal curve in Fig. 6.1(a) shows. For this reason, the information depth of UPS as well as of XPS extends only over few atomic layers. Chemical surface modifications or sample regions with nonintrinsic phases, often exposed by cleaved $YBa_2Cu_3O_{7-\delta}$ surfaces, will contribute a considerable fraction to the total photoemission intensity.

One possibility to enhance the bulk sensitivity of photoelectron spectroscopy is employing hard X-rays to shift the kinetic energy range of the photoelectrons towards higher energy. The resulting increase in the effective attenuation length (which is a quantity strongly determined by the inelastic mean free path) is indicated by the empirical extension of the universal curve into the hard X-ray range in Fig. 6.1(b) by Dallera *et al.* [108]. Further experimental data for effective attenuation lengths in hard X-ray photoelectron spectroscopy have very recently been published for a variety

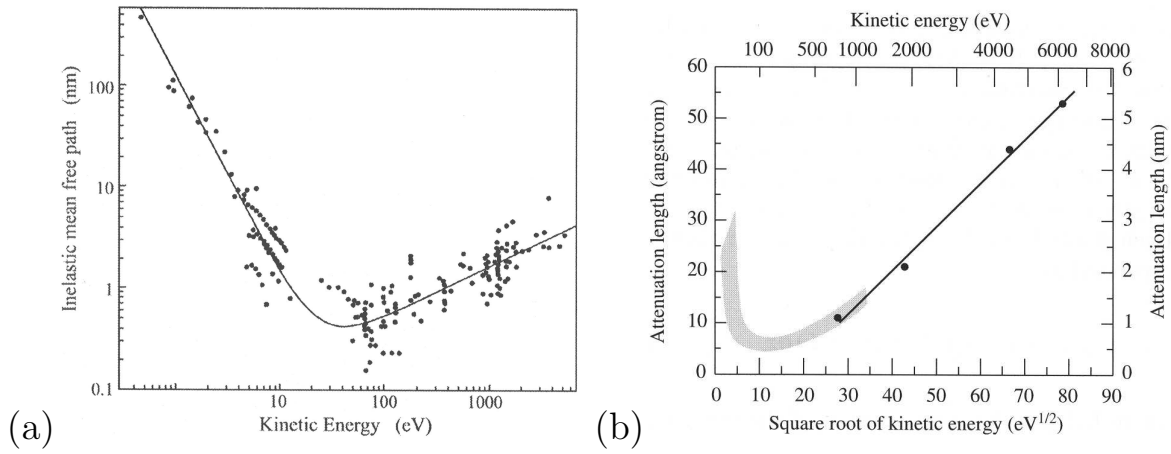

Figure 6.1: Universal curve of the inelastic mean free path. (a) The universal curve by Seah and Dench [105]). (b) An extension of the universal curve to higher electron kinetic energies based on experimental photoemission data by Dallera *et al.* [108].

of materials [109]. The second possibility to enhance the bulk sensitivity, exploiting the increase in inelastic mean free path for very slow photoelectrons by adjusting the photon energy less than 10 eV above the binding energy of the corresponding level, cannot be utilized for core level XPS. A tremendously large background signal of secondary electrons would have to be expected.

Photoelectron spectroscopy employing synchrotron radiation in the energy range of several keV for the investigation of valence bands and buried layers is a newly emerging field at high brilliance third generation synchrotrons. An early landmark photoemission experiment in 1974 on the valence band of gold employing hard X-rays [110] demonstrated the feasibility of such experiments but was not followed up because of insufficient X-ray intensity at that time. For core level spectroscopy X-ray photoemission was taken up again at second generation sources. The workshop held at the ESRF in 2003 [111] has demonstrated the increasing current interest in hard X-ray photoelectron spectroscopy. While much of the published work in this field is related to core level spectroscopy, the current trends indicate that valence band spectroscopy with hard X-rays will be very important in the future. Promising results have been obtained up to 6 keV photon energy so far [112–115].

We have now explored the energy range up to 13.5 keV to investigate *ex situ* prepared $YBa_2Cu_3O_{7-\delta}$ surfaces. It is known that the surface of this material is reactive, and usually bulk representative results can only be achieved in photoemission investigations on surfaces cleaved under UHV conditions at temperatures below 40 K. Sample preparation by cleaving for photoemission experiments in combination with XSW is laborious due to the additional requirement of strain-free sample mounting. In the present study we have investigated whether *ex situ* preparation at room temperature, which is relatively easy to accomplish, represents a sensible alternative. It was verified whether exploiting the increased sampling depth of HAXPES can efficiently reduce the fraction of nonintrinsic photoemission intensity.

High energy photoelectron spectroscopy using hard X-rays is hampered by low photoemission cross sections, which vary inversely as the third or higher power of the X-ray excitation energy. For this energy range, only calculated atomic cross sections are currently available [116] that have not been experimentally verified. One recent experimental determination of photoemission cross sections for shallow electronic levels of gold in the hard X-ray range was carried out by an ID32 collaboration around C. Kunz. The results are summarised in appendix F. The availability of well-collimated monochromatic X-rays with intensities of 10^{11} photons/s at better than 10 meV resolution makes attempts to compensate low photoemission cross sections by a high primary photon flux feasible. An additional asset not yet exploited in the present study is the possibility of efficiently focussing X-rays to spot sizes on the micrometre scale.

Present commercially available spectrometers operate at kinetic energies up to 6 keV. Recently, some research groups have extended the energy range of their spectrometers by biasing the sample positively. This reduces the collection efficiency but has produced interesting results. We have modified a commercial multi-channel hemispherical electron analyser by adding a specially designed retarding lens.

6.2 XPS Measurements

The HAXPES measurements were carried out at beamline ID32, using unfocussed radiation from two undulators and a Si(111) monochromator ($\Delta E_\gamma / E_\gamma = 1.3{\times}10^{-4}$). For some of the measurements at a photon energy of 8.0 keV, a Si(444) post-monochromator ($\Delta E_\gamma = 40$ meV) was used. The PHI electron analyser was set up with the supplementary retarding lens mounted, as shown in Fig. 4.3(b) on page 37, and with the corresponding horizontal manipulator installed.

The functioning of the modified spectrometer was demonstrated by a survey scan on gold presented in Fig. 6.2 with 13.5 keV excitation energy, covering a range of more than 12 keV in binding energy. For taking this spectrum only the Si(111) main monochromator was used with a photon flux on the sample of the order 10^{12} s^{-1} and 1.8 eV bandwidth. The (nominal) resolution of the analyser was set to 700 meV. The spectrum was recorded in increments by scanning the analyser over a range of 2.5 keV and then successively increasing the retarding voltage of the supplementary lens by 2 kV at each step. The defocussing of the retarding lens at the low kinetic energy (high binding energy) end of each recording step, which was discussed in section 4.1, resulted in reduced collection efficiency in the overlapping parts of the spectra.

An $YBa_2Cu_3O_{7-\delta}$ single crystal surface was prepared by cleavage at ambient atmosphere immediately before it was introduced into the UHV chamber. Intrinsic surfaces of this material are known to be chemically very reactive; a surface prepared in air will therefore be contaminated with water, carbon species and other molecules. For a chemical analysis with different surface sensitivity, survey spectra for the valence band and shallow core levels were recorded at gradually increasing photon energies of 5.1, 8.0, and 13.5 keV with the band pass of the Si(111) monochromator. In order to estimate the remaining XPS intensity coming from possible surface states, signals from selected core level that are known to be sensitive to chemical surface modifications were

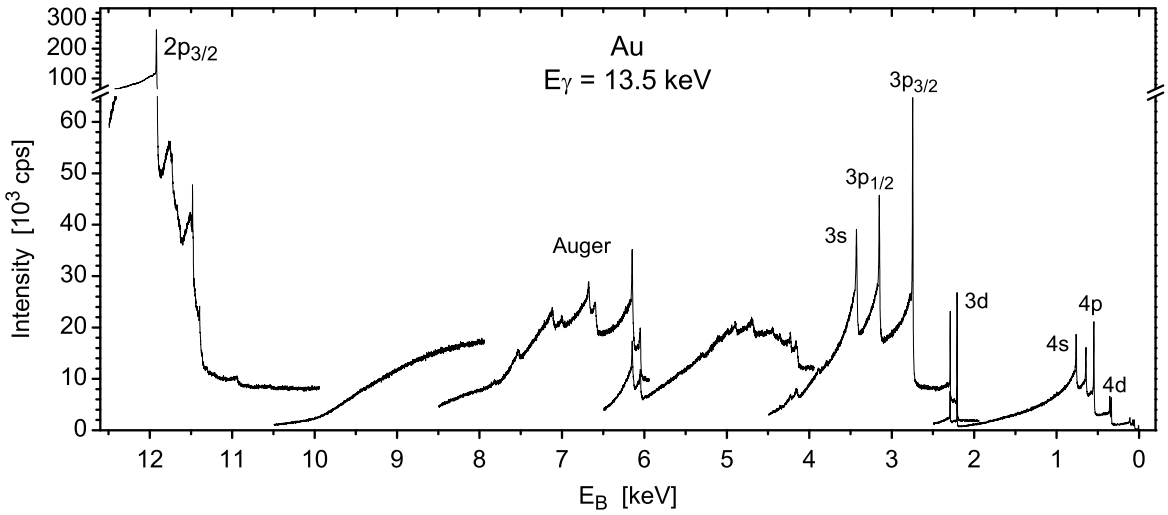

Figure 6.2: HAXPES survey spectrum for gold with $E_\gamma = 13.5$ keV. The six spectral sections correspond to retardation voltages on the supplementary lens of 0, 2, 4, 6, 8, and 10 kV. Pass energy 46.95 eV, sampling time 0.3 s/data point, total acquisition time 63 min.

inspected in more detail: Spectra for the Cu $2p_{3/2}$, Ba $3d_{5/2}$ and O $1s$ core levels and the valence band were recorded at 8.0 keV with a Si(444) monochromator in use. The analyser settings determined the overall resolution to 400 meV except for the valence band spectrum, which was taken with a resolution of 1.7 eV.

6.3 Discussion of the Results

The three HAXPES survey spectra taken between $E_\gamma = 5.1$ and 13.5 keV are compared in Fig. 6.3 to a spectrum recorded at 3.7 keV from a clean low-temperature cleaved surface. Surface contaminants are usually chemical species containing light elements, like carbon, oxygen, and hydrogen. The presence of carbon peaks is indicative of the contamination of the $YBa_2Cu_3O_{7-\delta}$ surface due to exposure to air. With rising photon energy the C $1s$ signal visibly diminishes, i.e., it decreases faster than signals originating from the bulk material. This has two reasons: On the one hand, light elements become difficult to detect by spectroscopic methods at high photon energies, owing to the rapid decrease of the photoabsorption cross sections for all their electronic levels. On the other hand, the bulk sensitivity of photoemission increases and the fractional signal contribution from the surface drops, owing to an increased effective attenuation length for the excited photoelectrons. At the highest energy of 13.5 keV, where the inelastic mean free path is of the order of 10 nm, the C $1s$ signal that comes from the sample surface has almost vanished.

The advantage of reduced surface sensitivity at high photon energies is coupled with the effect that states with high angular momenta have reduced intensities. This is the case for the Y $3d$ level at $E_\gamma = 13.5$ keV. The same has been observed for the

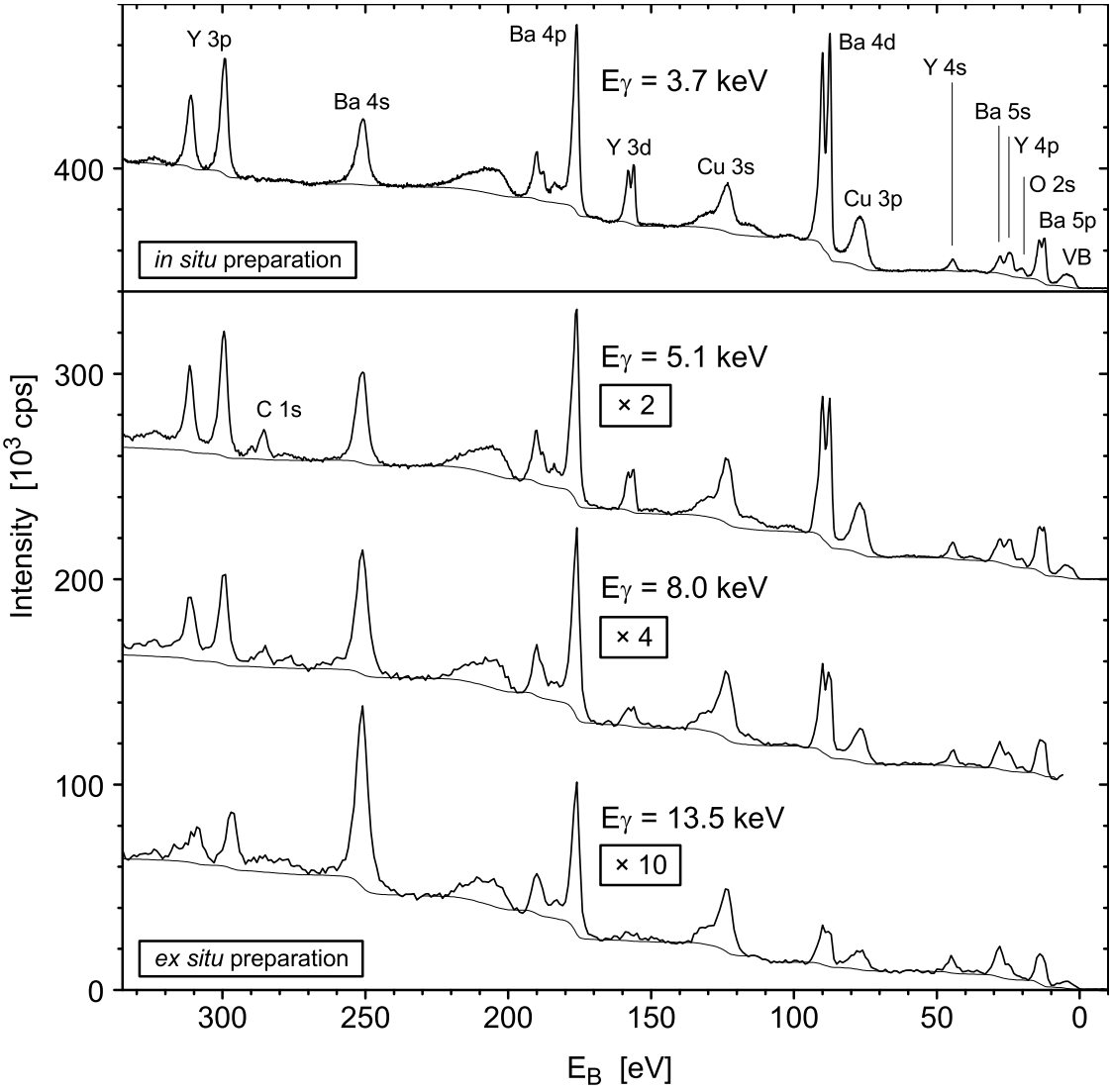

Figure 6.3: HAXPES survey spectra for an $YBa_2Cu_3O_{7-\delta}$ surface prepared *ex situ*. The reference spectrum at $E_\gamma = 3.7$ keV, taken from Fig. 8.2 on page 133, is representative of a clean surface of a low-temperature *in situ* cleaved crystal. The spectra for higher photon energies were taken from a crystal cleaved in ambient air. The given scaling factors for the individual curves are approximate, since the transmission of the supplementary analyser lens was not exactly identical for all photon energies.

Au $4f$ levels in Fig. F.1 on page 176. These observations agree with the prediction that the photoabsorption cross sections for the d and f shells display a stronger energy dependence than those for states with lower angular momentum [117]. The reason may be related to the expanded radial charge density distributions for these levels, which peak further away from the atomic core.

Chemically shifted signals that originate from surface states or chemically modified surface regions are suppressed at elevated photon energies by the decreased surface vs. bulk signal ratio. The photoionisation cross section for a chemically shifted component

generally does not drop faster with rising photon energy than the one for the main peak. Fig. 6.4 compares high-resolution HAXPES spectra for the Cu $2p_{3/2}$, Ba $3d_{5/2}$, and O $1s$ core levels recorded from $YBa_2Cu_3O_{7-\delta}$ surfaces that were prepared at ambient air pressure and under clean UHV conditions (taken from Fig. 8.2 on page 133). Identical barium spectra, which exhibit the same degree of peak asymmetry, and identical copper spectra, which show the same satellite-to-peak intensity ratio, were obtained for the two samples. The copper satellite peak exclusively originates from the $YBa_2Cu_3O_{7-\delta}$ bulk, while the main peak can contain contributions from nonintrinsic phases (details about the origin of the satellite are discussed in section 8.4 on page 139). The copper and barium spectra recorded from the *ex situ* prepared sample are representative of a clean surface; signal contributions from surface states or chemical surface modifications are efficiently suppressed. This is in agreement with the recent experimental finding by Panaccione *et al.* [118] that the surface signal contribution at 8 keV is typically less than 5%. The asymmetric line shape of the barium peak measured from the surface prepared in air appears to be characteristic of the bulk material.

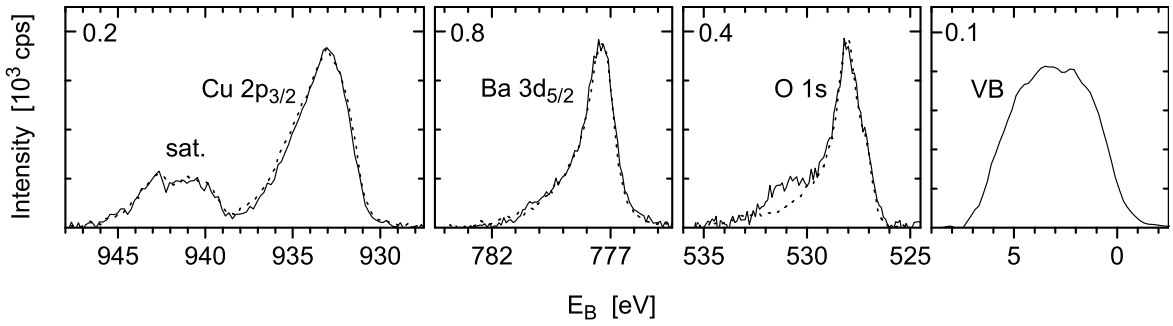

Figure 6.4: High-resolution core level and valence band HAXPES spectra for an $YBa_2Cu_3O_{7-\delta}$ surface prepared *ex situ*. Core level spectra recorded at 8.0 keV from a surface prepared at air (solid line) are compared to spectra taken at 3.7 keV from a surface prepared under clean conditions at low temperature (dotted line; taken from Fig. 8.2).

The chemical state of an $YBa_2Cu_3O_{7-\delta}$ surface cannot be judged, however, from chemical analysis of one or two core level spectra only. The oxygen spectrum reveals a small chemically shifted component at 531 eV binding energy that can be distinguished from the O $1s$ main peak at 528 eV. This component indicates chemical modifications of the sample surface over a depth of probably several angstroms in order to be measurable by HAXPES. It has to be noted, however, that moderate chemically shifted components have also been observed for crystals cleaved at low temperature in UHV. This observation may be related to impurity inclusions in the crystal that are exposed by the cleavage. Large inclusions will cause signal contributions that are not related to surface states and that cannot be suppressed by using hard X-rays.

The count rate of 80 cps attained for the $YBa_2Cu_3O_{7-\delta}$ valence band under the current conditions is sufficiently high to prove valence band spectroscopy with hard synchrotron radiation feasible. Exploiting the possibility of focussing the X-ray beam

to match the beam spot with the analyser focal spot size will gain another one or two orders of magnitude in intensity.

Summarising, photoelectron spectroscopy in the photon energy range up to 13.5 keV has enhanced bulk sensitivity. This is a consequence of an increased escape depth for photoelectrons with large kinetic energy. Signal contributions from surface states and contaminants can be efficiently suppressed; this relaxes the vacuum and surface preparation requirements for many materials. The XPS intensity from bulk states with higher angular momenta, however, can suffer from strongly reduced photoionisation cross sections. The feasibility of even valence band spectroscopy at hard X-ray energies with an undulator beam from a third generation synchrotron radiation source has been demonstrated. Experimental access to the truly intrinsic bulk electronic structure paves the way for investigations of e.g. strongly correlated electronic systems, where the surface electronic structure differs significantly from that of the bulk. The improved data quality will allow a more rigorous comparison with theoretical predictions. High energy photoemission in combination with the X-ray standing wave method provides access to higher order reflections providing higher order Fourier components for XSW imaging.

A newly developed commercial high-energy photoelectron spectrometer for electron energies up to 15 keV will be installed on beamline ID32 at the ESRF in 2007.

Chapter 7

Valence Electronic Structure of $SrTiO_3$

Site-specific photoemission, which uses XPS in combination with the XSW method, represents a recently established application of the XSW method for analysing the valence electronic structure of materials, as will be briefly described in the following introduction to motivate the present study of the $SrTiO_3$ valence band. After summarizing the known facts and describing the experimental data acquisition, the lattice site-specific analysis of the valence band and the angular-momentum assignment with the help of LDA calculations will be explained. The obtained atomically resolved electronic structure will be related to the structure of the unit cell in the subsequent section. Finally, the influence of the solid state formation on the photoionisation cross section for shallow electronic levels will be discussed.

7.1 Introduction

Atomic structure and chemical composition define the band structure of solids. The band structure in turn determines the electronic and optical properties of a material, such as the electronic transport and the electrical conductivity, or the colour and the ability to reflect and absorb light. Measuring electronic information spatially resolved on the atomic scale can reveal how the atomic structure and chemical composition are related to the electronic structure of the material. Conventionally, resonant photoemission has been used for this purpose: This technique is element-specific, since one of the constituting elements can be preferentially excited by choosing the photon energy around the resonance of an electronic transition. For the present study, the recently developed technique of site-specific photoemission described in section 3.4, which benefits from the large X-ray intensity available at third generation synchrotrons, was employed: This technique is site-specific, since the X-ray standing wave can be positioned in the unit cell such that one of the lattice sites is preferentially excited. Woicik *et al.* [5] used site-specific photoemission to quantitatively analyse the electronic structure of rutile TiO_2. We employed this method on the related, but more complex ternary oxide $SrTiO_3$: We have determined the site within the $SrTiO_3$ unit cell from which the

electrons in a specific region of the valence band originate. The site-specific analysis of the $SrTiO_3$ valence band was compared to Woicik's results for TiO_2. By comparing the result of the site-specific analysis of the valence band to the results of *ab initio* LDA calculations, *a priori* unknown photoionisation cross sections valence electrons were determined.

Already the first valence band XPS studies reported in the literature that were combined with the XSW technique were aiming at determining the asymmetry of the valence charge distribution in binary materials. Different author groups around J. Woicik have recorded XSW absorption profiles for core levels and the valence band of Ge and GaAs [2], of metallic Cu, covalent InP and ionic NiO [3], covering the entire range of solid-state bonding. For the binary compounds, the coherent position determined from the valence XPS signal was observed to deviate from the mean of the coherent positions determined from the two elemental core level signals. From this observation the authors concluded that the valence charge did not reside symmetrically between the two atoms. In their conclusion that the distribution be skewed towards the As in GaAs and the In in InP, however, the authors did not take differences in photoionisation cross section at the two sites into consideration. The authors correctly mentioned that the valence yield arose from part of the valence charge: The valence yield was measured only from the charge that resided in the vicinity of the atomic cores.

Site-specific photoemission has been employed to decompose the valence bands of NiO [3], GaAs [4], and α-Fe_2O_3 [119]. A demonstration that the rutile TiO_2 valence band spectrum can be decomposed in the titanium and oxygen contributions and can then be reconstructed based on theoretically calculated angular-momentum resolved lpDOS spectra has been shown recently by Woicik *et al.* [5]. The results of this study are described in more detail in section 7.7.

Photoionisation cross sections for valence and conduction electrons in solids are *a priori* unknown. Accurate experimental values can, in addition to the electronic information, be uniquely obtained by an XSW valence electronic structure analysis. Cross sections are inter alia dependent on the initial state wave function and on the gradient of the crystal potential, as expressed by Eq. 3.16 on page 20. During the assembly of the solid from isolated atoms, the charge in the outermost atomic orbitals is spatially redistributed specific to the forming compound, and the screened potential of the single atomic core that the electrons experience is substituted by the newly created crystal potential. Theoretical cross sections, which are calculated for single free atoms, may for this reason no longer be correct for the same atoms embedded in a solid.

Photoionisation cross sections for valence electrons have been experimentally determined for metallic and semiconducting material systems. Most of the valence band XPS studies reported in the literature do not pay particular attention to the determination of cross sections, and therefore data are scarce. It is interesting to note that all those studies mentioned in the following were already carried out in the newly explored hard X-ray range, for most of the part in order to minimise surface signal contributions.

Photoionisation cross sections for the valence and conduction band of gold have been measured by an ID32 collaboration around C. Kunz [120]. A brief summary of

this study is given in appendix F. Relative to the known cross section for a core level reference signal, the authors found the cross section for the Au 6*s*-derived conduction band to exceed the tabulated atomic value by a factor 5. This deviation was attributed to hybridization of the 6*s* electrons with the *d* band or to other solid state effects. No deviation beyond the experimental error was found for the 5*d*-derived valence band, however.

Panaccione *et al.* [121] have experimentally determined cross section ratios for the spatially more localised *d* states and the more free-electron-like *s* and *p* states in the valence band of silver. They found the cross section for the *s* and *p* states relative to that for the *d* states to be enhanced by a factor 2–3 in comparison to the theoretical prediction for atomic states. The trend is the same as for gold; increased electron delocalisation does not necessarily entail a reduction in cross section. The authors do not give explanations for the deviation observed. The authors have not determined the valence cross sections for the Ag 4*d*-, 5*s*- and 5*p*-derived states for photon energies up to 8 keV, using one of the measured core level XPS signals as a reference. Recent efforts by Kobayashi *et al.* [122,123] were directed towards the goal of comparing valence cross sections for the binary semiconductors GaAs and GaN. While the bond polarity for GaN is larger than for GaAs, the bonding overlap is less pronounced due to the larger energy separation of the involved atomic levels. The authors attempted to determine photoionisation cross sections for valence electrons by comparing XPS spectra for GaAs and GaN to theoretical DOS calculations. Unfortunately, the analysis is based on an incorrect analytical expression for the photoelectric cross section such that all the extracted values listed are incorrect. In addition, the chosen core level with 20 eV binding energy, which has been reported to even hybridize, may not provide the XPS intensity representative of its cross section and is therefore unsuitable as a cross section reference.

The following section summarises the information about the valence electronic structure of $SrTiO_3$ known at the beginning of our XPS/XSW study.

7.2 Motivation for the Site-specific Valence-band Studies

Many facts known about the bulk valence electronic structure of $SrTiO_3$ have been obtained from comparing UPS and XPS results with LCAO calculations. The calculations were performed to different degrees of accuracy, ranging from a tight binding treatment which used the O 2*p* and Ti 3*d* orbitals in the simplest case [124] to a more sophisticated LCAO model based on APW calculations [125], which included a more complete basis set of atomic orbitals with a larger number of orbital interactions taken into consideration. The valence energy bands were described as a mixture of states mainly derived from the O 2*p* and Ti 3*d* atomic orbitals, while the bands derived from all the other orbitals were neglected. This fact was taken as a reason in the majority of the publications for analysing the measured XPS spectra [73,126–129] as well as the UPS spectra [129–132] exclusively in terms of O 2*p* and Ti 3*d* signals. Possible contributions from strontium or barium occupying the central lattice site were not included

to explain the experimental valence photoelectron spectra. Most of the theoretical predictions are not in good agreement with the photoemission data.

Theoretical studies by de Groot *et al.* [133] of the $SrTiO_3$ valence electronic structure included strontium states, but the authors did not compare their LDA calculations to experimental results.

Wolfram and Ellialtıoğlu [129, 132, 134] have interpreted valence UPS spectra as a combination of O $2p$ and Ti $3d$ densities of initial states weighted by transition matrix elements. The authors ascribed the upper valence band region to nonbonding oxygen states. The lower valence band was attributed to bonding oxygen states with titanium d admixture of t_{2g} as well as of e_g symmetry. Differences in line shape of UPS and XPS spectra were explained by changes in the cross section ratio for the titanium and the oxygen signals [129, 130].

Resonant photoemission studies have provided direct experimental evidence of titanium involvement in the mainly oxygen-derived $SrTiO_3$ valence band. Author groups around Brookes [135] and Reihl [136] have measured valence photoemission at the Ti $3p \rightarrow 3d$ absorption edge in the ultraviolet. From intensity enhancements in the more strongly bound half of the valence spectrum they identified Ti $3d$ admixtures in the bonding subband. Apparently, no resonant photoemission studies at a strontium threshold in order to probe possible strontium valence contributions have been reported in the literature.

Briefly before the analysis of our XSW data was completed, a first attempt of using the XSW method to decompose the $SrTiO_3$ valence band XPS spectrum into SrO_3 and Ti contributions was published by Fujii *et al.* [137]. The authors selected a Bragg angle of 36° far away from back reflection such that the reflectivity curve was quite narrow. The experimental geometry was chosen sensitive to quadrupole effects at a beam energy of 4.75 keV. The authors ascribed the SrO_3 yield component mainly to oxygen without experimental confirmation and compared it to the oxygen component of rutile TiO_2 [5]. The strontium-oxygen bonding in strontium titanate was concluded to be covalent. The authors compared their experimental results to DV-Xα cluster calculations by scaling the lpDOS components with cross sections calculated for free atoms.

Photoionisation cross sections for valence electrons result as the scaling factors when comparing DOS calculations and experimental photoemission spectra. Experimental valence cross section ratios $\sigma(\text{O } p)/\sigma(\text{Ti } d)$ were determined in some of the publications mentioned above from photoemission on $SrTiO_3$ and $BaTiO_3$ in the X-ray regime [73, 126–129] and in the ultraviolet [129–131]. Selected theoretical angular-momentum dependent lpDOS components were mostly used for the comparisons made in the cited work.

7.3 Surface Preparation

For the XPS/XSW experiment the polished (001) surface of a pristine $SrTiO_3$ single crystal sample (supplier SPL, Netherlands), degreased by organic solvants in an ultrasonic bath, was cleaned by annealing in high vacuum at pressures $<1\times10^{-8}$ mbar

for 3 h at a temperature of ∼930 °C as measured by a pyrometer (emissivity setting $\varepsilon = 0.90$). The sample was cooled down to room temperature within 30 min. The deep black colour of the initially colourless and transparent sample was indicative of the reduction of the insulating crystal, which had become semiconducting and did not charge during the electron diffraction measurements. The strong LEED pattern shown in Fig. 7.1, characteristic of two 90° rotated domains of a c(4×2) reconstruction, was observed. Erdman *et al.* [76,138] have solved the structure of this reconstruction. The chemical composition of the surface is modified, but this modification is confined to the topmost layer, which is TiO_2 enriched. The surface was stable for the period of the XSW measurements as proved by an unchanged LEED pattern at the end of the experiment. Auger spectra and the XPS spectra recorded at the beamline showed no sign of surface contamination.

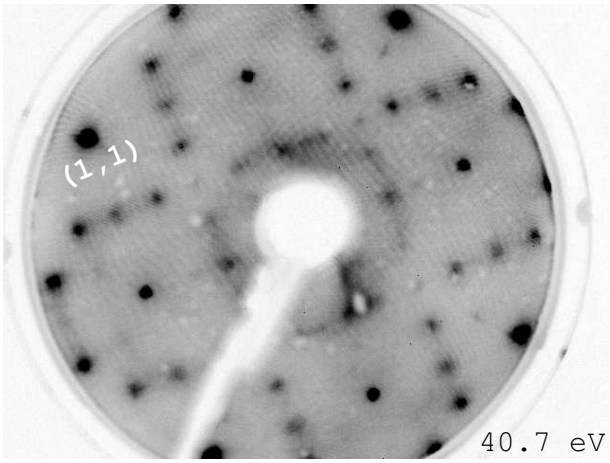

Figure 7.1: LEED pattern of a $SrTiO_3$(001) c(4×2) reconstruction. The surface was prepared by the annealing procedure described in the text.

The $SrTiO_3$ sample exhibited very good crystalline quality and was selected for the experiment out of a number of samples from different sources, which were characterised at beamline ID32. A mosaic spread of typically 0.05° was found for the majority of the samples, which is comparable to the Darwin width of the $SrTiO_3$(111) and $SrTiO_3$(112) reflections in backreflection geometry. The selected sample revealed a symmetric mosaic distribution of 0.0035° width as shown in Fig. 7.2, which in backreflection geometry did not cause any significant additional broadening to the rocking curves.

The sample was 10×5×1 mm in size. The nominal misorientation of the surface normal with respect to the [001] direction was less than 0.1°.

7.4 XPS/XSW Measurements

For the XSW measurements, the $SrTiO_3$ sample prepared by the procedure described in the previous section was transferred in a transportable vacuum chamber at a pressure of $\sim 5\times10^{-9}$ mbar from the large UHV system in the surface characterisation laboratory to the UHV chamber at the undulator beamline ID32. The transport chamber

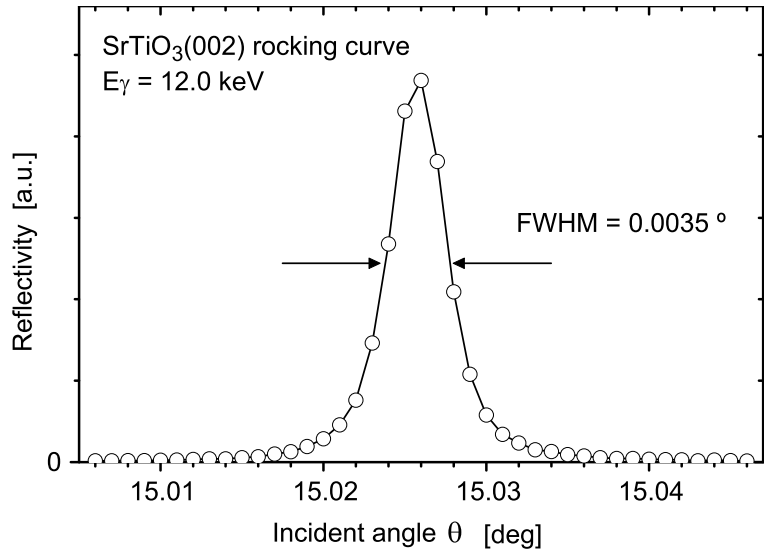

Figure 7.2: Reflectivity curve representing the mosaic spread of the $SrTiO_3$ single crystal that was used for the XSW measurement. The size of the incident beam was 0.4 × 0.08 mm. The data were recorded without **q** resolution, i.e., with the detector slits set wide open in order to attain a representative picture of the sample.

was docked on the UHV chamber at the beamline under clean conditions, and the sample was transferred over after evacuating the docking port to high vacuum. The beamline was set up in a quadrupole-insensitive geometry with the photoelectron spectrometer mounted in polarization direction of the X-ray beam. The incident beam was 1.0 × 0.8 mm in size. With a Si(111) monochromator in use, the energy bandpass for the radiation was ∼360 meV at 2.75 keV and ∼510 meV at 3.89 keV. An overall instrumental energy resolution of 435 meV at 2.75 keV photon energy was determined from the broadening of a gold Fermi edge shown in Fig. 7.3. The binding energy scale of XPS spectra was calibrated against the Fermi edge of the gold reference sample, which was in electric contact with the $SrTiO_3$. High-resolution XPS/XSW data sets were recorded simultaneously for the O 1s, Ti 2$p_{3/2}$ and Sr 3$p_{3/2}$ core levels ("first set" of core level data) and the valence band for both the $SrTiO_3$(111) and the (112) Bragg reflections close to backreflection geometry at an incident angle θ = 86–87° at 2.753 and 3.891 keV photon energy, respectively. Independently, additional XPS/XSW core level data sets, in the following referred to as the "second set" of core level XSW data, were recorded separately in quick scans for the purpose of removing residual influence of energy drift.

Removing the influences of photon energy drift proved to be important for a reliable data analysis. Long-term energy drift, which resulted from creeping of the monochromator mechanics and the varying heat load due to the changing ESRF ring current, was compensated by employing a self-centering control algorithm: While frequently cycling through a fast data acquisition loop, as sketched in Fig. 7.4, the photon energy scan range was regularly recentered around the rocking curve. Short-term residual drift of ∼40 meV occurred at each photon energy step between the recordings of the reflec-

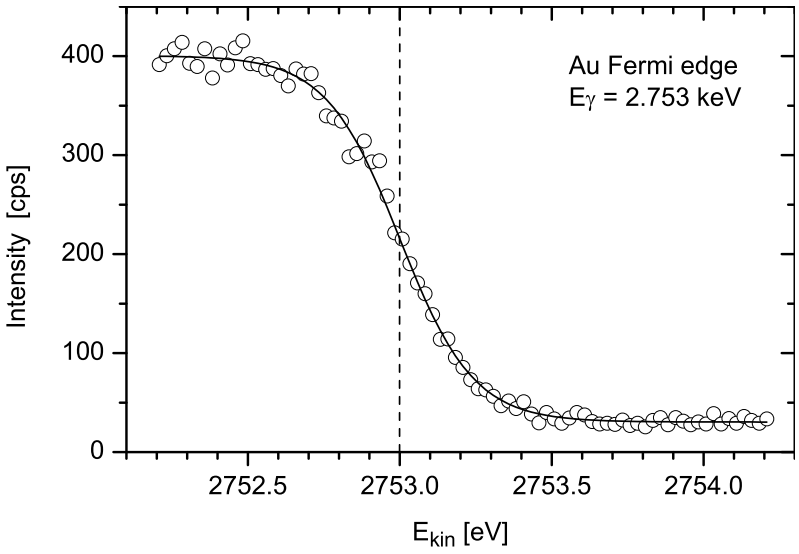

Figure 7.3: XPS spectrum of the Fermi edge of gold. The data were taken at room temperature with 11.75 eV pass energy for the PHI electron analyser. The curve was fitted by a Fermi function of $4kT = 102$ meV width convolved by a Gaussian function of 435 meV FWHM width, which represents the instrumental resolution. Sampling time: 2.5 s/data point. (The nonzero intensity beyond the Fermi edge resulted from photoexcitation by higher harmonics.)

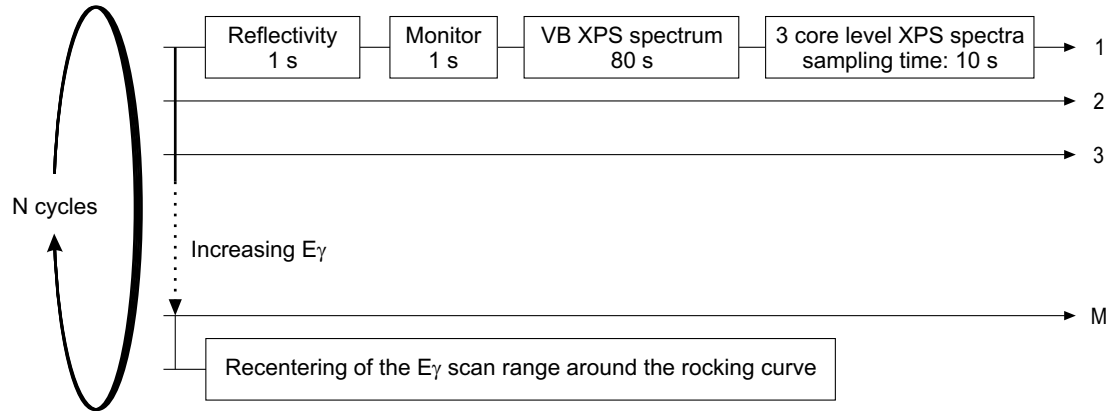

Figure 7.4: XSW data acquisition sequence. At each of the $M = 11$ photon energies, recordings of the reflectivity and the monitor values were followed by an XPS multiple range scan covering the valence band and three core level spectra. $N = 33$ cycles were recorded for the $SrTiO_3(111)$ and $N = 62$ cycles for the $SrTiO_3(112)$ reflection. For each electronic level, the N recorded spectra were aligned in energy (the valence band spectra relative to core level positions) and added together.

tivity and the core level XPS spectra. The residual drift was removed by correcting the energy alignment of core level XSW profiles and rocking curves to that of the second core level data set, which was not affected by drift.

A survey spectrum of the shallow core levels and the valence band of $SrTiO_3$ is shown in Fig. 7.5. The position of the upper edge of the valence band at 3.2 eV binding energy agrees well with the value reported by Chambers *et al.* [139]. The position of the Fermi level of the crystal bulk is at the top of the band gap just below the lower edge of the (empty) conduction band. The spectral feature at about 20 eV binding energy exhibits two shoulders and could be well described as a superposition of two sharp spin-orbit split Sr 4*p* level peaks and a broad O 2*s* level peak. But the large width of 5–6 eV rather indicates that these levels broaden into semi-core bands: The Sr 4*p* and O 2*s* semi-core orbitals mix to a small extent due to their very similar binding energies. This interpretation is supported by the band structure calculations in section 7.6. The Ti 3*p* and Sr 4*s* states also form a narrow band. The investigations of our study focus on the band structure next to the Fermi level.

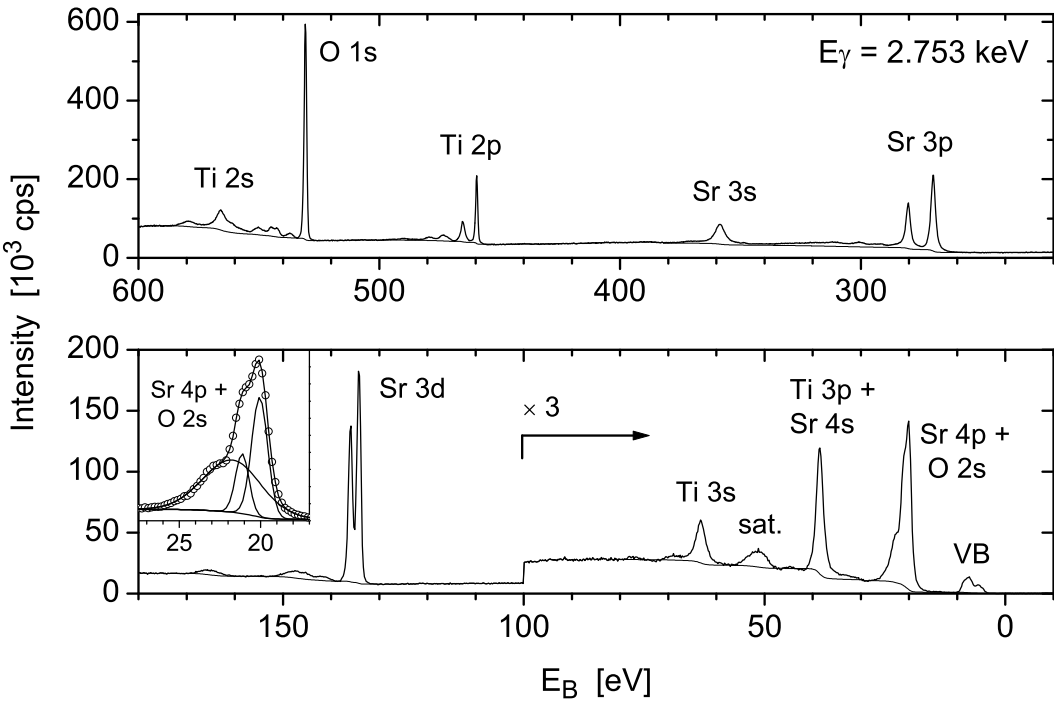

Figure 7.5: XPS survey spectrum of shallow core levels and the valence band of $SrTiO_3$. The spectral feature around 20 eV binding energy is shown in the inset on an expanded scale. The satellite structure at ∼50 eV binding energy is a Ti 3*p* loss peak.

The $SrTiO_3$(111) and $SrTiO_3$(112) reflections were selected for the task of a site-specific analysis of the valence band. The corresponding diffraction planes with respect to the $SrTiO_3$ perovskite structure are indicated in Fig. 7.6. These two reflections were chosen in order to identify the individual valence contributions originating from the strontium, titanium and oxygen site. Each lattice site in the perovskite unit cell is occupied by exclusively one element, and no element occupies more than one lattice site;

the terms "site-specific" and "element-specific" are synonymous. The lattice sites in the unit cell populated by oxygen atoms are assumed to be equivalent by symmetry; the local valence densities of states at the oxygen sites are identical under this assumption. Possible influence of broken crystal symmetry due to surface relaxation in the sampled volume on the XPS spectra is not taken into consideration. The contribution to the valence band coming from titanium can be identified by means of the (111) reflection, and the oxygen contribution can be identified from the (112) reflection. The strontium contribution can be retrieved by combining the results from the two measurements in (111) and (112) reflection. For determining the strontium contribution directly, the (102) reflection could have in principle been employed. But this reflection is of limited use only, because the comparatively weak reflectivity leads to a reduced XSW modulation: A low modulation contrast between different valence band contributions will result in a large margin of error for the analysis.

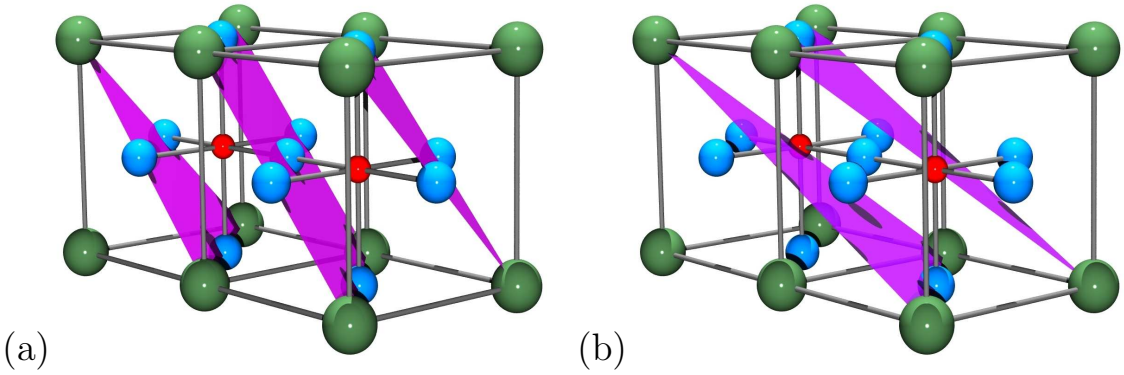

Figure 7.6: Schematic diagram of the $SrTiO_3(111)$ and the $SrTiO_3(112)$ reflections. The planes drawn represent the X-ray diffraction planes. (a) In the (111) reflection, the titanium atom at the centre of the unit cell is separated from the strontium (corners) and the three oxygen (face-centered) atoms by half a diffraction plane spacing d_{111} in [111]-direction. (b) In the (112) reflection, one strontium, one titanium and one oxygen atom lie on the diffraction planes, while two oxygen atoms lie midway inbetween.

The titanium contribution to the valence XPS yield can be identified in the (111) reflection because the coherent position of titanium $P_{\mathrm{Ti}}^{111} = 0.5$ (for the ideal crystal lattice) differs from the coherent positions of strontium and oxygen $P_{\mathrm{Sr}}^{111} = P_{\mathrm{O}}^{111} = 0$. Under the assumption that the dipole approximation applies, i.e., the photoelectron is emitted from the centre of the atom, the fractional valence yield that is preferentially excited when the maxima of the standing wavefield are located midway between the diffraction planes must originate from titanium. The yield preferentially excited at the diffraction planes must come from strontium and oxygen. The strontium and oxygen contributions, with coherent fractions $F_{\mathrm{Sr}}^{111} = F_{\mathrm{O}}^{111} = 1$ for the ideal bulk structure, will undergo very similar XSW modulations and cannot be separated in the (111) reflection. By means of the (112) reflection the contribution to the valence yield coming from oxygen can be identified. The oxygen is characterized by a coherent position $P_{\mathrm{O}}^{112} = 0.5$, while for strontium and titanium $P_{\mathrm{Sr}}^{112} = P_{\mathrm{Ti}}^{112} = 0$. Two of the oxygen atoms are separated by half a diffraction plane spacing such that their yield

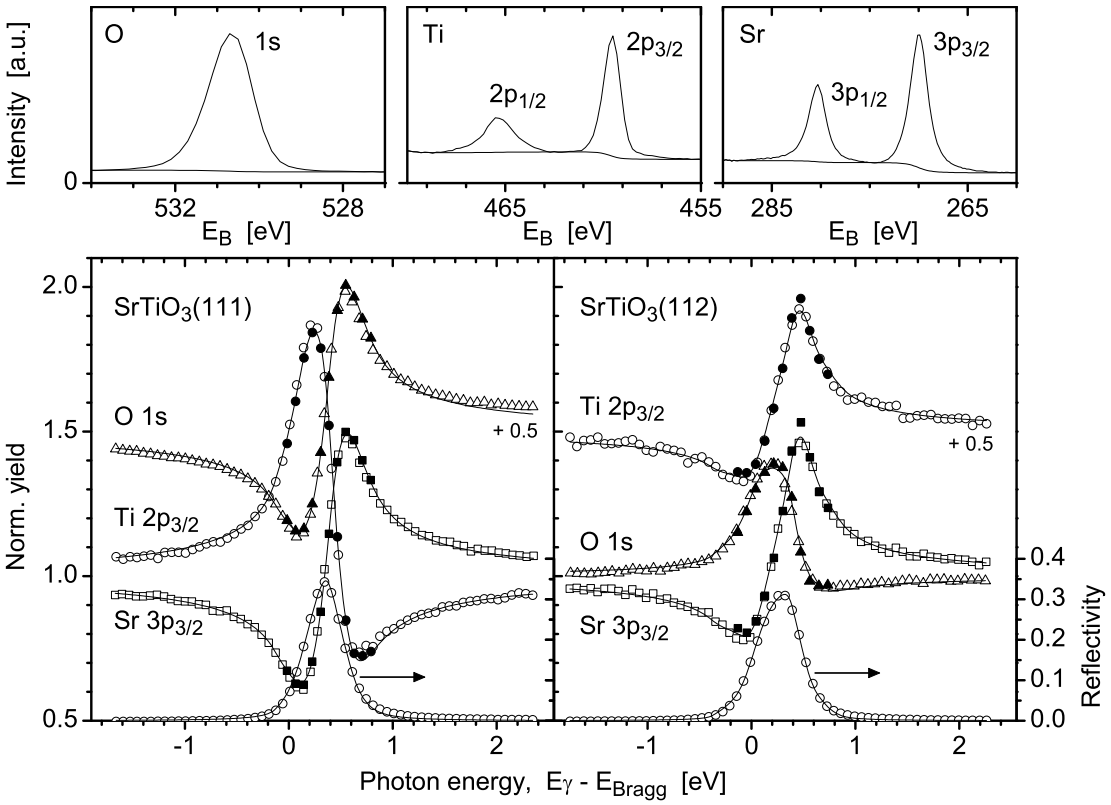

Figure 7.7: Core level XPS spectra and XSW yield for $SrTiO_3$. The core level XSW profiles recorded in parallel with the VB spectra (data set 1; full symbols) and the XSW profiles recorded independently (data set 2; open symbols) are congruent within the error bar. The lines represent the fittings to the data set 2. The yield is normalised to off-Bragg yield, and the profiles for the O 1s and Ti 2p levels were offset by 0.5 for clarity.

modulations cancel, and $F_{\mathrm{O}}^{112} = 1/3$. The reduction in XSW modulation contrast leads to an increased margin of error for the oxygen valence yield contribution.

Information about the modulation amplitude for the site-specific XSW valence yield contributions, which can be quantified in terms of coherent fractions, is not accessible by experiment directly. This information is provided by the XSW yield of the O 1s, Ti 2$p_{3/2}$ and Sr 3$p_{3/2}$ core levels presented in Fig. 7.7. Fitting the dipole expression for the XSW modulation given by Eq. 3.21 to the data yields the coherent positions and fractions listed in Tab. 7.1: The experimental coherent positions P^H for the second core level data set and the values for the ideal crystal lattice $P^{H\,theo}$ coincide within the error bar. For each reflection, the largest possible XSW phase contrast of 0.5 in coherent position is reflected by the practically inverted XSW profile line shapes. The coherent fractions F^H for the two core level data sets agree within the experimental error. If the dipole approximation could be applied, the XSW modulations of valence and core level signals were identical; all regions of an XPS spectrum emitted from one element underwent the same XSW modulation in this case. Values $F^H > 1$ indicate, however, that the dipole approximation is not fully valid here: Table B.3 on

Reflection	Element	Theoret. values for ideal bulk		Core level data set 2		Core level data set 1	Scaled data set 1
		$P^{H\,theo}$	$F^{H\,theo}$	P^H	F^H	F^H	$F^{H\,scaled}$
$SrTiO_3(111)$	Sr	0	1	0.01	0.99	1.00	1.00
	Ti	0.50	1	0.51	1.03	1.01	1.18
	O	0	1	0.01	0.95	0.95	0.95
$SrTiO_3(112)$	Sr	0	1	0.01	0.91	0.93	0.93
	Ti	0	1	0.00	0.76	0.77	0.90
	O	0.50	0.33	0.50	0.33	0.33	0.33

Table 7.1: Coherent positions and fractions determined from the $SrTiO_3$ core level data shown in Fig. 7.7. The theoretical values $P^{H\,theo}$ and $F^{H\,theo}$ are given for the ideal $SrTiO_3$ bulk structure, approximating the Debye-Waller-factor by unity. Fitting the second set of core level XSW data yielded the values P^H and F^H. Fitting the first set of core level XSW data with P^H as a fixed parameter resulted in the coherent fractions F^H. Scaling F^H to shallow electronic levels as described in appendix C resulted in $F^{H\,scaled}$.

page 164 gives coherent fractions for different electronic levels. To take the influence of quadrupole effects into consideration, the coherent fractions F^H are scaled to shallow electronic levels, as described in appendix C. The resulting values $F^{H\,scaled}$ are used to characterize the XSW modulation amplitudes of the site-specific valence yield contributions.

The XSW data for the valence band taken in the $SrTiO_3(111)$ and (112) reflections are shown in Figs. 7.8 and 7.9. The 11 XPS spectra of the valence band depicted in Figs. 7.8(a) and 7.9(a) were recorded under Bragg condition at 11 different photon energies, i.e., for 11 different standing wave positions with respect to the crystal lattice. The variation in line shape observed for the spectra becomes more clearly visible in the two-dimensional representation in Figs. 7.8(b) and 7.9(b). As the maxima of the wavefield traverse half the diffraction plane spacing and move over the distribution of atoms in the unit cell, the atoms experience a variation in wavefield intensity. Preferential excitation of an atom at a specific lattice site, when the wavefield passes, enhances those spectral features in the valence band that are characteristic of the yield contribution coming from this lattice site. The line shape of the VB spectrum $Y(E_B, E_\gamma)$ varies, as the XSW is moved, according to the changing linear combination

$$Y(E_B, E_\gamma) = \sum_{s\,=\,\mathrm{Sr,\,Ti,\,O_3}} I_s(E_\gamma) Y_s(E_B) \tag{7.1}$$

of yield contributions $Y_s(E_B)$ coming from the individual lattice sites s, which are populated by Sr, Ti and O_3. The yield contributions from the three oxygen sites in the unit cell, which are assumed to be equivalent by symmetry, are identical and have been combined in one single component. $Y_s(E_B)$ denotes the photoemission yield contribution to the valence band off of the Bragg condition for unity field intensity. Within the small energy range of a Bragg reflection, these contributions can be considered to be independent of photon energy. Each contribution $Y_s(E_B)$ undergoes a modulation,

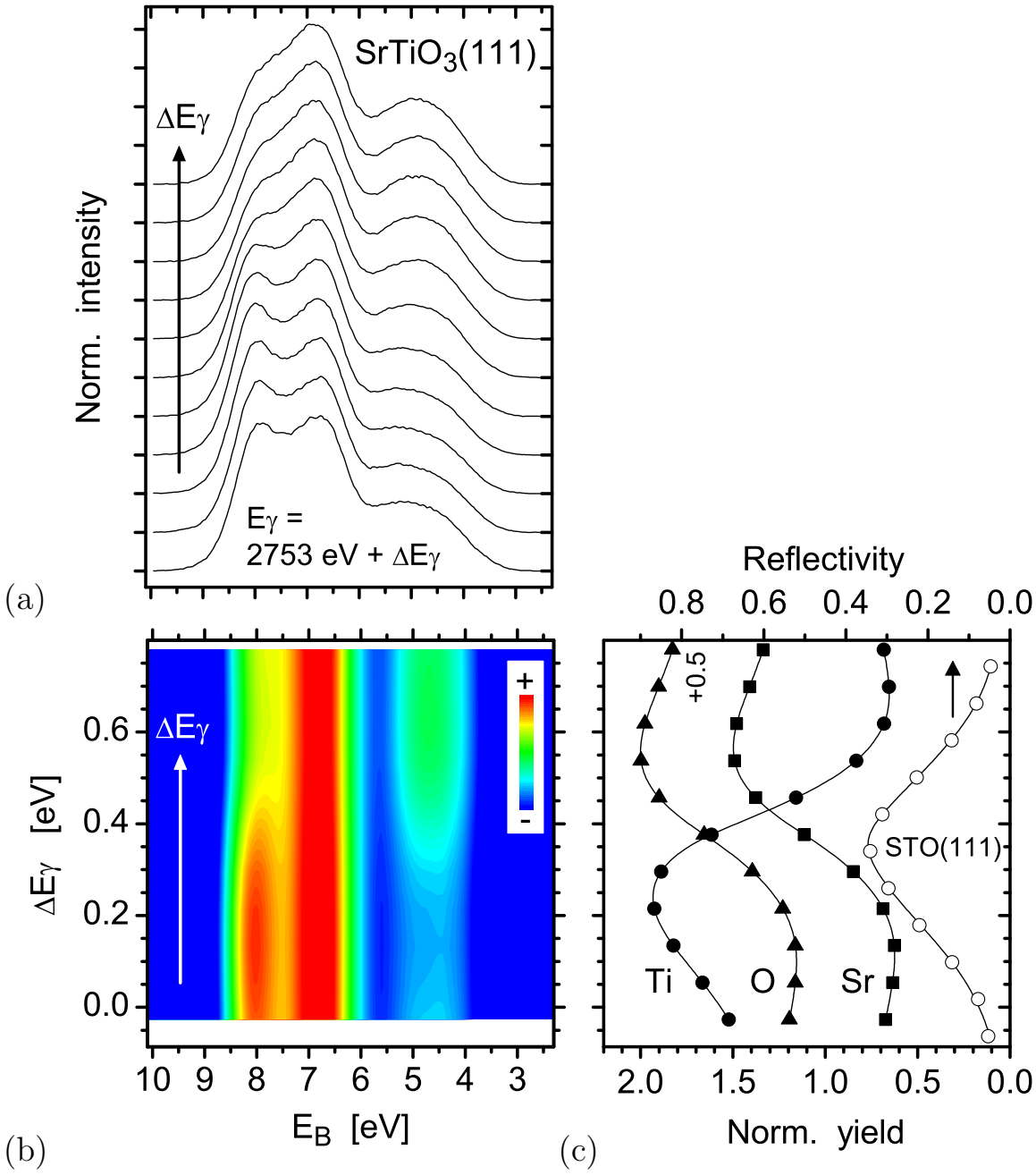

Figure 7.8: Valence band XSW data for the $SrTiO_3(111)$ reflection. (a) Changes in the line shape of the $SrTiO_3$ valence band XPS spectrum (normalized to area and offset) under XSW conditions when traversing the Bragg reflection by increasing the photon energy E_γ in steps of 80 meV. A single spectrum has $\sim 1.4\times10^4$ counts in the peak for normalised field intensity. (b) The 2D-representation of the same data shown in (a) elucidates the changes in line shape, which are largest at 4–5 eV and around 8 eV binding energy. (c) The core level yield XSW profiles for Sr, Ti and O represent the modulation of the site-specific contributions to the valence yield. The XSW profile for oxygen was offset by 0.5 for clarity.

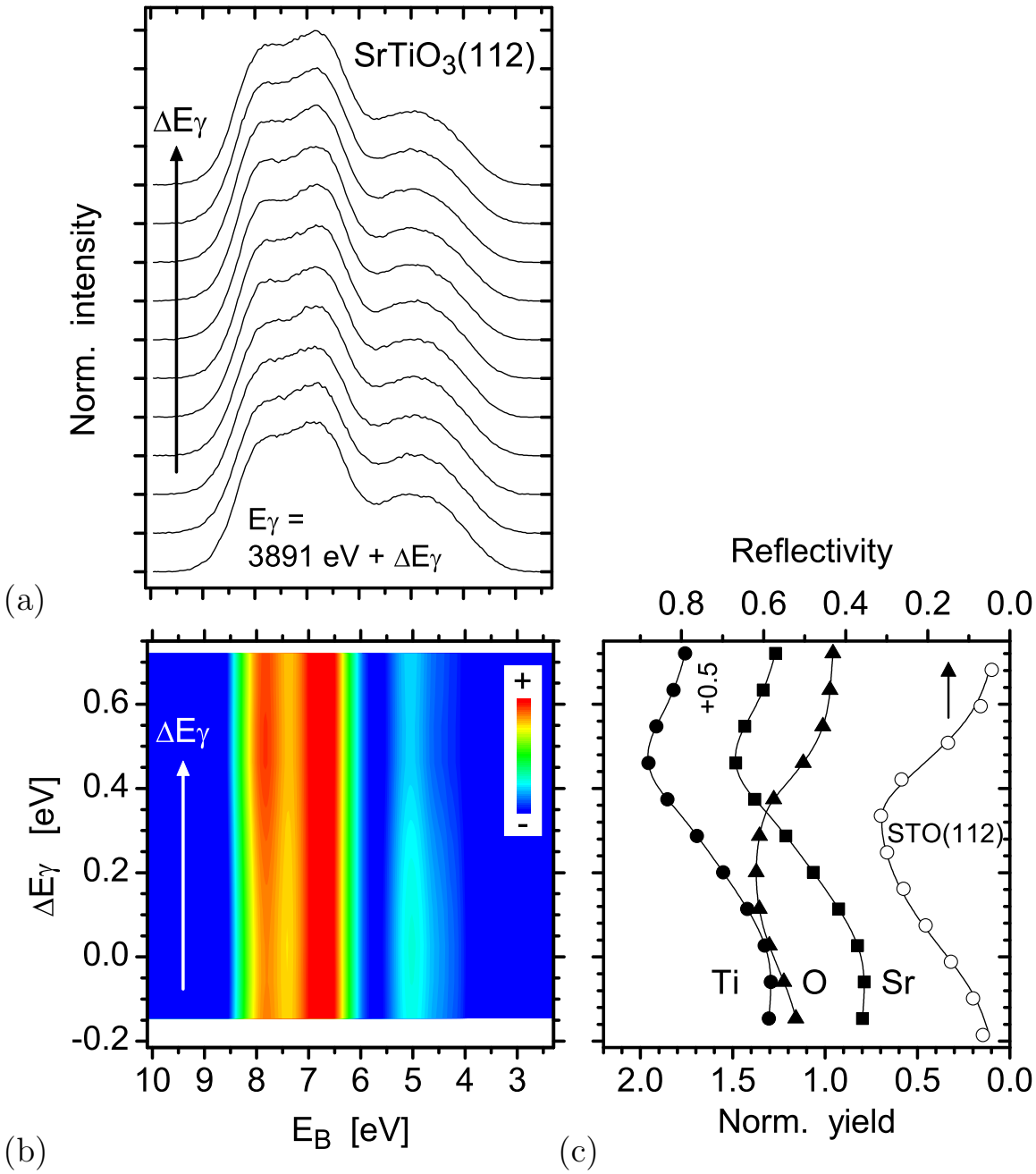

Figure 7.9: Valence band XSW data for the $SrTiO_3(112)$ reflection. The data are presented as in Fig. 7.8. (a) Changes in the line shape of the valence band spectrum recorded under XSW conditions with photon energy increments of 100 meV. The good intensity of $\sim 1.1 \times 10^4$ counts in the peak of a single VB spectrum under off-Bragg condition allows the line shapes to be separated. (b) The two-dimensional representation of the VB data reveals that the largest modulations in VB line shape occur at 7–8 eV and around 5 eV binding energy. (c) The core level yield XSW profiles for Sr, Ti and O. The XSW profile for titanium was offset by 0.5 for ease of viewing.

which in the dipole approximation is identical to the modulation of the core level yield $I_s(E_\gamma)$ of the corresponding element, as shown in Figs. 7.8(c) and 7.9(c).

The set of valence band spectra taken for the (111) reflection exhibits a much more pronounced modulation in line shape than the one measured for the (112) reflection. The magnitude of the VB modulation does not only depend on the modulation contrast between the individual yield contributions but also on their intensity ratios: In the (112) reflection, the dominating contributions from strontium and titanium are in phase, as Fig. 7.9(c) shows. The antiphase signal from the light element oxygen is weak and does not produce significant VB modulation. The reduced coherent fraction for oxygen $F_{\mathrm{O}}^{112} = 0.33$ lowers the line shape modulation additionally. In the (111) reflection, the strong strontium and titanium signals are antiphase with comparable intensity and this leads to a strong modulation in the valence band line shape.

Some of the spectral features of the valence band can be associated with their elemental origin already by comparing the modulations for the (111) reflection in Figs. 7.8(b) and (c). The valence region around 8 eV binding energy, where a loss in intensity occurs as the photon energy is increased, can be related to the only yield contribution that decreases in parallel, which is the contribution from the titanium. At the same time, the XPS intensity of strontium and oxygen increases, and this increase coincides with the broad valence band feature around 4–5 eV binding energy. For the (112) reflection in Figs. 7.9(b) and (c), the enhancement in the valence intensity at 7–8 eV binding energy can be ascribed to the increasing titanium and strontium yield contribution. The oxygen contribution decreases at the same time, and this produces the intensity loss in the valence band around 5 eV binding energy.

7.5 Site-Specific VB Decomposition

With the recordings of the modulated valence band spectra and the XSW intensity profiles of the site-specific valence contributions, which are known from core level signals, the site-specific partial yield spectra $Y_s(E_B)$ can be identified. No additional prior information is necessary except the experimental data presented in the previous section.

Each of the valence band spectra recorded under XSW conditions was described by Eq. 7.1 as a linear combination of the three contributions $Y_s(E_B)$. For each reflection, the 11 different linear combinations form an overdetermined system of equations

$$Y(E_B, E_{\gamma\ i}) = \sum_{s\,=\,\mathrm{Sr,\,Ti,\,O_3}} I_s(E_{\gamma\ i}) Y_s(E_B), \qquad i = 1, \ldots, 11. \tag{7.2}$$

A set of spectra $Y_s(E_B)$ that comes closest to solving the system was obtained for each reflection by least squares fitting using the algorithm from Press *et al.* [140]. The spectra are normalized to a homogeneous X-ray field of unity intensity, i.e., for the "one beam case". The entire XSW-specific information contained in the recorded data is exploited by this data processing step; the resulting yield contributions $Y_s(E_B)$ no longer contain any standing wave information. Each system of equations allowed separating the valence band yield merely into two instead of three yield contributions:

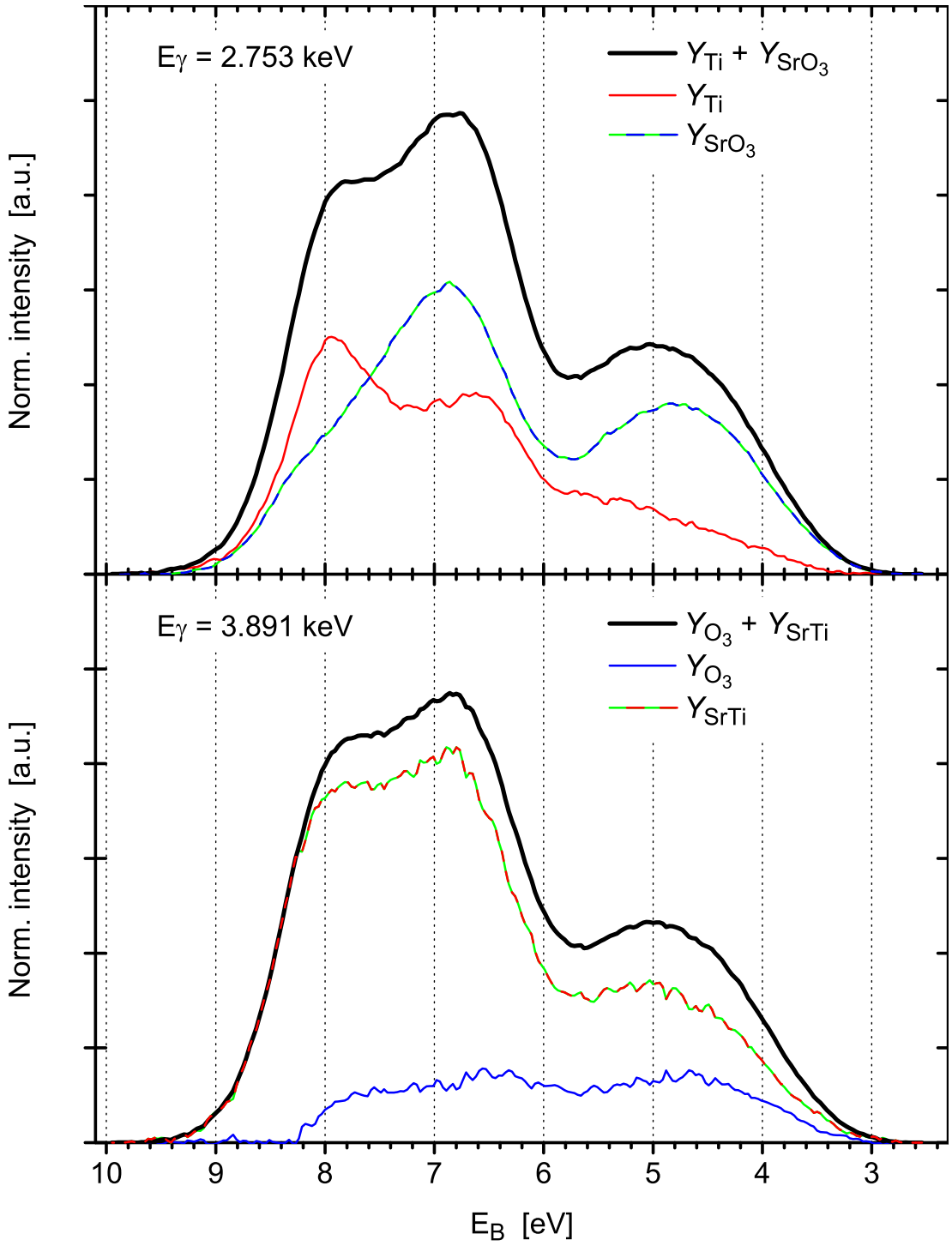

Figure 7.10: XSW analysis of the $SrTiO_3$ valence electronic structure. The partial intensity contributions to the valence band XPS spectrum originating from Ti, SrO_3, SrTi and O_3 were determined by utilizing the XSW information contained in the data, which were taken for the (111) reflection at 2.753 keV and for the (112) reflection at 3.891 keV photon energy. The partial spectra were obtained for a spatially homogeneous X-ray field of unity intensity at the Bragg photon energies.

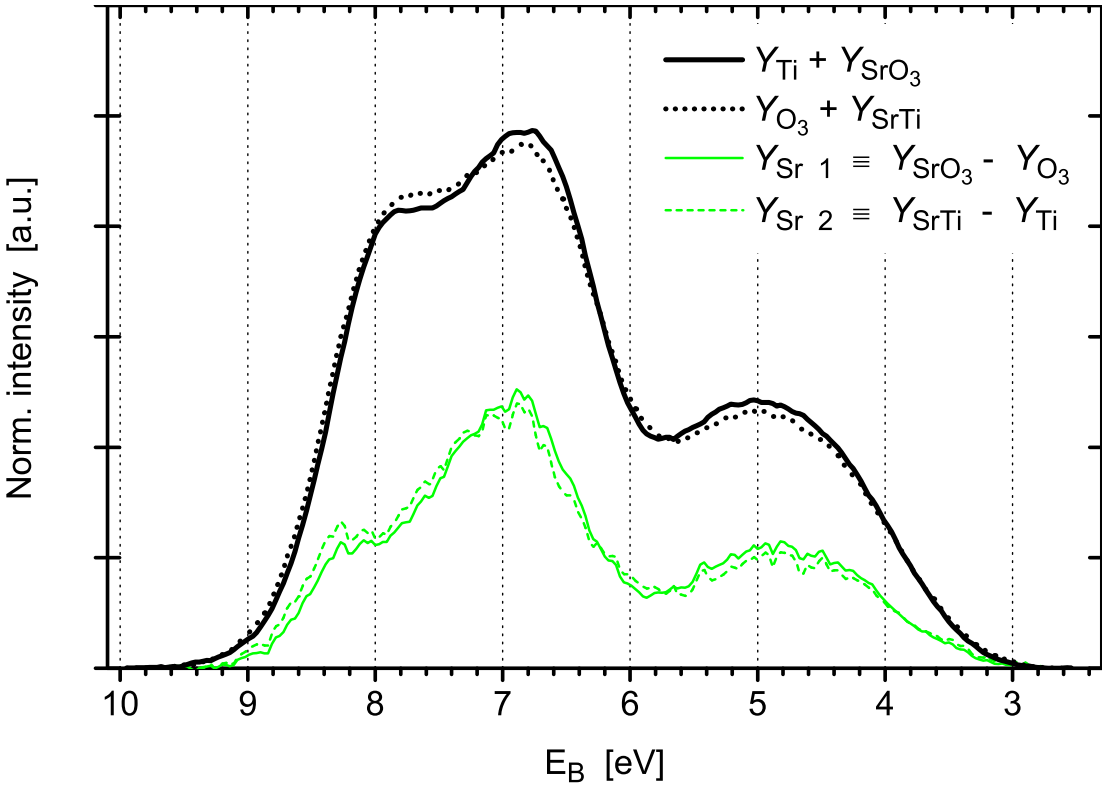

Figure 7.11: XSW analysis of the $SrTiO_3$ valence electronic structure. Approximate solutions for the strontium contribution to the valence band were determined by combining the analysis shown in Fig. 7.10. The valence band spectra were nomalised to area.

The Sr and O_3 components in the (111) reflection and the Sr and Ti components in the (112) reflection did not reveal sufficient modulation contrast, as evident from Figs. 7.8(c) and 7.9(c), and could not be separated in a reliable way. For this reason "mixed" components $Y_{SrO_3}(E_B) \equiv Y_{Sr}(E_B) + Y_{O_3}(E_B)$ for the (111) reflection and $Y_{SrTi}(E_B) \equiv Y_{Sr}(E_B) + Y_{Ti}(E_B)$ for the (112) reflection were obtained. By explicitly including the individual yield components from all three sites in the system of equations, all the slight differences between the site-specific coherent positions and fractions listed in Tab. 7.1 could be taken into consideration. The Ti and SrO_3 contributions separated by the (111) reflection and the SrTi and O_3 contributions separated by the (112) reflection are shown in Fig. 7.10. Adding together each pair of partial contributions resulted in the $SrTiO_3$ valence band spectrum for normalized beam intensity. The noise levels are representative of the statistical errors. The systematic errors, in particular for the oxygen component between 8 and 9 eV binding energy, are larger than the statistical errors and are discussed later.

Elemental valence components were obtained only for titanium and oxygen, $Y_{Ti}(E_B)$ and $Y_{O_3}(E_B)$, but not for strontium. Approximate solutions for strontium are found by combining the results from the two reflections: Fig. 7.11 shows two alternatives for the strontium component, $Y_{Sr\ 1}(E_B) \equiv Y_{SrO_3}(E_B) - Y_{O_3}(E_B)$ and $Y_{Sr\ 2}(E_B) \equiv$

$Y_{\mathrm{SrTi}}(E_B) - Y_{\mathrm{Ti}}(E_B)$. These solutions are approximate because combining spectra taken at different photon energies ignores the energy dependence of photoionisation cross sections: The component $Y_{\mathrm{Ti}}(E_B)$ at 2.753 keV is not congruent and therefore does not exactly cancel out with the titanium contribution in $Y_{\mathrm{SrTi}}(E_B)$ at 3.891 keV when being subtracted. Likewise, the component $Y_{\mathrm{O_3}}(E_B)$ at 3.891 keV and the oxygen contribution in $Y_{\mathrm{SrO_3}}(E_B)$ at 2.753 keV disagree. The spectrum $Y_{\mathrm{Sr\ 1}}(E_B)$ represents a better approximation for the true strontium component at 2.753 keV than the spectrum $Y_{\mathrm{Sr\ 2}}(E_B)$ at 3.891 keV does. This is because the discrepancy between the two subtracted titanium yields is larger than between the small oxygen yields. The similarity in line shape observed for $Y_{\mathrm{Sr\ 1}}(E_B)$ and $Y_{\mathrm{Sr\ 2}}(E_B)$ is fortuitous. The true strontium yield is underestimated by both approximate solutions. This will become clearly visible from the general survey of all spectra in Fig. 7.19.

An accurate solution for the strontium component can be reconstructed from the fitting results presented in the following section, where the data taken at different photon energies are combined in an adequate way. The implications of the site-specific valence band analysis will be discussed in section 7.7.

The $SrTiO_3$ valence band spectra that resulted from the XSW data were cross-checked by comparison to spectra recorded in XPS survey scans. Fig. 7.12 shows a valence band spectrum reconstructed by adding the partial valence yield components $Y_{\mathrm{Ti}}(E_B)$ and $Y_{\mathrm{SrO_3}}(E_B)$. The spectrum agrees well in line shape with a rapidly recorded XPS spectrum. The slight discrepancy between the curves results from a small XSW effect for the XPS survey scan, which was not recorded away from the Bragg range. The agreement in energy width confirms the proper energy alignment when adding together the raw spectra, which were collected during several hours in many XSW scans by the sequence shown in Fig. 7.4 on page 91.

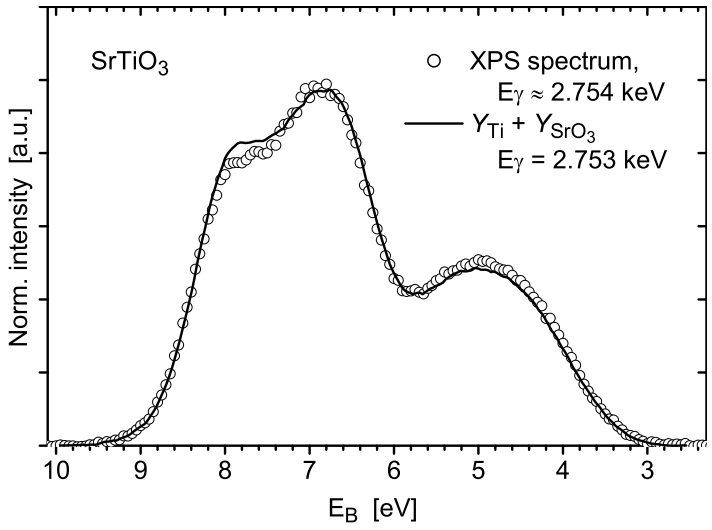

Figure 7.12: Comparison of $SrTiO_3$ valence band XPS spectra. The sum of the components $Y_{\mathrm{Ti}}(E_B) + Y_{\mathrm{SrO_3}}(E_B)$ taken from Fig. 7.10 represents the valence band spectrum for unity X-ray intensity at the Bragg photon energy. The spectra were normalized to area.

7.6 Angular-momentum Resolved VB Analysis

The angular-momentum resolved analysis of the site-specific valence yield components was achieved by comparing the results of the quantitative XSW analysis to the results of density functional theory (DFT) calculations. Comparison of data with theory gives also the unique opportunity to directly and accurately determine photoionisation cross sections for delocalized valence states. Comparing the resulting experimental cross sections for the solid with tabulated values, which are calculated for the free atom, is instructive for understanding how the solid state formation influences the photoionisation cross section.

Ab Initio Calculations of the Valence Electronic Structure

Densities of angular-momentum dependent site-specific valence states for bulk $SrTiO_3$ were calculated by F. Bottin [141] by state-of-the-art *ab initio* density functional theory (DFT) calculations in the local density approximation (LDA). Details about these calculations are repeated in appendix D for the interested reader. In the following, some general features of DFT are described, and we will focus on the results of the calculations.

DFT [142] in the Kohn-Sham formulation [143] is a very successful mathematical approach for describing the electronic ground state for a large class of material systems. In theoretical physics, an interacting system of N electrons is described by a many-particle wave function (Hartree-Fock), which is a function of $3N$ variables and, hence, can be very difficult to handle in computational calculations. The basic idea of DFT is to use the electron density as a fundamental quantity, which is a function of 3 spatial variables only. The Kohn-Sham equations basically represent single particle Schrödinger-like equations, where the effective potential includes all interactions with the other electrons. The application of DFT requires some approximations for the exchange-correlation potential to be made, which includes the mean many-body Coulomb repulsion and the effects resulting from the exclusion principle. The most frequently used approximation for DFT is the LDA approximation. The LDA approximation locally replaces the exchange-correlation interaction for an electron gas of inhomogeneous density by the (known) interaction for an electron gas of the local (homogeneous) density.

DFT calculations in the LDA approximation reveal inaccuracies, which mainly result from ignoring many-body interaction. The binding energy as well as the energy width of electronic bands are generally not exactly reproduced in LDA calculations. The width of the valence band as well as the band gap around the Fermi edge are often underestimated. In the *GW* approximation, where many-body effects are taken into consideration, the binding energy of valence lpDOS contributions can be corrected both towards higher or lower values, depending on the originating lattice site and angular momentum. For $SrTiO_3$, *GW* corrections have not much altered the LDA results; the valence band of $SrTiO_3$ is rigidly shifted towards higher binding energy away from the Fermi edge [144].

Site-specific densities of valence states (pDOS) were computed for strontium, tita-

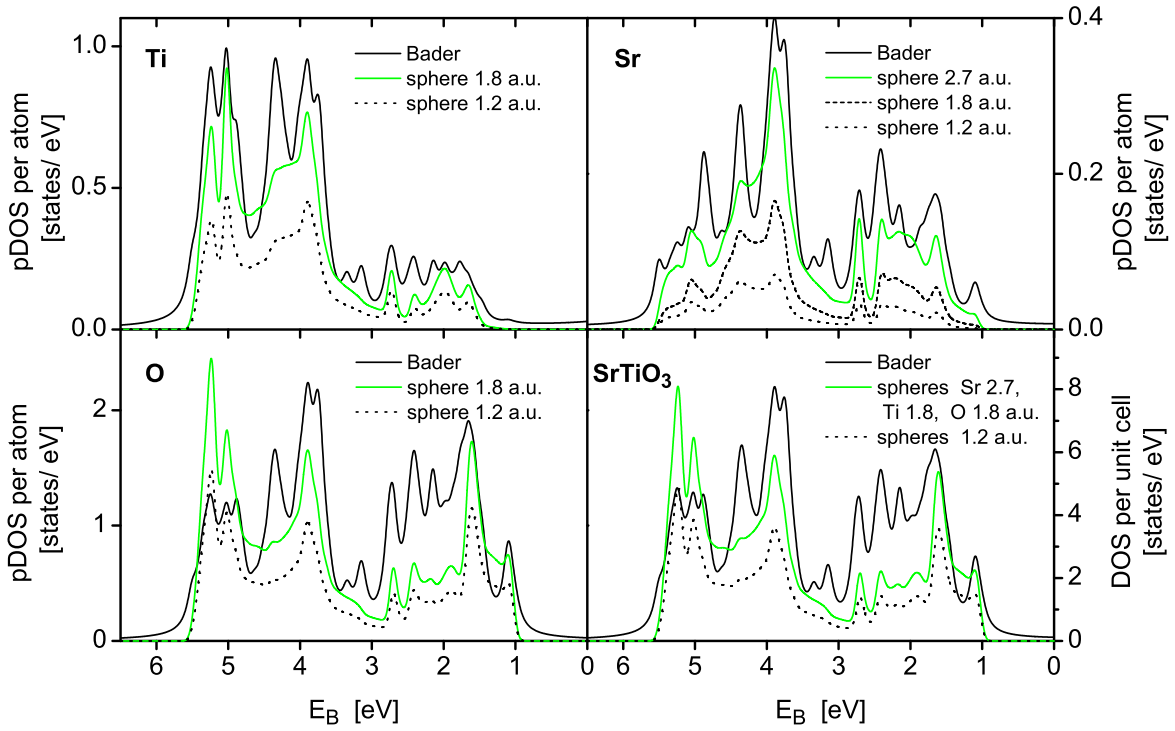

Figure 7.13: Comparison of pDOS spectra for $SrTiO_3$ calculated by projection within different volumes. The wave functions were projected within Bader basins and spheres of 2.7, 1.8, and 1.2 a.u. radius. The origin of the energy scale was arbitrarily set to the middle of the band gap. Van Hove singularities were removed by convolution with a Gaussian function of 100 meV FWHM.

nium, and oxygen by projecting calculated plane wave functions within different spatial regions in unit cell. A comparison of site-specific pDOS spectra calculated for a variety of different projection volumes is shown in Fig. 7.13: The projections were performed within Bader atomic basins, spheres of 2.7 (Sr) and 1.8 a.u. (Ti, O) radius, which are the largest spheres that can fit into the Bader basins, and within small spheres of 1.2 a.u. radius. The line shapes of the spectra calculated by projection within spheres are weakly dependent on the cutoff radius $\mathbf{r}_c$; the spectra basically differ by a scaling factor. The spectra calculated for the Bader basins and the largest spheres show good qualitative agreement in the cases of strontium and titanium but reveal some differences in the case of oxygen: Since the sphere of 1.8 a.u. radius partially extends over the Bader basin, spurious charge (occupied p states) from titanium around a binding energy of 5 eV is collected (this is even still the case for 1.2 a.u. radius). In contrast, a large amount of space charge with binding energies between 1.5 and 3 eV outside the sphere remains unconsidered.

Angular-momentum dependent site-specific densities of valence states (lpDOS) were computed by projecting calculated spherical wave functions within spheres. A comparison of lpDOS spectra calculated by projection within spheres of different sizes is shown in Fig. 7.14. The spectral line shape hardly changes with cutoff radius $\mathbf{r}_c$. Since the

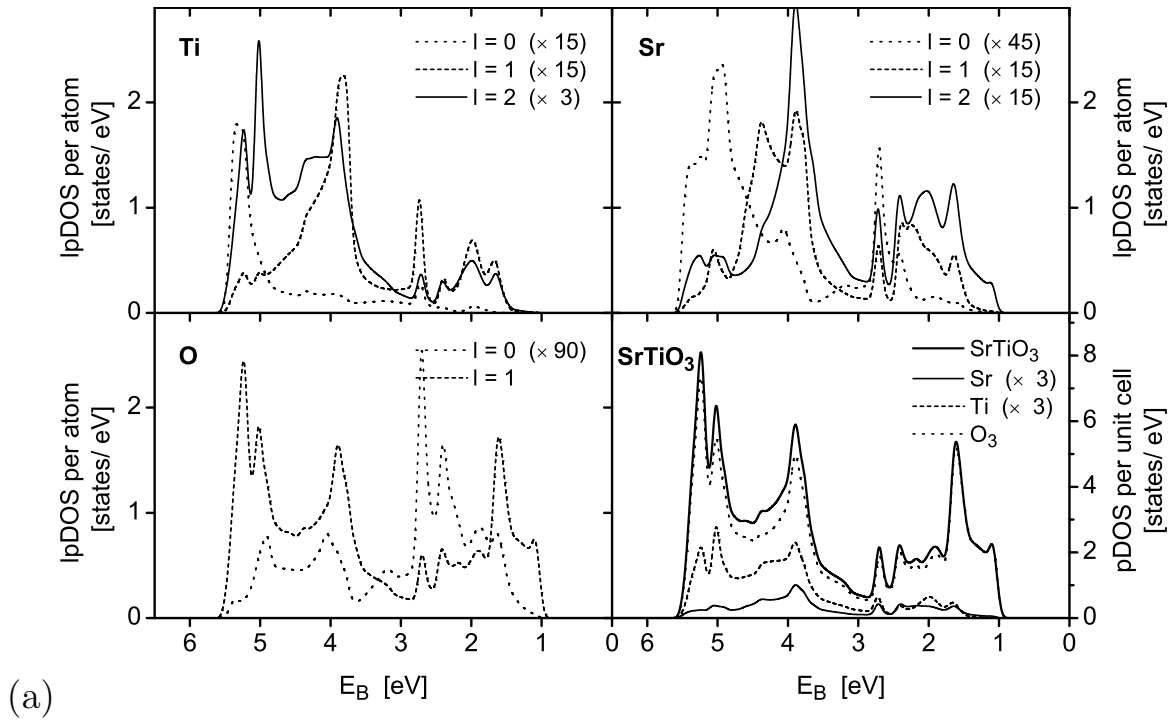

(a)

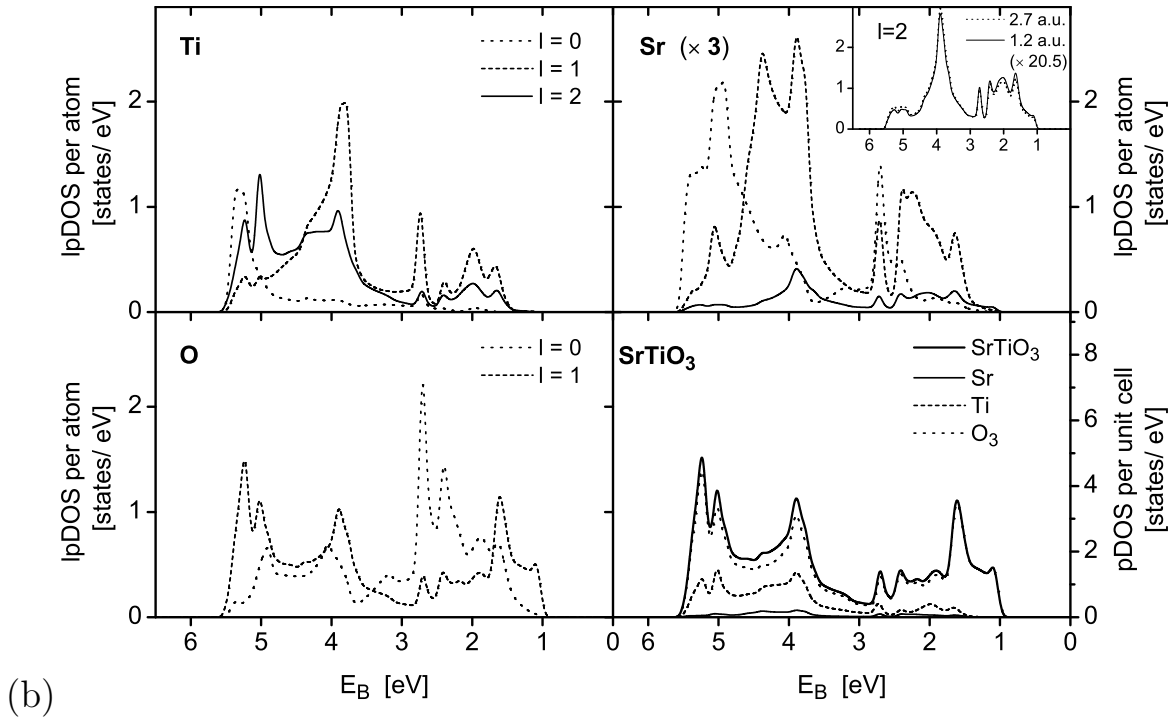

(b)

Figure 7.14: Comparison of lpDOS spectra for $SrTiO_3$ calculated by projection within different volumes. The lpDOS were integrated within spheres for Sr/Ti/O of (a) 2.7/1.8/1.8 a.u. and (b) 1.2/1.2/1.2 a.u. radius. The graphs were scaled by the given factors. The inset compares line shapes for Sr *d* lpDOS. All curves were convolved with a Gaussian function of 100 meV FWHM. The origin of the energy scale was set to the middle of the band gap.

radial distributions of s, p and d states around an atomic core are distinct, the number ratio between the angular-momentum dependent states inside the sphere exhibits a dependence on the cutoff radius. This is particularly true for the strontium, where the number of integrated valence d states enlarges by a factor $\sim$20 when increasing the sphere radius from 1.2 to 2.7 a.u., while their spectral distibution does not change. The very small number of d states at the oxygen site, five times less than s states, confirms that the radius of 1.8 a.u. is small enough to exclude Ti d states.

$SrTiO_3$ is a $3d$ metal oxide with a valence band mainly composed of p states at the oxygen site with some admixture of mainly Ti d states. The number of valence f states is negligible. The DOS spectra calculated by DFT have the usual margins of error, which result from the various approximations for the pseudopotentials and for summing up the wavefunctions in the vicinity of the cores.

Comparison of Data and Calculations

X-ray photoelectron spectroscopy does not reveal the density of occupied electronic states directly. The measured XPS intensity is rather proportional to the DOS weighted by the matrix elements for the electronic transition probability from a bound initial state to a plane wave final state far above the vacuum level, where the density of final states can be assumed to be constant. Electronic band structures, like the valence band, contain states of different angular momenta, which appear in the photoemission spectrum with different strength, because the transition matrix element depends on the angular momentum of the initial state. The partial valence yield contribution from the lattice site $s = \mathrm{Ti}, \mathrm{Sr}, \mathrm{O}_3$ is represented by a linear combination

$$Y_s(E_B, E_\gamma) = \sum_l Y_{s,l}(E_B, E_\gamma) \propto \sum_l C_{s,l}(E_\gamma)\sigma_{s,l}(E_\gamma)\rho_{s,l}(E_B) \tag{7.3}$$

of angular-momentum l resolved partial density of states $\rho_{s,l}(E_B)$. These lpDOS components are weighted by the according angular-momentum dependent total photoionisation cross sections per electron $\sigma_{s,l}(E_\gamma)$. The cross sections are normalized to the number of states. The factors $C_{s,l}(E_\gamma) = 1 + \beta_{s,l}(E_\gamma)$ take into consideration the dipole emission characteristics for the chosen XPS experimental geometry. The photon energy dependence is explicitly given to emphasize that the quantities concerned take on considerably different values at different Bragg reflections. In contrast, all photon energy dependences within an XSW scan range are negligible.

The lpDOS components $\rho_{s,l}(E_B)$ form a proper basis for the linear combination in Eq. 7.3, because the (nondegenerate) states in each component do not have significantly different photoionisation cross sections. The states in each component can share a common weighting factor $\sigma_{s,l}(E_\gamma)$, because the influence of spin-orbit interaction on the photoionisation cross section can be neglected: In a full relativistic treatment of the photoeffect, transition matrix elements depend on the total angular momentum quantum number j of the initial state. Spin-orbit coupling, the largest relativistic effect after kinetic energy corrections, leads to the fine structure for core levels, and modifies the transition matrix elements for the spin-orbit-split states. This is already evident from tabulated atomic cross sections, where the ratios do not represent the

occupancy of the degenerate doublets. The discrepancy in cross section is only small, typically $\leq$5% for strontium, titanium and oxygen core levels in the energy range of a few keV [145, 146]. Since valence states, even if exposed to the Madelung potential of an ionic solid, are better screened from the core potential than core states are, the magnetic field experienced by valence electrons and the resulting spin-orbit splitting is correspondingly smaller. This suggested that effects on the valence cross section resulting from spin-orbit interaction could be neglected. The lpDOS spectra calculated for unpolarised states are therefore suitable to form a basis in Eq. 7.3.

The lpDOS spectra were calculated as described in the previous section by projecting the spherical wave functions over angular momenta $l = 0, 1, 2$ for strontium and titanium and over $l = 0$ for the oxygen. The fraction of states with higher angular momenta, except oxygen p states, was negligible. The projected wave functions were integrated within spheres of 1.8 (titanium, oxygen) and 2.7 (strontium) a.u. radius around the atomic cores. The oxygen component with $l = 1$ was calculated by integrating the oxygen states within the Bader basin. The error from including the oxygen states with $l = 0$, a small fraction compared to the states with $l = 1$, within the Bader surface is insignificant.

The *a priori* unknown photoionisation cross sections for valence electrons can be determined in a direct way for each individual lattice site and angular momentum: The cross sections result as the scaling factors when fitting the theoretical lpDOS spectra to the four site-specific valence XPS spectra shown in Fig. 7.10. The cross sections are determined on an absolute scale; the yield from a core level with a tabulated photoionisation cross section served as an intra-atomic reference.

The data processing was performed by means of *MathCAD* [147] and *C* routines. The calculated lpDOS spectra were rescaled in binding energy, convolved and fitted to the photoemission spectra as described below. The data fitting made great demands on the robustness of the fitting algorithm, i.e., on its capability to converge towards a unique solution irrespective of the initial guess for the fitting parameters. Simple but robust grid search algorithms were employed for the fitting. In order to find the set of free parameters that best describes the data, one algorithm repeatedly cycles through an optimisation loop, varying the individual parameters one after another, until convergence is reached. This optimisation procedure is repeated on a stepwise refined parameter grid until the desired accuracy for the parameters is reached. An alternative, even more robust but also more time-consuming algorithm searches for the global minimum χ^2 on a chain of nested, gradually refined parameter subgrids.

The empirical linear rescaling of the energy axes of the lpDOS spectra was included in the data fitting procedure. DFT calculations generally do not exactly reproduce but commonly tend to underestimate the band gap as well as the energy width of the valence band. Owing to the various approximations in the DFT calculations, the energy scaling may differ for the different lattice sites and even for the angular momenta. For each element s, an expansion factor A_s and an offset B_s in binding energy were included in the set of fit parameters to transform the theoretical spectra by the assignment

$$\rho_{s,l}(E'_B) \rightarrow \rho_{s,l}(A_s E'_B + B_s) = \rho_{s,l}(E_B). \tag{7.4}$$

The area of the theoretical spectra, which represents the number of states, was kept

constant during the rescaling. Expanding the strontium and titanium lpDOS spectra by $A_{\mathrm{Sr}} = 1.14$ and $A_{\mathrm{Ti}} = 1.09$ and compressing the oxygen spectra by $A_{\mathrm{O}} = 0.96$ gave the best agreement with the data. The spectra for titanium and strontium were shifted by $B_{\mathrm{Sr}} = B_{\mathrm{Ti}} \approx 0.8$ eV and the oxygen spectra by $B_{\mathrm{O}} \approx 0.6$ eV towards higher binding energy. These values appear to be realistic as the band gap, with 2.1 eV underestimated by the calculations, is broadened towards the experimentally obtained value of about 3.2 eV [148]. An alternative comparison of data and calculations presented in appendix E is based on identically rescaled theoretical lpDOS spectra.

Convolution of the theoretical lpDOS spectra by a Gaussian function of 750 meV FWHM width appeared reasonable and resulted in a good agreement with the experimental data. The major contribution to the peak broadening of the order of 600 meV could most likely be ascribed to band bending in the surface region of the semiconducting $SrTiO_3$. Aiura *et al.* [149] mentioned band bending of 0.2 eV for an oxygen deficient $SrTiO_3$ crystal investigated by UPS. The radiation generated by a synchrotron, much more intense than from a laboratory source, causes a particularly large band bending effect that can limit the energy resolution of an XPS measurement, depending on the conductivity of the sample. The integral over the band bending profile actually yields an asymmetric response function for the convolution, but the asymmetry was neglected when a symmetric overall convolution function was chosen. The convolution further includes the instrumental resolution, which was measured to be 435 meV at 2.75 keV photon energy. The slight increase in instrumental resolution at 3.89 keV has little influence on the overall peak broadening.

The fitting of the four site-specific valence yield components, which were obtained by the XSW analysis, was carried out in three successive steps. Determining only a limited number of free parameters per step ensured physically sensible results with minimised error bars. In the first two steps, the elemental components $Y_{\mathrm{Ti}}(E_B)$ and $Y_{\mathrm{O_3}}(E_B)$ were fitted individually. The gained information was then utilized in the third step, when simultaneously fitting the two mixed components $Y_{\mathrm{SrTi}}(E_B)$ and $Y_{\mathrm{SrO_3}}(E_B)$ at different photon energies. Taking over the fitting results for $Y_{\mathrm{Ti}}(E_B)$ and $Y_{\mathrm{O_3}}(E_B)$ as fixed parameters to the third step represents a way of weighting: These results are granted higher credibility than the result of the more complex third step.

In the first step, the titanium valence yield contribution $Y_{\mathrm{Ti}}(E_B)$ at $E_\gamma = 2.753$ keV was fitted by the expression in Eq. 7.3 in the form

$$Y_{\mathrm{Ti}}(E_B, 2.75\ \mathrm{keV}) \propto \sum_{l=0}^{2} C_{\mathrm{Ti},l}\, \sigma_{\mathrm{Ti},l}\, \rho_{\mathrm{Ti},l}(E_B), \qquad \text{where} \qquad \sigma_{\mathrm{Ti},l} = a_{\mathrm{Ti},l}\, \sigma_{\mathrm{Ti},l}^{\mathrm{atomic}}$$

denotes the cross section per valence electron with angular momentum l at the titanium site. The proportionality sign accounts for the fact that the experimental spectra are given with arbitrary intensity scales. Five fit parameters were used: Two parameters A_{Ti} and B_{Ti} were used for adjusting the binding energy scale of the theoretical spectra. Three parameters $a_{\mathrm{Ti},l}$ were used for adjusting the angular-momentum dependent valence cross sections $\sigma_{\mathrm{Ti},l}$. In order to be able to include the constraint given by Eq. 7.5 in the fitting at a later instant, the cross sections $\sigma_{\mathrm{Ti},l}$ are expressed in terms of the values $\sigma_{\mathrm{Ti},l}^{\mathrm{atomic}}$ for orbitals of the free atom. These atomic orbitals, mostly the

shallowest occupied orbitals with angular momentum l, give the principal valence band contributions when the solid state is formed.

The parameters $a_{\mathrm{Ti},l}$ can be interpreted as correction factors for the atomic cross sections $\sigma^{\mathrm{atomic}}_{\mathrm{Ti},l}$; the correction accounts for the electronic rearrangement when going from the atomic to the solid state. The atomic cross sections $\sigma^{\mathrm{atomic}}_{\mathrm{Ti},l}$ are corrected for the dipole emission characteristics by the prefactors $C_{\mathrm{Ti},l}$ and are listed in Tab. 7.2. The obtained valence cross sections $\sigma_{\mathrm{Ti},l}$ are listed and discussed later in section 7.8 on page 124. The fitted curves are shown in the upper half of Fig. 7.15. The theoretical partial intensity from the titanium site $Y^{\mathrm{theo}}_{\mathrm{Ti}}(E_B) = \sum_{l=0}^{2} Y^{\mathrm{theo}}_{\mathrm{Ti},l}(E_B)$ shows very good agreement with the data. (The theoretical spectra that were scaled to the data are marked by the superscript "theo" to distinguish them from the experimental spectra.)

Quantity	E_γ [keV]	$s = \mathrm{Sr}$			$s = \mathrm{Ti}$			$s = \mathrm{O}$	
		$l=0$	$l=1$	$l=2$	$l=0$	$l=1$	$l=2$	$l=0$	$l=1$
$\beta_{s,l}$	2.753	1.998	1.502	0.960	1.992	1.098	0.489	1.977	0.307
	3.891	1.997	1.392	0.812	1.984	0.934	0.369	1.965	0.204
$C_{s,l}\,\sigma^{\mathrm{atomic}}_{s,l}$	2.753	168	1106	119	204	655	12.6	534	9.02
	3.891	82.4	433	31.9	91.3	205	2.64	194	2.14

Table 7.2: Theoretical β parameters and atomic photoionisation cross sections for Sr, Ti and O for $E_\gamma = 2.753$ and 3.891 keV. The listed values were cubic-spline interpolated from Trzhaskovskaya's[2] tables [145, 146] at the corresponding kinetic energies of the photoelectrons for orbitals in the following order: Sr $5s$, Sr $4p$, Y $4d_{3/2}$ (replacing Sr $4d$, which is not tabulated); Ti $4s$, Ti $3p$ (replacing Ti $4p$, which is not tabulated), Ti $3d_{3/2}$; O $2s$, O $2p$. The cross sections $\sigma^{\mathrm{atomic}}_{s,l}$ are given in barn per electron, taking the $2l{+}1$ degeneracy into account. $C_{s,l}(E_\gamma) = 1 + \beta_{s,l}(E_\gamma)$ is the anisotropy correction factor for the used XPS experimental geometry.

In the second step, the oxygen valence yield component $Y_{\mathrm{O}_3}(E_B)$ at $E_\gamma = 3.891$ keV was fitted alike the titanium component with two lpDOS spectra according to Eq. 7.3

$$Y_{\mathrm{O}_3}(E_B, 3.89\ \mathrm{keV}) \propto \sum_{l=0}^{1} C_{\mathrm{O},l}\,\sigma_{\mathrm{O},l}\,\rho_{\mathrm{O}_3,l}(E_B), \qquad \text{where} \qquad \sigma_{\mathrm{O},l} = a_{\mathrm{O},l}\,\sigma^{\mathrm{atomic}}_{\mathrm{O},l},$$

using four fitting parameters: Two parameters A_{O} and B_{O} were used for rescaling the energy axes of the theoretical spectra. Another two parameters $a_{\mathrm{O},l}$ were used to adjust the cross sections $\sigma_{\mathrm{O},l}$ for valence states with $l = 0$ and 1. Since the vast majority of oxygen valence states has $l = 1$, the lpDOS component with $l = 1$ could be represented by the Bader pDOS component, which is not decomposed over angular momentum. The fit result is shown in the upper half of Fig. 7.16.

[2]The relevant information is not the absolute cross section but the energy dependence of the $\sigma^{\mathrm{atomic}}_{s,0} : \sigma^{\mathrm{atomic}}_{s,1} : \sigma^{\mathrm{atomic}}_{s,2}$ ratio for each element s. In this respect, Scofield's tables [150] do not deviate significantly from Trzhaskovskaya's. (Note that Trzhaskovskaya's cross sections are listet as a function of electron kinetic energy, while Scofield's values are given as a function of the incident photon energy.)

In the third step, the valence yield contribution from strontium was implicitly compared to theory by fitting the components $Y_{\mathrm{SrO_3}}(E_B)$ at $E_\gamma = 2.753$ keV and $Y_{\mathrm{SrTi}}(E_B)$ at $E_\gamma = 3.891$ keV simultaneously, identifying the oxygen and titanium yield admixtures at the same time. The fitting held the difficulty that intensity and line shape of the included strontium component did not coincide at the two photon energies. The underlying energy dependences of the photoionisation cross sections as well as of the XPS angular distributions had to be taken into consideration. The oxygen and titanium admixtures were accounted for by the components $Y^{\mathrm{theo}}_{\mathrm{O_3}}(E_B)$ and $Y^{\mathrm{theo}}_{\mathrm{Ti}}(E_B)$ determined above. But likewise, the component $Y^{\mathrm{theo}}_{\mathrm{O_3}}(E_B)$ had to be transformed from 3.89 to 2.75 keV and $Y^{\mathrm{theo}}_{\mathrm{Ti}}(E_B)$ from 2.75 to 3.89 keV by scaling the subshell yields with the (*a priori* unknown) cross section ratio between the two energies. This was achieved as follows:

Consistency between the $\sigma_{s,0} : \sigma_{s,1} : \sigma_{s,2}$ ratios at 2.75 to 3.89 keV was attained by the condition

$$\left(\frac{\sigma_{s,l_1}(2.75\ \mathrm{keV})}{\sigma_{s,l_2}(2.75\ \mathrm{keV})}\right)\left(\frac{\sigma_{s,l_1}(3.89\ \mathrm{keV})}{\sigma_{s,l_2}(3.89\ \mathrm{keV})}\right)^{-1} \stackrel{!}{=} \left(\frac{\sigma^{\mathrm{atomic}}_{s,l_1}(2.75\ \mathrm{keV})}{\sigma^{\mathrm{atomic}}_{s,l_2}(2.75\ \mathrm{keV})}\right)\left(\frac{\sigma^{\mathrm{atomic}}_{s,l_1}(3.89\ \mathrm{keV})}{\sigma^{\mathrm{atomic}}_{s,l_2}(3.89\ \mathrm{keV})}\right)^{-1} \quad (7.5)$$

for any two angular momenta l_1 and l_2 for $s =$ Sr, Ti and O. The condition imposes the energy dependence of the subshell cross section ratios for the tabulated values on the experimental values. The condition determines the set of parameters $a_{s,l}$ for one of the photon energies. The condition determines how the line shape of site-specific yield spectra transforms with photon energy.

The absolute energy dependence of valence cross sections is *a priori* unknown and can deviate from the dependence of tabulated values for atomic levels. Scaling factors c_s were introduced to account for these deviations by

$$\frac{\sigma_{s,l}(3.89\ \mathrm{keV})}{\sigma_{s,l}(2.75\ \mathrm{keV})} = c_s \frac{\sigma^{\mathrm{atomic}}_{s,l}(3.89\ \mathrm{keV})}{\sigma^{\mathrm{atomic}}_{s,l}(2.75\ \mathrm{keV})}. \quad (7.6)$$

The factors c_s were determined for each element by the fitting.

The two yield components $Y_{\mathrm{SrO_3}}(E_B)$ and $Y_{\mathrm{SrTi}}(E_B)$ were fitted with three strontium lpDOS spectra and the already determined yield spectra for oxygen and titanium according to Eq. 7.3 in the form

$$\begin{aligned} Y_{\mathrm{SrO_3}}(E_B, 2.75\ \mathrm{keV}) \;&\propto\; Y^{\mathrm{theo}}_{\mathrm{O_3}}(E_B, 2.75\ \mathrm{keV}) + \sum_{l=0}^{2} C_{\mathrm{Sr},l}(2.75\ \mathrm{keV})\,\sigma_{\mathrm{Sr},l}\,\rho_{\mathrm{Sr},l}(E_B), \\ &\qquad \text{where} \quad \sigma_{\mathrm{Sr},l} = a_{\mathrm{Sr},l}\,\sigma^{\mathrm{atomic}}_{\mathrm{Sr},l}(2.75\ \mathrm{keV}), \\ Y_{\mathrm{SrTi}}(E_B, 3.89\ \mathrm{keV}) \;&\propto\; Y^{\mathrm{theo}}_{\mathrm{Ti}}(E_B, 3.89\ \mathrm{keV}) + \sum_{l=0}^{2} C_{\mathrm{Sr},l}(3.89\ \mathrm{keV})\,\sigma_{\mathrm{Sr},l}\,\rho_{\mathrm{Sr},l}(E_B), \\ &\qquad \text{where} \quad \sigma_{\mathrm{Sr},l} = a_{\mathrm{Sr},l}\,c_{\mathrm{Sr}}\,\sigma^{\mathrm{atomic}}_{\mathrm{Sr},l}(3.89\ \mathrm{keV}). \end{aligned}$$

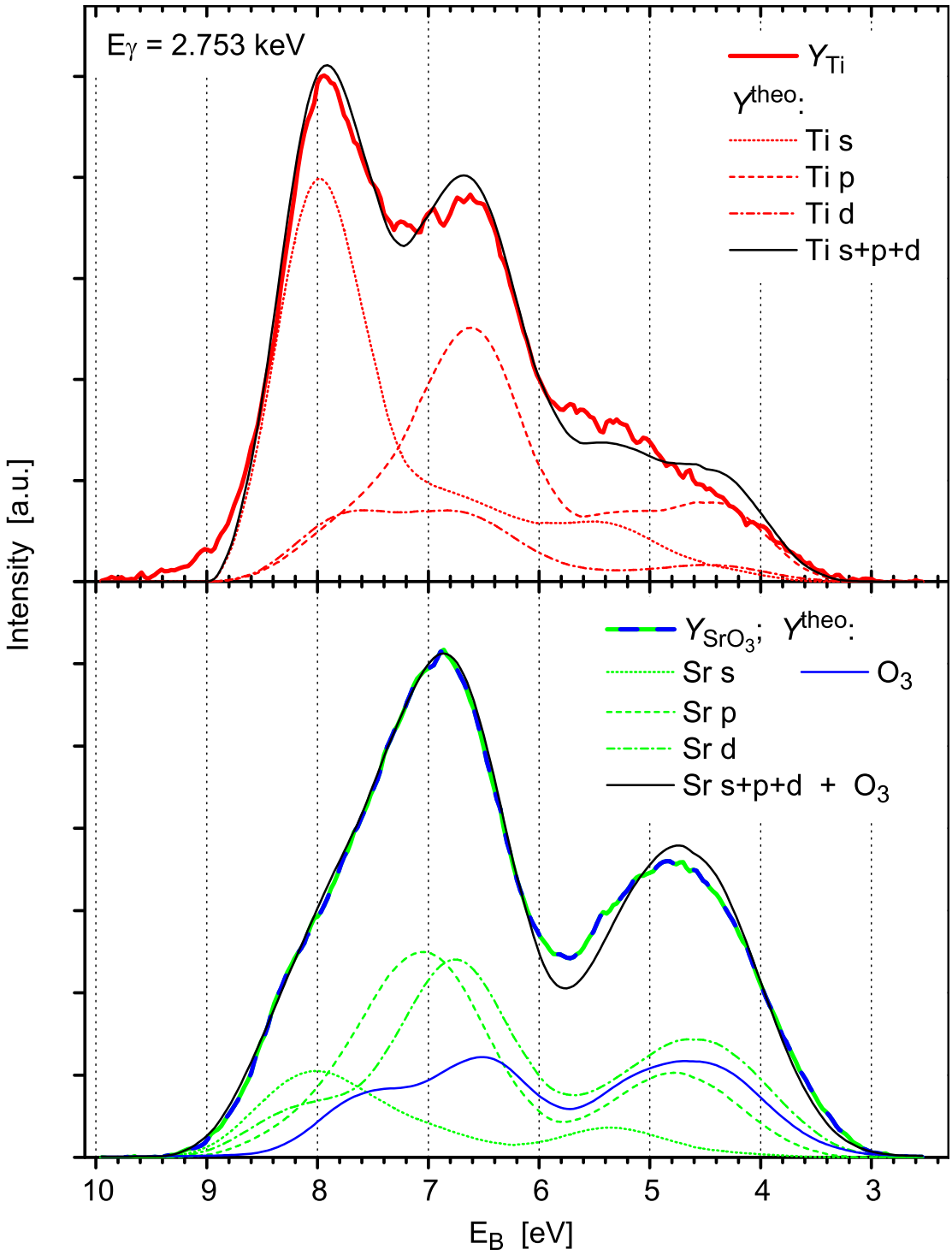

Figure 7.15: Comparison of experimental and calculated $SrTiO_3$ valence yield contributions from Ti and SrO_3. The contributions $Y_{\mathrm{Ti}}(E_B)$ and $Y_{\mathrm{SrO_3}}(E_B)$ were determined from XSW data taken in the $SrTiO_3(111)$ reflection. They were fitted by calculated angular-momentum l resolved yield contributions $Y^{\mathrm{theo}}_{s,l}(E_B)$ from the lattice sites $s = \mathrm{Ti}, \mathrm{Sr}, \mathrm{O}_3$. The angular momenta $l = 0, 1, 2$ are denoted by the symbols s, p, d.

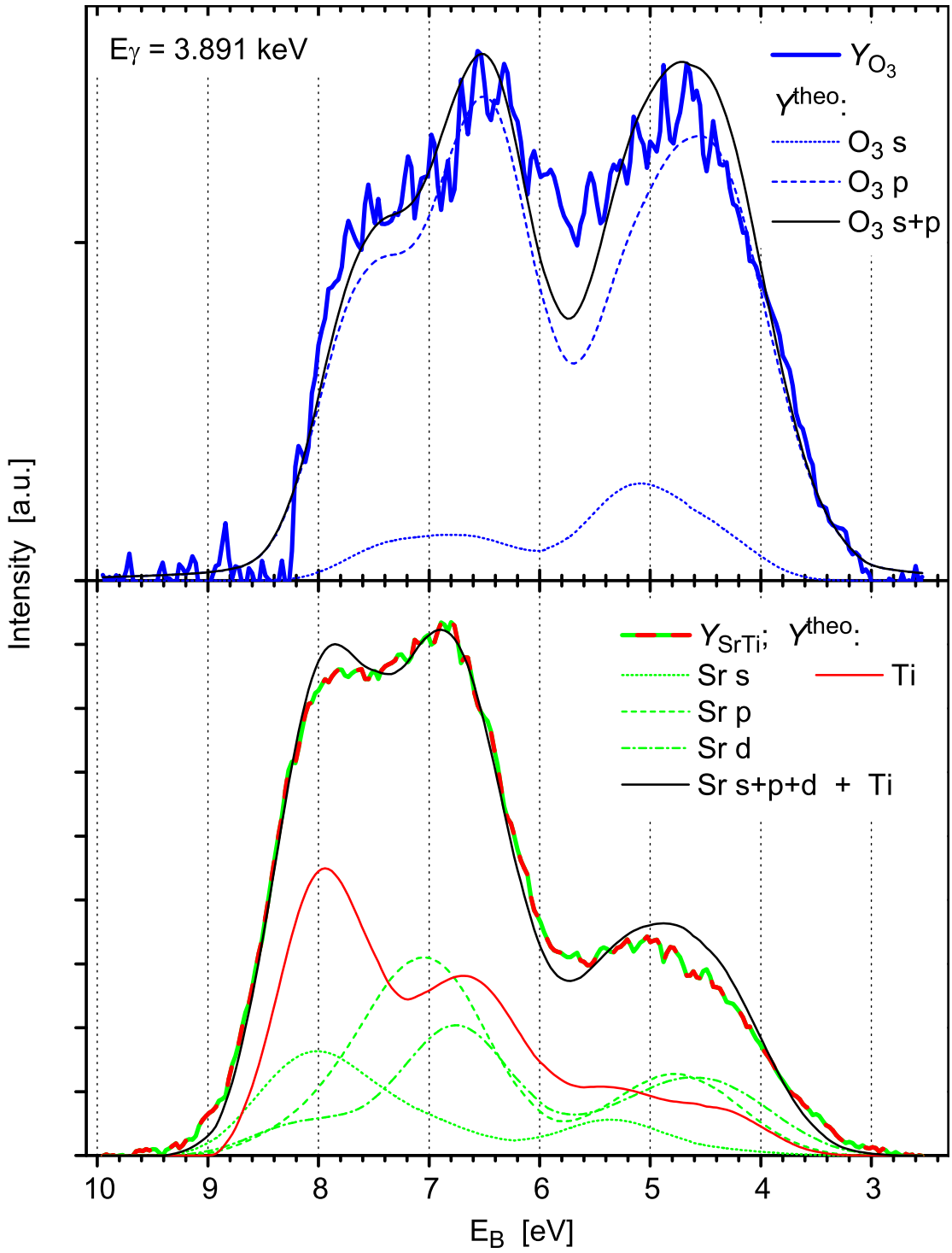

Figure 7.16: Comparison of experimental and calculated $SrTiO_3$ valence yield contributions from O_3 and SrTi. The contributions $Y_{O_3}(E_B)$ and $Y_{SrTi}(E_B)$ were obtained from XSW data recorded in the $SrTiO_3(112)$ reflection. They were fitted by calculated angular-momentum l resolved yield contributions $Y^{theo}_{s,l}(E_B)$ from the lattice sites $s = Ti, Sr, O_3$ by adjusting the photoionisation cross sections.

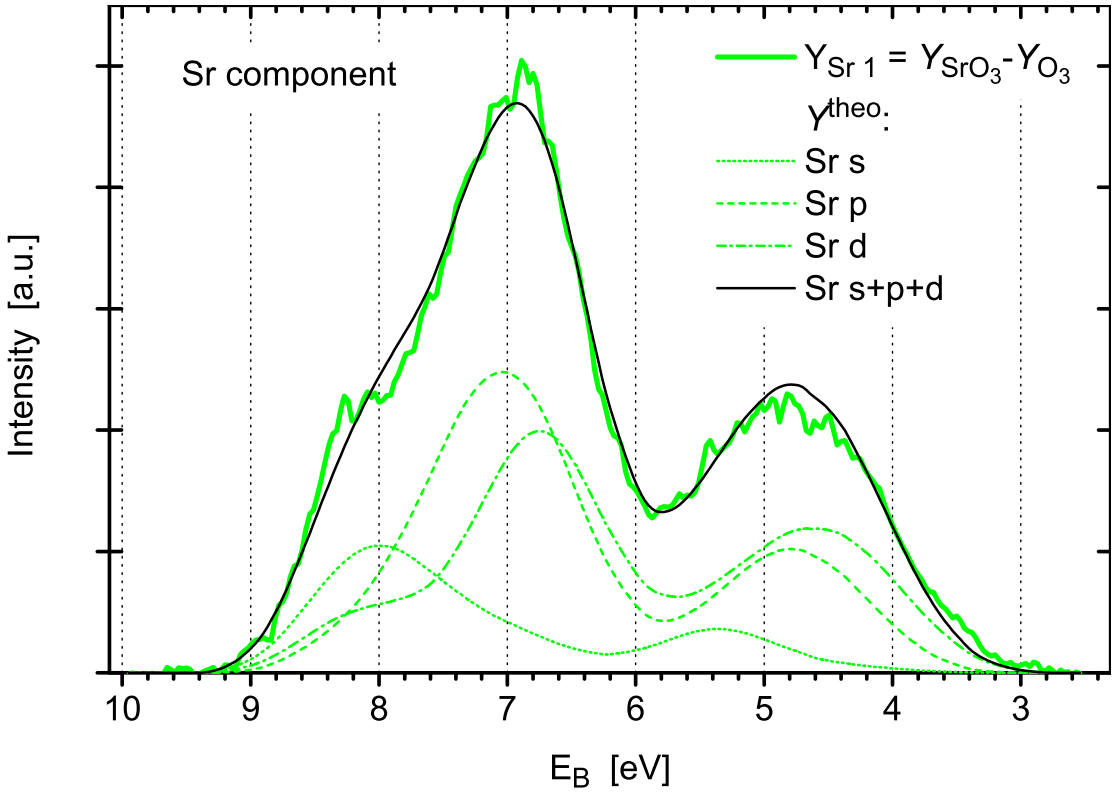

Figure 7.17: Comparison of experimental and calculated $SrTiO_3$ valence yield contributions from Sr. The experimental spectrum $Y_{SrO_3} - Y_{O_3}$ was obtained by combining data taken at different photon energies (compare Fig. 7.11) and represents an approximation of the strontium valence component. The curve was fitted by three angular-momentum l resolved yield contributions $Y^{\text{theo}}_{\text{Sr},l}(E_B)$.

Eight fitting parameters were used: Two parameters A_{Sr} and B_{Sr} were used for adjusting the binding energy scale of the strontium lpDOS spectra. Three parameters $a_{\text{Sr},l}$ were determined by scaling the cross sections $\sigma_{\text{Sr},l}$. Using the same set of parameters $a_{\text{Sr},l}$ for fitting both components Y_{SrO_3} and Y_{SrTi} ensured consistency between the fittings, which are shown in Figs. 7.15 and 7.16. The remaining three fitting parameters c_{Ti}, c_{O} and c_{Sr} were determined by the absolute scaling behaviour of the cross sections $\sigma_{s,l}(E_\gamma)$ for each element between the two photon energies.

Determining the photoionisation cross sections for valence electrons in the vicinity of the strontium atomic core by fitting one of the components $Y_{\text{Sr }1}(E_B)$ or $Y_{\text{Sr }2}(E_B)$ displayed in Fig. 7.11 will lead to inaccurate results. These spectra were produced by neglecting the energy dependence of the cross sections, when partial spectra obtained at distinct photon energies were subtracted. Furthermore, the photon energy for which these strontium spectra are valid is not well defined. Nevertheless, the strontium spectra can be fitted to crosscheck the results presented in Figs. 7.15 and 7.16, where the pronounced similarity of the base functions could have easily resulted in an erroneous fitting. Spectrum $Y_{\text{Sr }1}(E_B) = Y_{\text{SrO}_3}(E_B) - Y_{\text{O}_3}(E_B)$ shown in Fig. 7.17 was fitted with

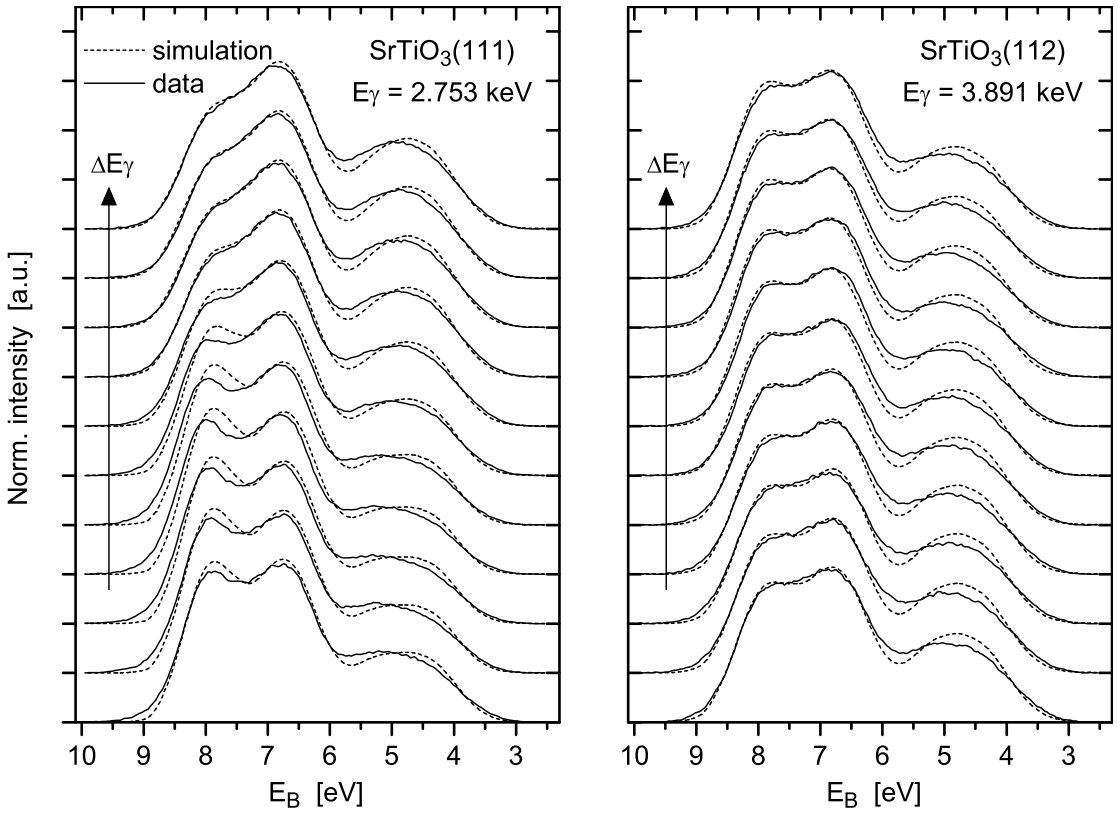

Figure 7.18: Comparison of line shapes for recorded and simulated $SrTiO_3$ valence band spectra. The simulation of the XSW effect was generated by modulating the l-resolved valence yield components obtained from the fitting. The experimental valence XPS spectra were taken from Figs. 7.8(a) and 7.9(a).

only three base functions. Also in this case, the Sr p and d components were hard to separate. The energy axes of the lpDOS spectra were rescaled as previously with parameters $A_{\mathrm{Sr}} = 1.14$ and $B_{\mathrm{Sr}} \approx 0.8$ eV, which gave the best fitting. The $s : p : d$ peak intensity ratio between the strontium yield components $Y^{\mathrm{theo}}_{\mathrm{Sr},l}$ of approximately $1 : 2 : 1.5$ midway between the bounds of $1 : 2 : 2$ at 2.75 keV and $1 : 2 : 1$ at 3.89 keV, confirming the above results.

With the theoretical l-dependent valence yield components $Y^{\mathrm{theo}}_{s,l}(E_B)$ gained from the fitting and the site-specific XSW modulation information, the XSW effect on the valence band spectrum under a Bragg condition could be simulated and compared to the recorded data. The comparison of the spectral line shapes in Fig. 7.18 shows generally good agreement but reveals some deviation in XSW modulation between the experimental and the simulated spectra. In particular, the simulated spectra are observed to overshoot at the position of the prominent titanium s peak around 8 eV binding energy in the $SrTiO_3(111)$ reflection. Rather than by a disagreement in line shape between experimental and theoretical spectra, this deviation can be explained by an overestimated XSW modulation for the valence XPS signal: The particularly large apparent coherent fraction of $F^{111}_{\mathrm{Ti}} = 1.18$ determined from a titanium core level signal

may not appropriately describe the XSW modulation of the titanium valence signal. This can be a consequence of quadrupole effects, which can lead to a dependence of the XSW modulation on the specific electronic level probed, as discussed in appendix B.

An alternative XSW analysis presented in appendix E is independent of the experimental XSW modulation information. The disagreement in line shape modulation is removed by this approach. At the same time, the fit quality of the four valence yield components resulting from the XSW analysis is comparable to that in Figs. 7.15 and 7.16.

In the following, the analysis that relies on the experimental XSW modulation information from core level XPS was given preference. The alternative analysis presented in the appendix has been left out of consideration.

7.7 Analysis and Discussion: Electronic Structure

The results of the *ab initio* DFT calculations are experimentally confirmed by a very good agreement, based on visual inspection, with the four partial valence XPS spectra in Figs. 7.15 and 7.16, which were obtained from a quantitative XSW analysis. One-particle calculations therefore occur to predict well the electronic properties of the perovskite $SrTiO_3$. The overview in Fig. 7.19 summarizes the results of the XSW analysis and the results of the comparison with the calculations:

The site-specific density of states of the $SrTiO_3$ valence band from the XSW analysis is presented in the last line of the figure. The analysis is based on the theoretical spectra to include an accurate solution for the strontium component, since the experimental strontium component could not be isolated by the XSW analysis. While the valence band of $SrTiO_3$ is predominantly composed of oxygen states, the oxygen contributes only a minor number of photoelectrons to the valence yield. The few titanium and strontium states are, however, vastly overrepresented by two about equally large yield contributions. It now becomes visible that the prominent triple peak structure of the valence band XPS spectrum actually results from the strontium and titanium contributions. Unlike in the ultraviolet spectral region, the structure does not reflect the oxygen contribution, as the also triply peaked oxygen pDOS spectrum may suggest at a first glance. Remarkable is the large yield contribution from strontium: The strontium atom does not entirely ionize, and the remaining valence states at the strontium site occur in the XPS spectrum considerably magnified by a large photoionisation cross section.

The individual site-specific valence yield components that were experimentally determined can be interpreted by comparison to the theoretical angular-momentum resolved components. The experimental spectra are shown in lines 1–3 of the figure in circular symbols. The strontium yield component is accurately described by the theoretical curve only. The two combinations $Y_{SrO_3}(E_B) - Y_{O_3}(E_B)$ and $Y_{SrTi}(E_B) - Y_{Ti}(E_B)$ taken from Fig. 7.17 approximate this solution differently well.

The essential chemical effects behind the observed spectral features can be accounted for within a σ and π bonding scheme of a molecular orbital model for a TiO_6 cluster. A molecular orbital scheme for a transition metal octahedrally coordinated

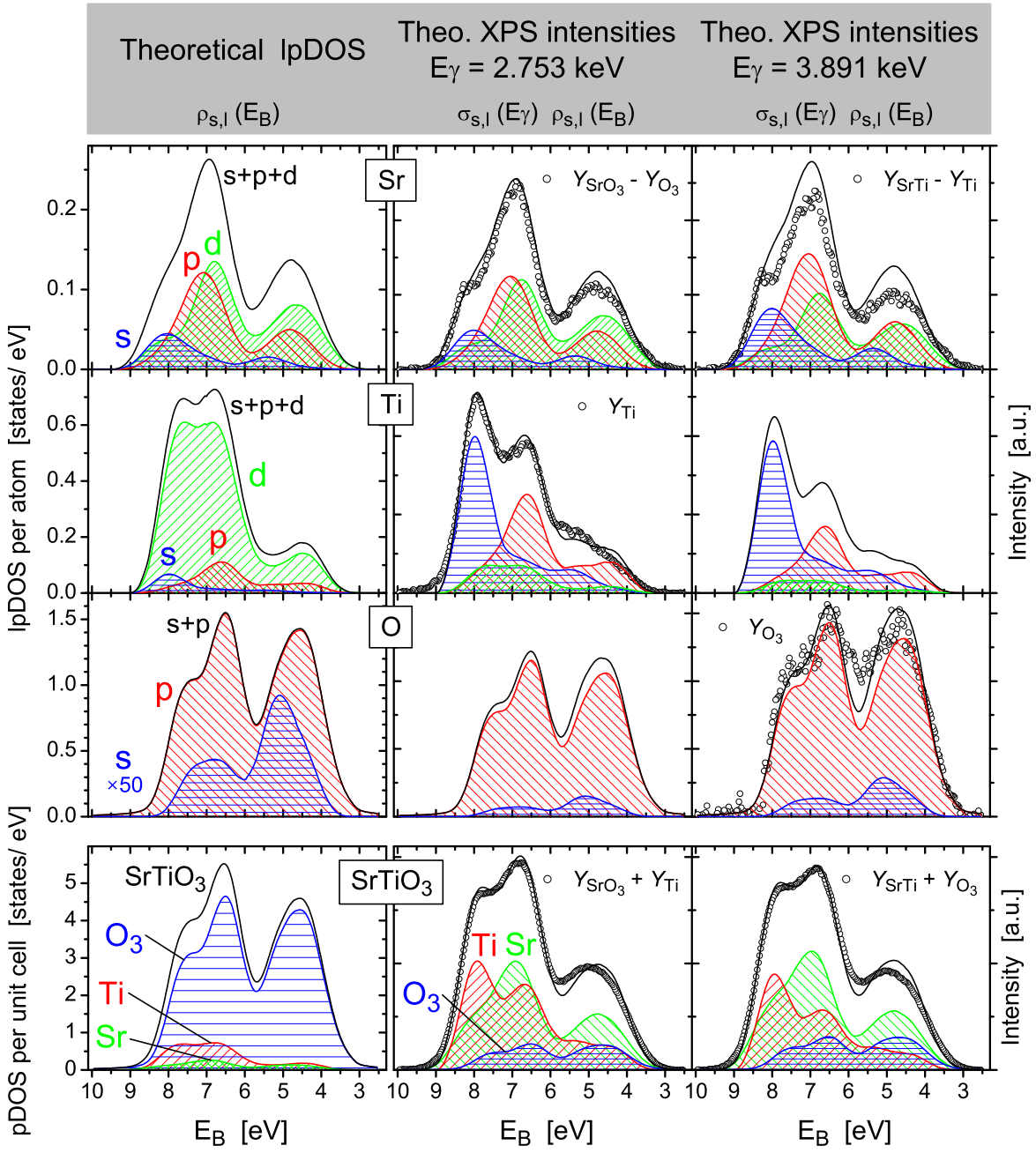

Figure 7.19: Summary of the results for the $SrTiO_3$ valence band. For the three lattice sites (lines 1–3) and the entire unit cell (line 4), the theoretical density of states (column 1) are compared to the theoretical XPS spectra for two photon energies (columns 2 and 3). The theoretical spectra are compared to the experimental site-specific spectra, which are given by the XSW analysis and are shown in circular symbols. The lpDOS are normalized to the total number of valence states, where the individual number of states $n_{s,l}$ are listed in Tab. 7.3. The theoretical yields, represented by the areas of the graphs, include a factor $(1 + \beta_{s,l})$ for the experimental geometry. The two valence band XPS spectra in line 4 are normalized to area for comparison.

to oxygen, as described in many textbooks, is illustrated in Fig. 2.2 on page 7. The influence of the strontium ion, which rests rather passively at the centre of the unit cell, is not included in this model and can be discussed separately.

The double peak structure observed for the titanium yield component does not reflect the predominant d states. It can rather be attributed to the energy shift between the magnified s and p single peaks. In very good agreement with the MO scheme, the XPS peak around 8 eV binding energy, mainly consisting of s electrons with some d admixture, may be entirely ascribed to σ bonding titanium states. π bonding and a minority of σ bonding states may compose the second peak at 6.5–7 eV binding energy: The p electron signal, which may be attributed to few σ states, dominates the admixture of d electrons, which may be representative of the much larger density of π states. The tail of the titanium spectrum towards the Fermi edge may be explained by a small number of π bonding states, which are raised in energy due to interaction with part of the σ bonds [10].

The line shape of the oxygen yield component exhibits a doubly lobed and a single lobed structure separated by a dip. The energy alignment of the titanium and the oxygen doubly lobed features (where the more strongly bound oxygen lobe can also be described as a shoulder) results from sharing of electrons of the spatially overlapping titanium-oxygen bonding orbitals. This observation directly evidences the partially covalent bonding character in this largely ionic material. The shoulder may, correspondingly, represent the σ bonding and the second lobe mainly the π bonding states. The third oxygen lobe at 4–5 eV binding energy basically has, except few π bonding titanium states, no correspondence in the titanium component and signifies, in accordance with the MO depiction, the nonbonding oxygen π states. The oxygen valence yield is representative of the p states. Only a small fraction of the oxygen valence yield comes from the very small number of s states.

The strontium ion rests highly but not fully ionized at the centre of the unit cell, as the existence of valence yield from strontium proves. The angular-momentum dependent size-specific composition of the strontium yield was found to be representative of the DOS composition. The strontium ion is ionically bound, essentially donating its electrons to the TiO_3 array. The covalent bonding contribution is expected to be small, owing to the large energy separation of the strontium atomic orbitals from the valence level. However, some residual covalency may be indicated by the agreement in binding energy of strontium and oxygen XPS features: The atomic O p_x and p_y orbitals[3], which are involved in π bonds with the titanium at 6.5–7 eV binding energy, establish some σ bonding interaction with the strontium ion at the same time [6]. This σ bonding interaction competes with the titanium-oxygen π interaction for these O p_x and p_y orbitals. But due to the low electronegativity of strontium, the strontium loses the competition for electrons to titanium, and the disturbance of the titanium-oxygen bonding is weak. The second peak observed in the strontium yield component at 4–5 eV may suggest that the oxygen π orbitals, i.e., the few bonding as well as the nonbonding (as far as the titanium is concerned) ones, interact with the strontium ion in the same way, which is made possible by their x, y-orientation in space. This picture

[3]The z axis is chosen along the titanium-oxygen-titanium bonds.

is supported by the increasingly covalent character of this kind of bonding interaction, which simulations [151] predict as the size of the central ion is increased.

The description of the $SrTiO_3$ electronic structure within a σ and π bonding scheme that is based on a cluster model has its limitations. The band formation in the solid is much more complex than for a single TiO_6 molecule. Band dispersion occurs, and a classification of bands or certain band ranges into either purely σ or π in character may be too rigorous. This tight-binding description should, while not being as accurate as first principle calculations, work out relatively well in case of the perovkites (that have been described as the "prototype" material class for such a description [133]), owing to the network of linear metal-oxygen-metal elements that forms the cubic structure. This is supported by two observations: The large dip measured in the oxygen yield component (and also in the valence band spectrum) confirms the clear splitting of the valence states into bonding and nonbonding subbands. And the bonding subband has a conspicuous titanium character, while the nonbonding subband contains titanium traces only. The relationship between these observations and the crystal structure will become more evident when comparing the electronic structures of $SrTiO_3$ and TiO_2.

Many XPS studies on $SrTiO_3$ reported in the literature require a more careful interpretation, as the results of our XSW analysis suggest. In a variety of studies, the $SrTiO_3$ electronic structure is inferred from comparing valence XPS spectra to theoretical DOS, which are calculated exclusively for titanium and oxygen. The work by Wolfram and Ellialtıoğlu [129] is a representative example. The composition of the valence yield determined by our XSW experiment already disproves all these analysis attempts: While the total valence DOS can be well described without including the small fraction of strontium states, XPS spectra cannot be quantitatively described in a satisfying way if the strontium yield contribution is disregarded. This finding for $SrTiO_3$ gives reason to reconsider identical attempts to analyse the electronic structure of the related perovskite $BaTiO_3$, like the one by Pertosa, Hollinger and Michel-Calendini [127]. The barium valence contribution is expected to be even larger than the strontium contribution, owing to the more covalent character of the bonding of the barium ion, and cannot be ignored.

The resonant photoemission measurements by Brookes *et al.* [135] and Reihl *et al.* [136] have proved Ti $3d$ admixture in the bonding region of the valence band. This is in agreement with titanium yield contributions predominantly occurring in the lower valence band, as revealed by the XSW analysis. At X-ray energies, the d yield contribution is masked by the more intense s and p components.

Fujii *et al.* [137] took XSW data for one reflection only and separated the SrO_3 and Ti components, but they did not separate the SrO_3 component further into elemental contributions. Our results prove the SrO_3 component to be largely dominated by strontium, while the authors assumed this component to originate mainly from oxygen and incorrectly concluded that the strontium-oxygen bonding in $SrTiO_3$ be covalent. It is widely agreed that the bonding character is highly ionic with a minor covalent contribution. Although they correctly mention that photoionisation cross sections for the solid state may deviate from their atomic values, the authors compared their data to theoretical cluster calculations without taking cross sections into account.

Comparison of $SrTiO_3$ and Rutile TiO_2 Electronic Structures

It is instructive to compare the electronic structure of $SrTiO_3$ to that of rutile TiO_2, a related oxide material that shares important structural properties with strontium titanate. The XSW technique proves here to be an ideal method to reveal how differences in crystal structure give rise to differences in the local electronic structure at each lattice site.

The crystal structures of rutile TiO_2 and $SrTiO_3$ exhibit some similarities but also differences. The structural properties of TiO_2, the primitive unit cell of which is shown in Fig. 7.20(a), have been described in detail by Glassford and Chelikowsky [152]. The unit-cell parameters are $a = 4.594$ Å and $b = c = 2.959$ Å. TiO_2 contains one chemical species of oxygen and one of titanium. Each titanium atom is surrounded by an octahedron of oxygen atoms, and the octahedron is the most conspicuous common structural element of both oxides. Unlike for $SrTiO_3$, it is distorted in TiO_2: It is elongated by 2% along its principal axis, which results in titanium-oxygen bonds of two different lengths. But more importantly, the projection of the octahedron onto the equitorial plane (which is normal to the principal axis) is rather rectangular than quadratic. Direct titanium-titanium interaction occurs along the $\langle 001 \rangle$ directions. This is not possible in $SrTiO_3$, where an oxygen atom lies midway inbetween each titanium pair. Each oxygen atom in TiO_2 is at the same time an apical oxygen atom of one octahedron and one of the equitorial oxygen atoms of another two octahedrons. While oxygen atoms in $SrTiO_3$ only occur in linear bonds with 180° bonding angle, each oxygen atom in TiO_2 is trivalent and has three coplanar titanium near neighbours. The sp^2 hybrid-like electronic configuration is well recognizable from the electron density distribution of the upper O $2p$ valence bands in the $(1\bar{1}0)$ plane, which was calculated by Glassford and Chelikowsky [152] and is shown in Fig. 7.20(b). Band calculations [133] predict that the oxygen-oxygen interactions are more prominent than in $SrTiO_3$, which is partially caused by the distortion of the octahedra. In $SrTiO_3$, $(pp\sigma)$ and $(pp\pi)$ interactions between oxygen atoms along the $\langle 001 \rangle$ directions do exist, but they are very weak. This is because these interactions have to surmount the whole distance across the faces of the unit cell, which is twice as large as the titanium-oxygen distance. Diagonal interaction of oxygen orbitals along the $\langle 110 \rangle$ directions is even weaker than the longitudinal interaction.

Woicik *et al.* [5] have determined the titanium and oxygen components of the rutile TiO_2 valence band, using the XSW technique. The authors measured valence XPS spectra of the binary compound at two different photon energies within the (200) Bragg range at ∼2.7 keV photon energy from a single-crystal sample prepared by Ar sputtering and annealing. The ratio of the site-specific valence yield contributions was determined from the ratio of the Ti $3p$ and O $2s$ core level signals. The extracted titanium and oxygen components were compared to *ab initio* DFT calculations. It shall be briefly noted that some details of the calculations differed from those for $SrTiO_3$: The DFT calculations were based on different pseudopotentials, and the charge integration in the calculations was performed within spheres of 1.4 (2.5) atomic units radius for oxygen (titanium), which the authors mentioned was equal to the known covalent radii of the atoms. The calculated lpDOS spectra are shown in Fig. 7.20(c).

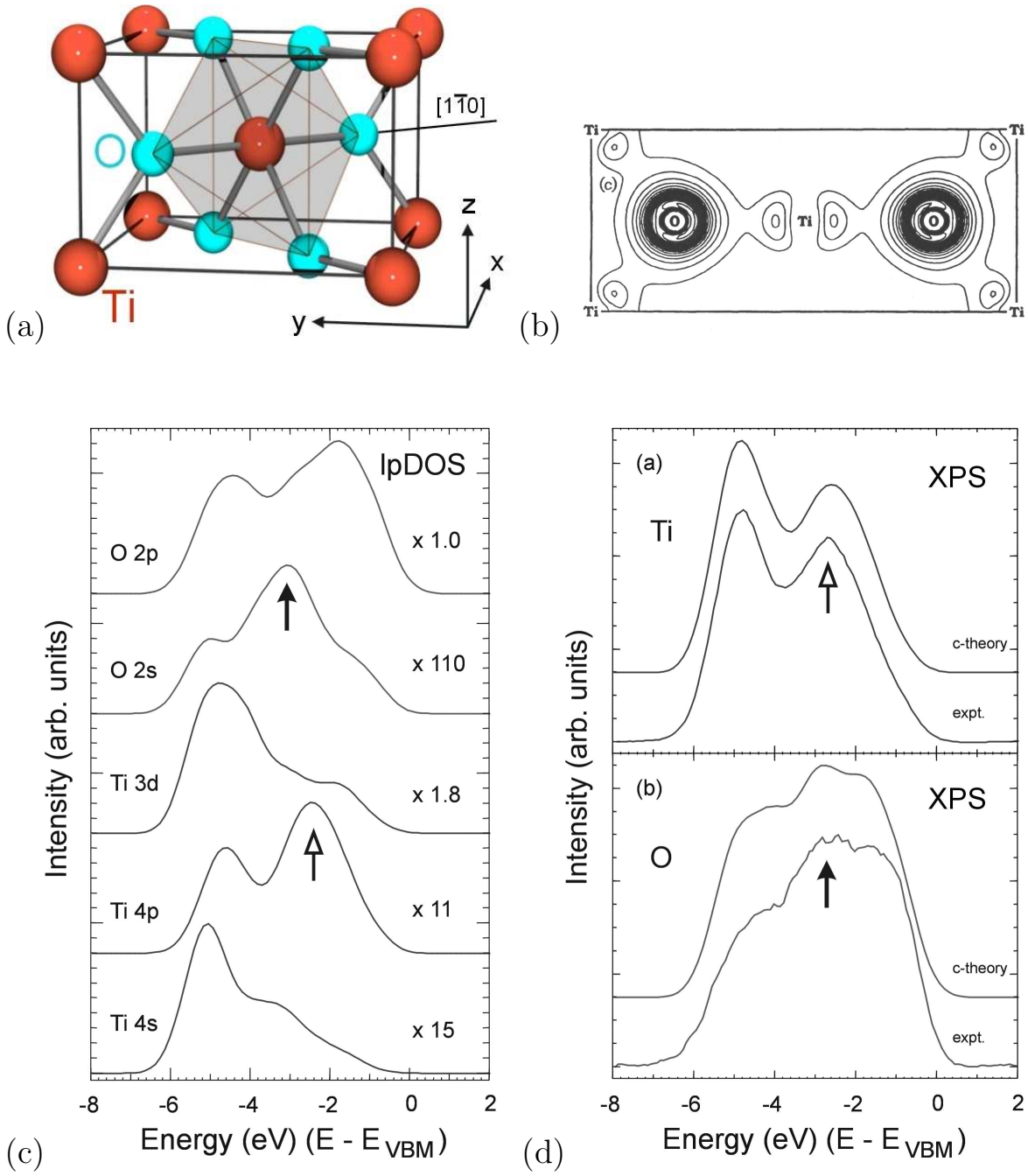

Figure 7.20: Results of an XPS/XSW study on the rutile TiO_2 valence band by Woicik *et al.* [5]. (a) Primitive unit cell for rutile TiO_2. The principal axis of the slightly distorted TiO_6 octahedron (shown shaded) is in $[1\bar{1}0]$ direction. (b) Charge density contour map for the upper O $2p$ valence bands in the $(1\bar{1}0)$ plane calculated by Glassford and Chelikowsky [152]. (c) Valence lpDOS calculated for the titanium and the oxygen lattice sites. (d) Comparison of experimental and theoretical site-specific valence yield components. The arrows identify spectral features that are mentioned in the text. Figures (a), (c) and (d) adapted from Woicik *et al.* [5, 43].

Woicik's *et al.* comparison of the experimental and calculated Ti and O valence yield components for TiO_2 in Fig. 7.20(d) showed a very good agreement. The authors interpreted the electronic structure as follows: The doubly lobed structure of the titanium yield component was attributed to σ (-5 eV energy) and π (-2.5 eV energy) bonding states, which were mirrored in the oxygen component at the same energy values. The oxygen peak at -1 eV energy was ascribed to nonbonding π states. A particularly beautiful result of this study was the aspect that the experimental oxygen valence yield spectrum could not be reproduced without including the theoretical O s component, as the full arrows in the figure indicate: The photoionisation cross section ratio compensates the about two orders of magnitude difference in the number of O s and p states. As a consequence, the insignificant fraction of oxygen s valence states is largely overrepresented in the oxygen valence yield and becomes visible in the XPS spectrum. Correspondingly, the peak in the partial titanium valence XPS spectrum indicated by the hollow arrow in Fig. 7.20(d) could not be reproduced without magnifying the small number of titanium p valence states by a relatively large photoionisation cross section.

The essential traits of the electronic structures of TiO_2 and $SrTiO_3$ are similar, owing to a joint principal structural element, the TiO_6 octahedron: The titanium valence yield components of both materials have a double peak structure in common. One peak originates from mainly s, the other one from p states, which occur magnified in the XPS spectra by a large photoionisation cross section. The oxygen components share a triply lobed structure. The s states are largely magnified, but they become clearly visible as the central lobe only in the case of TiO_2. The important difference between the two materials is the appearance of a deep minimum at $\sim$5.5 eV binding energy in the valence band XPS spectrum for $SrTiO_3$ and in its site-specific components. This minimum clearly separates, unlike for TiO_2, the bonding and the nonbonding states. This is recognizable in particular from the oxygen components, which would look almost identical if the minimum were removed. The titanium component has its intensity concentrated in the bonding region, while for TiO_2 the titanium intensity is rather spread out over the entire width of the valence band. This is also partially due to a larger energy splitting between the σ and π bonding states. These observations confirm that the distinction between the bonding and the nonbonding subbands is largely blurred in TiO_2. On one hand, this is a consequence of the additional band splitting caused by the distortion of the octahedra, which lowers the crystal symmetry. On the other hand, the titanium-titanium interactions and in particular the oxygen-oxygen interactions, which are enhanced by the distortion, make the tight-binding description less precise.

The formation of plane triangular sp^2-like σ-bonding oxygen hybrid orbitals in TiO_2 cannot be immediately recognized from the site-specific XPS spectra. The hybridization enables the formation of three equivalent oxygen bonds with equal electron density (or almost equivalent bonds, as TiO_2 contains bonds of two different lengths). This does not mean that the involved electrons are all equivalent, i.e., that they have all the same binding energy and angular momentum and leave one single mark in the site-specific XPS spectra: In the MO depiction, the equivalent bonds are formed by a linear combination of nonequivalent molecular orbitals, which again solves the Schrödinger

equation.[4] As a consequence, the states involved in a certain kind of bonding can extend over a finite spectral region and contribute to different spectral features. Hence, the classification of the individual features into distinctly σ bonding or π bonding in nature is blurred by the hybridization. For $SrTiO_3$, in contrast, oxygen occurs only with 180° bonding angles, and σ and π bonding oxygen states rather remain separated in binding energy.

Error Discussion

The accuracy of the site-specific analysis of the $SrTiO_3$ valence band can be assessed by estimating the influence of the error in XSW valence yield modulation, which constitutes the largest source of systematic error. A judgement on the comparison of data and theory is related to the volumes chosen for the projection of the wave functions in the DFT calculations.

The XSW analysis of the valence band spectrum was hampered by an uncertainty in the XSW modulation amplitude for the site-specific valence yield contributions. The modulation profiles for the partial valence yields could not be unequivocally derived from the core level signals due to the dependence on the particular electronic level probed. This ambiguity is discussed in appendix B.2. The margins of error resulting for the site-specific valence yield spectra were estimated from XSW simulations: The system of equations given by Eq. 7.2 on page 98 was solved with XSW modulation profiles $I_s(E_\gamma)$ artificially altered in amplitude for each of the lattice sites s. The amplitude alteration was achieved by recalculating the XSW profiles based on the dipole expression given by Eq. 3.21 on page 23 for a variety of different coherent fractions. Two different cases were examined: In the first case, the XSW contrast between those components with inverted XSW profiles was varied, i.e., between $Y_{SrO_3}(E_B)$ and $Y_{Ti}(E_B)$ in the (111) reflection and between $Y_{SrTi}(E_B)$ and $Y_{O_3}(E_B)$ in the (112) reflection. In the second case, the XSW contrast between those components with similar XSW profiles was varied, i.e., between $Y_{Sr}(E_B)$ and $Y_{O_3}(E_B)$ in the (111) reflection and between $Y_{Sr}(E_B)$ and $Y_{Ti}(E_B)$ in the (112) reflection.

An alternative, more robust approach for the XSW analysis may be to separate directly the two yield components by solving the system of nonlinear equations given by Eq. 7.2 for $s = SrO_3$, Ti in the (111) and $s = SrTi$, O_3 in the (112) reflection instead for $s = Sr$, Ti, O_3. The modulation profile $I_s(E_\gamma)$ for the mixed components can be assumed as the average of the elemental profiles.

Varying the XSW contrast between the components with inverted XSW profiles had little influence on the result. Reducing the apparent coherent fraction for titanium in the (111) reflection by as much as 15% had an effect within the order of the statistical error of the XPS spectra, as Fig. 7.21(a) shows. Varying the XSW contrast between components with similar XSW profiles, however, affected the result more strongly: Fig. 7.21(b) shows that a small increase in F_{Ti}^{112} of the order of its statistical error

[4] An experimental proof that hybrid orbitals are formed by nonequivalent electrons is e.g. the multiple peak structure of the valence band UPS spectrum for sulfur hexafluoride SH_6 (a molecule with O_h symmetry), which originates from σ bonding d^2sp^3 hybrids. A spectrum can be found in the book by Siegbahn *et al.* [153].

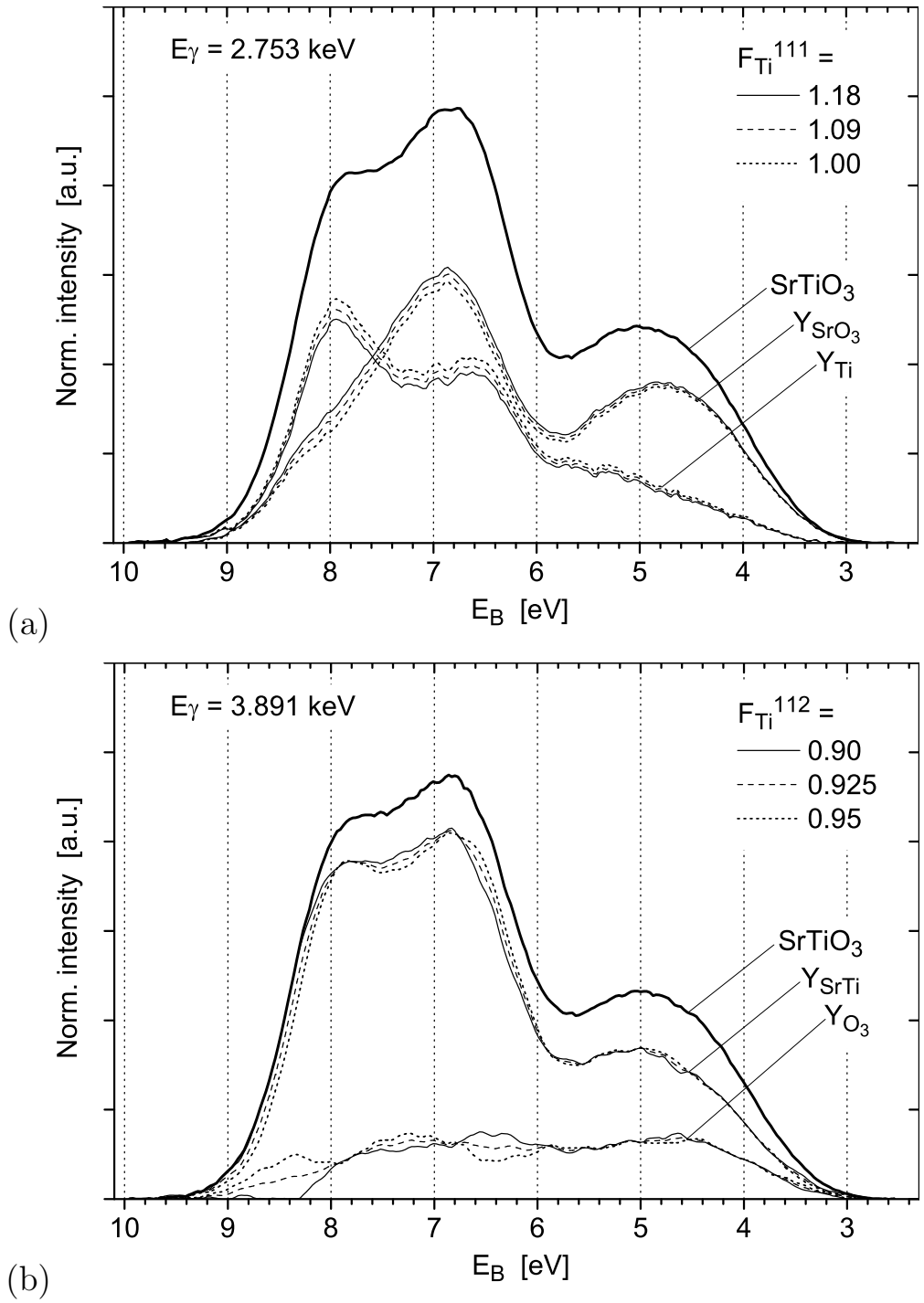

Figure 7.21: Error analysis for the $SrTiO_3$ valence band. (a) Hypothetical analysis of the valence band for the (111) reflection using the experimentally determined value $F_{\mathrm{Ti}}^{111} = 1.18$ and two hypothetical values. (The apparent coherent fraction does not represent a structural parameter but is employed as a parameter to quantify the XSW modulation amplitude, as it was suggested in appendix C.) (b) Hypothetical analysis for the (112) reflection (spectra smoothed). Besides the experimental value of $F_{\mathrm{Ti}}^{112} = 0.90$, two hypothetical values were used.

changed the result in particular around the steep flanks of the valence band spectrum, which is probably related to the limited accuracy in energy alignment of the valence band XSW data. The small oxygen component Y_{O_3} gains intensity in the range of 8–9 eV binding energy. The broadening in spectral width appears reasonable, since the oxygen component appeared quite narrow. This was noticed when the theoretical lpDOS spectra had to be compressed in order to adjust their energy scale according to Eq. 7.4 on page 106.

In order to assess the comparison of the experimental data to the theoretical calculations, the role of the chosen volumes for the projection of the wave functions in the DFT calculations needs to be discussed. The line shape of the theoretical pDOS and lpDOS spectra shown in Figs. 7.13 and 7.14, which were used for fitting the data, varies as a function of the projection volume. Hence, the fitting result depended on the choice of the projection volumes.

It is important to emphasize that an XPS valence spectrum is not representative of the total valence density of states. The spatial region, where photoexcitation can occur, is confined to the immediate vicinity of the atomic cores, where the gradient of the core potential is large enough to facilitate momentum conservation during the emission process. With increasing radial distance from the core, the transition probability rapidly decreases, and delocalized space charge is basically not seen by XPS. This is the physical prerequisite for the applicability of the dipole approximation to XPS on the valence band.

The comparison of data and theory was based on the assumption that the lpDOS components $\rho_{s,l}(E_B)$ represented good base functions in Eq. 7.3 on page 105 for fitting the site-specific yield spectra $Y_s(E_B, E_\gamma)$. This required all states with angular momentum l at site s to share the same weighting factor $\sigma_{s,l}(E_\gamma)$. Generally, the electrons that populate an electronic level contribute identically to its absolute cross section by collectively defining the amplitude of the initial state wave function. The lpDOS $\rho_{s,l}(E_B)$ do not form a sharp energy level but are degenerate; the states are spread out over a finite binding energy range. Valence states with different radial distributions, as σ and π bonding and nonbonding states in the tight binding depiction, populate distinct energy regions of the component $\rho_{s,l}(E_B)$. Owing to the radial dependence of the core potential gradient, the excitation probability varies across the energy range of the component $\rho_{s,l}(E_B)$: Distinct regions of the lpDOS component therefore require distinct weighting factors to produce its corresponding XPS yield spectrum.

Projecting the wave functions within spheres with cutoff radius $\mathbf{r}_c$ in the theoretical calculations is equivalent to assigning zero excitation probability to the charge density $\rho(\mathbf{r})$ with $|\mathbf{r}| > |\mathbf{r}_c|$. Selecting sufficiently small spheres to exclude all states in the spatial region that is transparent to X-rays thus represents an appropriate approach for calculating DOS for a comparison to XPS experiments. The radii of the site-specific XPS emission volumes may be still significantly smaller than the cutoff radii chosen for the calculations. Since the lpDOS components only scale but do not significantly differ in line shape for small cutoff radii, the used lpDOS components appeared to be representative of the valence states in the emission volume.

The comparison of data and theory could be improved by exclusively utilizing lpDOS components calculated by projection within small spheres. The oxygen p DOS

component obtained by projection within the Bader surface includes a large amount of nonbonding space charge with binding energies between 1.5 and 3 eV, as Fig. 7.13 showed. These states are disregarded when reducing the integration volume for the oxygen p component. The corresponding variation in spectral line shape could be exactly compensated in the fitting of the oxygen partial yield $Y_{\mathrm{O}_3}(E_B)$ by the peak of the oxygen s DOS component shown in Fig. 7.14. This would lead to an enlarged O s yield contribution.

7.8 Analysis and Discussion: Cross Sections

The photoionisation cross sections for the delocalised valence electrons were determined on an absolute scale. The angular-momentum dependent valence yield contributions from each lattice site were compared to the XPS yield from a reference core level with a tabulated photoionisation cross section. Using an intra-atomic reference is much easier to realize than determining quantities that are difficult to access, such as the unknown transmission of the photoelectron analyser, or the photon flux incident on the focal spot area of the analyser.

The total cross section of the $SrTiO_3$ valence band was determined by comparing the measured valence yield to that from the fully occupied Sr $3d$ level, with around 135 eV binding energy sufficiently strongly bound to remain unaffected by solid state effects, but shallow enough to assume the same transmission of the electron analyser optics as for the valence signal as confirmed by Kunz *et al.* [120]. The influence of dipole angular effects augmented the valence yield by a factor $C_{\mathrm{VB}} = 1+\beta_{\mathrm{VB}}$, where empirical effective dipole parameters of $\beta_{\mathrm{VB}}(2.753\ \mathrm{keV}) = 1.08$ and $\beta_{\mathrm{VB}}(3.891\ \mathrm{keV}) = 1.00$ were determined by the analysis described in the following. Removing the influence of dipole effects from the experimentally determined valence cross sections $C_{\mathrm{VB}}\,\sigma_{\mathrm{VB}} = 638$ barn at 2.753 keV and $C_{\mathrm{VB}}\,\sigma_{\mathrm{VB}} = 246$ barn at 3.891 keV yielded $\sigma_{\mathrm{VB}} = 306$ barn at 2.753 keV and $\sigma_{\mathrm{VB}} = 123$ barn at 3.891 keV. A crosscheck with the Sr $3p$ signal as a reference (about 275 eV binding energy) resulted in ∼40% larger values.

The angular-momentum dependent valence cross sections per electron $\sigma_{s,l}$ were calculated from the ratio

$$\frac{Y_{s,l}^{\mathrm{scaled}}}{\sum_{s,l} Y_{s,l}^{\mathrm{scaled}}} = \frac{C_{s,l}\,\sigma_{s,l}\,n_{s,l}}{C_{\mathrm{VB}}\,\sigma_{\mathrm{VB}}}, \qquad \text{where} \qquad C_{\mathrm{VB}} \equiv \frac{\sum_{s,l} C_{s,l}\,\sigma_{s,l}\,n_{s,l}}{\sum_{s,l} \sigma_{s,l}\,n_{s,l}}, \tag{7.7}$$

of the l-dependent site-specific valence yields $Y_{s,l}^{\mathrm{scaled}}$ and the total valence yield expressed by the sum in the denominator. The yields $Y_{s,l}^{\mathrm{scaled}}$ are identical to the spectral areas in Fig. 7.19. The dipole anisotropy factors $C_{s,l} = 1 + \beta_{s,l}$ calculated for the free atom from Tab. 7.2 were used, since values for the solid state are unknown. The values $\sigma_{s,l}$ represent the cross sections for a normalized initial wave function. The normalization was achieved by dividing the absolute cross sections $\sigma_{s,l}\,n_{s,l}$ by the number of valence electrons $n_{s,l}$ with angular momentum l at lattice site s. Since the spherical projections captured only 12.91 out of a total of 17.78 valence electrons per unit cell, scaling the number of states within the projection volumes

$n_{s,l}^{\text{spher.}} \equiv \int_{\text{VB range}} dE_B\, \rho_{s,l}(E_B)$ to the total number of valence states yielded the number of electrons $n_{s,l} \equiv n_{s,l}^{\text{spher.}}(n_s^{\text{Bader}} / \sum_s n_{s,l}^{\text{spher.}})$. Tab. 7.3 lists the normalized cross sections $\sigma_{s,l}$, which were determined for two photon energies.

s	n_s^{Bader}	l	$n_{s,l}^{\text{spher.}}$	$n_{s,l}$	2.753 keV			3.891 keV		
					$\sigma_{s,l}\, n_{s,l}$	$\sigma_{s,l}$	$\sigma_{s,l}^{\text{atomic}}$	$\sigma_{s,l}\, n_{s,l}$	$\sigma_{s,l}$	$\sigma_{s,l}^{\text{atomic}}$
Sr	0.689	s	0.061	0.088	14.8	167	56.0	8.88	100	27.5
		p	0.178	0.257	45.2	176	442	22.6	88.1	181
		d	0.238	0.344	66.7	194	60.7	23.6	68.6	17.6
Ti	1.836	s	0.067	0.096	40.4	419	68.2	15.2	158	30.6
		p	0.151	0.218	49.9	229	(312)	14.1	64.7	(106)
		d	1.053	1.522	25.1	16.5	8.46	4.78	3.14	1.93
O	5.084	s	0.029	0.039	2.31	19.5	179	1.70	14.4	65.4
		p	3.691	5.084	61.3	4.05	6.90	31.9	2.11	1.78
$SrTiO_3$	17.78	/	12.91	17.78	306	17.2	/	123	6.9	/

Table 7.3: Angular-momentum l dependent site-specific photoionisation cross sections for $SrTiO_3$ valence electrons. All values are given in barn. The number of states calculated by projection within spheres $n_{s,l}^{\text{spher.}}$ were scaled to the number of states inside Bader volumes n_s^{Bader}, which resulted in the number of states $n_{s,l}$ with l at lattice site s. The cross sections per electron $\sigma_{s,l}$ are compared to normalized values $\sigma_{s,l}^{\text{atomic}}$ calculated for atomic orbitals from Tab. 7.2. Details are explained in the text.

The systematic error for the obtained valence cross sections (disregarding the error bar of the tabulated Sr 3*d* reference value) includes the error of the valence cross section $C_{\text{VB}}\, \sigma_{\text{VB}}$ of 40% and an error of the anisotropy parameters $\beta_{s,l}$, which is estimated not to deviate more than 30% from the solid state values. Based on the experience gained during the data analysis, the error of the partial yields $Y_{s,l}^{\text{scaled}}$ that results from the XSW analysis and the fit is estimated not to exceed ±50% for titanium, strontium and the oxygen *p* states. For the oxygen *s* states, the alternative data analysis in appendix E suggested an error up to a factor 3. The particular choice of the cutoff radii for the spherical projections of the valence DOS has hardly any influence on the error of the valence cross sections. DOS spectra calculated by projection within small volumes are suitable for a comparison with XPS results, while projection within Bader basins will include space charge that is invisible to XPS. The total systematic error resulting from the various contributions amounts to ±65% (O *s*: +300%). Since the large error contribution from the valence cross section $C_{\text{VB}}\, \sigma_{\text{VB}}$ is identical for all the individual values $\sigma_{s,l}$, the relative disagreement between these values does not exceed ±50%.

The composition of the valence yield, corrected for angular effects in photoemission, is represented by the ratio of the cross sections $\sigma_{s,l}\, n_{s,l}$. In the ultraviolet, the large yield contribution from the oxygen causes the valence band spectrum to resemble the doubly peaked oxygen DOS spectrum. This is not the case in the X-ray regime, where the cross section for the light element oxygen is small so the oxygen has little influence on the valence band line shape.

The obtained normalized cross sections $\sigma_{s,l}$ vary over a range of two orders of

magnitude. The values for the Sr states and the Ti s and p states are one order of magnitude larger than the mean value for the valence states of 17 barn at $E_\gamma = 2.753$ keV. These states represent only a small fraction of the $SrTiO_3$ valence states, but they are highly overrepresented in the XPS spectrum. This was already observed by comparing the calculated XPS spectra and the lpDOS spectra in Fig. 7.19. The normalized cross section for strontium is nearly independent of angular momentum at the present photon energies; the strontium valence yield reflects the proportions of the lpDOS. The fact that the cross sections obtained for the titanium d and the oxygen p states are relatively small is no indication for electron delocalisation into bonding orbitals. Small normalized cross sections are predicted also for the free atom. Only deviations from these predictions can be interpreted as a sign of solid state effects. The ratio of the normalized cross sections $\sigma(\text{Ti } s)/\sigma(\text{Ti } d) = 25$ at 2.75 keV photon energy for $SrTiO_3$ compares to the ratio of 20 at 2.70 keV for TiO_2 as determined by Woicik *et al.* [5]. The ratio $\sigma(\text{O } s)/\sigma(\text{O } p) = 5$ is smaller but still of the same order as the ratio for TiO_2, which was reported to deviate by a factor 2 from the calculated ratio of 29. The similarity of the cross section ratios for the two oxides can be related to similar chemical environments of the titanium ion, which in both cases is octahedrally coordinated to oxygen ions.

A rigorous explanation for the differences between the cross sections for free atoms and atoms bound in a solid requires some knowledge about theoretical cross section calculations and is not aimed at within the framework of the thesis. In the following, a few simple arguments are given to describe influences of solid state effects on the photoionisation cross section.

The cross sections for valence electrons can be compared to those calculated for atomic orbitals only on a per-electron basis. A comparison on a per-electron basis is equivalent to comparing the transition matrix elements under the condition that the initial and (outgoing) final state wave functions are normalized. On one hand, a change in cross section when the solid is formed can therefore be interpreted as a change of the overlap integral of the wave functions (modulated by the transition operator), which indicates an electronic redistribution. The trend of the change towards either larger or smaller cross section may already be explained based on the simplistic picture that sizeable cross section contributions only originate from the vicinity of atomic cores. With increasing radial distance from the core, the contributions decrease rapidly, since the gradient of the crystal potential decreases and can no longer provide the momentum required for the photoemission process, as explained in context with Eq. 3.16 and the components of the transition matrix element depicted in Fig. 3.5 on page 21. On the other hand, changes in cross section when the solid is formed can also be interpreted as changes in the transition operator: In particular, the photoexcitation process in the free atom is facilitated by the gradient of a screened central potential, while in an oxide structure with a high ionic bonding contribution, the valence electrons are exposed to a large Madelung potential. This argument can explain increases in cross section per electron, when going from the atomic to the solid state, despite the increased delocalisation of valence states into spatial regions that are invisible to XPS (or that may become visible in the solid). Generally, the exact impact which the electronic redistribution or changes in the transition operator have on the photoionisation cross

section is difficult to estimate. It is *a priori* not clear to what extent changes in cross section are to be expected.

The normalized cross sections for the valence electrons, classified according to residental lattice site and angular momentum, are compared in Tab. 7.3 to the normalized cross sections for the $5s$, $4p$ and $4d$ atomic orbitals of strontium, the $4s$, $4p$ and $3d$ atomic orbitals of titanium and the $2s$ and $2p$ atomic orbitals of oxygen. These atomic orbitals provide the principal charge contributions to the valence band. The principal quantum number n of the atomic orbitals involved in the valence band formation is not evident from the calculated DOS spectra and is inferred from binding energy considerations. During solid state formation charge transfer occurs, in particular from the strontium ion to the TiO_3 array. This means that the valence charge with angular momentum l that resides at lattice site s is not necessarily derived predominantly from the orbital n, l of the element at lattice site s. This is in particular the case for the titanium p states, since the Ti $4p$ orbitals are unoccupied in the free atom. The Ti $4p$ atomic cross section is not tabulated, and a comparison is therefore not possible. The atomic value listed for the more strongly bound Ti $3p$ level is not appropriate for a comparison and is therefore set in brackets in Tab. 7.3.

For the valence electrons derived from atomic semi-core levels, like the Sr $4p$ and O $2s$ levels, a large decrease in normalized cross section is observed when going from the atomic to the solid state. While the outermost atomic shells are entirely reconfigured when the solid is formed, the more strongly bound semi-core shells are generally much less affected: The Sr $4p$ and O $2s$ levels mix to a little extent, owing to their similar binding energies, and provide a small contribution of states to the valence band. For the excitation of core level XPS signals, which can be seen in the survey scan in Fig. 7.5 on page 92, the cross sections calculated for the atomic orbitals remain approximately valid. The cross sections for the valence signal contributions, however, are significantly smaller. This deviation may be explained by a spatial redistribution of the valence charge derived from these electronic levels: While the semi-core electronic states reside in the close vicinity of the atomic core, the valence electronic states may be more delocalized in space.

For the least strongly bound electrons in the outermost atomic shells, two distinct trends are observed when the solid state is formed: The cross sections for the titanium states and the strontium s and d states are augmented, while for the oxygen p states a decrease was observed. The solid state effect is less pronounced for these weakly bound atomic shells than for semi-core shells. Since the outermost atomic shells typically have already delocalized charge distributions, the redistribution of charge during the solid state formation may not lead to large changes in photoionisation cross section. A larger influence than from the electronic redistribution may result from the generated Madelung potential, which affects the transition operator. The solid state effect comes to light clearly for the strontium s and d states: When the solid is formed, the strontium atom ionizes and loses a large part of its outermost electrons to the solid. From the point of view of the strontium ion, this is equivalent to a large delocalisation of charge. At the same time, the normalized cross section for the strontium valence states exceeds the value for the states in the free atom by about a factor 3. It appears plausible that the formation of the Madelung potential, providing large potential gradients over

large spatial regions, enhances the probability of photoexcitation in the vicinity of the strontium ion. The observed enhancements in cross section are basically identical for the strontium and the titanium states. For both elements, the same mechanism for the enhancements may be at work, since the net effect of the charge transfers is a loss of charge also at the titanium site.

For the oxygen p states the opposite trend, a reduction in cross section when going to the solid state was observed. The normalized cross section for O p valence states can be interpreted as a mean value for the σ-bonding, π-bonding and nonbonding states at the oxygen lattice site. The reduction in cross section may be attributed to the delocalization of the nonbonding and maybe part of the π-bonding states. The nonbonding electrons have lower binding energy than the σ- and π-bonding electrons and own the strongest free-electron-like character. This picture is supported by the pDOS spectra calculated within different integration volumes in Fig. 7.13 on page 103: Comparison of the spectra confirms that large parts of nonbonding oxygen states with 1–3 eV binding energy within the Bader volume are not even included by the large sphere of 1.8 a.u. radius around the oxygen atomic core. This is also true for part of the π-bonding states at 3.5–4.5 eV binding energy. The probability for photoexcitation of the space charge inbetween the atomic cores is close to zero. The delocalization of a large part of the O p valence states may explain the small cross section per electron.

7.9 Conclusion and Outlook

Summarising, the quantitative XSW analysis in combination with *ab initio* DFT calculations in the LDA approximation has revealed the relation between the lattice structure and the valence electronic structure of the ternary 3d metal oxide $SrTiO_3$. The valence yield components contributed by the strontium, the titanium, and the oxygen have been determined and agree very well with the theoretical one-particle calculations. The observed spectral features could be explained based on a σ and π bonding scheme. The composition analysis of the XPS valence yield has given the following picture: While they form the highest density of states in the valence band, the p states in the vicinity of the oxygen core are strongly underrepresented in photoemission spectra recorded at X-ray energies. The strontium states in contrast, which were ignored in previous valence electronic studies, are magnified in the spectra.

Angular-momentum dependent photoionisation cross sections were experimentally determined for individual valence states of $SrTiO_3$. The cross sections normalized to the number of valence states were compared to normalized tabulated values for the free atom. A significant reduction in normalized cross section compared to the tabulated value was obtained for those valence electrons that are derived from semi-core levels. This reduction may be understood as a consequence of electron delocalisation, which results in a reduced overlap of the initial and final state wave functions of the photoelectron. A reduction in normalized cross section was also observed for the p electrons at the oxygen site. The normalized cross section for electrons in the vicinity of the metal ions was found to increase despite delocalisation by typically a factor 3 when going from the atomic to the solid state. The increase can be interpreted as

an influence of the transition operator: The creation of the potential landscape when the solid is formed is the origin for an enhanced photoexcitation probability. Similar to the findings for valence states of the highly ionic oxide $SrTiO_3$, increased cross sections were also found for conduction states in metallic gold (appendix F), which interestingly does not have a Madelung potential (however, the estimated value for the effective attenuation length for carbon is yet to be confirmed).

This work has suggested future experiments. The valence electronic study on TiO_2 by the authors around Woicik and on $SrTiO_3$ by the our group could be completed by a study on strontium oxide, SrO, a material with a cubic rock salt structure. Common to all three oxides is the octahedral coordination of the oxygen ligands to a central atom, which is a covalently bound titanium atom in case of TiO_2 and $SrTiO_3$ and a ionically bound strontium ion in case of SrO. Mishra *et al.* [154] have proposed that the electronic properties of ternary and higher oxides may be explained in terms of the properties of simple binary oxides. This hypothesis could be experimentally tested, if the crystalline quality of SrO samples allows.

The electronic structure of $SrTiO_3$ could be compared to that of similar $ATiO_3$ perovskites, like $BaTiO_3$ or $LaTiO_3$, where the central A ion is embedded in similar titanium-oxygen lattice networks. The effects of the size of the A ion could be systematically studied. Oxides like V_2O_3 or HfO_2, the latter as a candidate for a new gate oxide material is also of interest in semiconductor industry, may be promising materials for a valence electronic structure analysis.

The influence of solid state effects on the photoionisation cross section, in particular the influence of the bond polarity and the particular electronic distribution, can probably be studied best on binary materials with good crystallinity, like on a series of different III-V semiconductors, where one element is systematically varied. Statements about individual bondings may be possible. The electronic structures of ternary materials, like $SrTiO_3$, may be too complex and the number of bonding interactions too large for a rigorous study of this kind. Cross section calculations for valence states would be interesting for comparison.

Measuring the angular emission anisotropy of the valence XPS signal as a function of binding energy provides complementary experimental information that may be of assistance for valence electronic studies. Mattsson *et al.* [155], who observed large variations in the dipole asymmetry parameter $\beta_{\mathrm{VB}}(E_B)$ throughout the valence band spectrum of benzole, C_6H_6, concluded that β is characteristic of the molecular orbital being ionized. Correspondingly, the spectrum of the dipole anisotropy factor $C_{\mathrm{VB}}(E_B) = 1 + \beta_{\mathrm{VB}}(E_B)$ represents a linear combination of the angular-momentum dependent values $C_{s,l}$, which are weighted by the product of cross section and density of states $\sigma_{s,l}\,\rho_{s,l}(E_B)$. The other way around, dipole anisotropy parameters for delocalised electrons in the solid can be experimentally obtained, once the valence band is known from the XSW analysis.

The experiment has suggested methodical improvements for future XSW investigations of valence electronic structures. For XSW in back reflection geometry, mounting the photoelectron analyser at the "double" magic angle at $\varphi = 90°$ and $\vartheta = 54.7°$ may improve the accuracy of the valence cross section determination. XPS intensity recorded at this detection angle does not require angular dipole or quadrupole

anisotropy corrections. The anisotropy parameters β, γ, and δ, which are not known for electrons in the solid and which are specific to the material system, are eliminated. Residual influence of anisotropy effects due to elastic scattering of the photoelectrons, which can magnify the effective detection solid angle of the electron analyser, cannot be avoided and will persist.

XSW experiments typically involve more than one Bragg reflection, like utilizing both the $SrTiO_3$(111) and (112) reflections for the present study. Performing the measurements for all reflections at the same photon energy can significantly simplify the data analysis, since the energy dependence of photoionisation cross sections does not need to be explicitly taken into consideration. The available Bragg reflections may not always be suitable to allow separating the individual valence yield contribution from each of the lattice sites. The contribution from certain sites, like from the strontium site in case of $SrTiO_3$, can only be determined by combining mixed yield components that contain contributions from more than one site. If the mosaic spread of the investigated sample is small enough to allow the back reflection condition to be lifted, mixed components recorded at the same photon energy can be directly combined by subtraction.

The XPS/XSW data acquisition mode can be further optimized to guarantee highest data quality and an efficient use of the available beam time. XSW scans over 11 equidistant photon energy steps within the Bragg range have been carried out. A higher XSW selectivity can be attained by selecting those photon energies, where the site-specific signals to be separated reveal the largest intensity contrast.

In order to better resolve the valence electronic structure of semiconducting samples, the spectral resolution may be improved by using doped samples to reduce band bending effects. The doping level must be low enough in order not to affect the electronic structure.

For probing valence electrons that are delocalised in the solid, monitoring an inelastic scattering process of the standing wavefield other than photoabsorption may be attempted. While photoexcitation of quasi-free electrons is inhibited, since the conservation of momentum cannot be maintained, Compton scattering is possible from unbound electrons (as well as from bound electrons). Compton scattering from valence electrons excited by an XSW field may be well detected in particular from light elements, owing to a high ratio of valence and core electrons. This has been demonstrated by Bushuev, Kazimirov and Koval'chuk [156] with Mo $K\alpha_1$ radiation ($E_\gamma = 17.5$ keV) for a slightly asymmetric Si(111) Laue reflection. However, monitoring the Compton scattering is hampered by an angular profile, which is strongly anisotropic in intensity and energy. The cross sections are small; values of 3 barn at $E_\gamma = 3$ keV and 11 barn at $E_\gamma = 15$ keV were calculated for germanium [157].

Chapter 8

Valence Electronic Structure of $YBa_2Cu_3O_{7-\delta}$

In comparison to the perovskite $SrTiO_3$, the valence electronic structure of which was analysed in chapter 7, the high-temperature superconductor $YBa_2Cu_3O_{7-\delta}$ has a more complex lattice structure, and a larger number of lattice sites contribute states to the valence band. It will be demonstrated in this chapter that the valence XPS yield mainly originates from one single element, the copper. By applying the XSW method it was attempted to discriminate contributions from nonequivalent lattice sites that are populated by different copper species.

8.1 Introduction

The high-temperature superconductor $YBa_2Cu_3O_{7-\delta}$ is structurally more complex than the perovskite $SrTiO_3$ and exhibits electronic properties, which have been subject of a large number of photoemission studies. The eight by symmetry nonequivalent lattice sites are populated by one barium, one yttrium, two copper and four different oxygen species, as marked in the sketch of the unit cell in Fig. 2.1(b) on page 6. A major contribution of valence states comes from the chain Cu(1) site and the in-plane Cu(2) site. Although the copper atoms on both sites are four-fold coordinated to oxygen, their local electronic structures show differences, as revealed by band structure calculations. When investigating the valence band of this oxide by XPS in combination with the X-ray standing wave technique, these differences should become visible. Separating valence contributions from different lattice sites, which are populated by the same element, is not possible with element-specific resonant photoemission: The site-specific XSW technique is unique in this respect.

The $YBa_2Cu_3O_{7-\delta}$ valence yield in the X-ray regime is dominated by the copper signals. This can already be predicted by a coarse estimate based on tabulated cross sections calculated for the free atom: Following the row of $3d$ transition metals in the periodic system of elements from the left to the right, the cross section normalized to the number of electrons for the $3d$ states continuously increases. The normalized cross section for Ti $3d$ states relative to the normalized value for O $2p$ states of $\sigma_{\mathrm{Ti}\,3d}/\sigma_{\mathrm{O}\,2p} \approx$

1.2 (1.7) for 3 (0.5) keV photon energy rises by an order of magnitude to a ratio of $\sigma_{\mathrm{Cu}\,3d}/\sigma_{\mathrm{O}\,2p} \approx 13$ (11). The $YBa_2Cu_3O_{7-\delta}$ valence band is, similar to the valence band of $SrTiO_3$, mainly composed of transition metal $3d$ and oxygen $2p$ states. However, the number ratio is shifted in favour of the transition metal states. Since the oxygen contribution to the $SrTiO_3$ valence yield is already relatively small, as confirmed by the results of the previous chapter, the increase in cross section for an in addition enlarged fraction of metal d states will cause the copper yield to clearly prevail over the oxygen yield. Correspondingly, owing to similar normalized cross sections $\sigma_{\mathrm{Ba}\,5p} \approx \sigma_{\mathrm{Y}\,4p} \approx \sigma_{\mathrm{Sr}\,4p}$, the valence yield contributions from yttrium and barium are also expected to be negligible compared to the predominating copper valence signal.

The partial density of states for the eight different lattice sites in Fig. 8.1 were calculated by self-consistent LAPW calculations by Krakauer, Pickett and Cohen [15] and by Larbaoui *et al.* [158], who additionally employed LDA and GGA schemes for a state-of-the-art treatment of exchange and correlation effects. The wave functions were

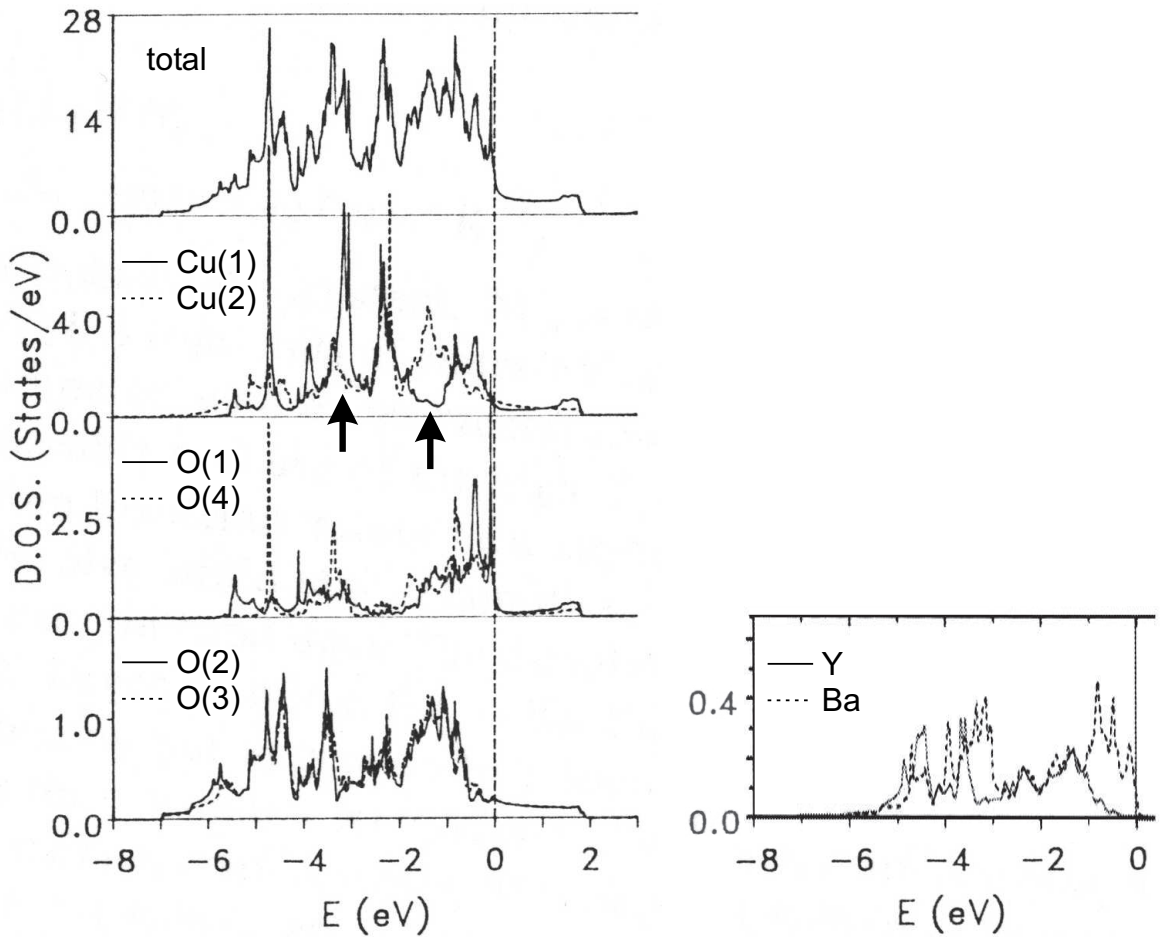

Figure 8.1: LAPW calculations of the DOS per unit cell and the pDOS per atom for $YBa_2Cu_3O_{7-\delta}$. Left figure adapted from Krakauer, Pickett and Cohen [15], right figure adapted from Larbaoui *et al.* [158]. The spectral features indicated by arrows are referred to in the text.

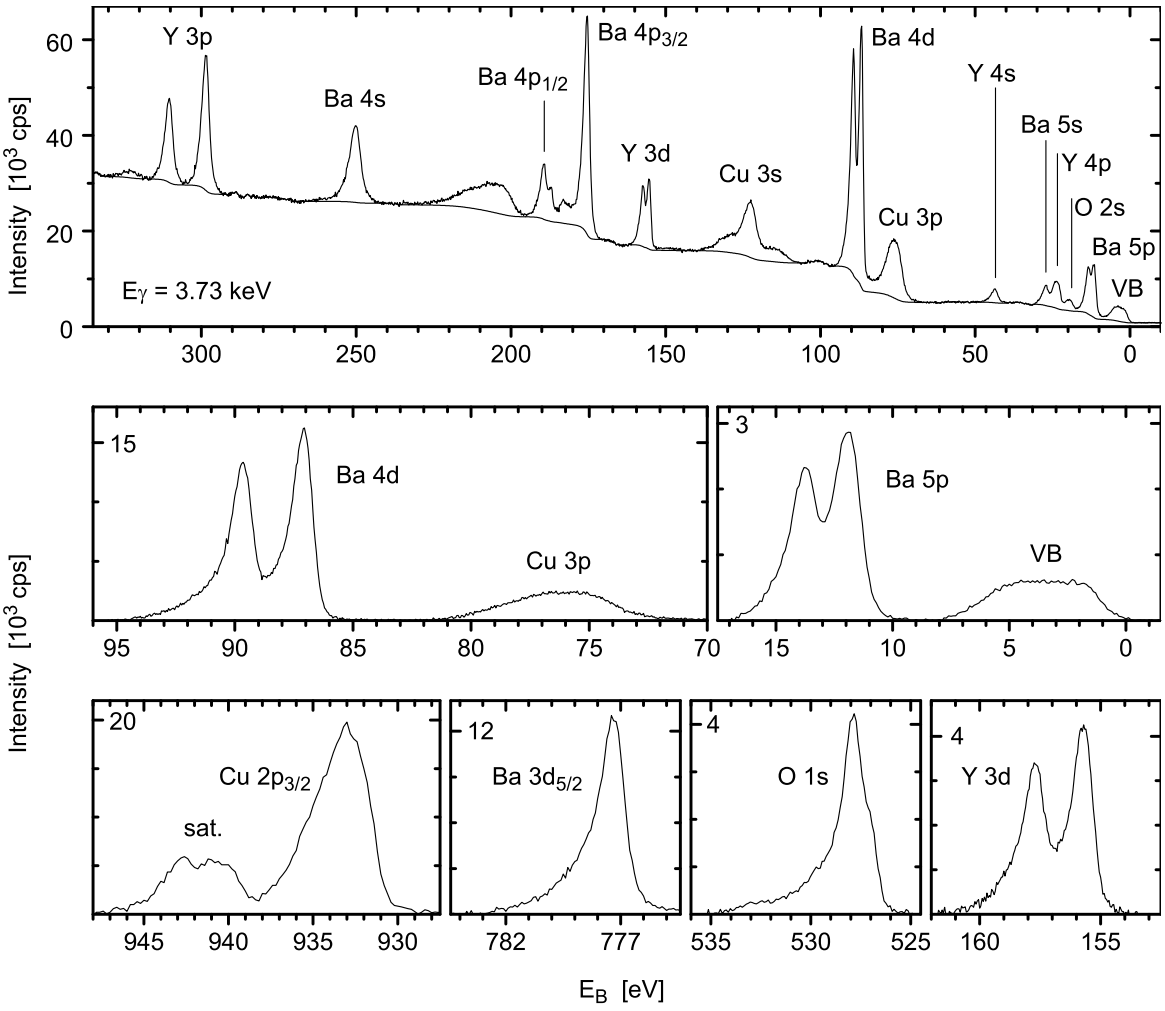

Figure 8.2: XPS survey spectrum and core level spectra for $YBa_2Cu_3O_{7-\delta}$. The survey spectrum from the clean surface of a low-temperature cleaved single crystal shows the core level signals identified and labelled. The individual core level spectra agree well with those shown by Brundle and Fowler [90].

projected within nonoverlapping spheres centered around the atomic cores. While the calculations by the two author groups differed in detail, the resulting pDOS spectra, which show considerable structure, were basically identical. The author group around Larbaoui pointed out the reasonable agreement of their *ab initio* calculations within the used approximations with available spectroscopic data for the band structure of $YBa_2Cu_3O_{7-\delta}$. Since the electrons in this material system are correlated, single particle calculations would usually be inappropriate. The partial density of states calculated for oxygen reveal metallic character, which results from strong hybridization of oxygen and copper states. The pDOS for the O(1) and O(4) sites and also for the O(2) and O(3) sites look very similar. This can be accounted for by their square four-fold coordination with the chain Cu(1) site and the in-plane Cu(2) site, respectively, and by the only weak coupling between planes and chains. Also a general similarity of the

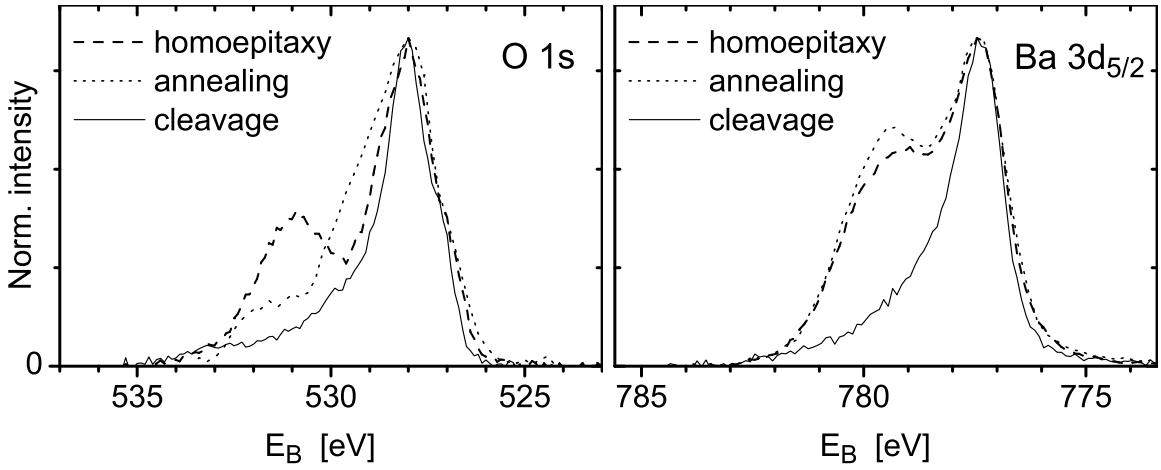

Figure 8.3: Comparison of core level XPS spectra from $YBa_2Cu_3O_{7-\delta}$ surfaces prepared by different methods. The O 1s and Ba $3d_{5/2}$ spectra were recorded from single crystal surfaces prepared by homoepitaxy (film of ∼15 nm thickness grown by PLD), annealing in pure oxygen (at $T = 450\,^{\circ}\mathrm{C}$ and 1 bar oxygen pressure for several days), and low-temperature cleaving (at $T \approx 50$ K). $E_\gamma = 2.7$ keV (homoepitaxy, annealing) and 3.7 keV (cleaved).

local electronic structures at the two copper sites results from their identical, four-fold coordination to oxygen. But they also exhibit differences, however, which are indicated by the arrows in Fig. 8.1: At about a binding energy of 3–3.5 eV, the density of Cu(1) states distinctively exceeds the pDOS for Cu(2). The spectra cross over in direction towards the Fermi edge, and the situation is reversed at about 1.5 eV binding energy. In contrast to the yttrium, the barium contributes states right up to the Fermi edge. The strong disagreement between the pDOS for yttrium and barium calls to mind that the often cited resemblance between the $YBa_2Cu_3O_{7-\delta}$ unit cell and a stack of three perovskite cells is confined to structural issues only.

Since about 95% of the copper valence states have d symmetry [158] and are equally weighted in the XPS spectrum by the same photoionisation cross section, the valence band XPS spectrum should be directly comparable to the pDOS spectra calculated for copper.

XPS/XSW measurements on $YBa_2Cu_3O_{7-\delta}$ have proved to be experimentally very challenging. The preparation of a clean surface, the crystalline quality of the sub-surface sample material that reflects the X-ray beam, and strain generation by the sample mounting are aspects discussed in the following section.

8.2 Surface Preparation and Characterization

$YBa_2Cu_3O_{7-\delta}(001)$ surfaces for XPS/XSW experiments have been prepared by various techniques: Epitaxial overlayers have been grown by PLD on the (001) surface of $NdGaO_3$, $SrTiO_3$ and $YBa_2Cu_3O_{7-\delta}$ single crystal substrates. Surfaces of as-grown $YBa_2Cu_3O_{7-\delta}$ crystals have been prepared by oxygen annealing. Low-temperature

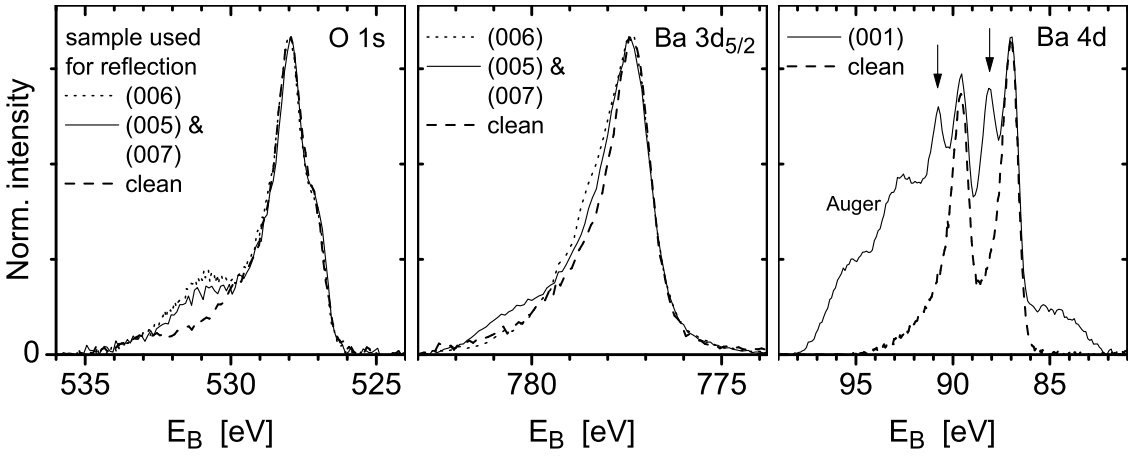

Figure 8.4: Chemical surface analysis: Core level XPS spectra for the $YBa_2Cu_3O_{7-\delta}$ samples. The O 1s, Ba $3d_{5/2}$ and 4d spectra recorded from the three cleaved surfaces, which were prepared for the XPS/XSW measurements for the $YBa_2Cu_3O_{7-\delta}$(005), (006), (007) and (001) reflection, are compared to the clean spectra from Fig. 8.2. The chemically shifted Ba 4d doublet is marked by arrows. The spectra were recorded at photon energies between 0.5 and 3.7 keV.

cleaving has been applied as a third method.

The chemical quality of $YBa_2Cu_3O_{7-\delta}$(001) surfaces can be readily assessed from the details of core level photoemission signals, which are a much more sensitive probe of the surface quality than the valence band region is. Fig. 8.2 shows spectra characteristic of a clean surface. Typical O 1s and Ba $3d_{5/2}$ spectra for surfaces prepared by the different techniques are compared in Fig. 8.3. Large chemically shifted components indicative of chemical surface modifications were observed for annealed samples and for epitaxial films. Clean surfaces were exclusively obtained by low-temperature crystal cleaving in UHV: The intrinsic O 1s spectrum shows a characteristic shoulder towards low binding energies and a tail on the high binding energy side. The spectrum is a poorly resolved superposition of peaks from nonequivalent lattice sites [90]. The asymmetric Ba $3d_{5/2}$ peak indicates a clean surface [159] with a certain areal fraction being BaO terminated.

XPS experiments in combination with XSW not only require an uncontaminated surface but also good crystalline quality of the bulk material underneath, which generates the standing wavefield. Satisfying these two requirements at the same time was a difficult task. Sample preparation by heteroepitaxy benefits from the significantly better crystallinity of $NdGaO_3$ and $SrTiO_3$ substrates. Homoepitaxy guarantees precise matching of the lattice spacing of the overlayer with the XSW period. This can considerably simplify the data analysis. $YBa_2Cu_3O_{7-\delta}$ crystals of not more than a few 10 μm thickness are particularly suitable as substrates, since they usually exhibit higher purity and better crystallinity than bulky crystals. However, the large amount of chemically modified phases on epitaxial and annealed surfaces compromises investigations of the valence electronic structure. An intrinsically clean surface can never be obtained for a PLD grown film, and low-temperature cleaving becomes the mandatory preparation method for this kind of study. For this reason, only those XPS/XSW

data will be discussed in the remaining chapter that were taken from samples prepared by cleaving. A demonstration that the XSW technique can be routinely employed to study $YBa_2Cu_3O_{7-\delta}$ single crystals with surfaces prepared by oxygen annealing has been published by the our group [160].

Cleavind did not always produce clean surfaces due to exposure of impurity inclusions. None of the three surfaces prepared for the XPS/XSW experiments was perfectly clean. The Ba $4d$ and O $1s$ spectra in Fig. 8.4 that were recorded during the chemical surface analyses preceding the XSW measurements, show chemically shifted components. The fact that almost intrinsic Ba $3d_{5/2}$ signals were observed shows that it is not always sufficient to rely exclusively on one single feature in the entire XPS spectrum to characterize the quality of a surface. Aging effects for the highly reactive surfaces were not observed for the duration of the XSW measurements.

The crystalline quality of the used $YBa_2Cu_3O_{7-\delta}$ crystals was found to be suitable for XSW measurements. The mosaic spread was comparable to the Darwin widths of the sample reflectivity in backscattering geometry. A number of as-grown samples with a thickness larger than 0.5 mm suitable for cleaving were characterized at beamlines ID32 and ID15c. The mosaic distribution, which was mostly asymmetric or revealed multiple peaks, was strongly dependent on the sampled surface region. The mosaic spread varied strongly around a mean of 0.1–0.2°, while the best values of 0.01–0.03° as shown in Fig. 8.5 were comparable to the best values measured by other groups [161].

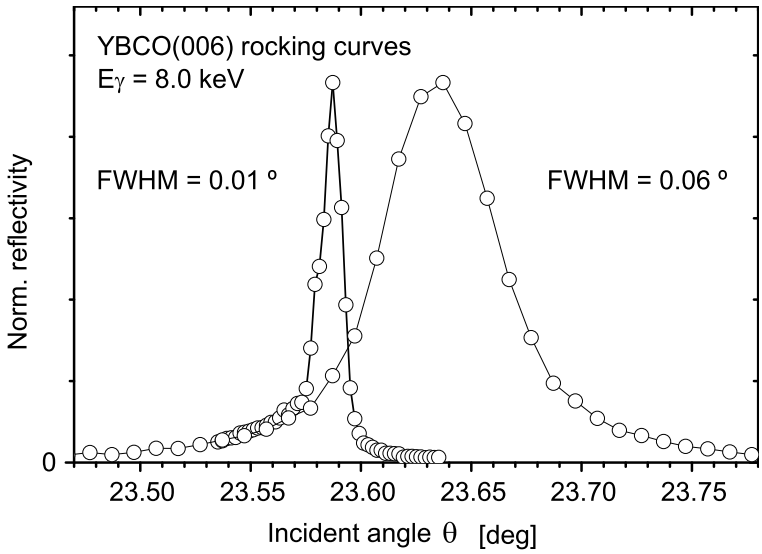

Figure 8.5: Mosaic spread of $YBa_2Cu_3O_{7-\delta}$ single crystals. Shown are a typical reflectivity curve and the narrowest curve out of several hundred measured. The incident beam was 0.1 × 0.15 mm in size. The data were recorded without $\mathbf{q}$ resolution.

The samples with the best crystalline quality were selected for the XSW measurements. The crystals were mounted in a way avoiding strain generation to the largest possible extent, which is crucial for XSW measurements in back reflection as discussed in section 4.3. Cleaving was carried out at temperatures below 40 K using the specially

designed cleaving devices presented in Fig. 4.10 on page 47. Only small regions of the cleaved areas, which were between 1 and 10 mm^2 in size, showed a mosaic spread small enough to allow XSW measurements.

The reflectivity curves recorded during the XPS/XSW measurements in (006) and (001) reflection were significantly broadened by the influence of mosaicity (or strain). The strongly reduced reflectivity led to a loss in XSW modulation. Simulated reflectivity curves for the ideal crystal lattice are presented in Fig. 8.6 for reference.

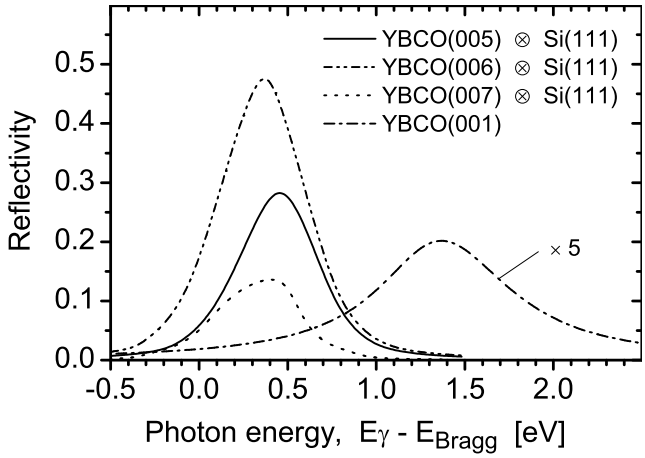

Figure 8.6: Simulation of $YBa_2Cu_3O_{7-\delta}(00\ell)$ reflectivity curves. The curves are simulated based on dynamical theory of X-ray diffraction for ideal crystals in back reflection and are convolved by the Si(111) reflectivity curve in order to include the broadening by the monochromator.

8.3 XPS/XSW Measurements

Cleaved surfaces of twinned $YBa_2Cu_3O_{7-\delta}$ crystals were freshly prepared and characterized, as described in the previous section, in the UHV chambers at the undulator beamlines ID32 and ID08. The crystals were grown by C. T. Lin [81] by the procedure described in section 4.3. Beamline ID32 was set up with the photoelectron analyser mounted within the polarisation plane of the beam at an angle $\vartheta = 45°$ with respect to the polarisation direction. A Si(111) monochromator was in use. The samples were cooled to a temperature of 40 K for the cleaving and the measurements. Beamline ID08 was equipped with a spherical grating monochromator with 1200 lines/mm and a Scienta SES-2002 photoelectron detector, which was mounted within the polarisation plane at $\vartheta = 55°$. The overall energy resolution of the setup was $\Delta E_\gamma \approx 150$ meV at 565 eV photon energy. The samples were held at 20 K.

XSW measurements on twinned crystals are confined to (00ℓ) Bragg reflections. The $YBa_2Cu_3O_{7-\delta}(005)$, (006) and (007) reflections, which are the three lowest accessible reflection orders with a Si(111) monochromator, and the (001) reflection were chosen for the XSW measurements. Tab. 8.1 lists, columnwise for each of the chosen reflections, the calculated coherent positions and fractions for six groupings of lattice

sites for a perfect lattice. The O(1) and O(4) sites as well as the O(2) and O(3) sites were combined, since the similarity of the partial DOS at these sites suggested that the individual valence yield contributions could not be experimentally distinguished. For the (005) and (006) reflections, all sites apart from the Y and the O(2,3) site, respectively, share the same coherent position. The contrast between the corresponding XSW absorption profiles results from different coherent fractions only and is for this reason expected to be weak. Strong XSW phase contrast between the XPS signals from Cu(1) and Cu(2) is only obtained for the (001) and (007) reflections. XSW measurements in (001) reflection benefit from high energy resolution and from high XPS count rates due to large photoionisation cross sections. However, a reflectivity as low as 0.04 for a perfect crystal strongly reduces the XSW modulation contrast. The modulation is larger in the (007) reflection with a reflectivity of 0.14, but the XSW measurement is hampered by low XPS count rates.

s	$P_s^{H\,theo}$				$F_s^{H\,theo}$			
	YBCO(hkl)				YBCO(hkl)			
	(001)	(005)	(006)	(007)	(001)	(005)	(006)	(007)
Y	0.5	0.5	0	0.5	1	1	1	1
Ba	0	0	0	0.5	0.401	0.881	0.787	0.249
Cu(1)	0	0	0	0	1	1	1	1
Cu(2)	0.5	0	0	0.5	0.616	0.175	0.668	0.998
O(1) + O(4)	0	0	0	0	0.694	0.519	0.972	0.839
O(2) + O(3)	0.5	0	0.5	0.5	0.722	0.779	0.130	0.592
Cu	0.5	0	0	0.5	0.077	0.450	0.779	0.332
O	0.5	0	0	0	0.115	0.668	0.343	0.021

Table 8.1: Theoretical coherent positions and fractions for $YBa_2Cu_3O_{7-\delta}(00\ell)$ reflections. The structural parameters for individual lattice sites and groupings of lattice sites s were calculated for the ideal lattice. The Debye-Waller factors were approximated by unity. The influence of inelastic scattering on the photoelectrons was not included in the listed values, i.e., the inelastic mean free path λ was assumed to be large compared to the c lattice constant, and the site-specific signal attenuation was disregarded. The coherent positions are given with respect to an origin fixed at the Cu(1) site.

XPS/XSW data sets were recorded at beamline ID32 for the $YBa_2Cu_3O_{7-\delta}$(005), (006) and (007) reflections at photon energies of 2.661, 3.193 and 3.725 keV, respectively, in back reflection geometry. The data were taken for the Y $2p_{3/2}$, Ba $3d_{5/2}$, O $1s$ and Cu $2p_{3/2}$ core levels and the valence band for the purpose of locating the origin of the valence signal.

High resolution XPS/XSW data for the purpose of the valence electronic structure analysis were measured for the (001) and (007) reflections. For the (007) reflection, valence band spectra for three different photon energies within the range of Bragg reflection were recorded: At each energy, raw spectra were continuously accumulated in quick scans for an acquisition time of about 80 min and superimposed afterwards. Reflectivity curves recorded before and after each acquisition period confirmed that the

photon energy was stable within ±0.1 eV. Hence, each of the three valence band spectra obtained was additionally smeared out in binding energy by not more than 0.2 eV. For the (001) reflection, a set of 14 spectra was recorded for the valence band at beamline ID08. The data were taken in the same mode as for the (007) reflection by collecting angle-integrated photoemission for 15 min per spectrum. Using the back reflection geometry was ruled out by a Bragg energy in the immediate vicinity of the oxygen K absorption edge. In this energy range, the energy profile of the absorption, which results from resonance phenomena, will be superimposed on the absorption profile resulting from the XSW effect. By selecting an incident angle of $\theta = 70°$, the kinematical Bragg energy was set to 563.5 eV. At this energy, constant absorption over the XSW scan range of a few electron volt, confirmed by the sample drain current in Fig. 8.7, allowed XSW scans to be carried out as energy scans. Angular XSW scans at fixed photon energy have proved to be disadvantageous: XSW absorption profiles were observed to become distorted by variations in XPS intensity, when the beam spot and the analyser focal point moved on the sample surface.

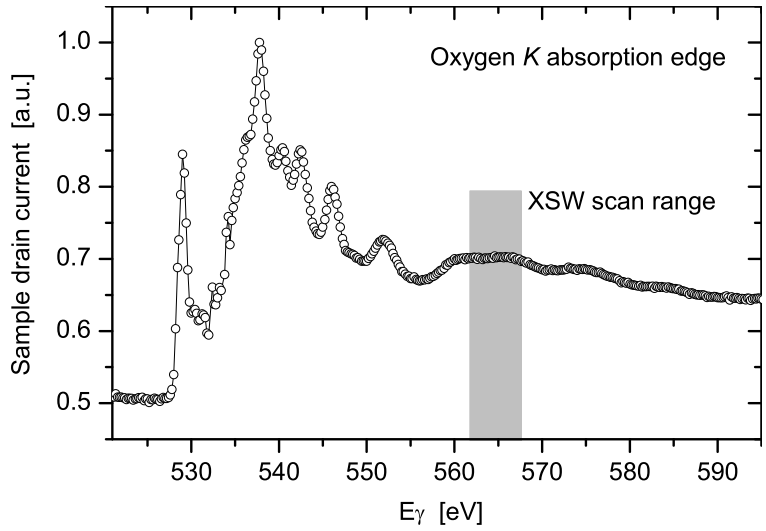

Figure 8.7: X-ray absorption spectrum for $YBa_2Cu_3O_{7-\delta}$ around the oxygen K edge at $E_\gamma = 530$ eV. The absorption, measured by the sample drain current, is constant over the XSW scan range (shown shaded) for the $YBa_2Cu_3O_{7-\delta}(001)$ reflection.

8.4 Analysis and Discussion

The information about the element-specific composition of the valence yield is contained in the line shape of its XSW modulation. Fig. 8.8 compares the (005), (006) and (007) XSW yield analyses for the $YBa_2Cu_3O_{7-\delta}$ valence band and the core levels. The amplitude of the XSW yield profiles has to be interpreted with caution, since the electron analyser was not mounted in a quadrupole-free geometry. The extracted coherent positions and fractions listed in Tab. 8.2 are presumably influenced by quadrupole effects. Throughout all the reflections, the valence signal, which is excited from the

part of the valence charge residing at atomic cores, shows a very similar response to the moving X-ray standing wavefield as the core level signal from copper. No response of the rare earth elements appears to be superimposed: In the (005) reflection, the yield profile for the yttrium reveals an inverted line shape, and the XSW dependence of the barium signal shows a distinctly larger modulation amplitude. The elemental core level signals unfortunately show little modulation contrast in each of the (006) and (007) reflections. Nevertheless, the (006) reflection confirms that the valence emission profile does not follow the oxygen profile. This becomes more evident from the coherent position $P_{\mathrm{O}}^{006} = 0.20$ for the oxygen, which in contrast to copper with $P_{\mathrm{Cu}}^{006} = 0.05$

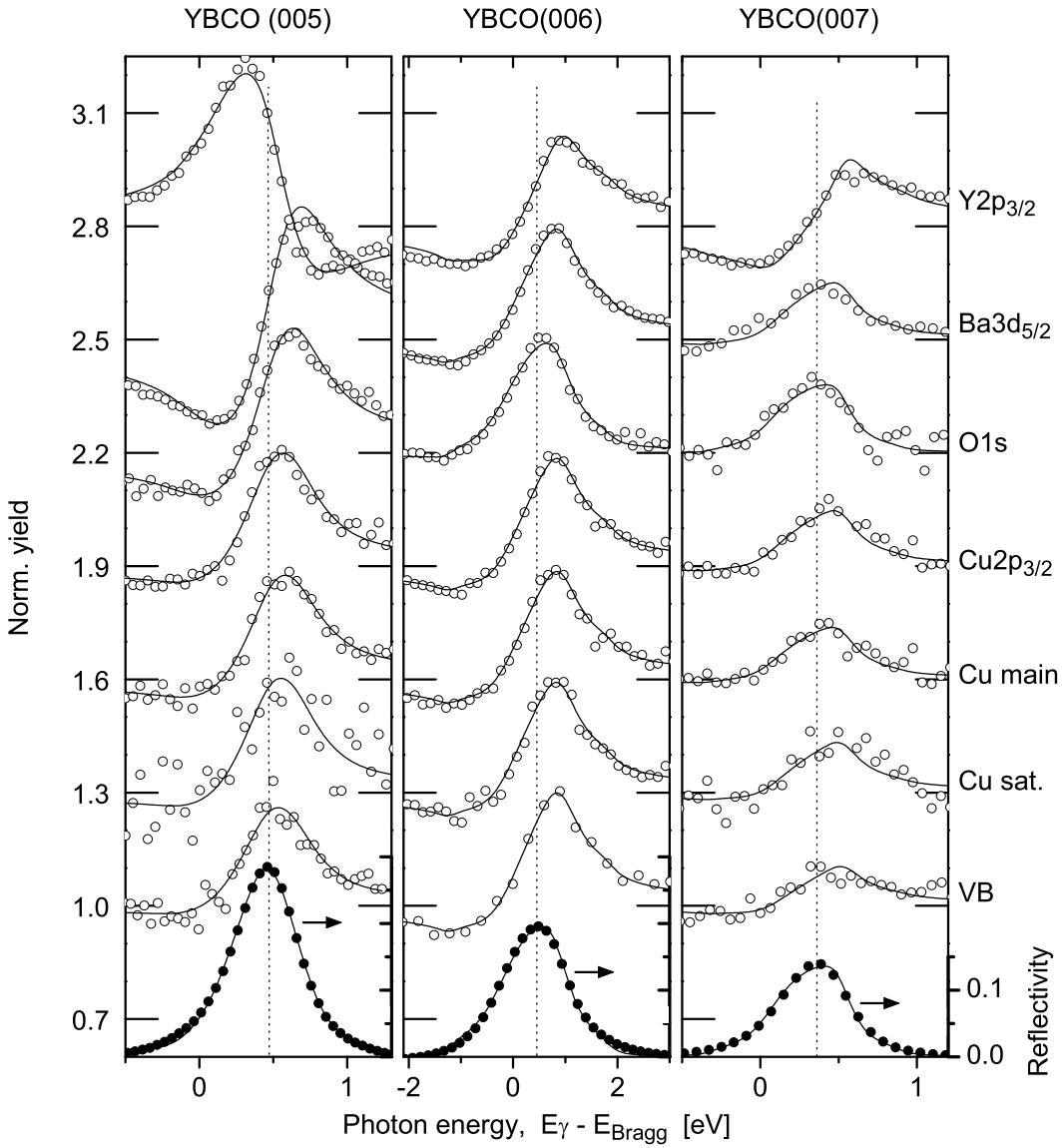

Figure 8.8: Core and valence level XSW yield for $YBa_2Cu_3O_{7-\delta}(00\ell)$ reflections. The curves for the individual electronic levels, as labelled on the right-hand side, are offset for clarity.

s	P_s^H			F_s^H		
	YBCO(hkl)			YBCO(hkl)		
	(005)	(006)	(007)	(005)	(006)	(007)
Y	0.513	0.989	0.466	0.459	0.708	0.692
Ba	0.964	0.067	0.533	0.671	0.529	0.152
Cu	0.004	0.053	0.522	0.236	0.531	0.150
Cu main	0.981	0.055	0.500	0.252	0.526	0.117
Cu sat.	0.014	0.062	0.477	0.210	0.523	0.212
O	0.987	0.196	0.753	0.436	0.276	0.125
VB	0.972	0.058	0.424	0.155	0.564	0.263

Table 8.2: Experimental coherent positions and fractions for $YBa_2Cu_3O_{7-\delta}(00\ell)$ reflections. The listed values were determined by fitting the dipole expression given by Eq. 3.21 to the XSW yield profiles presented in Fig. 8.8.

deviates from the value $P_{\mathrm{VB}}^{006} = 0.06$ for the valence band. The XSW data agree with the picture that the valence yield indeed originates mainly from the copper sites.

The XSW modulation of the Cu $2p_{3/2}$ main peak and its satellite have been analysed separately. Different XSW results for these two signals would be an indication for the existence of nonintrinsic copper species. The origin of the satellite structure, which is characteristic of copper in the (formal) oxidation state +II as in CuO, is associated with two possible final states for the photoexcitation [162]. The better screened $|\underline{c}3d^{10}\underline{L}\rangle$ final state, which leads to the main peak, is separated in energy by 9 eV from the more poorly screened $|\underline{c}3d^{9}\rangle$ final state, which gives rise to the satellite. $\underline{L}$ denotes a hole in one of the oxygen ligands, and $\underline{c}$ represents a core hole created in the $2p_{3/2}$ level by the photoemission process. The satellite signal exclusively originates from Cu^{II} in the intrinsic bulk material, while the main peak can also contain signal contributions from reduced Cu^{I} that is typically present in nonintrinsic phases. The agreement of the coherent positions and fractions for the main peak and the satellite structure within the experimental error confirms the results of the chemical surfaces analysis: The sample surface is not significantly contaminated.

The XSW data taken for the $YBa_2Cu_3O_{7-\delta}(001)$ reflection are presented in Fig. 8.9. The 14 valence band spectra shown in Fig. 8.9(a) were recorded within the energy range of the Bragg reflection for 14 different positions of the X-ray standing wavefield relative to the crystal lattice. The spectra do not show any variation in line shape in response to the spatial intensity variation of the X-ray field, as the two-dimensional representation of the spectra in Fig. 8.9(b) confirms. Traversing the Bragg reflection by increasing the photon energy, the intensity maximum of the wavefield is moved from the planes, which terminate the unit cell and contain the copper oxide chains, across the unit cell towards the diffraction planes, which contain the yttrium site at the centre of the unit cell. The wavefield passes the Cu(1) and Cu(2) sites one after the other, which contribute the by far largest components to the valence yield. Due to the atomic number ratio, the Cu(1) : Cu(2) signal intensity ratio is expected to be about 1 : 2. The XSW modulations of the individual components were not experimentally

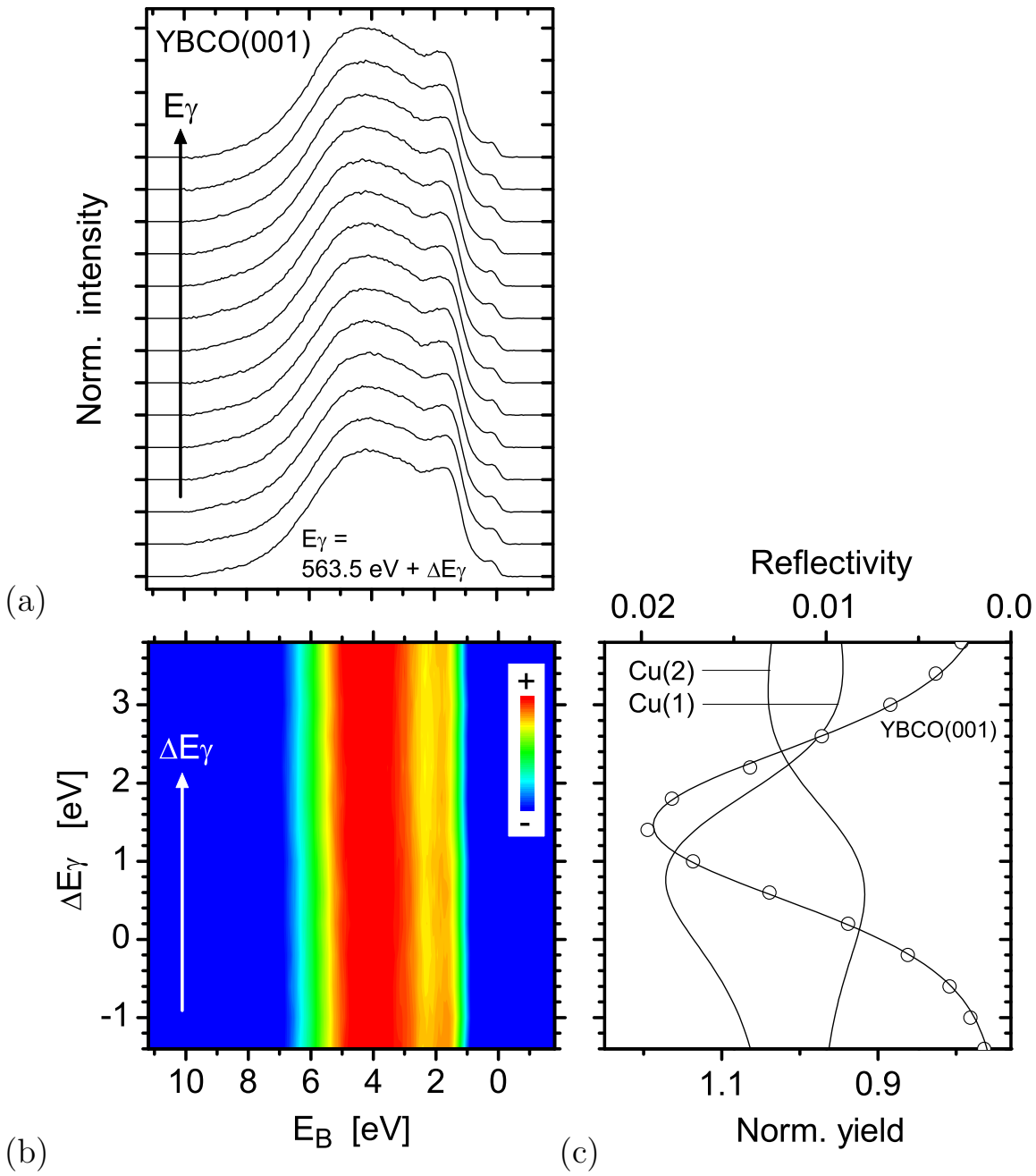

Figure 8.9: Valence band XSW data for the $YBa_2Cu_3O_{7-\delta}(001)$ reflection. (a) Changes in the line shape of the valence band spectrum recorded under XSW conditions. The photon energy increases by 400 meV from spectrum to spectrum. The Fermi edge of the valence band is clearly resolved. The low X-ray energy allowed very good statistics of 2×10^5 counts in the peak of a single VB spectrum off of the Bragg condition. (b) Two-dimensional representation of the VB data. (c) Experimental reflectivity curve and XSW yield profiles for the Cu(1) and Cu(2) sites simulated for an imperfect lattice.

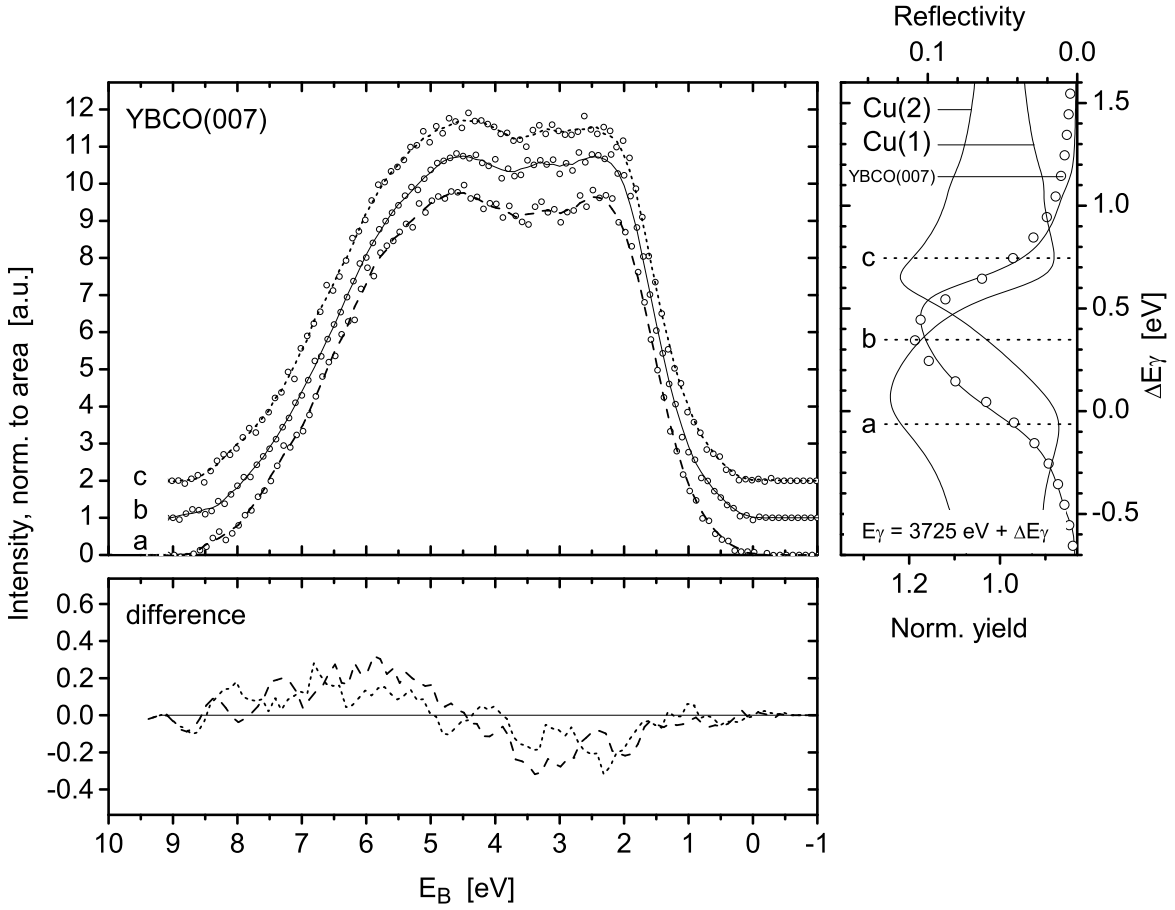

Figure 8.10: Valence band XSW data for the $YBa_2Cu_3O_{7-\delta}$(007) reflection. The spectra, recorded under XSW conditions in steps of 400 meV, were smoothed as represented by lines. A single spectrum has $\sim 5 \times 10^3$ counts in the peak for normalized field intensity. The lower panel shows the differences of curves (a) and (c) with respect to curve (b) on a five times expanded scale. The S-shape of the curve represents systematic errors during background subtraction.

accessible from the core level signal and were, hence, simulated. The reflectivity curve and the two XSW yield curves shown in Fig. 8.9(c) were convolved by a Gaussian function of 1.86 eV FWHM width to take the mosaic spread into consideration. The influence of structural disorder reduces the reflectivity to 0.02, which is about 50% of the reflectivity of the ideal lattice. Surprisingly, no XSW effect was observed for the $YBa_2Cu_3O_{7-\delta}$ valence band in (001) Bragg reflection. It is possible that the XSW modulation contrast, which suffered from the very low reflectivity, was insufficient to bring out the signature of the individual copper components. This gave reason for repeating the measurements in the (007) reflection, where a larger reflectivity was expected.

$YBa_2Cu_3O_{7-\delta}$ valence band spectra taken at three different photon energies within the range of the (007) Bragg reflection are presented in Fig. 8.10. The contrast between the XPS signals from the Cu(1) and Cu(2) sites was maximized by placing the wavefield

intensity maximum in the unit cell on either the Cu(1) or Cu(2) coherent position. Even having exploited the larger XSW modulation of the (007) Bragg reflection, no variation in line shape was observed for the valence band spectra. The difference between the spectra (a) and (c) with the largest modulation contrast is within the experimental error and is therefore not significant. The measurement for the (007) reflection was repeated two times, as shown in Fig. 8.11, but apart from deviations in spectral shape caused by the surface chemistry no modulations were observed.

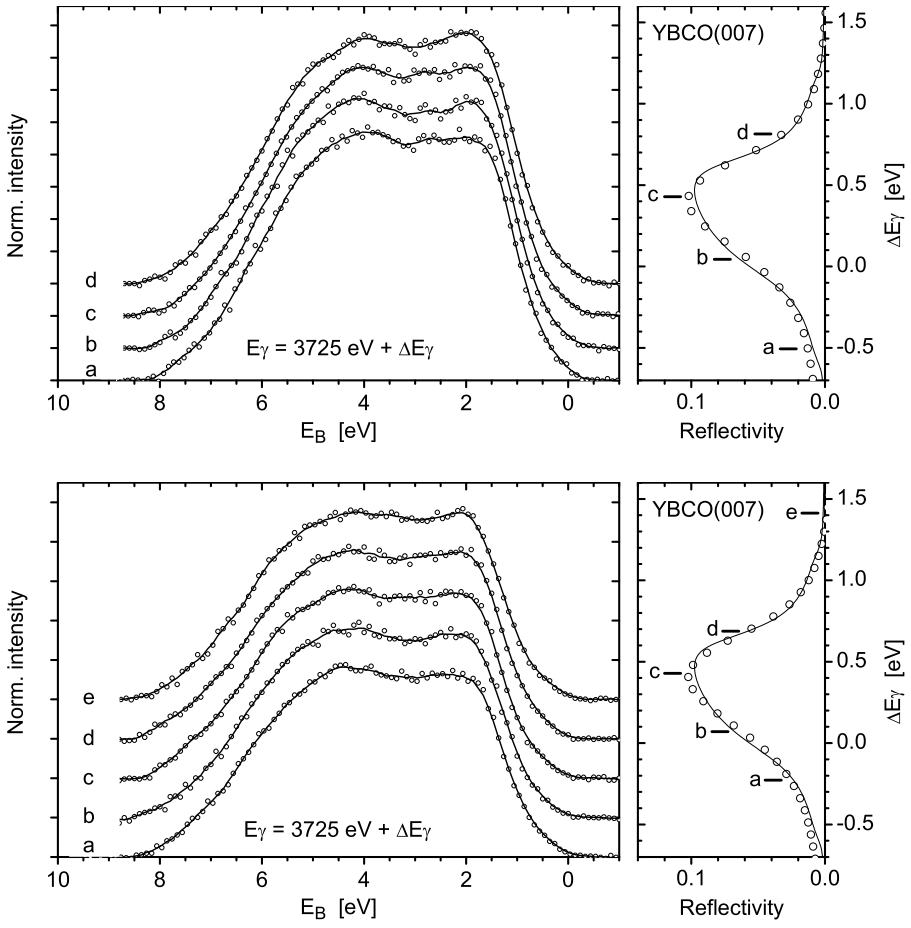

Figure 8.11: Valence band XSW data for the $YBa_2Cu_3O_{7-\delta}$(007) reflection. Repeat of the measurement shown in Fig. 8.10.

Summarising, the XSW study confirmed that the $YBa_2Cu_3O_{7-\delta}$ valence yield in the X-ray regime mainly originated from the copper sites. This agrees with estimations based on tabulated photoionisation cross sections. Preferentially exciting different lattice sites in the $YBa_2Cu_3O_{7-\delta}$ unit cell was not observed to cause changes in the valence band XPS spectrum. Hence, the XSW study has shown that the valence yield contributions from the Cu(1) and Cu(2) sites are identical within the experimental resolution. This is in contrast to theoretical predictions for the site-specific density of states, however: The partial DOS spectra calculated for the Cu(1) and Cu(2) site reveal differences in line shape. Owing to these differences, line shape variations of the

valence band XPS spectrum were expected to occur when scanning the photon energy through the energy range of a (suitable) Bragg reflection. The site-specific DOS spectra that were used for the comparison with the data were calculated by integrating the valence states within nonoverlapping spheres [15,158]. Since the amount of space charge in $YBa_2Cu_3O_{7-\delta}$ is theoretically predicted to be relatively small [15], the calculated spectra should not contain many delocalised states that are invisible to XPS. It can be concluded that the data do not confirm the theoretically calculated density of states at the two copper sites.

Comparing the valence band spectra recorded at 565 eV and 3.725 keV in Figs. 8.9 and 8.10 reveals some difference in spectral line shape. The calculations predicted the vast majority of 95% of the copper states to have d symmetry. The presence of a minority of other valence states, which have photoionisation cross sections with an energy scaling behaviour distinct from that of the Cu d states, becomes immediately noticeable from the observed discrepancy between the spectra. Angular-momentum resolved DOS calculations may help to identify yield contributions from Cu s and p states in the valence XPS spectra.

Valence contributions from several elements, the yttrium, the barium and the oxygen, could not be identified in the present study. Unfavourable cross section ratios led to imbalances between the individual valence yield contributions. It is a limitation of the XSW technique that only comparable site-specific valence yield contributions can be separated. In the present study, the copper valence yield was significantly larger than the contributions from other lattice sites.

Chapter 9

Conclusion and Outlook

In this thesis, the X-ray standing wave method has been employed for studying the interface structure and valence electronic properties of $YBa_2Cu_3O_{7-\delta}$ and $SrTiO_3$, using third generation synchrotron light. Valence photoelectron spectroscopy has been extended into the hard X-ray region.

The X-ray standing wave technique has conventionally been used as a tool for structure determination with chemical selectivity and very high spatial resolution power. A classical application was the determination of the adsorption site coordinates for atoms and molecules deposited on crystal surfaces. Finding the atomic position relative to the crystal surface by triangulation, i.e., by measuring the distance of the adsorber site relative to the substrate in three independent directions, required in principle no more than recording the XSW absorption profiles across the ranges of three different Bragg reflections. The availability of most brilliant X-ray light at third generation storage rings has allowed developing and improving the X-ray standing wave technique, and new fields of application have recently emerged: The first one is XSW real space imaging, which exploits the possibility to record large data sets within reasonable periods of time for structural studies. In this thesis, XSW real space imaging has been used to investigate the nucleation mechanism, i.e., the growth of the initial monolayer, of the high temperature superconductor $YBa_2Cu_3O_{7-\delta}$ on the (001) surface of $SrTiO_3$. Besides extensive structural studies, the brilliant radiation also made investigations of the electronic structure feasible: A second novel application is the XSW valence electronic structure analysis, which was used to investigate the correlation between structural and electronic properties for two oxide compounds, $SrTiO_3$ and $YBa_2Cu_3O_{7-\delta}$. The parts of the valence band of $SrTiO_3$, which can be assigned to the strontium, titanium, and oxygen sites of the lattice, were unambiguously identified. This thesis has further dealt with exploring the hard X-ray region up to 13.5 keV photon energy for photoelectron spectroscopy on core levels as well as the valence band. Hard X-ray photoelectron spectroscopy (HAXPES) was used to chemically analyse the reactive $YBa_2Cu_3O_{7-\delta}(001)$ surface prepared at ambient air.

The structural investigations on 0.5 and 1.0 ML coverages of $YBa_2Cu_3O_{7-\delta}$ prepared by pulsed laser deposition (PLD) on $SrTiO_3(001)$ have helped to gain an insight into the nucleation process of a heteroepitaxially grown multi-elemental material with a complex unit cell. In contrast to bulk material, thin films deposited by PLD gen-

erally grow under conditions far away from thermodynamic equilibrium. Correspondingly, the nucleation processes can be very different: While crystal growth starts by a spontaneous nucleation in a locally undercooled zone of a melt and continues by stoichiometric accumulation of more and more material by a material-specific mechanism, quite complicated processes can occur during the nucleation of thin films. Our XSW study of the nucleation mechanism has shown that, prior to the formation of the bulk $YBa_2Cu_3O_{7-\delta}$ phase on the $SrTiO_3(001)$ substrate surface, a precursor phase is formed: Three-dimensional XSW real space images of elemental atomic distributions directly confirm that coverages of less than one monolayer thickness are composed of $BaCuO_{3-x}$ (BCO) and $YCuO_{3-x}$ (YCO) perovskite subunits. An initial stacking sequence of mainly (BCO)–(BCO)–(YCO) is found, starting from the substrate interface. The stacking order suggests that the precipitating material, which at all stages during the PLD deposition is stoichiometric, permanently rearranges. By atomic reordering the deposited material attempts to arrange in the $YBa_2Cu_3O_{7-\delta}$ sequence from the very beginning of the growth. The formation of a perovskite precursor phase is forced by surface and interface energies. Supplementary SXRD information shows that the substrate surface is not entirely wetted during the nucleation; the deposited material nucleates in islands. As soon as a critical amount of material has been deposited, the complex $YBa_2Cu_3O_{7-\delta}$ material with bulk stoichiometry forms. Our results confirm complementary real-space information obtained by previous STM and STS studies, which could not directly probe the lattice and interfacial structure of the film. The understanding gained from the XSW direct imaging study has helped to unravel the nucleation mechanisms of $YBa_2Cu_3O_{7-\delta}$ on the (001) surface of $SrTiO_3$.

Site-specific photoemission spectroscopy applied to the valence band of $SrTiO_3$ has allowed correlating the electronic and atomic structures of the ternary oxide. Electronic properties, in particular band structures and the density of states, have been successfully predicted by density functional theory for a large variety of different materials. Photoelectron spectroscopy, which is the most important tool for studying the electronic structure of solids, has often not been able to directly verify these theoretical predictions, owing to a lack of spatial resolution power. If applied in combination with the XSW technique, photoemission spectroscopy becomes site specific. The valence band or superpositions of chemically shifted core level signals can be decomposed, i.e., individual lattice sites can be probed for their partial signal contribution. We have experimentally decomposed the valence band XPS spectrum of $SrTiO_3$ into the partial yield components contributed from the strontium, the titanium, and the oxygen sites without additional prior information necessary. The site-specific yield components were decomposed further over angular momentum by comparison to LDA calculations, using the photoionisation cross sections as scaling factors. The valence band XPS spectrum of $SrTiO_3$ agrees very well with the results of the one-particle calculations. The p states in the vicinity of the oxygen core, which represent the highest density of states in the valence band, are strongly underrepresented in the photoelectron spectrum in the X-ray regime. The very low density of states at the strontium ion, in turn, appear strongly overweighted. With the help of a σ and π bonding scheme for an octahedral TiO_6 unit, the spectral features could be related to the atomic structure. Similarities in the valence electronic structures of $SrTiO_3$ and rutile TiO_2, a material investigated

by another research group, could be related to common structural features.

A priori unknown photoabsorption cross sections for angular-momentum dependent site-specific valence states of $SrTiO_3$ were uniquely determined. The experimental cross sections deviate from values calculated for the free constituent atoms, which can be interpreted as a result of the solid state formation: Delocalisation of electrons, which are contributed by atomic semi-core levels to the valence band when going from the atomic to the solid state, accounts for a reduction in cross section (normalised to the number of valence states). Despite delocalisation effects, increases in photoabsorption cross section were obtained for valence states in the vicinity of metal ions. This unexpected behaviour can be related to the formation of highly ionic solid. Electrons with low binding energies no longer experience the screened central potential of a free atom but are exposed to a large Madelung potential. The operator in the transition matrix element, which depends on the gradient of the crystal potential, furnishes an increase in the spatial region where photoexcitation can take place. The photoabsorption cross section thus increases as a consequence of the solid state formation.

Site-specific photoemission spectroscopy applied likewise to the valence band of $YBa_2Cu_3O_{7-\delta}$, a more complex oxide, did not confirm the site-specific density of valence states predicted by LDA calculations. Copper states of d symmetry represent the highest density of valence states and also contribute the dominating electron yield to the valence XPS spectrum. Theoretical calculations have predicted the local density of valence states at the two inequivalent Cu(1) and Cu(2) sites to be distinct. Remarkably, the site-specific density of copper states were found to be equal within the experimental error. The valence photoelectron yield originating from s or p states is small. Its presence becomes apparent, however, from the distinct line shapes of the valence band measured in the hard and in the soft X-ray ranges. The change in line shape results from distinct energy scaling behaviours of the angular-momentum dependent photoionisation cross sections.

Photoelectron spectroscopy in the hard X-ray range (HAXPES) benefits from enhanced bulk sensitivity, which results from an increased attenuation length for photoelectrons with high kinetic energy. Signal contributions from surface states and contaminants can be efficiently suppressed, and reactive surfaces can be prepared under less stringent vacuum conditions. In a technical development, the operational range of a commercial photoelectron analyser has been extended by adding a supplementary retarding lens (designed by C. Kunz). At photon energies of up to 13.5 keV, carbon signals from the surface of an $YBa_2Cu_3O_{7-\delta}$ sample prepared in ambient air were observed to significantly diminish. However, also the signal intensity from bulk states with higher angular momenta or from light elements can strongly suffer from low photoionisation cross sections. The possibility of focussing, in turn, may allow compensating the low photoabsorption cross sections of valence states in the hard X-ray regime by a high primary photon flux.

Experimental techniques that appeared to be impossible yesterday have become the standard techniques of today. It will therefore be interesting to pursue the development of HAXPES in the future. An experimental station for hard X-ray photoelectron spectroscopy is currently being set up at beamline ID32 at the ESRF. A newly developed commercial electron analyser with an operational range of electron energies

up to 15 keV will be installed in the near future. There are several good reasons for performing photoemission studies in the hard X-ray range: (a) the large escape depth of ∼10 nm for photoelectrons with 10 keV energy leads to an improved bulk sensitivity; (b) monochromatic hard X-rays are available with an energy resolution of ∼10 meV; (c) photoemission can be combined with other hard X-ray techniques, like X-ray diffraction or X-ray standing waves, where higher reflection orders can be reached; (d) HAXPES may become an important tool for nondestructive chemical analysis and for accessing the electronic structure of buried interfaces, clusters and nanocrystalline materials. HAXPES is a rapidly growing and promising field of activity.

Appendix A

List of Symbols

The following list gives an overview of the abbreviations that are used in the text:

AES	*Auger electron spectroscopy*
AFM	*Atomic force microscopy*
AO	*Atomic orbital*
APW	*Augmented plane wave*
ARPES	*Angle resolved photoelectron spectroscopy*
a.u.	*atomic unit* — the Bohr radius; convenient unit of atomic distances: 1 a.u. $= \hbar^2/me^2 = 0.529$ Å
cps	*counts per second*
DFT	*Density functional theory*
DOS	*Density of states*
EAL	*Effective attenuation length*
ESCA	*Electron spectroscopy for chemical analysis* — An alternative expression for PES introduced by K. Siegbahn.
ESRF	*European Synchrotron Radiation Facility*
FWHM	*Full width at half maximum*
GGA	*Generalized gradient approximation* — An approximation used in theoretical DFT calculations.
HAXPES	*Hard X-ray photoelectron spectroscopy* — PES employing hard X-rays in the energy range of 5–15 keV.
HRTEM	*High-resolution transmission electron microscopy*
HTS	*High-temperature superconductor* or *superconductivity*
IMFP	*Inelastic mean free path* — The average distance that an electron with a given energy travels in a solid between successive inelastic collisions.
LAPW	*Linearized augmented plane wave*
LCAO	*Linear combination of atomic orbitals*
LDA	*Local density approximation* — An approximation used in theoretical DFT calculations.
LEED	*Low energy electron diffraction*
lpDOS	*angular-momentum l resolved partial density of states* — Density of states with angular momentum l in the vicinity of a specific lattice site.

MBE	*Molecular beam epitaxy*
ML	*Monolayer*
MO	*Molecular orbital* — An orbital formed as a linear combination of AOs within the framework of the LCAO method.
pDOS	*partial density of states* — Density of states in the vicinity of a specific lattice site.
PLD	*Pulsed laser deposition*
QMS	*Quadrupole mass spectrometry* — QMS is frequently used for residual gas analysis in UHV equipment.
R2P2	Rotary multiport distribution vessel for sample transfer and sample handling; trademark by Vacuum Generators.
RHEED	*Reflection high energy electron diffraction*
r.l.u.	*reciprocal lattice units* — Unit used for the reciprocal space.
Ry	*Rydberg* — the ground-state binding energy of the hydrogen atom; convenient unit of atomic energies: 1 Ry $= me^4/2\hbar^2 = 13.6$ eV
STM	*Scanning tunneling microscopy*
STS	*Scanning tunneling spectroscopy*
SXRD	*Surface X-ray diffraction*
TEM	*Transmission electron microscopy*
UPS	*Ultraviolet photoelectron spectroscopy* — PES in the ultraviolet energy range.
UHV	*Ultra high vacuum*
VB	*Valence band*
XPS	*X-ray photoelectron spectroscopy* — PES in the photon energy range up to few keV.
XSW	*X-ray standing waves*

The following table lists frequently used quantities. Vectors are denoted in bolds.

$\mathbf{A}(\mathbf{r})$	Vector potential (of an electromagnetic wave)
$a\ (a^\dagger)$	Annihilation (creation) operator in the second quantisation depiction
β, γ, δ	Electric dipole, electric quadrupole and magnetic dipole asymmetry parameters, which describe the angular anisotropy of the photoelectron intensity distribution
d_{hkl}	Spacing between the (hkl) diffraction planes of an X-ray standing wavefield
ΔE_γ	Difference between the photon energy E_γ of the incident beam and the "kinematical" Bragg energy E_{Bragg}, $\Delta E_\gamma = E_\gamma - E_{Bragg}$
E_γ	Photon energy
E_B	Binding energy of an electronic state in an atom
$\mathbf{e}$	Polarisation vector of an electromagnetic wave
F_s^H	Coherent fraction for an element s for a reflection $\mathbf{H}$
$\mathbf{H}$	Reciprocal lattice vector for the $\mathbf{H} = (hkl)$ Bragg reflection
h, k, l	Miller indices

$\mathbf{k}$	Wave vector of an X-ray beam with $\|\mathbf{k}\| = 2\pi/\lambda$
l	Orbital angular momentum of an electron
M_s	Debye-Waller factor for an atom at lattice site s
$\nu(E)$	Phase of the Bragg reflected wave with respect to the incident wave
P_s^H	Coherent position for an element s for a reflection $\mathbf{H}$
$\mathbf{q}$	Momentum transfer, difference between the wave vectors of the reflected and the incident beam.
Q	Phenomenological forward/backward asymmetry parameter, which describes the anisotropic angular intensity distribution of photoelectrons excited by an interference X-ray field
$R(E)$	Reflectivity
$\rho_{s,l}$	Density of (valence) states with angular momentum l in the vicinity of lattice site s
S_R, $\|S_I\|$, ψ	Phenomenological quadrupole parameters in the expression for the XSW photoelectron yield, which depend on the angular momentum of the initial state and on the interference of multipole terms in the transition matrix element
$\sigma_{s,l}$	Angle-integrated photoionisation cross section per electron for an electronic state with angular momentum l at lattice site s
$Y_s(E_B)$	Photoelectron yield originating from the vicinity of lattice site s

Appendix B

Determination of Quadrupole Parameters

The experimental geometry chosen for the real space imaging study in chapter 5 was, with photoelectron detection angles $\vartheta = 45°$ and $\varphi = 0°$ as specified in Fig. 3.4 on page 19, sensitive to multipolar effects. The modulation amplitude of the XSW photoelectron yield recorded for an element showed a dependence on the specific electronic level probed. This dependence indicated that the dipole approximation could not be applied. The dependence could at least partially be accounted for by the quadrupole effect, as will be shown in this appendix.

To be able to remove the influence of the quadrupole effect from the imaging data, approximate values for quadrupole parameters were determined by experiment for a number of electronic shells. For this purpose, the XSW yield profiles for multipolar primary (XPS) and isotropic secondary (Auger) emission are compared in section B.1. An alternative approach is discussed in section B.2, where the XSW photoelectron yields recorded in two distinct experimental geometries at $\vartheta = 45$ and $0°$ are compared.

B.1 Auger Electron vs. Photoelectron Detection

Possible occurrence of multipole effects has to be carefully taken into consideration when deriving structural information from XSW data. The modulation of the XSW photoelectron yield is characterised by two parameters, a phase and an amplitude. In the simplest case, which is the case that the dipole approximation can be applied, the phase and the amplitude are the structural parameters P^H and F^H for the probed element. Otherwise, the phase and the amplitude can be influenced by anisotropic angular effects in photoemission: Owing to the **k**-dependence introduced in the photoelectron angular distribution, the modulation amplitude can either be enlarged but also be reduced significantly. The phase can be altered as well though the effect here is comparatively small. If the occurrence of multipole effects remains unnoticed, erroneously applying the dipole approximation will result in obtaining incorrect structural parameters P^H and F^H for the probed element.

The influence of the quadrupole effect on the XSW photoemission yield can be

experimentally quantified. The quadrupole effect causes the modulation of the XSW photoemission yield to deviate from the modulation of XSW Auger yield, which has been excited exclusively by the photon field. The Auger yield is, like the dipolar photoemission yield, a proportional monitor of the XSW field absorption as long as the part of the Auger yield stimulated by secondary electrons, i.e., by the inelastic background from the sample, is negligible. The structural parameters P^H and F^H for the probed element are obtained by fitting the dipole expression given by Eq. 3.21 on page 23 to the XSW Auger yield. The (correlated) quadrupole parameters S_R, $|S_I|$ and ψ can then be determined by fitting the quadrupole expression given by Eq. 3.22 to XSW photoelectron yield profiles, using the parameters P^H and F^H gained from the Auger/XSW data as fixed parameters. To allow comparison of experimental and theoretical results as described in the following, Nelson *et al.* [38] parametrized the quadrupole expression in terms of two independent quantities, the quadrupole amplitude parameter q and the dipole-quadrupole phase shift Δ, by

$$S_R = \frac{1 + q\cos\Delta}{1 - q\cos\Delta} \quad \text{and} \quad S_I = |S_I|e^{i\psi} = \frac{1 + iq\sin\Delta}{1 - q\cos\Delta},$$
$$\text{where} \quad |S_I| = \frac{(1 + q^2\sin^2\Delta)^{1/2}}{1 - q\cos\Delta} \quad \text{and} \quad \psi = \arctan(q\sin\Delta). \qquad \text{(B.1)}$$

The same parametrization was used by Lee *et al.* [163] in terms of a phenomenological forward/backward asymmetry parameter $Q = q\cos\Delta$, which was introduced by Fisher *et al.* [164].

Alternatively, a simplified parametrization can often be used [42]. The three parameters S_R, $|S_I|$, and ψ are correlated via $|S_I| = 0.5(S_R + 1)\sqrt{1 + \tan^2\psi}$ for backscattering geometry. The XSW phase ψ is smaller than 0.1 rad for light elements at $E_\gamma < 5$ keV and is therefore frequently smaller than the experimental error in the phase $(2\pi P^H - \psi)$. For this reason, the influence of the phase ψ can often be neglected such that $|S_I| \approx 0.5(S_R + 1)$ for backscattering geometry. With this approximation, the two correlated parameters $|S_I|$ and S_R can be determined by introducing solely one additional fitting variable.

The photoemission asymmetry parameters β, γ, and δ, which describe the anisotropic angular distribution of the emitted photoelectrons excited by a single X-ray beam, are available from calculations. These parameters can be compared to the experimental parameters q and Δ for the two X-ray beam case via the forward/backward asymmetry parameter Q. There does not seem to exist the possibility of a direct comparison, since the expression for the two-beam case given by Eq. 3.22 cannot be parametrized in terms of β, γ, and δ. The quantity Q represents a link between the theoretical and experimental parameters for all angular momenta: By comparing the ratio of quadrupole and dipole terms in the expression for the XPS intensity between the cases of a single X-ray beam (i.e., $R = 0$) and the interference field of two coherent beams, Nelson *et al.* [38] made the correspondence

$$Q(\vartheta, \varphi) = q\cos\Delta = \frac{(\gamma\cos^2\vartheta + \delta)\sin\vartheta\cos\varphi}{1 + \beta P_2(\cos\vartheta)} \qquad \text{(B.2)}$$

for back reflection geometry.

El. level	F^H	P^H	q	Δ	S_R	$\lvert S_I\rvert$	ψ	Q
Sr LMM	0.966	0.011						
Sr $2p$			0.084 ±0.001	0.947 ±0.006	1.103 ±0.001	1.054 ±0.001	0.011 ±0.000	0.049 ±0.001
Sr $3p$			0.106 ±0.003	0.336 ±0.022	1.222 ±0.007	1.112 ±0.003	0.006 ±0.000	0.100 ±0.003
Sr $3d$			0.220 ±0.002	− 0.151 ±0.014	1.556 ±0.005	1.279 ±0.003	− 0.005 ±0.001	0.217 ±0.002
Sr $4s$			0.106 ±0.003	− 0.360 ±0.058	1.220 ±0.006	1.111 ±0.004	− 0.006 ±0.001	0.099 ±0.003
Ti LMM	0.921	0.031						
Ti $2p$			0.273 ±0.002	0.366 ±0.007	1.684 ±0.006	1.349 ±0.003	0.016 ±0.000	0.255 ±0.002
O KLL	0.811	0.033						
O $1s$			0.350 ±0.002	0.639 ±0.004	1.781 ±0.006	1.421 ±0.004	0.033 ±0.000	0.281 ±0.002
Y LMM	0.816	0.027						
Y $2s$			0.280 ±0.005	− 1.819 ±0.077	0.871 ±0.003	0.969 ±0.020	− 0.042 ±0.001	− 0.069 ±0.021
Y $2p$			0.060 ±0.004	− 2.073 ±0.021	0.944 ±0.003	0.973 ±0.002	− 0.008 ±0.001	− 0.029 ±0.002
Y $3p$			0.069 ±0.007	− 0.132 ±0.187	1.147 ±0.015	1.073 ±0.008	− 0.001 ±0.002	0.068 ±0.007
Y $3d$			0.209 ±0.005	− 0.820 ±0.047	1.333 ±0.010	1.180 ±0.010	− 0.024 ±0.001	0.143 ±0.008
Ba MNN	0.404	0.004						
Ba $3p$			0.291 ±0.020	0.984 ±0.018	1.384 ±0.031	1.227 ±0.021	0.038 ±0.003	0.161 ±0.012
Ba $3d$			0.456 ±0.011	0.864 ±0.011	1.841 ±0.029	1.504 ±0.020	0.053 ±0.001	0.296 ±0.008
Ba $4p$			0.440 ±0.034	1.055 ±0.016	1.554 ±0.056	1.368 ±0.044	0.058 ±0.004	0.217 ±0.018
Ba $4d$			0.449 ±0.020	0.812 ±0.022	1.894 ±0.058	1.522 ±0.039	0.050 ±0.002	0.309 ±0.015

Table B.1: Quadrupole parameters experimentally determined for electronic levels of Sr, Ti, O, Y, and Ba at $E_\gamma = 3.180$ keV. Fitting the XSW data shown in Fig. B.1 yields the structural parameters P^H and F^H and the quadrupole parameters q and Δ with their statistical errors. The corresponding values S_R, $|S_I|$, and ψ result from conversion through Eq. B.1. The phenomenological asymmetry parameter was calculated by $Q = q\cos\Delta$.

For the specific case of an s initial state in the two X-ray beam case, analytical expressions for the quadrupole parameters S_R, $|S_I|$ and ψ were derived by Vartanyants and Zegenhagen [28, 41, 42]. The emission channels for electric dipole and quadrupole transitions interfere, and the interference between the channels for the incident and the reflected beam was taken into consideration by including cross terms of the matrix elements. The obtained analytical expressions can be related to the parameters β, γ, and δ: The quadrupole parameter γ is related to the complex parameter $\tilde{\gamma}$ used in reference [42] by $\gamma = 3\,\Re[\tilde{\gamma}]$. The magnetic dipole term is zero and, therefore, the parameter $\delta = 0$, while the electric dipole parameter $\beta \approx 2$ for s initial states [32]. For initial states with higher angular momentum, analytical expressions for the parameters S_R, $|S_I|$ and ψ have apparently not yet been calculated.

The XSW measurements were carried out at beamline ID32, which was set up with the photoelectron analyser mounted at $\vartheta = 45°$ and $\varphi = 0°$. XSW data were recorded

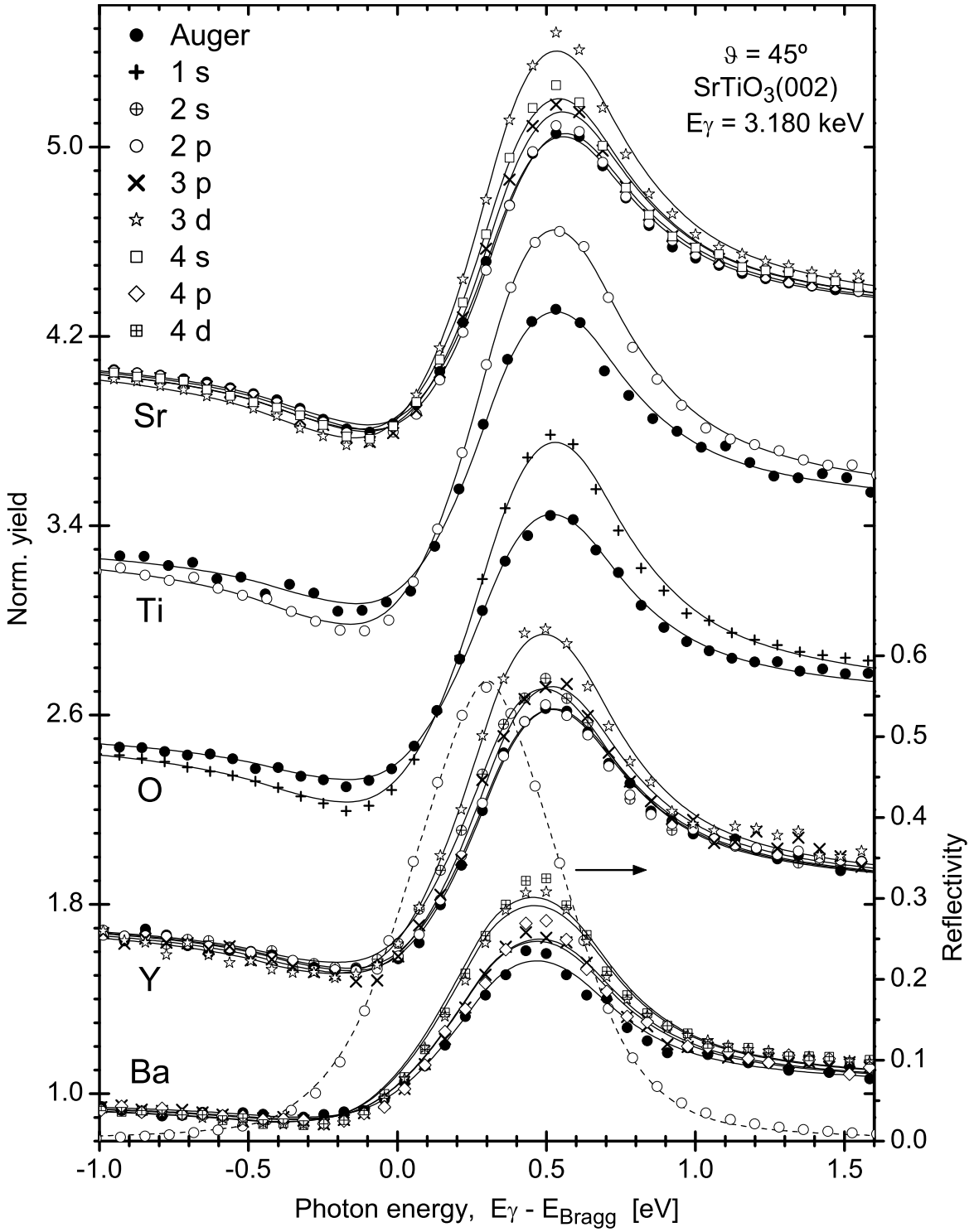

Figure B.1: XSW yield profiles for Auger and XPS signals from a variety of electronic shells. The lines represent the fittings of the dipole and quadrupole expressions to the Auger and XPS data, respectively. The data curves were offset by multiples of 0.8. The fitting parameters are listed in Tab. B.1. The reflectivity curve and a fit according to the dynamical theory of X-ray diffraction are shown at the bottom.

El. level	E_{kin} [eV]	β	γ	δ	Q
Sr 2p	1240	1.472	0.276	0.030	0.094
Sr 3p	2910	1.485	0.578	0.024	0.171
Sr 3d	3046	0.869	0.834	0.147	0.342
Sr 4s	3141	1.998	0.023	0.000	0.006
Ba 3p	2117	1.658	0.060	0.008	0.021
Ba 3d	2400	1.167	0.594	0.090	0.226
Ba 4p	3001	1.696	0.171	0.007	0.050
Ba 4d	3090	1.167	0.663	0.083	0.241

El. level	E_{kin} [eV]	β	γ	δ	Q
Y 2s	807	1.989	0.054	0.000	0.014
Y 2p	1100	1.468	0.202	0.028	0.073
Y 3p	2881	1.503	0.550	0.022	0.162
Y 3d	3024	0.891	0.830	0.143	0.337
O 1s	2649	1.974	1.119	0.000	0.288
Ti 2p	2726	1.094	0.841	0.078	0.289

Table B.2: Quadrupole parameters and forward/backward asymmetry parameters Q calculated for electronic levels of Sr, Ti, O, Y, and Ba at $E_\gamma = 3.180$ keV. The listed values were cubic-spline interpolated from Trzhaskovskaya's tables [145,146] at the given kinetic energies of the photoelectrons. The parameter Q was calculated for $\vartheta = 45°$ and $\varphi = 0°$ via Eq. B.2.

for the $SrTiO_3(002)$ reflection in back reflection geometry (angle of incidence $\theta = 86$–$87°$) at $E_\gamma = 3.180$ keV for the electronic levels and Auger transitions listed in the first column of Tab. B.1. The data for strontium, oxygen and additionally for the valence band were taken on one and for titanium on another $SrTiO_3$ single crystal, which had been vacuum-annealed at pressures $<1\times10^{-8}$ mbar at a temperature of $\sim$930 °C for 3 h. The data for barium and yttrium were recorded from an $YBa_2Cu_3O_{7-\delta}$ layer of 1.0 ML thickness deposited on a $SrTiO_3$ single crystal. It was the same sample used for the XSW imaging study described in chapter 5.

Selecting the $SrTiO_3(002)$ reflection minimises the influence of electron-induced Auger yield on the modulation of the measured XSW Auger yield. In this reflection, the geometrical structure factors for strontium, titanium and oxygen are identical for an ideal $SrTiO_3$ crystal lattice. Furthermore, these values are similar to those for the yttrium and barium contained in a thin overlayer of ideal $YBa_2Cu_3O_{7-\delta}$. As a consequence, the XSW yield modulations for all elements are similar. Electron-induced Auger yield contributions cannot, hence, significantly alter the XSW Auger yield modulation of the probed absorption site in case of an ideal lattice.

The experimental XSW photoelectron yield profiles for Sr, Ti, O, Y, and Ba are shown in Fig. B.1. The amplitudes of the XSW yield modulations reveal a clear dependence on the electronic level, while the line shapes do not show a visible dependence. The variation in amplitude indicates that non-dipole effects are already significant at photon energies of few keV. Deviations of the XPS yield modulation from the Auger yield modulation are caused by multipole effects. Fitting theoretical expressions to the XSW data yields structural parameters P^H and F^H and quadrupole parameters q and Δ, which are converted into values S_R, $|S_I|$, and ψ through Eq. B.1. The results are listed in Tab. B.1. The quadrupole parameters were determined based on the assumption that electron-induced Auger yield contributions had no influence on the modulation of the measured XSW Auger yield. However, the widely differing coherent fractions F^H obtained for the constituent elements of $SrTiO_3$ suggest that this assumption is not strictly fulfilled for the $SrTiO_3(002)$ reflection, given the fact that element-specific disorder is not expected for $SrTiO_3$. The uncertainty about the influence of electron-induced Auger yield contributes to the systematic error of the

determined quadrupole parameters.

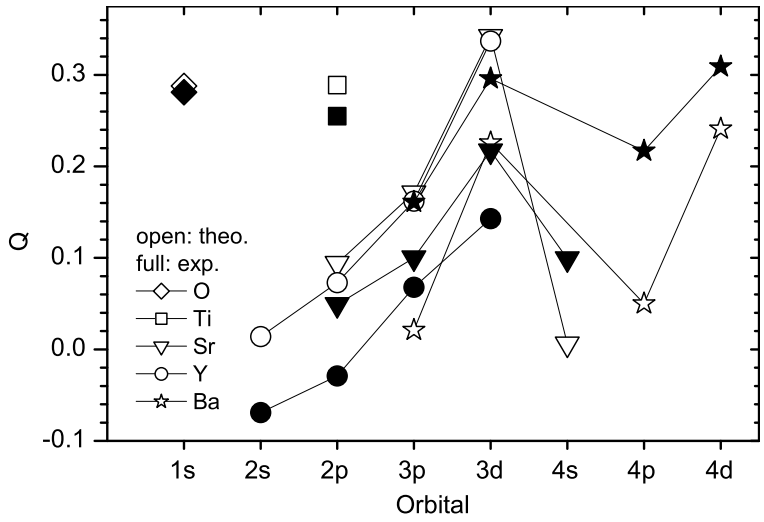

Figure B.2: Comparison of calculated and experimental forward/backward asymmetry parameters Q. The values in Tab. B.2 calculated for $E_\gamma = 3.180$ keV are compared to the experimental values listed in Tab. B.1 for $\vartheta = 45°$.

Theoretical values for the quadrupole strength parameter Q were calculated via Eq. B.2 from tabulated photoemission asymmetry parameters for the free atom and are listed in Tab. B.2. The experimental Q values, which are listed in the last column of Tab. B.1, show the same dependence on the electronic level (and, hence, on the orbital angular momentum of the initial state), as the comparison in Fig. B.2 visualizes. This qualitative agreement suggests that the dependence of the XSW yield modulation on the electronic level can at least partially be explained by the quadrupole effect. Discrepancies between the absolute values can most likely be related to systematic errors of the structural parameters F^H and P^H caused by secondary excitation, which propagate to the error of the experimental Q values. In the literature, experimental asymmetry parameters Q have apparently been documented only for the light element oxygen. The reported values show very good agreement with our experimental value $Q = 0.281$ for the O 1s level at $E_\gamma = 3.18$ keV: Jackson *et al.* [165] found $Q = 0.27\pm0.01$ at 3.0 keV, Schreiber *et al.* [166] reported $Q = 0.31\pm0.03$ at 2.6 keV, and Lee *et al.* [163] obtained values scattering around $Q = 0.3$ for photon energies between 2.7 and 3 keV.

Influences of the quadrupole effect were not only observed in core level but also in valence XPS. Fitting the dipole expression given by Eq. 3.21 to the XSW photoemission yield recorded from the valence band of $SrTiO_3$, as shown in Fig. B.3, resulted in the physically meaningless value $F_{\mathrm{VB}}^{002} = 1.12$. This result confirms the findings by Woicik *et al.* [3], who reported similar XSW modulation amplitudes for valence and shallow core level emission for Ge and Cu; the results for the latter case are shown in Fig. 3.7(a) on page 25. Removing the influence of the quadrupole effect from XSW data taken on valence or conduction bands is not possible, since the coherent fraction of the corresponding electronic states is generally unknown. An attempt to determine

the coherent position and fraction of valence states from valence band XSW data with the help of core level XSW data is described in appendix C.

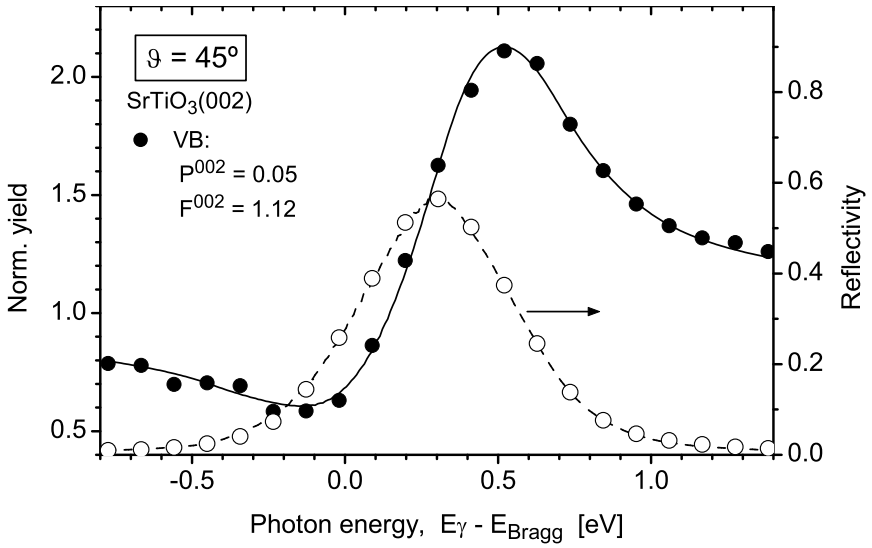

Figure B.3: XSW photoelectron yield recorded from the $SrTiO_3$ valence band at $E_\gamma = 3.180$ keV. The parameters P^{002} and F^{002} were determined by fitting the dipole expression given by Eq. 3.21 to the data curve.

Summarising, the modulation dependence of the XSW photoemission yield on specific electronic levels was analysed. The results showed that the dipole approximation can generally not be applied to XPS in combination with XSW in the photon energy range of few keV. Quadrupole parameters were empirically determined for a variety of electronic levels and elements. The parameters can be used to remove the influence of multipole effects from the XSW imaging data presented in chapter 5. The accuracy of the parameters, however, may have been limited by ignoring Auger yield excited by secondary electrons. In order to obtain results of improved accuracy, and with the intention to confirm the results presented in this section, an alternative approach to determine quadrupole parameters was (unsuccessfully) attempted, as documented in the following section.

B.2 Quadrupole-sensitive and -insensitive XPS Geometries

The experimental determination of quadrupole parameters as described in the previous section requires accurate knowledge of the structural parameters F^H and P^H of the specific sample in use. These parameters may be obtained more reliably from the XSW modulation of dipolar photoemission instead of Auger signals. However, more experimental effort is required to set up a quadrupole-insensitive XPS geometry. Calculations confirmed [103] that photoemission excited by an X-ray interference field from states with orbital angular momentum $l = 1$, which is the majority type

of state probed in the XSW imaging study described in chapter 5, should not exhibit quadrupole contributions along the polarisation direction of the incident X-ray beam.

The XSW measurements were performed at beamline ID32 at two distinct photoelectron detection angles. XPS/XSW data for a variety of electronic levels of Sr, Ti, O, Ba, Y, and Cu were recorded in a geometry sensitive to quadrupole effects at $\vartheta = 45°$ and $\varphi = 0°$ and, after rotating the UHV chamber by 45°, in a (supposedly) quadrupole-insensitive geometry at $\vartheta = 0°$. The data for the two different analyser angles were taken on the same surface spot of a $SrTiO_3$ single crystal sample covered with an $YBa_2Cu_3O_{7-\delta}$ layer of 1.0 ML thickness. It was the same sample used for the XSW imaging experiment. The $SrTiO_3(111)$ back reflection at 2.753 keV photon energy was chosen with photoelectron take-off angles of 90° (at $\vartheta = 45°$) and 45° (at $\vartheta = 0°$).

The experimental XSW photoelectron yield curves recorded at $\vartheta = 0°$ are shown in Fig. B.4 and those taken at $\vartheta = 45°$ in Fig. B.5. The change in analyser position brought about a change in XSW yield modulation for each electronic level, from which quadrupole parameters could have in principle been determined. For the geometry at $\vartheta = 0°$, a strongly subshell-dependent variation in XSW yield modulation was observed for each element. This is, however, an unexpected result: It disproves the XPS signal detected along the polarisation direction to be purely dipolar. In dipole approximation, the XSW modulations of all subshell signals coming from one element are identical. Non-dipolar effects therefore prevented us from gaining empirical quadrupole parameters from the present experiment.

Tab. B.3 correlates the parameters F^H and P^H, which were obtained by fitting the XSW dipole expression given by Eq. 3.21 to the data sets recorded at $\vartheta = 0$ and 45°. The quantity F^H does not have the meaning of the structural coherent fraction here. It represents a measure for the modulation amplitude of the XSW yield. Fig. B.6 compares the fitting parameters graphically. The two data sets exhibit a qualitatively very similar dependence of the modulation amplitude on the electronic subshell. This is a strong indication that the XPS signals detected along the polarisation direction of the incident beam at $\vartheta = 0°$ were affected by multipole effects. F^H shows the tendency to increase monotonously with rising photoelectron kinetic energy. Calculations predict that influences of the quadrupole effect exhibit a strong characteristic dependence on the orbital angular momentum l rather than on the principal quantum number n at high kinetic electron energies [38]. However, a clear dependence on angular momentum is not observed from the data. This suggests additional effects to be present.

The influence of multipole effects on the XSW photoelectron yield detected in polarisation direction may be explained by the finite solid angular acceptance of the photoelectron analyser and elastic scattering of the photoelectrons. The unscattered photoelectron signal emitted along the polarisation direction is strictly dipolar. Integrated photoelectron detection over the finite solid angular range of the spectrometer will, however, necessarily include nondipolar yield contributions. The influence of elastic scattering will effectively further enlarge the solid angle from which photoelectrons are detected: Photoelectrons, which are on their way from the excited atom through the bulk to the sample surface, can be scattered into the acceptance solid angle of the analyser. This effect will blur the anisotropic XPS angular distribution. The influence

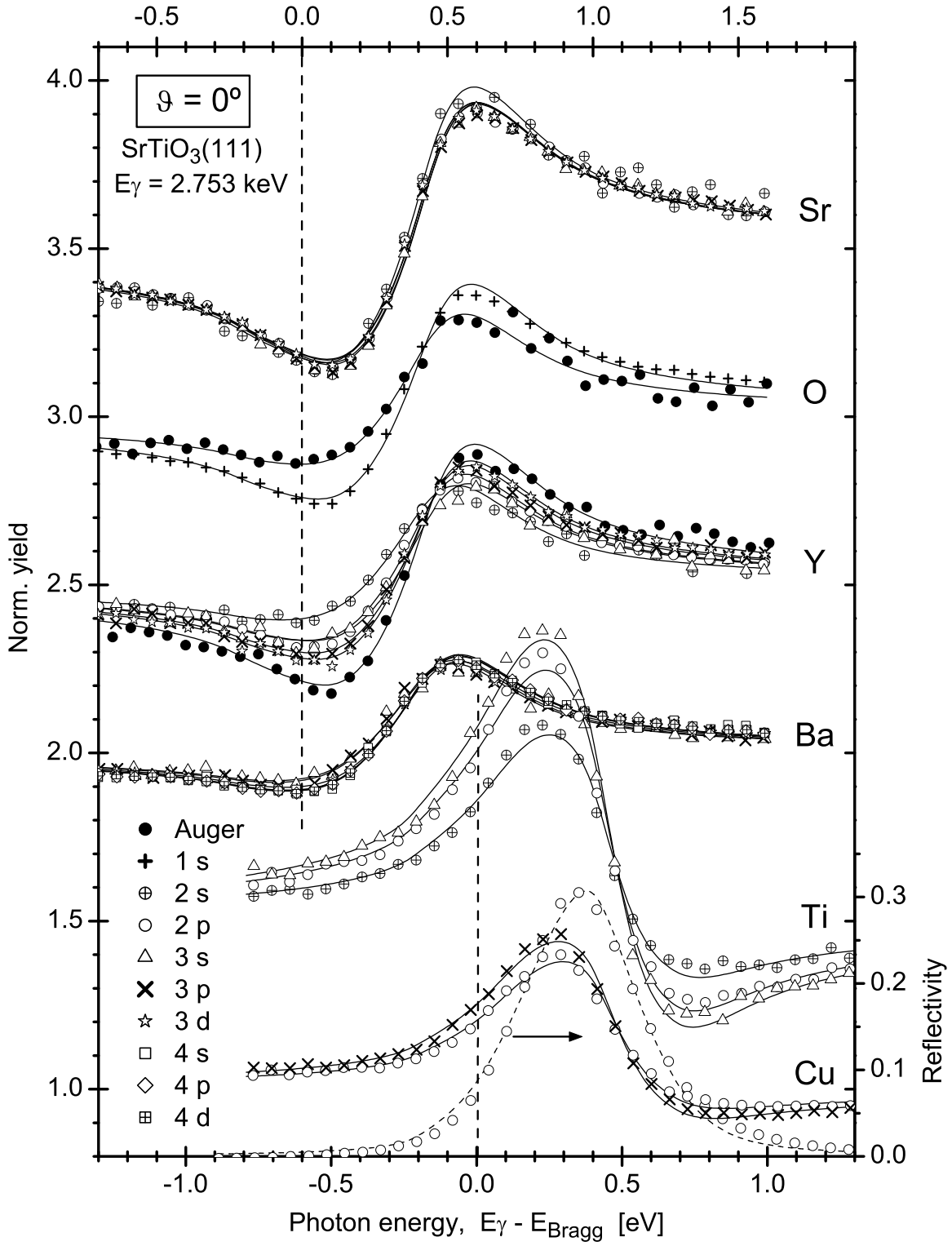

Figure B.4: XSW photoelecton yield for a variety of electronic shells recorded with the detector mounted in polarisation direction at $\vartheta = 0°$. The lines represent the fittings to the data with the dipole expression for the XSW modulation given by Eq. 3.21. The fitting parameters are listed in Tab. B.3. The data curves are offset by multiples of 0.5.

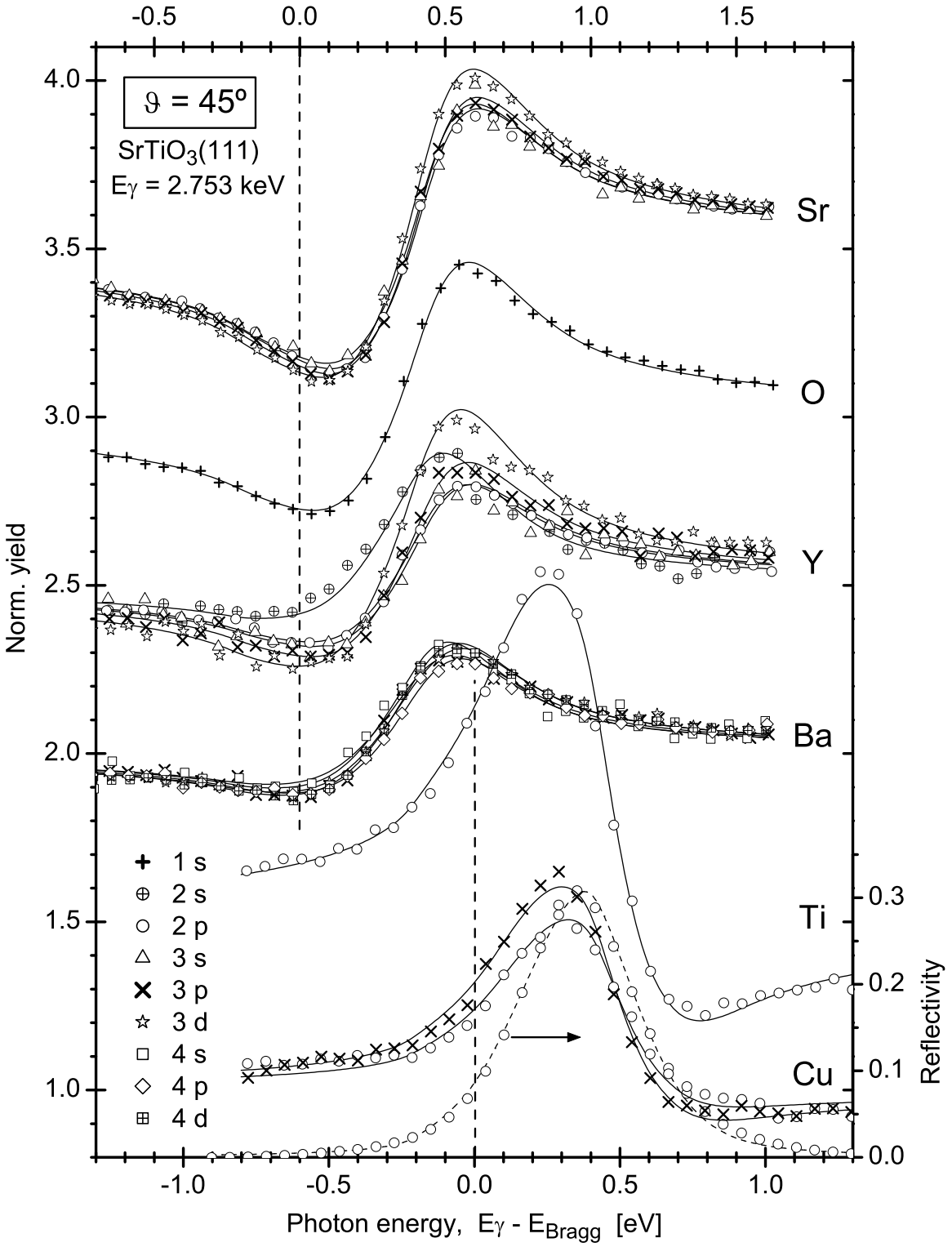

Figure B.5: XSW photoelecton yield for a variety of electronic shells recorded with the detector mounted at $\vartheta = 45°$. The lines represent the fittings to the data with the quadrupole expression given by Eq. 3.22. The reflectivity curve and a fit according to the dynamical theory of X-ray diffraction are shown at the bottom.

El. level	P^H		F^H	
	ϑ		ϑ	
	0°	45°	0°	45°
Sr 2s	0.014	/	1.036	/
Sr 2p	0.003	0.993	0.998	1.038
Sr 3s	0.000	0.001	1.022	1.012
Sr 3p	0.000	0.000	1.010	1.084
Sr 3d	0.003	0.019	0.993	1.154
Ti 2s	0.517	/	0.685	/
Ti 2p	0.506	0.477	1.044	1.360
Ti 3s	0.503	/	1.216	/
O KLL	0.997	/	0.564	/
O 1s	0.007	0.023	0.814	0.908
Cu 2p	0.537	0.456	0.319	0.391
Cu 3p	0.519	0.464	0.420	0.577

El. level	P^H		F^H	
	ϑ		ϑ	
	0°	45°	0°	45°
Y LMM	0.004	/	0.928	/
Y 2s	0.003	0.065	0.464	0.416
Y 2p	0.002	0.988	0.624	0.627
Y 3s	0.989	0.984	0.622	0.669
Y 3p	0.003	0.005	0.713	0.741
Y 3d	0.004	0.047	0.758	0.881
Ba 3s	0.992	/	0.403	/
Ba 3p	0.997	0.003	0.416	0.490
Ba 3d	0.991	0.008	0.461	0.513
Ba 4s	0.997	0.024	0.483	0.477
Ba 4p	0.997	0.992	0.487	0.506
Ba 4d	0.999	0.014	0.491	0.526

Table B.3: Parameters P^H and F^H for the XSW data shown in Figs. B.4 and B.5. The parameters were determined by fitting the dipole expression given by Eq. 3.21 to the data, which were recorded with the photoelectron detector mounted at $\vartheta = 0$ and 45°. The values P^H are given with respect to an origin chosen at the bulk strontium site. A graphical comparison of the listed values is shown in Fig. B.6.

of multipole effects can therefore become sizeable also in polarisation direction.

The proposed angular integration effect cannot, however, account for the large differences in yield modulation observed for strontium ($z = 38$) and yttrium ($z = 39$), two neighboured elements in the periodic table with similar electronic configurations in the ground state: While the modulation of the strontium yield diplays a very weak dependence on the subshell, the contrary is the case for yttrium. The calculated quadrupole parameters γ and δ [145] are comparable for the two elements and cannot explain the contrast. The fact that the strontium and yttrium XPS signals originate from different depths below the sample surface cannot explain the contrast either. The elastic mean free path of the photoelectrons, which can be assumed to be shorter than the inelastic mean free path of maybe 30 Å, is of the order of the film thickness of ∼1.2 nm. The resulting blurring effect on the angular photoelectron distribution should be comparable for the two elemental signals.

It is not yet understood whether elastic scattering can account for the discrepancy in modulation between the XSW photoemission data shown in Figs. B.1 and B.5. The data sets were recorded both in a geometry sensitive to multipole effects at $\vartheta = 45°$. The difference in photon energy of ∼400 eV does not cause the quadrupole parameters to largely differ for the two data sets and, hence, cannot explain the distinct XSW modulations observed. Different electron take-off angles of $\alpha = 45°$ (Fig. B.1) and $\alpha = 90°$ (Fig. B.5) may possibly be accountable. In order to accurately estimate the influence of the take-off angle on the XSW yield modulation, Monte Carlo type simulations of the electron scattering are required.

Summarising, XSW experiments with photoelectron detection along the polarisa-

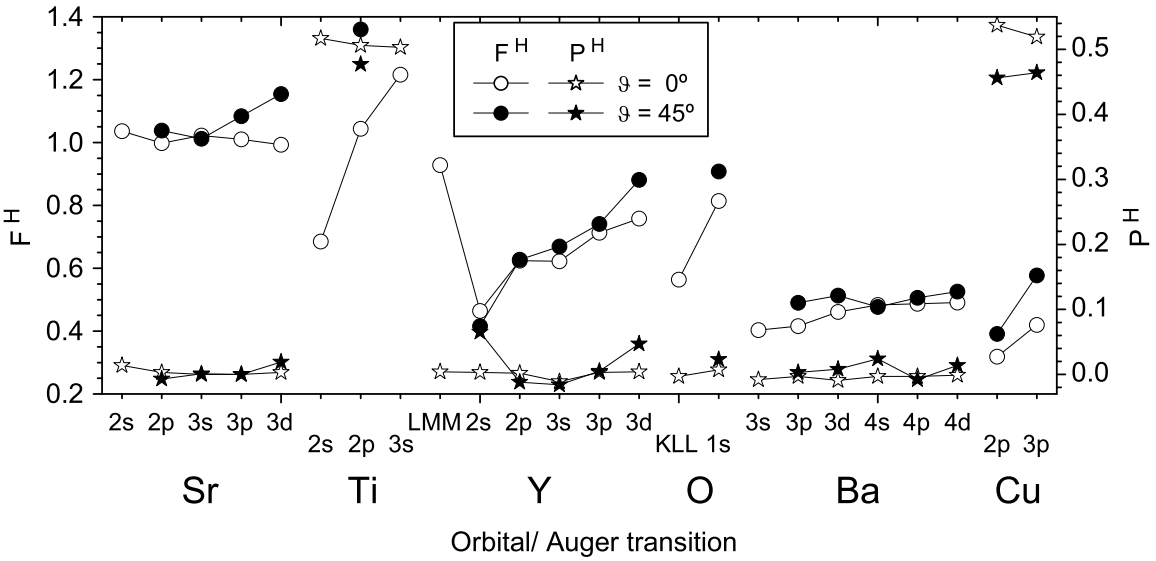

Figure B.6: Graphical comparison of the parameters P^H and F^H listed in Tab. B.3.

tion direction of the incident beam — a supposedly quadrupole-insensitive detection geometry — revealed influences of multipole effects. The occurrence of multipole effects is most likely related to elastic electron scattering and is, hence, inevitably linked to XPS as an analytical tool. Elastic scattering appears to have a relatively large influence, as moving to a quadrupole-insensitive detection geometry has not significantly suppressed quadrupole effects.

The obtained results have to be confirmed by independent measurements to exclude possible experimental fault, not obvious at present. The ideal sample to determine quadrupole parameters is a single atomic layer of an element to minimise the the ratio of sample thickness and photoelectron elastic mean free path.

Appendix C

Non-dipolar Effects in Valence XPS

In section 7.4, the XSW modulation information for site-specific contributions to the valence XPS yield for a $SrTiO_3$ sample was derived from core level signals. A prudent proceeding was necessary, as described in the following.

The measured coherent fractions F^H appeared unexpectedly large (except the value F_{Ti}^{112}). Coherent fractions of the order of unity usually indicate close to perfect crystal structure such as for semiconductor crystals. This is by far not the case for $SrTiO_3$. Furthermore, considerable difference in coherent fractions between different elements, like for strontium and titanium in the (112) reflection, is not expected. Neither ion exchange nor the presence of interstitial lattice sites, giving rise to element-specific disorder, have been reported for $SrTiO_3$. An independent measurement under the same conditions on a different sample, compare Tab. B.3 on page 164, confirmed the values determined for the (111) reflection. Our results do not agree with earlier values reported by Zegenhagen *et al.* [99], who measured the inelastically scattered radiation from strontium and titanium in a structural XSW study in (002) reflection. For two measurements on different surface spots of the same crystal, the authors found a coherent fraction identical for both elements of 0.6 in one case and 0.7 in the other case and attributed the divergence from unity to structural imperfections. This result appears consistent with the almost just as low value 0.76 obtained for titanium in the (112) reflection. Coherent fractions found by fluorescence measurements rather set an upper limit on the values found by XPS as a consequence of the higher sensitivity to the better ordered crystal bulk [167]. This has led to the conclusion that the coherent fractions obtained in our measurements cannot be explained in a convincing way by the structural properties of the sample.

The coherent fraction is basically a measure of the modulation amplitude of the XSW yield. It is likely that the modulation amplitudes of the experimental data were influenced by quadrupole effects. Fig. B.3 on page 160 shows the XSW photoemission yield recorded from the valence band of a $SrTiO_3$ sample in (002) reflection; the coherent fraction determined by assuming the dipole expression to apply exceeds unity. As discussed in appendix B.2, the XSW modulation amplitude was observed to be dependent on the specific electronic level probed, although an experimental geometry insensitive to multipole effects had been chosen and the dipole approximation was expected to apply. This observation can likely be explained by elastic scattering of

photoelectrons into the detector solid angle of acceptance. The core level among the variety of core levels, whose XSW profile described best the modulation of the site-specific valence band contribution, was selected based on the following assumption: The modulation amplitude of the XSW yield appears to be a monotonous function of the binding energy of the electronic level probed for an element. Hence, the modulation of the XSW yield of the shallowest core level appears most representative of the modulation of the elemental valence yield contribution.

The current approach is very empirical in nature, since the strong dependence of quadrupole effects on orbital angular momentum is not taken into consideration. While the underlying effect is not removed, the modulations of the shallow core level yield and the partial valence yield will nearly match under the assumption made, and the influence of the effect will almost cancel out. While there is no evidence whether the assumption is strictly true, Woicik's *et al.* result for copper provides some support: The XSW profiles for a shallow Cu core level and the Cu valence level, depicted in Fig. 3.7 on page 25, are almost identical. Tab. B.3 on page 164 correlates coherent fractions for different electronic levels. Rescaling the coherent fractions F^H to the shallowest levels measured resulted in the scaled values $F^{H\,scaled}$ listed in Tab. 7.1. As the dipole expression for the XSW modulation was applied when quantifying the modulation amplitudes, values larger than unity can be obtained for the coherent fraction. These values have to be interpreted rather as a fitting parameter than a structural parameter.

Appendix D

LDA Calculations for $SrTiO_3$

Densities of angular-momentum dependent site-specific valence states for bulk $SrTiO_3$ were calculated by F. Bottin [141] by *ab initio* DFT calculations in the LDA approximation. Details about the DFT calculations are summarized in this appendix.

The calculations for $SrTiO_3$ were performed by generating norm-conserving pseudopotentials within the local density approximation according to the Troullier-Martins scheme [168] for the strontium, titanium and oxygen atoms, using the $FHI98PP$ code [169]. Pseudopotentials are constructed in order to eliminate the core states and to describe the valence states by smooth node-free pseudo wave functions in order to lower the cutoff energy for the series expansion of the wave functions. Pseudopotentials reproduce the true potential outside the core region such that the wave functions far away from the atomic cores are correctly described. Core orbitals with binding energies $\geq$60 eV were frozen in the pseudopotentials, which were generated using reference electronic configurations $4s^2 4p^6 5s^1$ for strontium, $3s^2 3p^6 4s^0 3d^4$ for titanium and $2s^2 2p^4$ for oxygen with cutoff radii for the $s/p/d$ channels of 2.0/2.5/2.2 (Sr), 1.3/1.4/1.8 (Ti) and 1.4/1.75/1.4 a.u. (O) and cutoff energies of 60 (Sr), 170 (Ti) and 90 Ry (O).

The valence density of states was calculated, employing the $ABINIT$ code [170], by using 20 occupied unpolarized states ($3 \cdot 6$ electrons for oxygen + 12 electrons for titanium + 10 electrons for strontium = 40 electrons) and 14 unoccupied unpolarized states. The wave functions for all states were expanded over a plane-wave basis set. A plane-wave cutoff energy of 140 Ry and a $6 \times 6 \times 6$ Monkhorst-Pack mesh [171] for the integration of the states in reciprocal space were sufficient to obtain good convergence. The mesh corresponds to 10 k-points in the irreducible Brillouin zone. The resulting equilibrium lattice parameter for $SrTiO_3$ of 3.885 Å differed by only -0.5% from the true value.

Site-specific densities of valence states (pDOS) were computed by projecting all the plane wave functions in real space within spheres. In addition, a second set of pDOS spectra was calculated within atomic basins defined by Bader surfaces. The integration within Bader surfaces yielded the number of valence states at the strontium, titanium, and the oxygen site. These numbers are required in section 7.8 to determine photoionisation cross sections that are normalised to the number of individual valence states. The partitioning of the entire unit cell into polyhedral site-specific regions in order to separate the total valence electronic density between the atoms can be achieved

without arbitrariness within the framework of the Bader theory [172], which is a theory of quantum mechanics in spatially confined subsystems. All charge

$$q_j = \int_{S_j} d\mathbf{r}\rho(\mathbf{r}) \tag{D.1}$$

contained in an atomic basin bounded by Bader surfaces $S_j(\mathbf{r}) \equiv \{(\mathbf{r}) : d\rho(\mathbf{r})/dn = 0\}$, first formulated in [173], is associated with the atom j irrespective of the origin of the charge before the solid state formed. The zero flux condition is visualized in Fig. D.1. Ionic charges of $q_{\mathrm{O}} = -1.259\ e$, $q_{\mathrm{Ti}} = 2.222\ e$ and $q_{\mathrm{Sr}} = 1.568\ e$ were obtained by the Bader calculations. A charge of the strontium ion close to its formal charge of +II indicates that the character of the strontium bonding is mainly ionic. The site-specific density of states is described by

$$\begin{aligned} \rho_s(E_B) &= \sum_{n,k} \kappa_{nk}\delta(E_B - E_{nk}) \\ &\text{with} \quad \kappa_{nk} = \textstyle\int_{S_j} d\mathbf{r}|\Psi_{nk}(\mathbf{r})|^2 \qquad \text{(Bader basin)} \\ &\text{or} \quad \kappa_{nk} = |\langle\Psi_{nk}(\mathbf{r})|\Theta(\mathbf{r}-\mathbf{r}_c)|\Psi_{nk}(\mathbf{r}')\rangle|^2 \qquad \text{(sphere)} \end{aligned} \tag{D.2}$$

with s = Sr, Ti, and O, where $\Psi_{nk}(\mathbf{r})$ represents the plane wave functions. The projection within spheres is achieved by the Heavyside step function $\Theta(\mathbf{r} - \mathbf{r}_c) = 0$ for $|\mathbf{r}| > |\mathbf{r}_c|$.

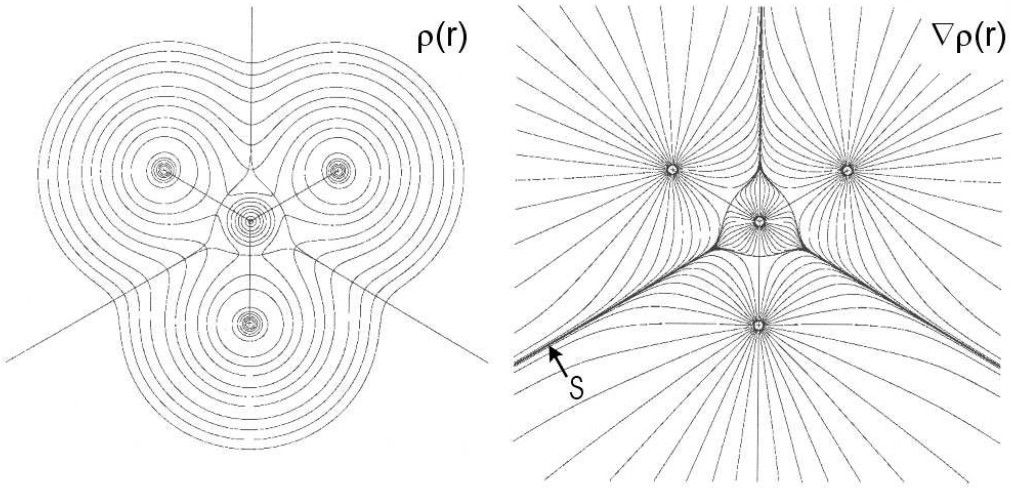

Figure D.1: Visualization of the Bader zero flux condition for a planar BF_3 molecule. The contours represent surfaces of constant charge density $\rho(\mathbf{r})$ and their gradients $\nabla\rho(\mathbf{r})$. Bader surfaces S indicated by an arrow separate four Bader basins. Figure taken from [174].

In order to obtain the angular-momentum dependent site-specific densities of valence states (lpDOS), a base transformation from a plane to spherical wave basis set

is needed. The spherical wave functions were projected within spheres, applying a projector $|l\rangle\langle l|$ for the angular-momentum dependent decomposition:

$$\rho_{s,l}(E_B) = \sum_{n,k} \kappa_{nkl}\delta(E_B - E_{nk}) \quad \text{with} \quad \kappa_{nkl} = |\langle \Psi_{nk}(\mathbf{r})|\Theta(\mathbf{r}-\mathbf{r}_c)|l\rangle\langle l|\Psi_{nk}(\mathbf{r}')\rangle|^2. \quad \text{(D.3)}$$

Bloch states do not have a defined angular momentum, and the angular momentum l is therefore not a good quantum number. The projection yields the density of states with the expectation value l.

Appendix E

VB Structure Analysis: Alternative Approach

The comparison of the valence band line shapes in Fig. 7.18 on page 113 has revealed some disagreement in XSW modulation between the experimental and the simulated spectra. The simulations were generated by modulating calculated partial valence yield spectra identical to the experimental core level XSW yield. The disagreement suggested that the core level modulation may not have been representative of the valence signal modulation.

An alternative fitting approach is presented in the following. This approach does not require experimental XSW modulation information. Another three parameters per reflection, the elemental coherent fractions, can be included in the set of fitting parameters. The analysis procedure is self-consistent and will result in the correct XSW modulation amplitudes for the site-specific valence yield contributions. In principle, this means that no experimental core level data are required: The coherent fractions can be recovered from the valence band data.

In the approach presented here, all coherent fractions were assumed to be identical. Only the value F_{O}^{112} for oxygen in the (112) reflection was assumed to take on one third of the common value, as predicted for the ideal crystal lattice. This means that one single additional fitting parameter f was included in order to adjust the modulation amplitude of the partial valence yield contributions. The motivation for this approach was given by an attempt of including a coherent fraction for each individual site-specific contribution into the fitting as described in the previous paragraph. This approach shall be briefly outlined in the following:

The coherent fractions for all lattice sites and reflections were introduced as additional fitting parameters. The six coherent fractions were varied by a generic optimisation algorithm, which cycled through the XSW decomposition routine and the fitting routine previously described. For each set of coherent fractions, the algorithm simulated the XSW effect for the valence band, based on the resulting theoretical l-resolved valence yield spectra. The algorithm searched for the set of coherent fractions that gave the best agreement of simulated and measured valence band line shapes. In this approach, all theoretical lpDOS spectra were identically rescaled in binding energy. However, the algorithm did not converge against a physically sensible solution

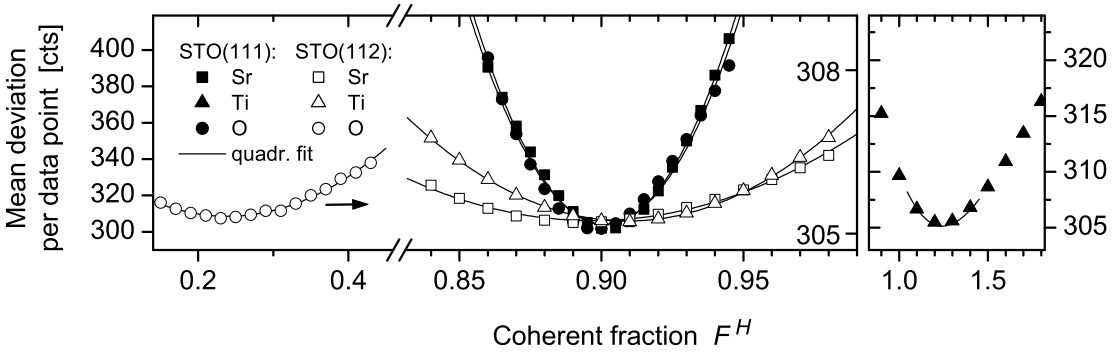

Figure E.1: Comparison of the agreement between experimental and simulated XSW data. The modulated line shapes of the measured and the simulated $SrTiO_3$ valence band spectra were compared: Each of the six graphs represents the goodness of the agreement as a function of one of the six coherent fractions, which were used as variable parameters as described in the text. One coherent fraction was varied at a time with the other five values fixed. The curvature of the graphs for F_{O}^{112} and F_{Ti}^{111} was expected to be very low and is a real effect.

for the set of coherent fractions; F_{O}^{112} tended to converge to zero, while F_{Ti}^{111} tended to diverge: The optimisation algorithm was interrupted at an arbitrary instant, and the agreement of the simulated and measured spectra was verified when varying each of the six coherent fractions at a time as shown in Fig. E.1. This indicated that the best agreement was obtained if $F_{\mathrm{Sr}}^{111} \approx F_{\mathrm{O}}^{111}$ and $F_{\mathrm{Sr}}^{112} \approx F_{\mathrm{Ti}}^{112}$. This result was likewise obtained by fixing F_{O}^{112} and F_{Ti}^{111} at their present values at the moment, when the algorithm was stopped, and letting the optimisation algorithm continue until convergence. Identical coherent fractions for strontium and oxygen in the (111) reflection and for strontium and titanium in the (112) reflection appear plausible: Under this condition, the smoothest line shapes for the site-specific yield spectra were obtained from the XSW decomposition. This was already suggested by the error analysis for the XSW decomposition in Fig. 7.21 on page 122. By assuming $F_{\mathrm{Sr}}^{111} \approx F_{\mathrm{Sr}}^{112}$, $F_{\mathrm{Ti}}^{111} \approx F_{\mathrm{Ti}}^{112}$ and $F_{\mathrm{O}}^{111} \approx 3F_{\mathrm{O}}^{112}$ and with the two relations above, $F_{\mathrm{Sr}}^{111} \approx F_{\mathrm{O}}^{111} \approx F_{\mathrm{Ti}}^{111}$ could be inferred. It was also reasonable to conclude $3F_{\mathrm{O}}^{112} \approx F_{\mathrm{Sr}}^{112} \approx F_{\mathrm{Ti}}^{112}$. These relations gave reason to include only one single additional fitting parameter f, which served for adjusting the XSW modulation amplitude equally for all valence signal components.

The best agreement of the experimental and simulated spectra was indicated in Fig. E.2(a) by the smallest χ^2 for a common coherent fraction $f \approx 0.88$. Correspondingly, $f/3 \approx 0.29$ for oxygen in the (112) reflection. These values are consistent with $F_{\mathrm{VB}}^{112} = 0.69$ measured for the valence band signal in (112) reflection, provided that the dipole approximation can be applied, and valence electron emission only occurs strongly localised at the atomic cores: Assuming an ideal lattice, a fractional valence yield contribution from the oxygen site of ∼18% in the (112) reflection, compare the decomposition shown in Fig. 7.10 on page 99, will result in a modulation amplitude $F_{\mathrm{VB}}^{112} = (0.82 + 0.06) - 0.12 = 0.76$. A slightly smaller value of 0.69 would be obtained for a structural coherent fraction $f = 0.91$. This value agrees very well with the ob-

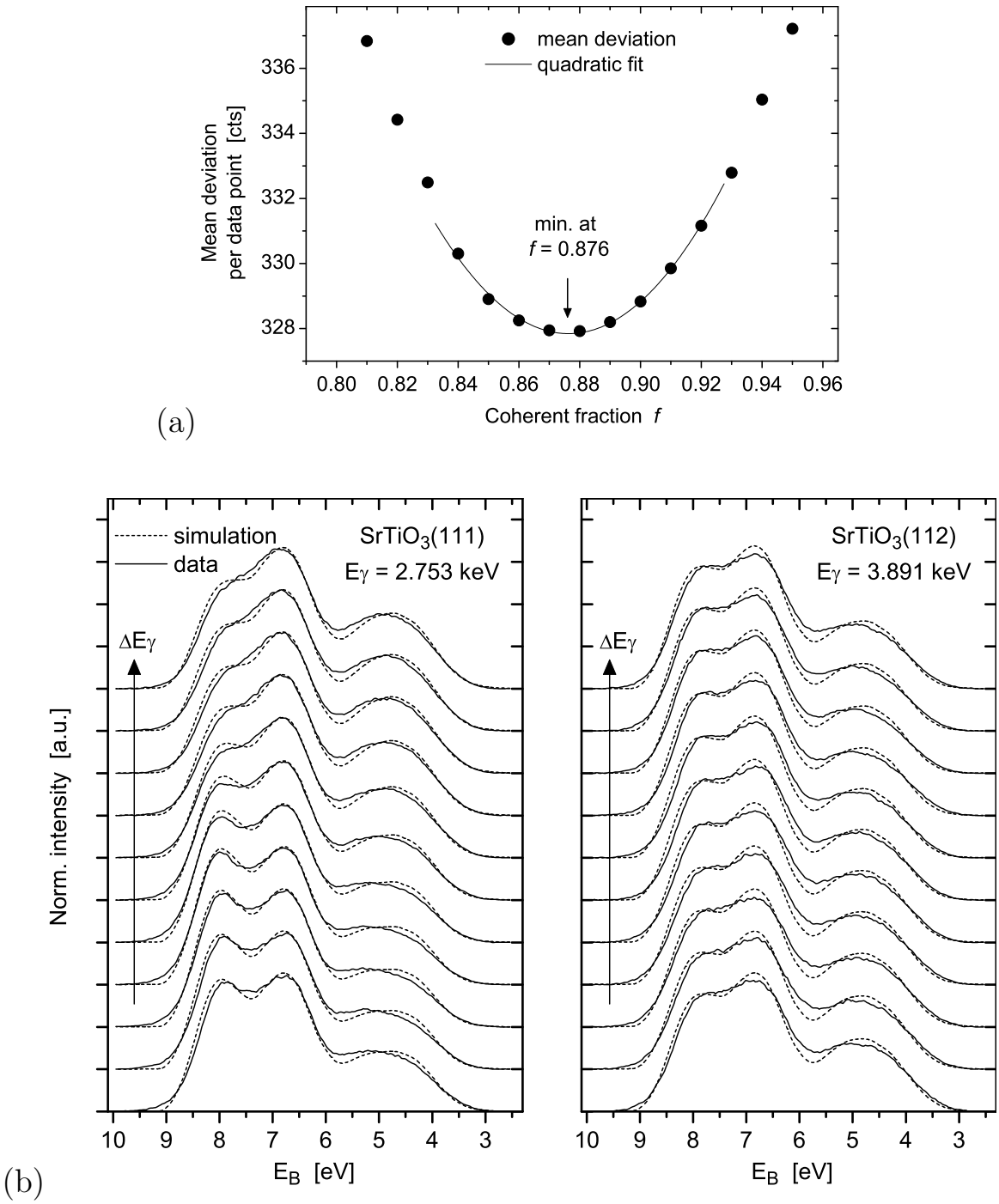

Figure E.2: Comparison of line shapes for measured and simulated $SrTiO_3$ valence band spectra. (a) Goodness of the agreement between the two XSW-modulated data sets as a function of coherent fraction. (b) XSW-modulated line shapes of the recorded raw and the simulated valence band spectra for $f = 0.876$. The details of the simulations are described in the text. (The experimentally recorded spectra are taken from Figs. 7.8(a) and 7.9(a).)

tained coherent fraction of 0.88. On the other hand, a structural coherent fraction of this order appears to be too large for a material like $SrTiO_3$. This suggests that photoemission from the valence band is most likely affected, just like the core level signals, by either quadrupole effects or the unknown effect presented in appendix B.2.

The experimentally recorded spectra and their simulations in Fig. E.2(b) show very good agreement in line shape. The good agreement obtained despite the very strong constraints imposed on the fitting makes this comparison highly meaningful: A minimum of free parameters was used by including one single fitting parameter for all the site-specific XSW modulation amplitudes, and by linear rescaling all of the theoretical lpDOS spectra in binding energy identically. (While empirical element-dependent rescaling would be also possible, identical rescaling maintains the uniformity of the calculated spectra [141], in particular with regard to the fact that GW corrections mainly rigidly shift the valence band towards lower binding energy [144]). The agreement in XSW modulation has much improved in comparison to the simulation in Fig. 7.18. The fitting seemed to be physically sensible although it differed slightly from the previously presented results in Fig. 7.19 on page 115. The O s contribution was enhanced by a factor 3. The ratio of the similarly shaped Sr p and d components, which are difficult to separate, was altered by a factor 3 in favour of the p component. Agreement with the ratio obtained for the strontium spectrum in Fig. 7.17 could not have been expected, since the theoretical spectra were rescaled differently in binding energy in this case.

There are no criteria, which help to decide which kind of data treatment is the best suited. The data analysis presented in this section and the analysis presented in section 7.6 can be considered as equally reliable. In this situation it was decided to give preference to the data analysis, which included the site-specific XSW modulation information that was experimentally measured by core level XPS. For the further discussion of the valence electronic structure and the photoionisation cross sections, we refrained from the results presented in this section. However, the uncertainty in weighting of the O s contribution was taken into consideration in the error bar for the photoionisation cross section.

Appendix F

Hard X-Ray Photoemission on Gold

A HAXPES experiment aiming at the determination of photoionisation cross sections between 5 and 14.5 keV photon energy for the $4f$, $5s$ and $5p$ levels and the $5d$ and $6s$ bands of gold was carried out by an ID32 collaboration led by C. Kunz and has been reported in two publications [120, 175].

Photoionisation cross sections were determined on an absolute scale. The tabulated photoabsorption cross section of C $1s$, which is well established from classical transmission measurements, was used as a reference. Cross sections were determined by comparing the photoemission yield from the individual gold levels to that from the C $1s$ level of a graphite sample. The C $1s$ subshell cross section accounts for almost the entire total cross section.

The hard X-ray photoemission spectra shown in Fig. F.1 were recorded from a freshly cleaved sample of highly oriented pyrolytic graphite (HOPG) that was partially covered with a dc-sputtered thin film of gold. Photoelectron spectroscopy in the 10 keV range was facilitated by the specially designed, home-built HAXPES setup at beamline ID32 shown in Fig. 4.3 on page 37.

During the data analysis (performed by C. Kunz), particular attention was paid to the following three issues:

(i) The XPS angular distribution: The dipole approximation is known to be no longer applicable in the hard X-ray range. Higher order multipole terms need to be taken into consideration to describe the asymmetric angular distribution of photoemitted electrons correctly. For electron kinetic energies beyond 5 keV, no asymmetry parameters were available in the literature at the time of the data analysis. A quadrupole correction was applied to the data. It was based on the asymmetry parameters calculated for 5 keV. The influence of angular effects was shown to be too small to account for the discrepancy between cross section data and calculations.

(ii) The effective attenuation length: The EALs for the photoelectrons are different in gold and carbon. In order to determine the gold cross sections by comparing the Au signals to the reference C $1s$ intensity, the amounts of probed material and therefore the ratio of the EALs for the escaping electrons needs to be known. The

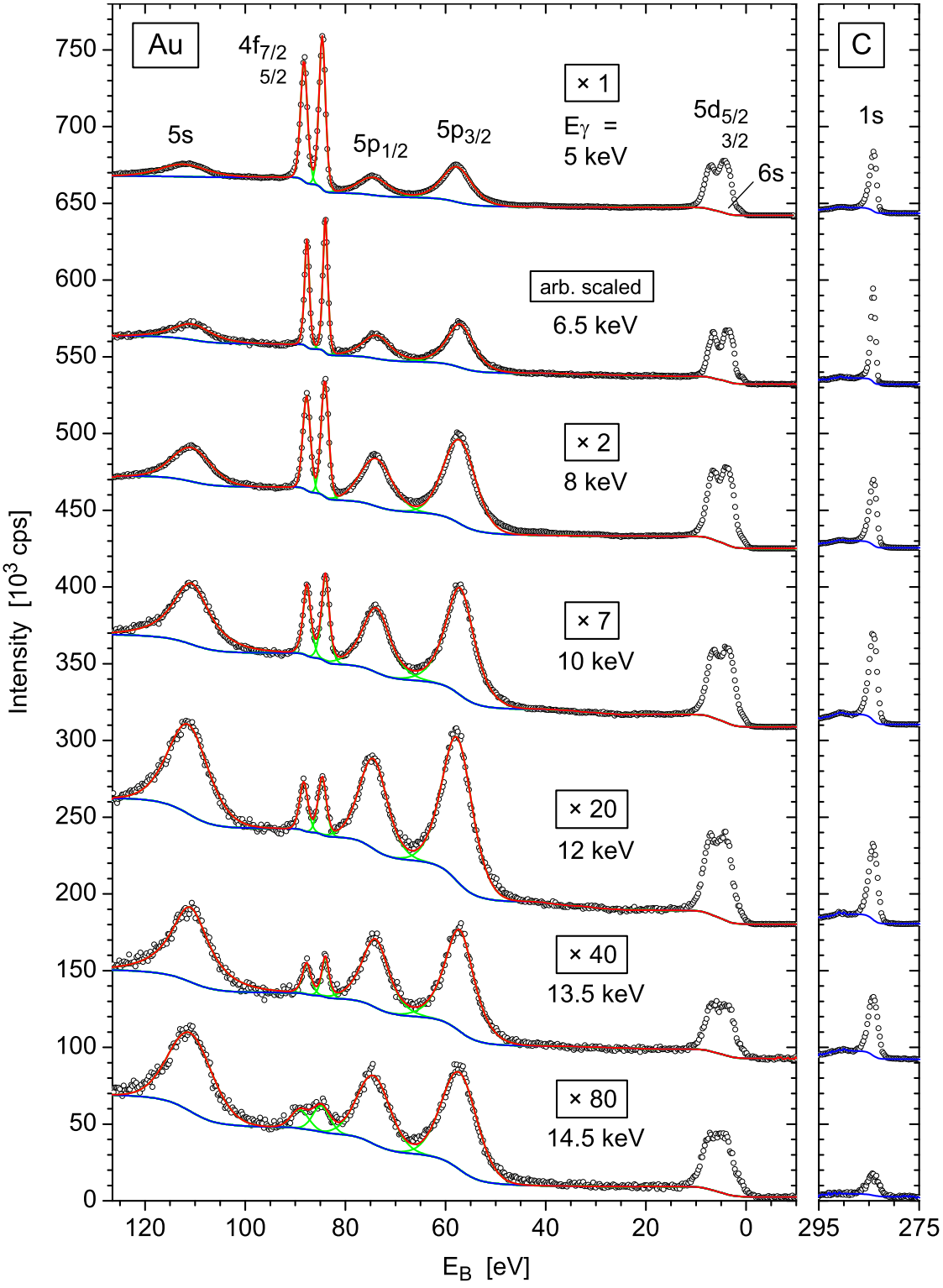

Figure F.1: HAXPES spectra for shallow core levels and the valence band of gold. The gold spectra and the C 1*s* reference spectrum taken at different photon energies are scaled up by the given factors. The data nicely show the predicted [117] relatively rapid decrease in intensity from the *f* states with rising photon energy.

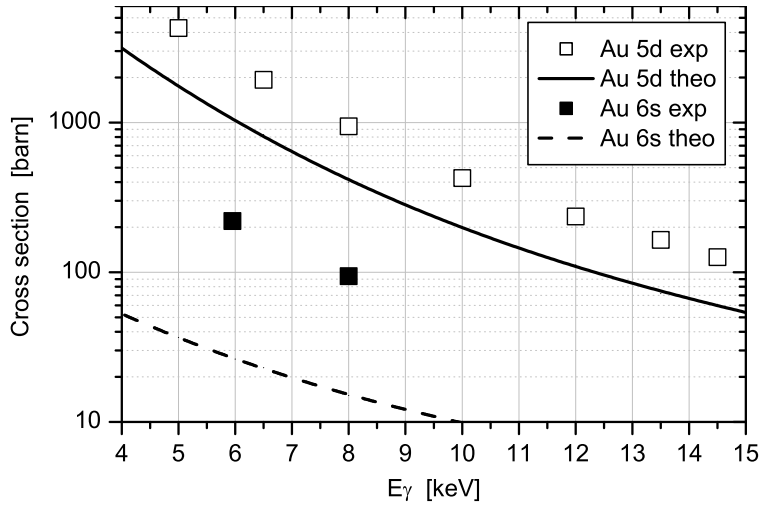

Figure F.2: Experimental and calculated cross sections for Au 5*d* and 6*s* levels. The cross sections measured for the valence band (*d* band) and the Au 6*s*-derived conduction band are compared to atomic values calculated by Scofield [150]. Figure taken from Kunz *et al.* [120].

determined cross sections rely on an EAL ratio estimated by an extrapolation of available data into the hard X-ray range.

(iii) The collection efficiency: As a technical aspect, the transmission of the analyser arrangement consisting of the PHI analyser and the supplementary retarding lens was tested. Suggestions to enhance the count rate were made, like focussing of the X-ray beam to match the size of the focal point of the spectrometer.

The extracted cross sections were compared to Scofield's calculations for atomic orbitals [150]. Fig. F.2 shows the results for the Au 5*d*- and 6*s*-derived states. Independent of binding energy, the cross sections measured for each of the gold core levels exceeded the tabulated values by a factor 2–3. The same deviation was found for the valence band (*d* band) near the Fermi edge, i.e., for electrons that are involved in the metallic bonds. The quasi-free Au 6*s*-derived electrons in the conduction band revealed a cross section almost an order of magnitude larger than the tabulated values. It was suggested to attribute this deviation to hybridization with the overlapping valence band or to other solid state effects.

The energy scaling behaviour of the cross sections does not deviate from the atomic scaling over a large energy range of several keV. This is also true for the Au 5*d*-derived electrons, i.e., possible solid state effects do not become more pronounced when going to shorter radiation wavelength. The lack of Au 6*s* data does not allow a statement for the cross section of the conduction band.

References

[1] T. Haage, J. Zegenhagen, H.-U. Habermeier, and M. Cardona, *Nucleation mechanism of $YBa_2Cu_3O_{7-\delta}$ on $SrTiO_3(001)$*, Phys. Rev. Lett. **80**, 4225 (1998).

[2] J. C. Woicik, E. J. Nelson, and P. Pianetta, *Direct measurement of valence-charge asymmetry by X-ray standing waves*, Phys. Rev. Lett. **84**, 773 (2000).

[3] J. C. Woicik, E. J. Nelson, D. Heskett, J. Warner, L. E. Berman, B. A. Karlin, I. A. Vartanyants, M. Z. Hasan, T. Kendelewicz, Z. X. Shen, and P. Pianetta, *X-ray standing-wave investigations of valence electronic structure*, Phys. Rev. B **64**, 125115 (2001).

[4] J. C. Woicik, E. J. Nelson, T. Kendelewicz, P. Pianetta, M. Jain, L. Kronik, and J. R. Chelikowsky, *Partial density of occupied valence states by X-ray standing waves and high-resolution photoelectron spectroscopy*, Phys. Rev. B **63**, 041403 (2001).

[5] J. C. Woicik, E. J. Nelson, L. Kronik, M. Jain, J. R. Chelikowsky, D. Heskett, L. E. Berman, and G. S. Herman, *Hybridization and bond-orbital components in site-specific X-ray photoelectron spectra of rutile TiO_2*, Phys. Rev. Lett. **89**, 077401 (2002).

[6] J. B. Goodenough, *Metallic oxides*, Prog. Solid State Chem. **5**, 145 (1971), see p. 232.

[7] D. W. Fischer, *X-ray band spectra and molecular-orbital structure of rutile TiO_2*, Phys. Rev. B **5**, 4219 (1972).

[8] C. N. R. Rao and B. Raveau, *Transition metal oxides*, Wiley-VCH, Weinheim, 2nd edition, 1995.

[9] F. A. Cotton, *Chemical applications of group theory*, John Wiley & Sons, New York, 3rd edition, 1990.

[10] M. Tsukada, C. Satoko, and H. Adachi, *Surface electronic structure of $SrTiO_3$ studied by the DV-Xα cluster method*, J. Phys. Soc. Jpn. **48**, 200 (1980).

[11] T. Siegrist, S. Sunshine, D. W. Murphy, R. J. Cava, and S. M. Zahurak, *Crystal structure of the high-T_c superconductor $Ba_2YCu_3O_{9-\delta}$*, Phys. Rev. B **35**, 7137 (1987).

[12] R. P. Sharma, F. J. Rotella, J. D. Jorgensen, and L. E. Rehn, *Neutron diffraction and ion-channeling investigations of atomic displacements in $YBa_2Cu_3O_{7-\delta}$ between 10 and 300 K*, Physica C **174**, 409 (1991).

[13] G. Burns, *High-temperature superconductivity: an introduction*, Academic Press, Inc., San Diego, 1992.

[14] B. W. Veal and C. Gu, *Photoemission studies of the valence bands in $YBa_2Cu_3O_{7-\delta}$*, J. Electron Spectrosc. Relat. Phenom. **66**, 321 (1994).

[15] H. Krakauer, W. E. Pickett, and R. E. Cohen, *Analysis of electronic structure and charge density of the high temperature superconductor $YBa_2Cu_3O_7$*, J. Supercond. **1**, 111 (1988).

[16] H. L. Edwards, J. T. Markert, and A. L. de Lozanne, *Energy gap and surface structure of $YBa_2Cu_3O_{7-x}$ probed by scanning tunneling microscopy*, Phys. Rev. Lett. **69**, 2967 (1992).

[17] D. J. Derro, E. W. Hudson, K. M. Lang, S. H. Pan, J. C. Davis, J. T. Markert, and A. L. de Lozanne, *Nanoscale one-dimensional scattering resonances in the CuO chains of $YBa_2Cu_3O_{6+x}$*, Phys. Rev. Lett. **88**, 097002 (2002).

[18] D. P. Woodruff, *Surface structure determination using X-ray standing waves*, Rep. Prog. Phys. **68**, 743 (2005).

[19] S. Hüfner, *Photoelectron spectroscopy: Principles and applications*, Springer-Verlag, 2nd edition, 1996.

[20] S. Hüfner, S. Schmidt, and F. Reinert, *Photoelectron spectroscopy — An overview*, in Zegenhagen and Kunz [111], page 8.

[21] A. Damascelli, Z. Hussain, and Z.-X. Shen, *Angle-resolved photoemission studies of the cuprate superconductors*, Rev. Mod. Phys. **75**, 473 (2003).

[22] J. Zegenhagen, *Surface structure determination with X-ray standing waves*, Surf. Sci. Rep. **18**, 199 (1993).

[23] J. Stanzel, W. Weigand, L. Kilian, H. L. Meyerheim, C. Kumpf, and E. Umbach, *Chemisorption of NTCDA on Ag(111): A NIXSW study including non-dipolar and electron-stimulated effects*, Surf. Sci. Lett. **571**, 311 (2004).

[24] C. J. Powell, A. Jablonski, I. S. Tilinin, S. Tanuma, and D. R. Penn, *Surface sensitivity of Auger-electron spectroscopy and X-ray photoelectron spectroscopy*, J. Electron Spectrosc. Relat. Phenom. **98-99**, 1 (1999).

[25] A. Yamasaki, A. Sekiyama, S. Imada, M. Tsunekawa, A. Higashiya, A. Shigemoto, and S. Suga, *Bulk sensitive photoelectron spectroscopy with soft and hard X-rays: Soft X-ray ARPES toward high resolution HAXPES*, in Zegenhagen and Kunz [111], page 136.

[26] G. Ertl and J. Küppers, *Low energy electrons and surface chemistry*, chapter 3, Wiley-VCH, Weinheim, 2nd edition, 1985.

[27] Yasutaka Takata, SPring-8, Japan, private communication.

[28] I. A. Vartanyants and J. Zegenhagen, *Photoelectric scattering from an X-ray interference field*, Solid State Commun. **113**, 299 (2000).

[29] Jörg Zegenhagen, ESRF, Grenoble, private communication.

[30] J. Cooper and R. N. Zare, *Angular distribution of photoelectrons*, J. Chem. Phys. **48**, 942 (1968).

[31] J. W. Cooper, *Multipole corrections to the angular distribution of photoelectrons at low energies*, Phys. Rev. A **42**, 6942 (1990).

[32] J. W. Cooper, *Photoelectron-angular-distribution parameters for rare-gas subshells*, Phys. Rev. A **47**, 1841 (1993).

[33] A. Derevianko, W. R. Johnson, and K. T. Cheng, *Non-dipole effects in photoelectron angular distributions for rare gas atoms*, At. Data Nucl. Data Tables **73**, 153 (1999).

[34] A. Derevianko, O. Hemmers, S. Oblad, P. Glans, H. Wang, S. B. Whitfield, R. Wehlitz, I. A. Sellin, W. R. Johnson, and D. W. Lindle, *Electric-octupole and pure-electric-quadrupole effects in soft-X-ray photoemission*, Phys. Rev. Lett. **84**, 2116 (2000).

[35] B. W. Batterman, *Effect of dynamical diffraction in X-ray fluorescence scattering*, Phys. Rev. **133**, A759 (1964).

[36] B. W. Batterman, *Detection of foreign atom sites by their X-ray fluorescence scattering*, Phys. Rev. Lett. **22**, 703 (1969).

[37] D. P. Woodruff, *Normal incidence X-ray standing wave determination of adsorbate structures*, Prog. Surf. Sci. **57**, 1 (1998).

[38] E. J. Nelson, J. C. Woicik, P. Pianetta, I. A. Vartanyants, and J. W. Cooper, *Quadrupole effects in core and valence photoelectron emission from crystalline germanium measured via a spatially modulated X-ray interference field*, Phys. Rev. B **65**, 165219 (2002).

[39] B. W. Batterman and H. Cole, *Dynamical diffraction of X-rays by perfect crystals*, Rev. Mod. Phys. **36**, 681 (1964).

[40] M. von Laue, *Röntgenstrahlinterferenzen*, chapter 22, Akademische Verlagsgesellschaft, Frankfurt am Main, 3rd edition, 1960.

[41] I. A. Vartanyants and J. Zegenhagen, *Quadrupole contribution to the angular resolved photoemission from an X-ray interference field*, Phys. Stat. Sol. (b) **215**, 819 (1999).

[42] I. Vartanyants, T.-L. Lee, S. Thiess, and J. Zegenhagen, *Non-dipole effects in X-ray standing wave photoelectron spectroscopy experiments*, in Zegenhagen and Kunz [111], page 196.

[43] J. C. Woicik, *Site-specific valence X-ray photoelectron spectroscopy*, Synchrotron Radiation News **17**, 48 (2004).

[44] L. Cheng, P. Fenter, M. J. Bedzyk, and N. C. Sturchio, *Fourier-expansion solution of atom distributions in a crystal using X-ray standing waves*, Phys. Rev. Lett. **90**, 255503 (2003).

[45] D. P. Woodruff, B. C. C. Cowie, and A. R. H. F. Ettema, *Surface structure determination using X-ray standing waves: A simple view*, J. Phys.: Condens. Matter **6**, 10633 (1994).

[46] B. E. Warren, *X-ray diffraction*, Dover Publications, Inc., Mineola, New York, 1990.

[47] K. M. Siegbahn, *Electron spectroscopy — an outlook*, J. Electron Spectrosc. Relat. Phenom. **5**, 3 (1974).

[48] K. M. Siegbahn, *Electron spectroscopy for atoms, molecules and condensed matter*, Nobel lecture, 1981, `http://nobelprize.org/physics/laureates/1981/siegbahn-lecture.html`.

[49] G. J. Jackson, J. Lüdecke, D. P. Woodruff, A. S. Y. Chan, N. K. Singh, J. McCombie, R. G. Jones, B. C. C. Cowie, and V. Formoso, *Chemical-shift X-ray standing wave studies: coadsorption site determination of PF_x fragments on Ni(111)*, Surf. Sci. **441**, 515 (1999).

[50] G. J. Jackson, D. P. Woodruff, R. G. Jones, N. K. Singh, A. S. Y. Chan, B. C. C. Cowie, and V. Formoso, *Following local adsorption sites through a surface chemical reaction: CH_3SH on Cu(111)*, Phys. Rev. Lett. **84**, 119 (2000).

[51] A. Hauschild, K. Karki, B. C. C. Cowie, M. Rohlfing, F. S. Tautz, and M. Sokolowski, *Molecular distortions and chemical bonding of a large π-conjugated molecule on a metal surface*, Phys. Rev. Lett. **94**, 036106 (2005).

[52] T.-L. Lee, S. Warren, B. C. C. Cowie, and J. Zegenhagen, *Chemically resolved structure of the Sn/Ge(111) surface*, Phys. Rev. Lett. **96**, 046103 (2006).

[53] T. Higuchi, T. Tsukamoto, S. Yamaguchi, Y. Tezuka, and S. Shin, *Ti-O hybridization effect of Nb-doped $SrTiO_3$ by resonant photoemission spectroscopy*, Jpn. J. Appl. Phys. **40**, L201 (2001).

[54] T. Higuchi, T. Tsukamoto, S. Yamaguchi, Y. Tezuka, and S. Shin, *Ti-O hybridization effect of lightly La-doped $SrTiO_3$ observed by resonant photoemission spectroscopy*, Jpn. J. Appl. Phys. **41**, 5674 (2002).

[55] G. Thorkildsen, R. H. Mathiesen, and H. B. Larsen, *Angle calculations for a six-circle κ diffractometer*, J. Appl. Crystallog. **32**, 943 (1999).

[56] Christof Kunz, Universität Hamburg, and Michel Renier, ESRF mechanics service group, private communication.

[57] SIMION 3D v. 7.0, Ion and electron optics software, D. A. Dahl, Idaho National Engineering and Environmental Laboratory, 1999.

[58] D. Dijkkamp, T. Venkatesan, X. D. Wu, S. A. Shaheen, N. Jisrawi, Y. H. Min-Lee, W. L. McLean, and M. Croft, *Preparation of Y-Ba-Cu oxide superconductor thin films using pulsed laser evaporation from high T_c bulk material*, Appl. Phys. Lett. **51**, 619 (1987).

[59] D. Bhattacharya, R. K. Singh, and P. H. Holloway, *Laser-target interactions during pulsed laser deposition of superconducting thin films*, J. Appl. Phys. **70**, 5433 (1991).

[60] R. K. Singh, B. Bhattacharya, and J. Narayan, *Subsurface heating effects during pulsed laser evaporation of materials*, Appl. Phys. Lett. **57**, 2022 (1990).

[61] S. Proyer, E. Stangl, M. Borz, B. Hellebrand, and D. Bäuerle, *Particulates on pulsed-laser deposited Y-Ba-Cu-O films*, Physica C **257**, 1 (1996).

[62] R. K. Singh and J. Narayan, *Pulsed-laser evaporation technique for deposition of thin films: Physics and theoretical model*, Phys. Rev. B **41**, 8843 (1990).

[63] J. Gonzalo, C. N. Afonso, and J. Perrière, *The role of film re-emission and gas scattering processes on the stoichiometry of laser deposited films*, Appl. Phys. Lett. **67**, 1325 (1995).

[64] R. K. Singh and D. Kumar, *Pulsed laser deposition and characterization of high-T_c $YBa_2Cu_3O_{7-x}$ superconducting thin films*, Mat. Sci. Eng. **R22**, 113 (1998).

[65] T. Haage, *Untersuchungen zu dem Wachstum der mikroskopischen Struktur und den Transporteigenschaften dünner $YBa_2Cu_3O_{7-\delta}$-Schichten auf gestuften Substratoberflächen*, PhD thesis, Universität Stuttgart, Fakultät Physik, 1997, article in german.

[66] K. Kamigaki, H. Terauchi, T. Terashima, Y. Bando, K. Iijima, K. Yamamoto, K. Hirata, K. Hayashi, I. Nakagawa, and Y. Tomii, *Anomalous misfit strain relaxation in ultrathin $YBa_2Cu_3O_{7-\delta}$ epitaxial films*, J. Appl. Phys. **69**, 3653 (1991).

[67] L. Cao and J. Zegenhagen, *Elemental substitution and strain in $RBa_2Cu_3O_{7-\delta}$ superconducting thin films*, Phys. Stat. Sol. (b) **215**, 587 (1999).

[68] T. Haage, H.-U. Habermeier, and J. Zegenhagen, *Periodic step structure of clean and $YBa_2Cu_3O_{7-\delta}$-covered vicinal $SrTiO_3$(001) surfaces*, Surf. Sci. Lett. **370**, L158 (1997).

[69] R. Bormann and J. Nölting, *Stability limits of the perovskite structure in the Y-Ba-Cu system*, Appl. Phys. Lett. **54**, 2148 (1989).

[70] R. H. Hammond and R. Bormann, *Correlation between the in situ growth conditions of YBCO thin films and the thermodynamic stability criteria*, Physica C **162-164**, 703 (1989).

[71] P. Schleger, W. N. Hardy, and B. X. Yang, *Thermodynamics of oxygen in $Y_1Ba_2Cu_3O_x$ between 450°C and 650°C*, Physica C **176**, 261 (1991).

[72] V. E. Henrich, G. Dresselhaus, and H. J. Zeiger, *Surface defects and the electronic structure of $SrTiO_3$ surfaces*, Phys. Rev. B **17**, 4908 (1978).

[73] F. L. Battye, H. Höchst, and A. Goldmann, *Photoelectron studies of the $BaTiO_3$ and $SrTiO_3$ valence states*, Solid State Commun. **19**, 269 (1976).

[74] Q. D. Jiang and J. Zegenhagen, *$SrTiO_3$(001) surfaces and growth of ultra-thin $GdBa_2Cu_3O_{7-x}$ films studied by LEED/AES and UHV-STM*, Surf. Sci. Lett. **338**, L882 (1995).

[75] Q. D. Jiang and J. Zegenhagen, *c(6×2)- and c(4×2)-reconstruction of $SrTiO_3$(001)*, Surf. Sci. **425**, 343 (1999).

[76] N. Erdman, O. Warschkow, M. Asta, K. R. Poeppelmeier, D. E. Ellis, and L. D. Marks, *Surface structures of $SrTiO_3$(001): A TiO_2-rich reconstruction with a c(4×2) unit cell*, J. Am. Chem. Soc. **125**, 10050 (2003).

[77] O. N. Tufte and E. L. Stelzer, *Piezoresistive properties of reduced strontium titanate*, Phys. Rev. **141**, 675 (1966).

[78] O. N. Tufte and P. W. Chapman, *Electron mobility in semiconducting strontium titanate*, Phys. Rev. **155**, 796 (1967).

[79] H. P. R. Frederikse, W. R. Thurber, and W. R. Hosler, *Electronic transport in strontium titanate*, Phys. Rev. **134**, A442 (1964).

[80] R. A. Powell and W. E. Spicer, *Photoemission investigation of surface states on strontium titanate*, Phys. Rev. B **13**, 2601 (1976).

[81] Chengtian Lin, Crystal growth service group, Max-Planck-Institut für Festkörperforschung Stuttgart, private communication.

[82] C. T. Lin and A. Kulakov, *In situ observation of ferroelastic detwinning of $YBa_2Cu_3O_{7-\delta}$ single crystals grown by flux*, in *Wissenschaftlicher Tätigkeitsbericht*, Max-Planck-Institut für Festkörperforschung Stuttgart, 2002.

[83] C. T. Lin, W. Zhou, W. Y. Liang, E. Schönherr, and H. Bender, *Growth of large untwinned single crystal of YBCO*, Physica C **195**, 291 (1992).

[84] C. T. Lin, *Screw dislocations of $YBa_2Cu_3O_{7-\delta}$ single crystals revealed by chemical etching*, J. Cryst. Growth **143**, 110 (1994).

[85] C. T. Lin, *Study of growth spirals and screw dislocations on $YBa_2Cu_3O_{7-\delta}$ single crystals*, Physica C **337**, 312 (2000).

[86] A. Erb, E. Walker, J.-Y. Genoud, and R. Flükiger, *10 years of crystal growth of the 123- and 124- high T_c superconductors: From Al_2O_3 to $BaZrO_3$ — Progress in crystal growth and sample quality and its impact on physics*, Physica C **282-287**, 459 (1997).

[87] Eva Brücher, Chemical service group, Max-Planck-Institut für Festkörperforschung Stuttgart, private communication.

[88] R. S. List, A. J. Arko, Z. Fisk, S.-W. Cheong, S. D. Conradson, J. D. Thompson, C. B. Pierce, D. E. Peterson, R. J. Bartlett, N. D. Shinn, J. E. Schirber, B. W. Veal, A. P. Paulikas, and J. C. Campuzano, *Photoemission from single crystals of $EuBa_2Cu_3O_{7-x}$ cleaved below 20 K: Temperature-dependent oxygen loss*, Phys. Rev. B **38**, 11966 (1988).

[89] R. P. Vasquez, *Intrinsic photoemission signals, surface preparation, and surface stability of high temperature superconductors*, J. Electron Spectrosc. Relat. Phenom. **66**, 209 (1994).

[90] C. R. Brundle and D. E. Fowler, *Characterization of $YBa_2Cu_3O_x$ using core- and valence-level XPS*, Surf. Sci. Rep. **19**, 143 (1993).

[91] M. C. Schabel, C.-H. Park, A. Matsuura, Z.-X. Shen, D. A. Bonn, R. Liang, and W. N. Hardy, *Angle-resolved photoemission on untwinned $YBa_2Cu_3O_{6.95}$. I. Electronic structure and dispersion relations of surface and bulk bands*, Phys. Rev. B **57**, 6090 (1998).

[92] J. Als-Nielsen and D. McMorrow, *Elements of modern X-ray physics*, John Wiley & Sons, Chichester, 2001.

[93] T. Haage, J. Zegenhagen, J. Q. Li, H.-U. Habermeier, M. Cardona, C. Jooss, R. Warthmann, A. Forkl, and H. Kronmüller, *Transport properties and flux pinning by self-organization in $YBa_2Cu_3O_{7-\delta}$ films on vicinal $SrTiO_3(001)$*, Phys. Rev. B **56**, 8404 (1997).

[94] J. Zegenhagen, T. Haage, and Q. D. Jiang, *Microscopic structure and structuring of perovskite surfaces and interfaces: $SrTiO_3$, $RBa_2Cu_3O_{7-\delta}$*, Appl. Phys. A **67**, 711 (1998).

[95] A. Kazimirov, L. X. Cao, G. Scherb, L. Cheng, M. J. Bedzyk, and J. Zegenhagen, *X-ray standing wave analysis of the rare-earth atomic positions in $RBa_2Cu_3O_{7-\delta}$ thin films*, Solid State Commun. **114**, 271 (2000).

[96] A. Kazimirov, T. Haage, L. Ortega, A. Stierle, F. Comin, and J. Zegenhagen, *Excitation of an X-ray standing wave in a $SmBa_2Cu_3O_{7-\delta}$ thin film*, Solid State Commun. **104**, 347 (1997).

[97] M. Nakanishi, H. Hashizume, T. Terashima, Y. Bando, O. Michikami, S. Maeyama, and M. Oshima, *Structure of the growth interface of Y-Ba-Cu-O analogs on $SrTiO_3(001)$ substrates*, Phys. Rev. B **48**, 10524 (1993).

[98] T.-L. Lee, S. Warren, L. X. Cao, S. Thiess, B. C. C. Cowie, and J. Zegenhagen, *Atomic structure of $GdBa_2Cu_3O_{7-\delta}$ superconductor thin films on $NdGaO_3(001)$ probed by X-ray standing waves and photoelectron spectroscopy*, in Zegenhagen and Kunz [111], page 216.

[99] J. Zegenhagen, T. Siegrist, E. Fontes, L. E. Berman, and J. R. Patel, *Epitaxy of ultrathin films of $YBa_2Cu_3O_{7-\delta}$ on $SrTiO_3(001)$ investigated with X-ray standing waves*, Solid State Commun. **93**, 763 (1995).

[100] M. O. Krause, *Atomic radiative and radiationless yields for K and L shells*, J. Phys. Chem. Ref. Data **8**, 307 (1979).

[101] B. L. Henke, E. M. Gullikson, and J. C. Davis, *X-ray interactions: photoabsorption, scattering, transmission, and reflection at E = 50–30,000 eV, Z = 1–92*, At. Data Nucl. Data Tables **54**, 181 (1993), for a calculator on the Web see `http://www-cxro.lbl.org/optical_constants/`.

[102] H. Kiessig, *Interferenz von Röntgenstrahlen an dünnen Schichten*, Ann. Phys. (Leipzig) **10**, 769 (1931), article in german.

[103] Tien-Lin Lee, ESRF, Grenoble, private communication.

[104] M. Lei, J. L. Sarrao, W. M. Visscher, T. M. Bell, J. D. Thompson, A. Migliori, U. W. Welp, and B. W. Veal, *Elastic constants of a monocrystal of superconducting* $YBa_2Cu_3O_{7-\delta}$, Phys. Rev. B **47**, 6154 (1993).

[105] M. P. Seah and W. A. Dench, *Quantitative electron spectroscopy of surfaces: a standard data base for electronic inelastic mean free paths in solids*, Surf. Interf. Anal. **1**, 2 (1979).

[106] Y. A. Abramov, V. G. Tsirelson, V. E. Zavodnik, S. A. Ivanov, and I. D. Brown, *The chemical bond and atomic displacements in* $SrTiO_3$ *from X-ray diffraction analysis*, Acta Crystallogr. **B51**, 942 (1995).

[107] S. L. Chaplot, *Phonon dispersion relation in* $YBa_2Cu_3O_7$, Phys. Rev. B **37**, 7435 (1988), and references therein for experimental X-ray and neutron diffraction data.

[108] C. Dallera, L. Duò, L. Braicovich, G. Panaccione, G. Paolicelli, B. C. C. Cowie, and J. Zegenhagen, *Looking 100 Å deep into spatially inhomogeneous dilute systems with hard X-ray photoemission*, Appl. Phys. Lett. **85**, 4532 (2004).

[109] M. Sacchi, F. Offi, P. Torelli, A. Fondacaro, C. Spezzani, M. Cautero, G. Cautero, S. Huotari, M. Grioni, R. Delaunay, M. Fabrizioli, G. Vankó, G. Monaco, G. Paolicelli, G. Stefani, and G. Panaccione, *Quantifying the effective attenuation length in high-energy photoemission experiments*, Phys. Rev. B **71**, 155117 (2005).

[110] I. Lindau, P. Pianetta, S. Doniach, and W. E. Spicer, *X-ray photoemission spectroscopy*, Nature **250**, 214 (1974).

[111] J. Zegenhagen and C. Kunz, editors, *Proceedings of the workshop on hard X-ray photoelectron spectroscopy, ESRF, Grenoble, 11–12 Sept. 2003*, number 547 in Nucl. Instrum. Meth. in Phys. Res. A, 2005.

[112] K. Kobayashi, M. Yabashi, Y. Takata, T. Tokushima, S. Shin, K. Tamasaku, D. Miwa, T. Ishikawa, H. Nohira, T. Hattori, Y. Sugita, O. Nakatsuka, A. Sakai, and S. Zaima, *High resolution high energy X-ray photoelectron spectroscopy using third-generation synchrotron radiation source, and its application to Si-high k insulator systems*, Appl. Phys. Lett. **83**, 1005 (2003).

[113] Y. Takata, K. Tamasaku, T. Tokushima, D. Miwa, S. Shin, T. Ishikawa, M. Yabashi, K. Kobayashi, J. J. Kim, T. Yao, T. Yamamoto, M. Arita, H. Namatame, and M. Taniguchi, *A probe of the intrinsic valence band electronic structure: Hard X-ray photoemission*, Appl. Phys. Lett. **84**, 4310 (2004).

[114] A. Chainani, T. Yokoya, Y. Takata, K. Tamasaku, M. Taguchi, T. Shimojima, N. Kamakura, K. Horiba, S. Tsuda, S. Shin, D. Miwa, Y. Nishino, T. Ishikawa, M. Yabashi, K. Kobayashi, H. Namatame, M. Taniguchi, K. Takada, T. Sasaki, H. Sakurai, and E. Takayama-Muromachi, *Bulk electronic structure of* $Na_{0.35}CoO_2{\cdot}1.3H_2O$, Phys. Rev. B **69**, 180508(R) (2004).

[115] G. Paolicelli, A. Fondacaro, F. Offi, G. Stefani, G. Cautero, M. Cautero, B. Krastanov, P. Lacovig, P. Pittana, R. Sergo, R. Tommasini, P. Torelli, M. Sacchi, M. Grioni, G. Monaco, and G. Panaccione, *Bulk sensitive photoemission: first results of the VOLPE project at the ESRF*, J. Electron Spectrosc. Relat. Phenom. **144–147**, 963 (2005).

[116] M. B. Trzhaskovskaya, V. K. Nikulin, V. I. Nefedov, and V. G. Yarzhemsky, *Non-dipole second order parameters of the photoelectrons angular distribution for elements z = 1–100 in the photoelectron energy range 1–10 keV*, At. Data Nucl. Data Tables **92**, 245 (2006).

[117] Christof Kunz, Universität Hamburg, Germany, private communication.

[118] G. Panaccione, G. Cautero, M. Cautero, A. Fondacaro, M. Grioni, C. Henriquet, G. Monaco, M. Mulazzi, F. Offi, L. Paolasini, G. Paolicelli, P. Pittana, M. Sacchi, G. Stefani, and P. Torelli, *Results and perspectives in hard X-ray photoemission spectroscopy (HAXPES) from solids*, Nucl. Instrum. Meth. in Phys. Res. B **246**, 106 (2006).

[119] C.-Y. Kim, M. J. Bedzyk, E. J. Nelson, J. C. Woicik, and L. E. Berman, *Site-specific valence-band photoemission study of α-Fe_2O_3*, Phys. Rev. B **66**, 085115 (2002).

[120] C. Kunz, S. Thiess, B. C. C. Cowie, T.-L. Lee, and J. Zegenhagen, *Outer sub-shell photoabsorption cross-sections determined by X-ray photoelectron spectroscopy up to 14.5 keV*, in Zegenhagen and Kunz [111], page 73.

[121] G. Panaccione, G. Cautero, M. Cautero, A. Fondacaro, M. Grioni, P. Lacovig, G. Monaco, F. Offi, G. Paolicelli, M. Sacchi, N. Stojić, G. Stefani, R. Tommasini, and P. Torelli, *High-energy photoemission in silver: resolving d and sp contributions in valence band spectra*, J. Phys.: Condens. Matter **17**, 2671 (2005).

[122] K. Kobayashi, Y. Takata, T. Yamamoto, J. J. Kim, H. Makino, K. Tamasaku, M. Yabashi, D. Miwa, T. Ishikawa, S. Shin, and T. Yao, *Intrinsic valence band study of molecular-beam-epitaxy-grown GaAs and GaN by high-resolution hard X-ray photoemission spectroscopy*, Jpn. J. Appl. Phys. **43**, L1029 (2004).

[123] K. Kobayashi, *High-resolution hard X-ray photoelectron spectroscopy: Application of valence band and core level spectroscopy to materials science*, in Zegenhagen and Kunz [111], page 98.

[124] A. H. Kahn and A. J. Leyendecker, *Electronic bands in strontium titanate*, Phys. Rev. **135**, A1321 (1964).

[125] L. F. Mattheiss, *Energy bands for $KNiF_3$, $SrTiO_3$, $KMoO_3$, and $KTaO_3$*, Phys. Rev. B **6**, 4718 (1972).

[126] P. Pertosa and F. M. Michel-Calendini, *X-ray photoelectron spectra, theoretical band structures, and densities of states for $BaTiO_3$ and $KNbO_3$*, Phys. Rev. B **17**, 2011 (1978).

[127] P. Pertosa, G. Hollinger, and F. M. Michel-Calendini, *Covalency effects in transition-metal perovskitelike compounds: Partial densities of p and d states and photoelectron valence-band spectra*, Phys. Rev. B **18**, 5177 (1978).

[128] F. M. Michel-Calendrini, P. Pertosa, and G. Metrat, *Electronic structure of ABO_3 perovskites: ESCA experiments and band structure for $BaTiO_3$, $KNbO_3$ and $KTaO_3$*, Ferroelectrics **21**, 637 (1978).

[129] T. Wolfram and Ş. Ellialtıoğlu, *Model for the X-ray photoelectron distribution of d-band perovskites*, Phys. Rev. B **19**, 43 (1979).

[130] R. Courths, *Ultraviolet Photoelectron Spectroscopy (UPS) and LEED Studies of $BaTiO_3$ (001) and $SrTiO_3$ (100) Surfaces*, Phys. Stat. Sol. (b) **100**, 135 (1980).

[131] R. Courths, *Valence band UPS spectra and partial p and d density of states in $SrTiO_3$, $BaTiO_3$ and $LiNbO_3$*, Ferroelectrics **26**, 749 (1980).

[132] T. Wolfram and Ş. Ellialtıoğlu, *Concepts of surface states and chemisorption on d-band perovskites*, in *Theory of chemisorption*, edited by J. R. Smith, Topics in current physics, chapter 6, Springer-Verlag, Berlin, 1980.

[133] F. M. F. de Groot, J. Faber, J. J. M. Michiels, M. T. Czyżyk, M. Abbate, and J. C. Fuggle, *Oxygen 1s X-ray absorption of tetravalent titanium oxides: A comparison with single-particle calculations*, Phys. Rev. B **48**, 2074 (1993).

[134] Ş. Ellialtıoğlu and T. Wolfram, *Electronic density of states for the perovskites*, Phys. Rev. B **15**, 5909 (1977).

[135] N. B. Brookes, D. S. L. Law, T. S. Padmore, D. R. Warburton, and G. Thornton, *The electronic structure of $SrTiO_3$ from a direct-transition analysis of angle-resolved photoemission data*, Solid State Commun. **57**, 473 (1986).

[136] B. Reihl, J. G. Bednorz, K. A. Müller, Y. Jugnet, G. Landgren, and J. F. Morar, *Electronic structure of $SrTiO_3$*, Phys. Rev. B **30**, 803 (1984).

[137] T. Fujii, M. Kimura, H. Yoshikawa, and S. Fukushima, *Site-specific valence-band X-ray photoelectron spectra of a $SrTiO_3$ single-crystal by X-ray standing wave technique*, Solid State Commun. **136**, 375 (2005).

[138] N. Erdman, K. R. Poeppelmeier, M. Asta, O. Warschkow, D. E. Ellis, and L. D. Marks, *The structure and chemistry of the TiO_2-rich surface of $SrTiO_3(001)$*, Nature **419**, 55 (2002).

[139] S. A. Chambers, T. Droubay, T. C. Kaspar, M. Gutowski, and M. van Schilfgaarde, *Accurate valence band maximum determination for $SrTiO_3(001)$*, Surf. Sci. **554**, 81 (2004).

[140] W. H. Press, S. A. Teukolsky, W. T. Vetterling, and B. P. Flannery, *Numerical recipes in C: The art of scientific computing*, chapter 15.4, Cambridge University Press, 2nd edition, 1992.

[141] François Bottin, CEA Bruyères-le-Châtel, France, private communication.

[142] P. Hohenberg and W. Kohn, *Inhomogeneous electron gas*, Phys. Rev. **136**, B864 (1964).

[143] W. Kohn and L. J. Sham, *Self-consistent equations including exchange and correlation effects*, Phys. Rev. **140**, A1133 (1965).

[144] F. M. F. Cappellini, S. Bouette-Russo, B. Amadon, C. Noguera, and F. Finocchi, *Structural properties and quasiparticle energies of cubic SrO, MgO and $SrTiO_3$*, J. Phys.: Condens. Matter **12**, 3671 (2000).

[145] M. B. Trzhaskovskaya, V. I. Nefedov, and V. G. Yarzhemsky, *Photoelectron angular distribution parameters for elements $z = 1$ to $z = 54$ in the photoelectron energy range 100–5000 eV*, At. Data Nucl. Data Tables **77**, 97 (2001).

[146] M. B. Trzhaskovskaya, V. I. Nefedov, and V. G. Yarzhemsky, *Photoelectron angular distribution parameters for elements $z = 55$ to $z = 100$ in the photoelectron energy range 100–5000 eV*, At. Data Nucl. Data Tables **82**, 257 (2002).

[147] MathCAD v. 6.0, Calculation software package, Mathsoft Inc., Cambridge, MA, 1995, `http://www.mathsoft.com`.

[148] M. Cardona, *Optical properties and band structure of $SrTiO_3$ and $BaTiO_3$*, Phys. Rev. **140**, A651 (1965).

[149] Y. Aiura, I. Hase, H. Bando, T. Yasue, T. Saitoh, and D. S. Dessau, *Photoemission study of the metallic state of lightly electron-doped $SrTiO_3$*, Surf. Sci. **515**, 61 (2002).

[150] J. H. Scofield, *Theoretical photoionization cross sections from 1 to 1500 keV*, Lawrence Livermore National Laboratory Report UCRL-51326, University of California, Livermore, CA, 1973.

[151] S. Matsushima, S. Kohiki, and M. Oku, *Difference of electronic structures between $SrTiO_3$ and $BaTiO_3$*, J. Ceram. Soc. Jpn. **108**, 952 (2000).

[152] K. M. Glassford and J. R. Chelikowsky, *Structural and electronic properties of titanium dioxide*, Phys. Rev. B **46**, 1284 (1992).

[153] K. Siegbahn, C. Nordling, G. Johansson, J. Hedman, P. F. Hedén, K. Hamrin, U. Gelius, T. Bergmark, L. O. Werme, R. Manne, and Y. Baer, *ESCA applied to free molecules*, North-Holland Publishing Company, Amsterdam, 1969.

[154] K. C. Mishra, K. H. Johnson, and P. C. Schmidt, *A comparative study of the electronic structures of titanium dioxide and strontium titanate*, J. Phys. Chem. Solids **54**, 237 (1993).

[155] L. Mattsson, L. Karlsson, R. Jadrny, and K. Siegbahn, *Valence electron spectrum of C_6H_6 excited by linearly polarized HeI Radiation*, Physica Scripta **16**, 221 (1977), note that this volume contains a number of interesting related articles.

[156] V. A. Bushuev, A. Y. Kazimirov, and M. V. Koval'chuk, *Determination of the valence-electron component of the atomic scattering factor of silicon by means of a Compton effect excited by an X-ray standing wave*, JTEP Lett. **47**, 187 (1988).

[157] E. Storm and H. I. Israel, *Photon cross sections from 1 keV to 100 MeV for elements z = 1 to z = 100*, Nucl. Data Tables **A7**, 565 (1970).

[158] K. Larbaoui, A. Tadjer, B. Abbar, H. Aourag, B. Khelifa, and C. Mathieu, *State of the art simulations in electronic structure and total energy for the high temperature superconductor $YBa_2Cu_3O_7$*, J. Alloys Comp. **403**, 1 (2005).

[159] R. P. Vasquez, *Alkaline earth core level photoemission spectroscopy of high temperature superconductors*, J. Electron Spectrosc. Relat. Phenom. **66**, 241 (1994).

[160] S. Thiess, T.-L. Lee, C. T. Lin, L. X. Cao, C. Aruta, S. Warren, B. C. C. Cowie, and J. Zegenhagen, *X-ray standing wave photoemission study of a $YBa_2Cu_3O_{7-\delta}$ single crystal*, Phys. Stat. Sol. (b) **233**, R5 (2002).

[161] R. Liang, D. A. Bonn, and W. N. Hardy, *Growth of high quality YBCO single crystals using $BaZrO_3$ crucibles*, Physica C **304**, 105 (1998).

[162] W. R. Flavell and R. G. Egdell, *Parallel valence- and core-level photoemission studies of the metal-to-nonmetal transition in $YBa_2Cu_3O_{7-\delta}$*, Phys. Rev. B **39**, 231 (1989).

[163] J. J. Lee, C. J. Fisher, D. P. Woodruff, M. G. Roper, R. G. Jones, and B. C. C. Cowie, *Non-dipole effects in photoelectron-monitored X-ray standing wave experiments: characterisation and calibration*, Surf. Sci. **494**, 166 (2001).

[164] C. J. Fisher, R. Ithin, R. G. Jones, G. J. Jackson, D. P. Woodruff, and B. C. C. Cowie, *Non-dipole photoemission effects in x-ray standing wavefield determination of surface structure*, J. Phys.: Condens. Matter **10**, L623 (1998).

[165] G. J. Jackson, B. C. C. Cowie, D. P. Woodruff, R. G. Jones, M. S. Kariapper, C. Fisher, A. S. Y. Chan, and M. Butterfield, *Atomic quadrupolar photoemission asymmetry parameters from a solid state measurement*, Phys. Rev. Lett. **84**, 2346 (2000).

[166] F. Schreiber, K. A. Ritley, I. A. Vartanyants, H. Dosch, J. Zegenhagen, and B. C. C. Cowie, *Non-dipolar contributions in XPS detection of X-ray standing waves*, Surf. Sci. Lett. **486**, L519 (2001).

[167] J. Zegenhagen, G. Materlik, and W. Uelhoff, *X-ray standing wave analysis of highly perfect Cu crystals and electrodeposited submonolayers of Cd and Tl on Cu surfaces*, J. X-ray Sci. Tech. **2**, 214 (1990).

[168] N. Troullier and J. L. Martins, *Efficient pseudopotentials for plane-wave calculations*, Phys. Rev. B **43**, 1993 (1991).

[169] M. Fuchs and M. Scheffler, *Ab initio pseudopotentials for electronic structure calculations of poly-atomic systems using density-functional theory*, Comput. Phys. Commun. **119**, 67 (1999), more information on the software: `http://www.fhi-berlin.mpg.de/th/fhi98md/fhi98PP/`.

[170] X. Gonze, J.-M. Beuken, R. Caracas, F. Detraux, M. Fuchs, G.-M. Rignanese, L. Sindic, M. Verstraete, G. Zerah, F. Jollet, M. Torrent, A. Roy, M. Mikami, P. Ghosez, J.-Y. Raty, and D. C. Allan, *First-principles computation of material properties: the ABINIT software project*, Comput. Mater. Sci. **25**, 478 (2002), more information on the ABINIT project can be found under `http://www.abinit.org/`.

[171] H. J. Monkhorst and J. D. Pack, *Special points for Brillouin-zone integrations*, Phys. Rev. B **13**, 5188 (1976).

[172] R. F. W. Bader, T. Tung Nguyen-Dang, and Y. Tal, *Quantum topology of molecular charge distributions. II. Molecular structure and its change*, J. Chem. Phys. **70**, 4316 (1979).

[173] R. F. W. Bader and P. M. Beddall, *Virial field relationship for molecular charge distributions and the spatial partitioning of molecular properties*, J. Chem. Phys. **56**, 3320 (1972).

[174] R. F. W. Bader, `http://www.chemistry.mcmaster.ca/faculty/bader`.

[175] S. Thiess, C. Kunz, B. C. C. Cowie, T.-L. Lee, M. Renier, and J. Zegenhagen, *Hard X-ray photoelectron spectroscopy from 5–14.5 keV*, Solid State Commun. **132**, 589 (2004).

Acknowledgements

During my thesis work at the ESRF in Grenoble I enjoyed the co-operation with many people. I would like to thank all those who contributed to the success of this thesis work by guiding, supporting and encouraging me:

My thesis adviser **Jörg Zegenhagen** gave me the chance to work in an inspiring scientific environment. He granted me all the freedom I wished during the experimental work, including the chance to familiarize myself with a wealth of scientific equipment that I had at my disposal, while at the same time, he was available for advice and discussion at truly any time. He encouraged me to visit the MRS conference and research groups overseas. His enduring support during the difficult time of writing is very highly appreciated. He devoted time to proof reading the thesis manuscript.

I would like to thank especially **Robert Johnson** and **Kurt Scharnberg** for assuming the responsibility to report on this thesis.

I had the pleasure of working closely with two postdocs, later scientists, who shared their knowledge and experience with me: In particular, I deem myself lucky in having worked together with **Tien-Lin Lee**. I very highly appreciate the thorough introduction to synchrotron work he gave me, his readiness to help and to discuss physical issues. We shared a lot of sleepless synchrotron night shifts together. Tien-Lin also taught me the methodical approach to successfully plan and prepare synchrotron experiments. I enjoyed sharing an office with him, where we had kilogrammes of French grapes in summer. Finally, I will not forget to mention his contagious enthusiasm and his nice sense of humour. Thanks Tien-Lin for what I have learned from you. Furthermore, I am very grateful to **Lixin Cao**, who introduced me to UHV technology at the beginning of my thesis work. I have profited a lot from his expertise in preparing high temperature superconducting films by pulsed laser deposition. Beyond physics, it was a pleasure to learn about Chinese culture from Lixin. I remember the moon cakes he brought to the beamline one day.

Beamline ID08 staff members **Federica Venturini** and **Nicholas Brookes** supported me to carry out the standing waves experiment on $YBa_2Cu_3O_{7-\delta}$ in the soft X-ray range. Special thanks to **Carmela Aruta**, who especially arrived from Italy to participate in the experiment (and who brought delicious — and highly memory-loaded — Perugia bonbons). **Kenneth Larsson** provided skillful technical assistance by preparing parts of the experimental rig.

I would like to thank **Vedran Vonk**, who let me have several days of his in-house beamtime at beamline ID15c at the ESRF.

Lively exchange of thoughts per email with **Ivan Vartanyants** about the influence of multipole effects in photoemission on XSW data was helpful. I am also indebted to

François Bottin, who carried out the *ab initio* density functional theory calculations for $SrTiO_3$ and who came to the ESRF for a visit to present his results.

For excellent technical support I would like to thank **Hamid Djazouli** and **Lionel André**, who rapidly and reliably solved smaller and larger problems in the surface characterisation laboratory and at the beamline. Likewise, the accomplished help from the mechanics workshop lead by **Werner Schmid** is appreciated. During the technical preparations of the HAXPES experiment I profited from the scientific experience of **Christof Kunz** and the technical knowledge of **Michel Renier**. Participating in the planning of this experiment was an enriching experience for me. **Oliver Bunk** provided practical advice in TEX.

Superior $YBa_2Cu_3O_{7-\delta}$ single crystals were kindly provided by **Chengtian Lin** from the crystal growth service group of the Max-Planck-Institut für Festkörperforschung in Stuttgart. **Eva Brücher** from the chemical service group of the MPI Stuttgart recorded magnetisation curves for a number of superconductor crystals and films. **Iraida Snigireva** from the microimaging laboratory at the ESRF carried out gold sputter deposition on various samples.

All members of the ID32 surface science group at the ESRF have contributed to the truly pleasant working atmosphere during all the years. Beyond those mentioned above, I would like to thank **Bruce Cowie**, **Yvonne Gründer**, **Helena Isern-Herrera**, **Isabelle Joumard**, **Laure Libralesso**, **Manuel Perez**, **Frank Renner**, **Christian Rettig**, **Thomas Schröder**, and **Samantha Warren**. Not only during long working hours but also during nice chats and coffee breaks I became friends with many colleagues, also from the neighbour beamlines ID01 and ID03 and other beamlines around the ring. **Paul Lyman** and **Didier Wermeille** were pleasant temporary office mates. I would like to thank **Till Metzger** for good advice.

Last but not least, I would like to thank especially my sister **Ulrike** and my parents, **Dorothea** and **Willi Thieß**, for their personal as well as financial support during all the years, making it possible for me to gain an excellent education.

Sebastian Thieß